


Spring 1-1-2017

Advances in Design and Optimization Using Immersed Boundary Methods

Ashesh Sharma

University of Colorado at Boulder, sharma.ashesh@ymail.com

Follow this and additional works at: https://scholar.colorado.edu/asen_gradetds

 Part of the [Applied Mathematics Commons](#), [Engineering Commons](#), and the [Other Physics Commons](#)

Recommended Citation

Sharma, Ashesh, "Advances in Design and Optimization Using Immersed Boundary Methods" (2017). *Aerospace Engineering Sciences Graduate Theses & Dissertations*. 190.

https://scholar.colorado.edu/asen_gradetds/190

This Dissertation is brought to you for free and open access by Aerospace Engineering Sciences at CU Scholar. It has been accepted for inclusion in Aerospace Engineering Sciences Graduate Theses & Dissertations by an authorized administrator of CU Scholar. For more information, please contact cuscholaradmin@colorado.edu.

**Advances in Design and Optimization using Immersed
Boundary Methods**

by

Ashesh Sharma

B.E., Mechatronics Engineering, Manipal University, India, 2011

M.S., Mechanical Engineering, University of Florida, USA, 2013

A thesis submitted to the

Faculty of the Graduate School of the

University of Colorado in partial fulfillment

of the requirements for the degree of

Doctor of Philosophy

Department of Ann and H.J. Smead Aerospace Engineering Sciences

2017

This thesis entitled:
Advances in Design and Optimization using Immersed Boundary Methods
written by Ashesh Sharma
has been approved for the Department of Ann and H.J. Smead Aerospace Engineering
Sciences

Prof. Kurt K. Maute

Prof. John A. Evans

Date _____

The final copy of this thesis has been examined by the signatories, and we find that both the content and the form meet acceptable presentation standards of scholarly work in the above mentioned discipline.

Sharma, Ashesh (Ph.D., Aerospace Engineering Sciences)

Advances in Design and Optimization using Immersed Boundary Methods

Thesis directed by Prof. Kurt K. Maute

This thesis is concerned with topology optimization which provides engineers with a systematic approach to optimize the layout and geometry of a structure against various design criteria. Traditional topology optimization uses density-based methods to capture topological changes in geometry. Density-based methods describe a structural layout using artificial elemental densities. To obtain a good resolution of the geometry, fine meshes are required. This however leads to large computational costs in 3D. Using coarser but practical meshes results in blurred structural boundaries and unreliable prediction of physical response along those boundaries. Using immersed boundary methods instead, such as the extended finite element method (XFEM), alleviates these issues. The XFEM provides clear description of the geometry, and approximation of the physical response along boundaries has been shown to converge to the approximation using body-fitted meshes. This thesis focuses on the use of XFEM for topology optimization. Design geometry in this thesis is tracked precisely using the level set method (LSM).

The LSM-XFEM approach is used to solve variety of multiphysics design and optimization problems. However, being a relatively new field of study the LSM-XFEM approach continues to pose many interesting challenges limiting its applicability to topology optimization. The goal of this thesis is to present advances made towards making LSM-XFEM more viable and reliable for design and optimization of multiphysics problems. Specifically, i) The numerical behavior of XFEM-based shape sensitivities has not yet been investigated. This thesis presents a first-of-its kind study on the numerical behavior of shape sensitivities using the XFEM. ii) The matter of overestimation of stresses using the XFEM, a longstanding issue with no concrete resolution available in the literature, is addressed for robust stress-based

optimization. iii) LSM-based topology optimization is known to suffer from slow design evolution resulting from localized sensitivities. A recently proposed concept of geometric primitives as design variables alleviates this issue. Literature on this concept has been restricted to single material problems using linear elasticity. Using the XFEM, this thesis extends the concept of geometric primitives as design variables to multiphase multiphysics problems in 3D.

Dedication

To my parents, thank you both for supporting me in every possible way to help me achieve my goals and fulfill my dreams.

Acknowledgements

Firstly, I would like to thank my parents for their never ending support which has helped me achieve one of the most cherished dreams of my life, i.e. to study in the USA which has allowed me to participate in research work of such a magnitude.

I would like to thank my advisor, Prof. Maute, for taking me on as a doctoral student regardless of my lack of prior experience in the field. In addition to advising me on my research, thank you for being a constant source of knowledge even on the most fundamental topics.

I would further like to thank my defense committee members, Prof. Evans, Prof. Doostan, Prof. Felippa, and Prof. Vernerey. I am grateful for their willingness to serve on my committee, and for the constructive criticism they have provided.

I would also like to thank my lab colleagues for providing valuable guidance at many stages of my research, as well as for the memorable time spent outside work. It has truly been wonderful working with everyone.

Contents

Chapter	
1	Introduction 1
1.1	Context 1
1.2	Motivation 4
1.3	Research goals and contributions 12
1.4	Theoretical background 13
1.4.1	Geometry description 14
1.4.2	Geometry mapping and modeling the physical response 17
1.5	Physical models of interest 22
1.5.1	Topology optimization 26
1.6	Structure of the thesis 31
2	Advances in Design 33
2.1	Gradient-stabilized stresses 33
2.1.1	Ghost penalty for stabilizing displacement gradients 34
2.1.2	XFEM informed smoothing of stresses 36
2.1.3	Application to cantilever beam problem 36
2.1.4	Galerkin Gradient Least Squares Stabilization 40
2.1.5	Outlook and future work 41
2.2	Modeling uncertainty in material geometry 42

2.2.1	Active stochastic subdomain	44
2.2.2	Application to linear elastic bimaterial plate	46
2.2.3	Outlook and future work	48
3	Behavior of Shape Sensitivities	51
3.1	Verification of shape sensitivities	54
3.2	Effect of geometry discretization and LSF on shape sensitivities	56
3.3	Effect of XFEM informed smoothing of stresses on sensitivities	62
3.4	Outlook and future work	64
4	Advances in Design Optimization	67
4.1	Stress-based optimization	68
4.1.1	Application to L-beam	70
4.1.2	Outlook and future work	75
4.2	Topology Optimization using Geometric Primitives	75
4.2.1	Ribs as geometric primitives for topology optimization	77
4.2.2	Anisotropic smoothing	79
4.2.3	Numerical examples	82
4.2.4	Outlook and future work	93
5	Summary	95
	Bibliography	98
	Appendix	
A	Publication 1: Heaviside enriched extended stochastic FEM for problems with uncertain material interfaces [71]	110

B	Publication 2: On shape sensitivities with heaviside-enriched XFEM [114]	126
C	Publication 3: Stress-based Topology Optimization using Spatial Gradient Stabilized XFEM [113]	151
D	Implementation Details	174
D.1	A parallel multilevel filter framework	174
D.1.1	Constructing the physical design variable level	177
D.1.2	Constructing the pseudo physical design variable level	178
D.1.3	Constructing the abstract physical design variable level	179
D.1.4	Updating the tree	179
D.2	Constructing $\nabla\phi$ using a point cloud	179

Tables

Table

4.1	Parameter list for topology optimization of single-phase 3D linear elastic L-beam.	72
4.2	Parameter list for topology optimization of two-bar truss problem. All dimensions in m.	84
4.3	Parameter list for topology optimization of steady passive thermo-elastic problem. All dimensions in mm.	88
4.4	Parameter list for topology optimization of unsteady active thermo-elastic problem. All dimensions in mm.	91

Figures

Figure

1.1	Initial design (left most) undergoing various types of design changes: Size change (second from left); Shape change (second from right); Topological change (right most).	2
1.2	Examples of geometry mapping undergoing shape change.	4
1.3	Design and optimization model.	14
1.4	LSM description of merging inclusions: n dimensional circular bodies (left); $n + 1$ dimensional LSF (middle); Iso-contours of the LSF (right).	15
1.5	Complex geometry representation using an LSF: Shell structure supported by truss members(left); Interwoven fibers of a composite (right).	16
1.6	Heaviside-enriched XFEM framework in 1D: Interpolation of solution field using generalized Heaviside enrichment (top); Mapping of integration domains for an intersected element (bottom).	19
1.7	Interface shift schematic.	21
1.8	Heaviside-enriched XFEM framework in 2D: Interpolation of solution field using generalized Heaviside enrichment (top); Mapping of integration domains for an intersected element (bottom).	22
1.9	Schematic of the model problem.	23
1.10	A structure undergoing topology optimization to increase stiffness of the structure subject to volume constraint.	27

2.1	Stabilized faces in a two-phase problem.	34
2.2	Cantilever beam setup (top), and mesh $h = 0.05m$ (bottom). Stresses are monitored along the highlighted region. All dimensions are in m.	37
2.3	Stress (N/m^2) profile along the material interface: Area weighted smoothing (left), Area weighted smoothing with $\gamma_u = 0.1$ (middle), XFEM informed smoothing with $\gamma_u = 0, \gamma_\tau = 0$ (right).	38
2.4	Stress (N/m^2) profile along the material interface: XFEM informed smoothing with $\gamma_u = 0.1, \gamma_\tau = 10^{-4}$ (left), $\gamma_u = 0.1, \gamma_\tau = 10^{-3}$ (middle), and $\gamma_u = 1.0, \gamma_\tau = 10^{-2}$ (right).	38
2.5	Stress field distribution using: Area weighted smoothing (left) and XFEM informed smoothing with $\gamma_u = 0.1, \gamma_\tau = 10^{-4}$ (right).	39
2.6	Stress field distribution in absence (left) and in presence (right) of GGLS. . .	41
2.7	X-SFEM model.	42
2.8	Schematic of the stochastic model problem.	43
2.9	1D spatial intersection configuration example (left) and corresponding active stochastic subdomain for $u_{3,1}^2$ (right)	45
2.10	Example of a sliver configuration of an active stochastic subdomain in 2D (left), and minimum bounding rectangle defined using a rotated coordinate system (right).	46
2.11	Problem setup for a bimaterial plate with mesh size $h = 0.1m$	47
2.12	Regular (left) and enriched (right) degree of freedom using the C^0 enrichment function [94] for the x-displacement at $\mathbf{x} = (0.9, 0)$ as a function of ξ with spatial mesh refinement.	47
2.13	Level 1 degrees of freedom for phase 1 (left) and phase 2 (right) using the generalized Heaviside enrichment strategy for the x-displacement at $\mathbf{x} = (0.9, 0)$ as a function of ξ with spatial mesh refinement.	48

2.14	Error convergence using the X-SFEM with respect to p . Solid and dashed lines represent the Heaviside and C^0 -continuous enrichment functions, respectively.	49
3.1	Degrees of freedom for node located at $\mathbf{x} = (16.75, 3)$, in Figure 3.4	52
3.2	$\partial R/\partial s$ for degrees of freedom plotted in Figure 3.1	53
3.3	Perturbing intersection points for finite differencing in (3.3).	54
3.4	Heat diffusion problem setup with strip inclusion. All dimensions in m . . .	54
3.5	Accuracy of semi-analytical shape sensitivities: Response function (left) and corresponding shape sensitivities (right).	56
3.6	Heat diffusion problem setup with circular inclusion. All dimensions in m . .	57
3.7	Level set functions described in (3.9) with zero level set contour.	58
3.8	Dependence of shape sensitivities on geometry discretization: Response function (left), and sensitivities corresponding to response function (middle) and perimeter (right) using LSF_1	59
3.9	$d\mathcal{Z}/d\mathbf{s}$ (top) and $d(per)/d\mathbf{s}$ (bottom) for nodal level set design variables. . .	61
3.10	Influence of $ \nabla\phi $ on the response function and corresponding shape sensitivities	62
3.11	Influence of variation of $ \nabla\phi $ (curvature) on the response function and corresponding shape sensitivities	63
3.12	Comparison of stress sensitivities along material interface for $h = 0.025m$ (left) and $h = 0.005m$ (right).	64
3.13	Discretized consistent (left) and continuum consistent (right) approach for perturbing points of interest for computation of semi-analytical sensitivities (3.3).	65
3.14	Stress sensitivities using discretized consistent (left) and continuum consistent (right) approach for XFEM informed smoothing with $\gamma_u = 0.1$ and $\gamma_\tau = 10^{-4}$.	65
4.1	Variation of stress constraints as a function of the tuning coefficient β	71

4.2	(a) Cross-sectional view of the L-beam problem setup; Finite element mesh, $h = 0.2m$, with initial seeding in 3D for load case RE: (b) Top view; (c) Perspective view; (d) Slice along the thickness. All dimensions are in m	71
4.3	Evolution of normalized compliance for 3D linear elastic L-beam.	73
4.4	Evolution of stress and volume constraints for 3D linear elastic L-beam.	73
4.5	Stress distribution in optimized design for 3D linear elastic L-beam: (a) Without stress constraints; (b) With stress constraints	74
4.6	Design evolution resulting from localized sensitivities in traditional LSM (left) and more universal sensitivities using geometric primitives (right).	75
4.7	Example of a 3D rib as a geometric primitive.	78
4.8	Support domain for isotropic smoothing (left) and anisotropic smoothing (right).	80
4.9	Material boundaries in 2D (left) and 3D (right).	80
4.10	Difference in affect of perimeter penalty (left) and anisotropic smoothing (right).	81
4.11	Problem setup for two-bar truss problem (left) and MBB beam problem (right). All dimensions in m	82
4.12	Evolution of ribs for two-bar truss problem (left) and MBB beam problem (right).	85
4.13	Oscillations in LSF for two-bar truss problem caused by partially disappearing ribs (left), and elimination of oscillations in LSF upon penalization of area of ribs (right).	86
4.14	Convergence plots for two-bar truss problem.	86
4.15	Convergence plots for MBB beam problem.	87
4.16	Passive thermo-elastic problem setup (left) and mesh with fiber inclusions (right).	87
4.17	Deformed cross-sectional view with fibers reflected about axis of symmetry (left) and u_z plotted on cross-sectional view of deformed design (right).	89
4.18	Comparison of displacement profile against target displacement.	89

4.19	Convergence plots for steady passive thermo-elastic optimization problem. . .	90
4.20	Active thermo-elastic problem setup (left) and mesh with fiber inclusions (right). 90	
4.21	Deformed cross-sectional view with fibers reflected about axis of symmetry (left) and u_z plotted on cross-sectional view of deformed design (right). Deformation of design amplified by a factor of 75.	92
4.22	Comparison of the temperature and displacement plots between the initial (left) and converged (right) designs. Deformation of design amplified by a factor of 75.	92
4.23	Convergence plots for unsteady active thermo-elastic optimization problem. .	93
4.24	Future work should focus on a hybrid approach.	93
D.1	Tree of variables.	174
D.2	Example decomposition of variables with dependencies in a parallel multilevel filter framework.	175

Chapter 1

Introduction

1.1 Context

Aggressive measures to cut manufacturing costs by reducing weights gave rise to the field of structural optimization. Structural optimization aims at finding the optimal design of a mechanical structure against various design criteria such as stiffness, allowable stress, allowable mass, desired displacement profile, etc. Before the advent of computational techniques, structural components such as beams and plates were optimized using variational calculus [108]. Development of the finite element method (FEM) gave rise to numerical structural optimization [111]. Initial applications were to trusses in civil engineering. Changes in design were limited to variation in size as determined by the cross-sectional areas of beams or thickness of plates. This class of optimization came to be known as size optimization. Size optimization was followed by shape optimization wherein the goal is to determine the optimal shape of internal and external structural boundaries without altering the topology. Shape optimization was traditionally associated with Lagrangian approaches wherein the nodal coordinates of a finite element mesh constitute the design variables [51]. In contrast, topology optimization allows significant changes in both the layout and the geometry of the structure. Figure 1.1 presents a simple comparison depicting the differences between size, shape, and topological changes in a design.

Topology optimization was pioneered in [13] as a porous material distribution problem, wherein properties of the material were evaluated using the homogenization theory

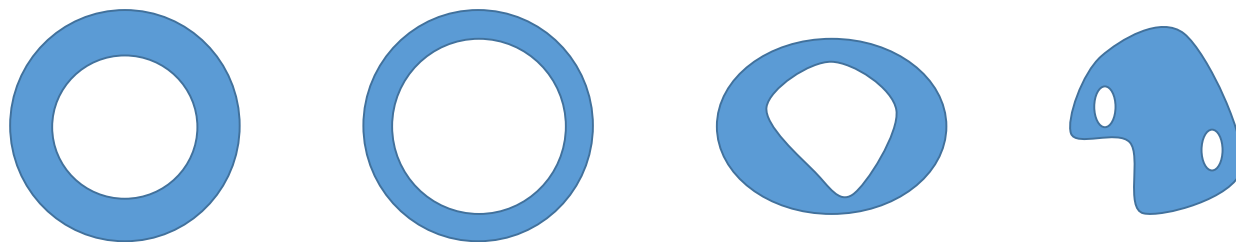


Figure 1.1: Initial design (left most) undergoing various types of design changes: Size change (second from left); Shape change (second from right); Topological change (right most).

[38]. Soon after, the concept of solid isotropic material with penalization (SIMP) was introduced in [11] as means to improving the convergence of the material distribution to 0 – 1 solutions. Both these approaches qualify as density-based methods, and have become very popular for performing topology optimization. Artificial elemental densities constitute the design variables in a density-based method, hence the name. Since their inception significant research has been performed in the area of density-based methods including resolving numerical instabilities [116] as well as extending topology optimization to various physics ranging from photonics [57] to Stokes flow [15] to natural convection [2]. For a better insight into the developments made in the field of density-based methods, the reader is referred to the comprehensive reviews in [12, 115]. During the optimization process in density-based methods, there may exist grey regions comprising of elements with intermediate densities. Unless the geometry is aligned with the discretization of the density field, the geometry is either smeared across elements or approximated by a jagged boundary as shown in Figure 1.2. Either scenario leads to a lack of resolution of the geometry. As a result it is challenging to predict the physical response of a system accurately along the material geometry. To obtain a good resolution of the geometry, fine meshes are required. This however leads to large computational costs in 3D.

Level set methods (LSM) are often viewed as an alternative to density-based methods. Introduced in [98] the LSM presents a flexible framework for tracking an evolving geometry.

Using the LSM the interface between material phases is defined implicitly by iso-contours of a level set function (LSF) as discussed in Section 1.4.1. The LSM results in crisp material boundaries, avoiding obscurity of intermediate material phases associated with density-based methods. Level set-based topology optimization requires mapping of the geometry to a mechanical model. Common ways to map the geometry include a conforming discretization [1, 61], density-based mapping [4, 132], and immersed boundary methods [82, 90]. Conforming discretization differs from shape optimization methods in that shape changes are governed by the evolution of an LSF [28]. Density-based mapping usually involves either element-wise constant material fractions or a direct point-wise mapping of the LSF onto a density distribution [28]. Conforming discretization and density-based mapping suffer from the same drawbacks as those involved with body-fitted meshes for shape optimization and density-based methods, respectively. In contrast immersed boundary methods [88, 119] have been incorporated in topology optimization [76, 127] to alleviate issues associated with conforming discretization and density-based mapping. Figure 1.2 presents a comparison between the above mentioned options for geometry mapping.

Over the past couple of decades several immersed boundary methods have been proposed to obtain an accurate representation of a deforming material geometry in absence of a conforming mesh. Also, approximation of the response along boundaries has been shown to converge to the approximations using body-fitted meshes. Furthermore a crisp representation of the material geometry facilitates robust enforcement of boundary conditions along the material geometry. Immersed boundary methods involve resolving a physical system on a fixed (Eulerian) grid with the geometry of the immersed body defined using Lagrangian markers. As shown in Figure 1.2 although the discretization of the design domain is fixed, the change in location of the structural boundary is clearly captured. The term "immersed boundary method" was first used in reference to an approach developed in [102] for simulating cardiac mechanics and associated blood flow on a fixed finite difference (FD) grid. Since then the concept of immersed boundaries has been extended to finite volume (FV) methods

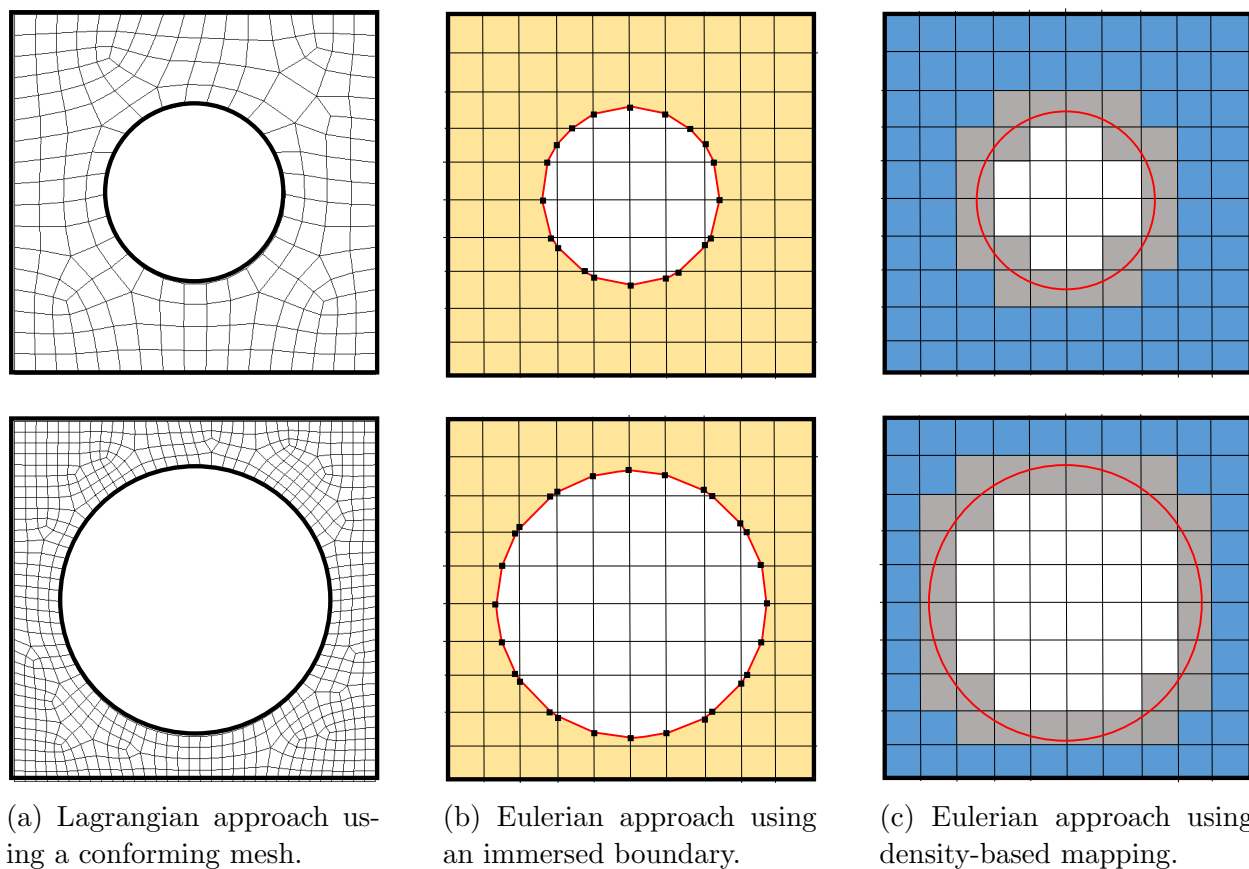


Figure 1.2: Examples of geometry mapping undergoing shape change.

[87, 104] as well as FEM [40, 120]. In the context of topology optimization we focus on immersed boundary methods for FEM. Various immersed boundary methods for FEM have been proposed in the literature such as the generalized finite element method (GFEM) [120], the extended finite element method (XFEM) [88], and the finite cell method (FCM) [101].

1.2 Motivation

Owing to its popularity over its counterparts this thesis focuses on the use of the XFEM for topology optimization. The XFEM extends the standard FEM by enriching the solution space to capture discontinuities in either the state variables or their spatial gradients

within an element. Various options for constructing the enriched solution space exist, an overview of which has been provided in [40]. Section 1.4.2 provides a detailed discussion on the XFEM approach adopted in this thesis. The LSM-XFEM has been successfully applied to a wide range of design and optimization problems involving a variety of physics such as incompressible Navier-Stokes [65, 112], heat diffusion [68], linear elasticity [71, 129], fluid-structure interaction [42, 56], natural convection [24], dendritic solidification [138], damage [91], and contact mechanics [72], among others. In the context of topology optimization the LSM-XFEM approach is often classified as a generalized shape optimization approach [32]. This classification stems from the fact that the approach allows for topology modifications as existing holes can merge or disappear. Notwithstanding the extensive research on LSM-XFEM, the approach is less than two decades old and continues to present many interesting challenges limiting its applicability to topology optimization problems. The open topics associated with LSM-XFEM in the context of topology optimization can be divided into three broad categories as discussed below:

- (i) **Response related:** This category concerns areas of research that influence directly the analysis of the physical problem, and thus concern design using XFEM. Some of the major open topics in this category are:
 - (a) Numerical behavior of shape sensitivities. Shape sensitivities quantify the effect that a change in shape has on the response of the design. Shape sensitivity analysis in general comprises of computing the derivative of a response function (e.g. strain energy, stress, perimeter, etc.) with respect to parameters describing the domain geometry [114]. Naturally shape sensitivities are important to determining the outcome of the optimization process. However, literature focusing on shape sensitivities using the XFEM is sparse. An analytical sensitivity study to address material-material interface problems in multi-component system was presented in [139] wherein the sensitivities are derived from a material-material

interface model. More recently in [92] an analytical approach to performing sensitivity analysis for shape optimization of bi-material structures was developed. Like the studies mentioned above, other studies on XFEM-based shape or topology optimization usually present an approach to computing the shape sensitivities without any discussion on the numerical behavior of shape sensitivities. Consequently questions concerning the smoothness and robustness of shape sensitivities computed using the XFEM have not been answered yet. Furthermore the influence of discretization of geometry using the XFEM on shape sensitivities has not yet been investigated.

- (b) Overestimation of stresses. Stress-based topology optimization has garnered the attention of many researchers as accounting for stress measures allows to design engineering structures based on strength of materials. Overestimation of stresses using the XFEM has been a long standing issue. In the XFEM, a material interface too close to a node can lead to small intersected areas. These small regions present vanishing zones of influence for certain degrees of freedom. Aside from adversely affecting the condition number of the system, small intersections can result in uncontrolled displacement gradients across element edges leading to localized stress peaks (Section 2.1) and inaccurate stress sensitivities (Section 3.3) which can further affect the outcome of the topology optimization process. For a nonlinear structural model inaccurate displacement gradients can affect the stability of the system of equations. Improving stresses in the vicinity of a singularity such as a crack-tip has been a widely studied topic [107, 135]. However, these studies are specific to open interfaces (cracks usually end inside a domain). Little work has been focused at improving the prediction of stresses resulting from small intersection areas due to closed material interfaces. One of the first studies to bring this issue to light was [127]. They

highlighted the problem of overestimation of stresses resulting from extremely small (or large) ratios of intersected areas in an intersected element. To maintain the accuracy of the computed stresses, strategies such as elimination of small intersections by shifting the material interface were suggested. Recently in [106] to circumvent the problem of overestimation of stresses, elements with small intersection areas were ignored from the finite element analysis. Additionally, stresses were post-processed using the patch recovery method of [147] to give smoothed stress values at the nodes. In [90] an area weighted smoothing was performed to post-process stresses associated with intersected elements. However as mentioned in [90], the approach does not ensure elimination of overestimated stress values. Recently the B-spline Finite Cell Method was used to achieve a high-order continuity and stress accuracy along cell boundaries [19]. Low-order finite elements, given their simplicity and ease of implementation are the most popular choice of interpolation for topology optimization problems. The influence of small intersection areas on the accuracy of spatial gradients is aggravated when using low-order elements. The literature currently lacks a robust approach for accurately predicting stresses in the vicinity of small intersections using low-order XFEM.

- (c) Consistent integration in time. Temporally evolving geometries are frequently found in the real world and are relevant in many engineering applications such as additive manufacturing, wind turbines, etc. The XFEM is particularly useful in these applications as it is able to resolve discontinuities such as phase change and fluid-structure interaction in the problem domain. The temporally evolving structural geometry can be easily tracked implicitly using the LSM. Majority of XFEM-based studies involving time dependent geometry ignore the time dependency of enrichment formulations by using a semi-discretized approach

wherein the temporal integration is performed using finite differencing. As discussed in [22], this introduces some ambiguities since the approximation space varies due to the time dependence of the enrichment function. As a result the appropriate choice of the approximation spaces for the test and trial functions is not clear. The discontinuous Galerkin space-time approach in [23] provides insight into the appropriate choice of the test and trial functions for semi-discrete approaches. In [39] an approach was introduced requiring the evaluation of enrichment functions on the current and previous time step. This approach is stable only for weak discontinuities. In [53] an enrichment consistent time integration scheme for the problem of premixed combustion in 2D and 3D was developed. However, their approach made use of semi-Lagrangian techniques to adequately handle time integration based on finite difference schemes. Recently in [74] numerical studies applying space-time XFEM to multiphase problems in 3D space were presented. Space-time XFEM resolves consistently and robustly all of the aforementioned issues. However, the study was restricted to meshes constructed using hypertriangles. Inconsistent evaluation of the response of a temporally evolving interface is bound to cause inconsistencies in the corresponding transient sensitivity analysis for topology optimization. As a result topology optimization problems involving temporally evolving geometry have not yet been considered in the context of the XFEM.

- (ii) **Convergence related using the LSM:** This category comprises of topics that are related to the convergence of the optimization process using the LSM. Some of the major open topics in this category are:
 - (a) Extremely localized sensitivities leading to slow design evolution. LSM-based topology optimization is known to suffer from slow design evolution resulting from localized sensitivities, as discussed in Section 4.2. Furthermore, the num-

ber of design variable in traditional topology optimization frameworks scale with the mesh density. A recently proposed concept of geometric primitives as design variables [9, 47] provides a platform for alleviating these issues. Furthermore, geometric primitives as design variables allow for geometry information to be directly incorporated into the topology optimization framework. This new approach presents immense possibilities to improving the flexibility of LSM-based topology optimization as further discussed in Section 4.2. The literature however, is currently restricted to single material problems using linear elasticity. In addition, unlike for node-based design variables [28] no regularization approaches to ensure smooth material geometries have been investigated yet. Non-smooth boundaries can significantly affect the shape sensitivities and as a result the convergence of the optimization process as discussed in Section 3.2.

- (b) **Topological derivatives.** Traditionally, LSM-based approaches are shape optimization approaches as holes are allowed to merge and disappear but not reappear. As a result the outcome of the shape optimization process depends on the initial design. Consequently, the concept of topological derivatives [34, 117] has been used to insert holes during the optimization process [17, 20, 41]. However whenever a new hole is inserted, for all practical purposes a new optimization problem is generated resulting in a discontinuous optimization process leading to slow optimization convergence rates [28]. Furthermore, there is an inherent decision making concern with the idea of topological derivatives. The question, when should holes be inserted for an unbiased topology optimization, remains largely unanswered.

- (iii) **Geometry related using the LSM:** This category comprises of topics that are related to the definition of the geometry in the context of LSM-based topology optimization. Some of the major open topics in this category are:

- (a) Minimum feature size control. Controlling the minimum feature size of an optimized design is important to ensure that the physics in the vicinity of the feature is accurately resolved, and also to maintain practicality of the design in regards to manufacturing. There has been extensive research performed to control the minimum feature size in LSM-based topology optimization. For instance in [21] a quadratic energy functional is incorporated in the objective function for shape feature control. In contrast in [48], control of component length scale was achieved using a structural skeleton method based on the sign distance information. For an overview of existed techniques for feature size control in the context of LSM-based topology optimization, the interested reader is referred to the comprehensive review in [80]. Notwithstanding the extensive research performed to control the minimum feature size, the concept continues to suffer from an inherent decision making issue. The question when should the feature size control be enforced is yet unanswered. As one can imagine if always enforced, the feature size control will prevent any holes from merging and thus prevent any changes in the design topology.
- (b) Controlling the gradient of the LSF. The ability to represent changes in geometry using LSM-based topology optimization can deteriorate when the magnitude of the spatial gradient of the LSF along the material interface becomes too flat or too steep. Too steep of an LSF will result in significantly diminished sensitivities leading to a small change in material geometry for relatively significant changes in the LSF. In contrast, too flat of an LSF will result in magnified sensitivities leading to large changes in material geometry for relatively small changes in the LSF. The most popular approach for resolving this issue involves solving a convective level set re-initialization equation [97] to produce a signed-distance LSF ($\nabla\phi = 1$ everywhere), see e.g [4, 132]. However, the major

drawback with this approach is the fact that re-initialization of an LSF will usually move the zero iso-contour introducing inconsistencies in the optimization process [28]. Furthermore the re-initialization scheme is time consuming given the fact that a convective equation needs to be solved frequently. Consequently the issues of maintaining a sign distance LSF without having to solve an additional equation remains an open topic, with recent efforts focusing on incorporating the re-initialization information in either the level set governing equation [146] or as part of the objective or constraint formulation [58].

The above topics list only a few of the many open topics associated with LSM-XFEM-based topology optimization. While no review of open topics associated with XFEM-based topology optimization has yet been performed, the interested reader is referred to the comprehensive review in [28] for an overview of open topics concerning LSM-based topology optimization. Furthermore, the comprehensive review in [40] although a bit dated, is a good read on methodological associated with XFEM.

Additional motivation of this thesis is unrelated to topology optimization, and concerns purely XFEM-based design. Fabrication techniques even as precise as additive manufacturing are one of the primary sources introducing geometric uncertainty. Accounting for geometric uncertainty is essential for realistic predictions of heterogeneous materials. Examples with geometric uncertainty include engineered composites and sintered materials among others. The eXtended stochastic finite element method (X-SFEM) [95] was proposed to extend the XFEM to the stochastic domain using a polynomial chaos expansion (PCE) [136] to approximate the degrees of freedom based on the random parameters characterizing the geometry. The X-SFEM has previously been studied for problems with weak discontinuities in the problem domain [70, 94, 95, 96]. In contrast to the intrusive concept of X-SFEM, a non-intrusive approach combining XFEM with Monte Carlo simulation is studied in [54, 110] for uncertainty quantification in homogenization of random heterogeneous media. However

as widely known, non-intrusive approaches have limited flexibility in terms of a connection with the physical problem. A generic framework in the literature is missing that can be used for problems with either weak or strongly discontinuous solution in the problem domain.

1.3 Research goals and contributions

The primary goal of this thesis is to present recent advances made in the field of XFEM-based topology optimization, with a secondary goal of presenting advances made in the field of XFEM-based design. We do so by addressing some of the issues mentioned in Section 1.2. Specifically, the research goals of this thesis are summarized through the following major contributions of the current work:

- (i) We aim to develop and study a robust approach to computing the shape sensitivities using the XFEM. We investigate in detail the advantages and challenges that the adopted approach poses to the computation of shape sensitivities via the adjoint method, for both material-void and material-material problems. Through numerical examples we further study the dependency of the shape sensitivities on spatial resolution and interface conditions. Furthermore we compare both numerically and analytically, the XFEM-based shape sensitivities against shape sensitivities obtained by the classical Lagrangian approach using a body-fitted mesh.
- (ii) Focusing on the issue of overestimation of stresses using the XFEM, improving the prediction of stresses presents another goal of this thesis. We adopt a recently proposed fictitious domain approach [18] for penalization of displacement gradients across element faces surrounding the material geometry. In addition, a novel XFEM informed stabilization scheme is proposed for robust computation of stresses. Through numerical studies the penalized spatial gradients combined with the stabilization scheme is shown to greatly improve prediction of stresses and stress sensitivities along the material geometry. The proposed approach is applied to a benchmark

topology optimization problem in 2D and 3D using linear and hyperelastic materials, for single phase as well as multiphase designs.

- (iii) Building on the work in [47, 93] we aim to demonstrate how to perform 3D XFEM-based topology optimization using geometric primitives. An assemblage of geometric primitives can result in a final structure with irregular surface along the boundaries. This feature is unattractive from an analysis and manufacturing point of view. Furthermore a non-smooth representation of the material geometry can cause issues in convergence of the optimization process as discussed in Chapter 4. We resolve this issue by introducing an anisotropic filter for smoothing along structural boundaries. Single and multiphase steady state and transient examples are presented using the proposed approach.
- (iv) Unrelated to topology optimization, but in consonance with the objective of this thesis to present advances in design using the XFEM, we propose an approach to model problems with either a weak or a strong discontinuity across a random material interface. The work presented in this thesis constitutes only a part of the research on XFEM-based design of geometric uncertainty presented in [69]. The specific contribution of this thesis pertains to the development of "active stochastic subdomains" as discussed in Section 2.2. The convergence and accuracy of the proposed method is demonstrated using problems with continuous and discontinuous solutions in the problem domain.

1.4 Theoretical background

This section discusses our choice of technique for describing the material geometry, followed by our choice of immersed boundary technique associated with the design and optimization studies performed in this thesis. We further present and discuss our framework for performing topology optimization in the current study. Figure 1.3 presents an overview

of the tools used.

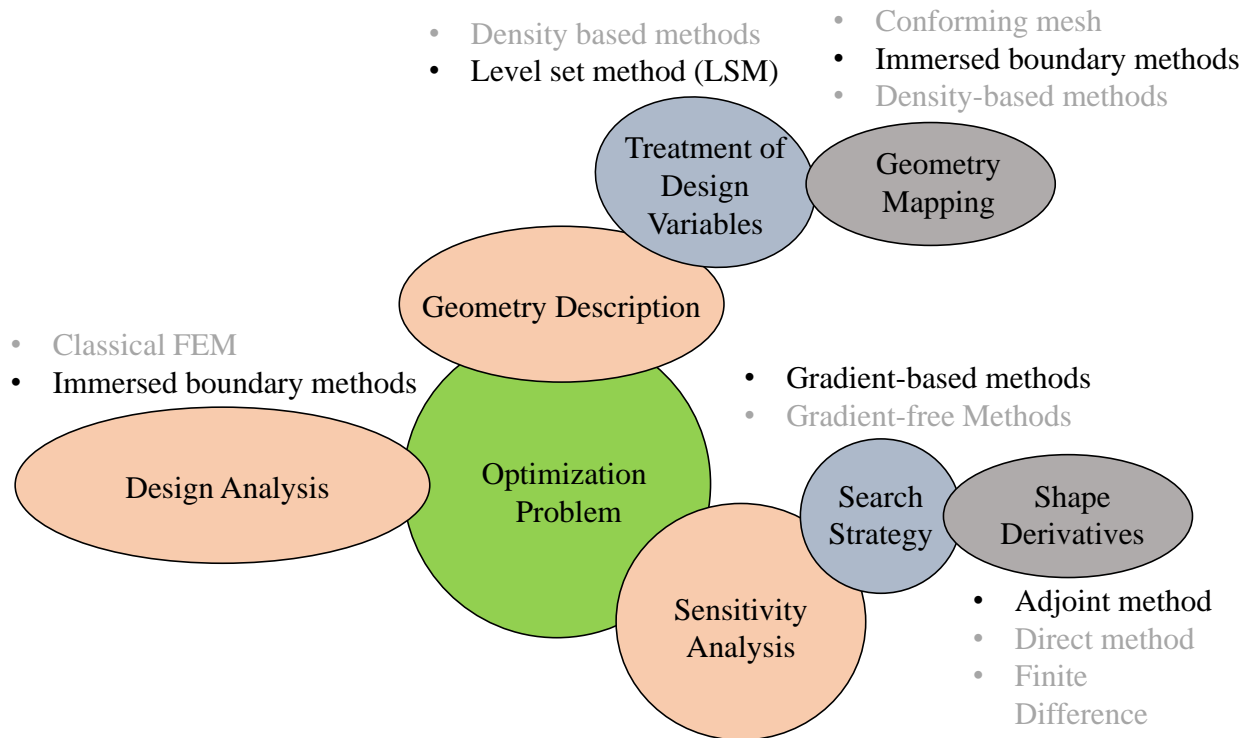


Figure 1.3: Design and optimization model.

1.4.1 Geometry description

Over the years researchers have used various strategies to define the geometry of material domains. Classical approaches for parametrization of shapes were either based on CAD models or were CAD-free, both of which provide an explicit representation of the material geometry. CAD models include the use of Bézier curves, B-splines, and NURBS for the representation of material geometry [14, 49]. CAD-free parametrization involves describing the material geometry directly using finite element meshes as described in [36, 62]. In contrast to explicit boundary representations, Level set Methods (LSM) [98] present a framework for defining the material boundaries implicitly by iso-contours of a level set function (LSF). Moreover, LSM allows for a convenient treatment of topological changes as shown in Figure

1.4. As with explicit approaches mentioned above, an LSF presents crisp description of the boundaries. The LSM due to its ability to handle complex shapes (Figure 1.5) along with its ease of implementation, has been naturally associated with immersed boundary methods [19, 40]. We thus employ the LSM to describe the material geometry in this thesis.

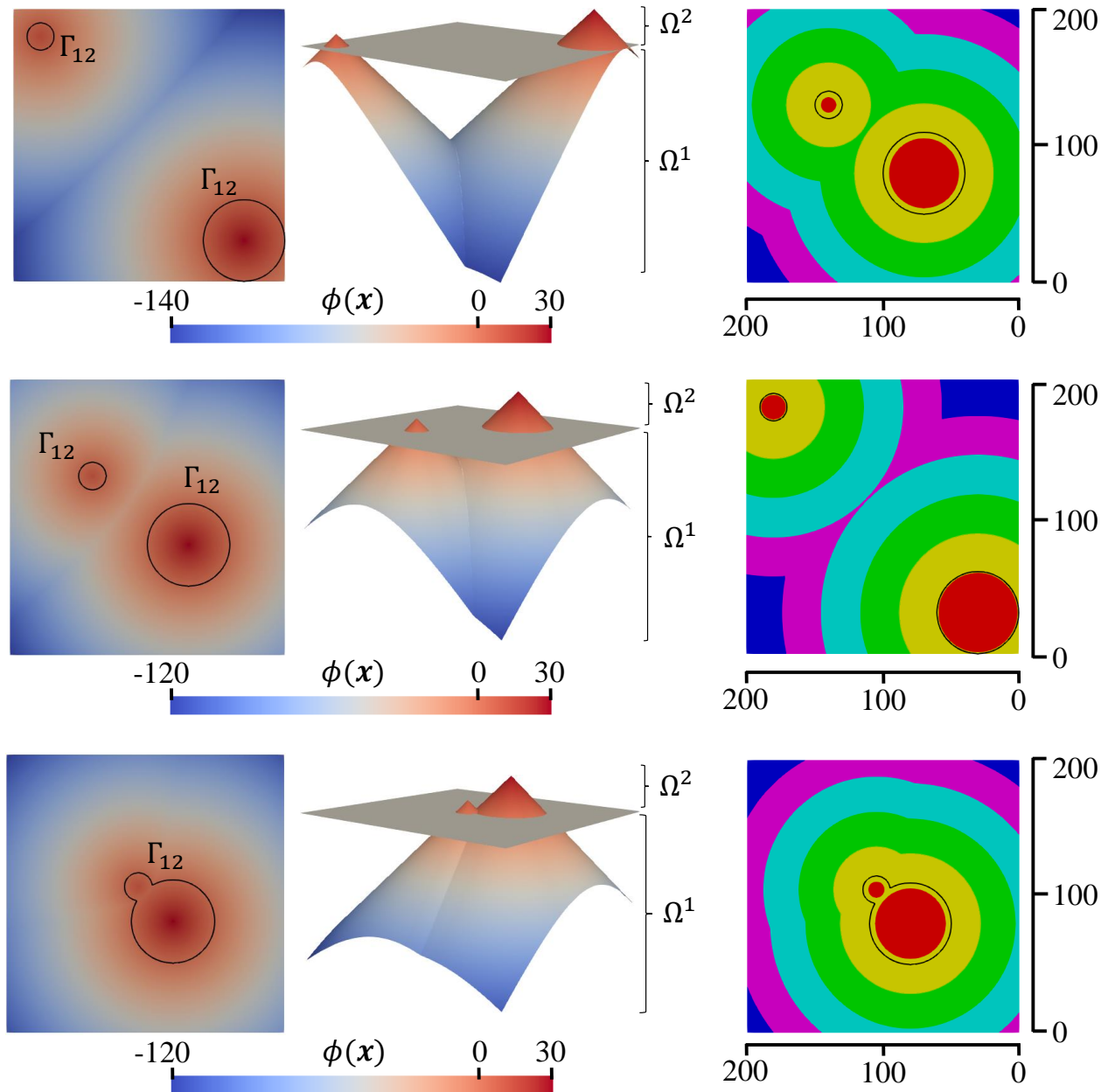


Figure 1.4: LSM description of merging inclusions: n dimensional circular bodies (left); $n+1$ dimensional LSF (middle); Iso-contours of the LSF (right).

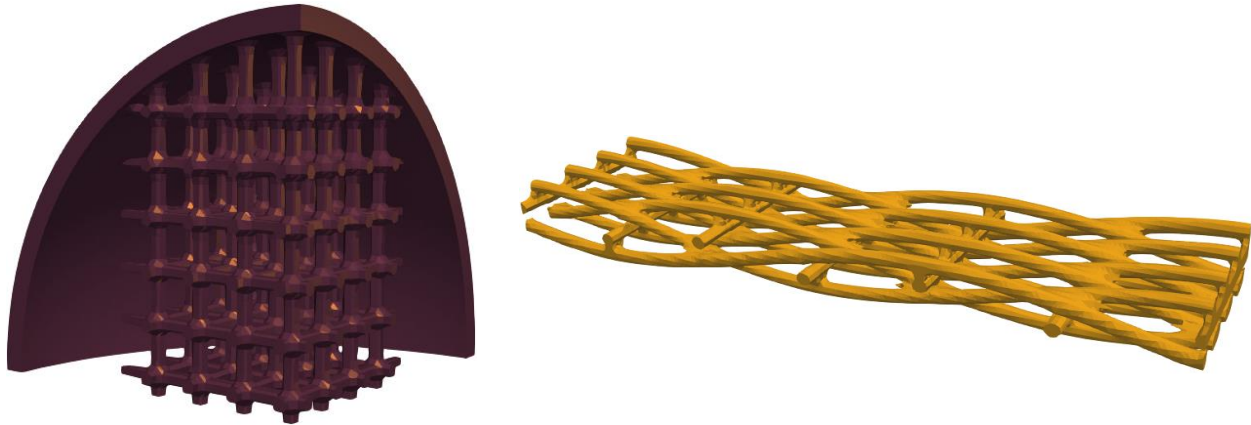


Figure 1.5: Complex geometry representation using an LSF: Shell structure supported by truss members(left); Interwoven fibers of a composite (right).

The LSM uses an $n + 1$ dimensional LSF, $\phi(\mathbf{x})$, to describe the surface geometry, Γ_{12} , of an n dimensional body, Ω^2 , immersed in a domain, Ω^1 . Considering a two-phase problem, the material layout can be defined using an LSF as follows:

$$\begin{aligned} \phi(\mathbf{x}) &< 0 \quad \forall \mathbf{x} \in \Omega^1, \\ \phi(\mathbf{x}) &> 0 \quad \forall \mathbf{x} \in \Omega^2, \\ \phi(\mathbf{x}) &= 0 \quad \forall \mathbf{x} \in \Gamma_{12}. \end{aligned} \tag{1.1}$$

The surface geometry $\Gamma_{12} = \partial\Omega^1 \cap \partial\Omega^2$ represents the interface between the two phases, and is represented by the zero iso-contour contour in this thesis. Each phase may represent a different material or a different physics. Multiple LSFs can be combined using min/max functions to present a single LSF. As an example in Figure 1.4, merging of two bodies is depicted using a continuous LSF. The continuous LSF is generated by blending two separate LSFs using a differentiable form of the min/max function such as the Kreisselmeier-Steinhauser (KS) function [64]:

$$\phi(\mathbf{x}) = \frac{1}{\beta} \ln \left(e^{\beta\phi_1(\mathbf{x})} + e^{\beta\phi_2(\mathbf{x})} \right), \tag{1.2}$$

where the factor β controls the sharpness of approximating the maximum of the LSFs, $\phi_1(\mathbf{x})$

and $\phi_2(\mathbf{x})$. The LSFs describe a circle of radius r_i centered at \mathbf{x}_i^c :

$$\phi_i(\mathbf{x}) = r_i - |\mathbf{x} - \mathbf{x}_i^c|. \quad (1.3)$$

Another popular approach to combining LSFs is through p-norm functions.

Multiple functions can be used to model more than two phase regions. The use of multiple LSFs originated in image processing [128]. The concept is popularly referred to as the color LSM, and requires m LSFs to model $n = 2^m$ different phase regions [131]. The work of this thesis however is restricted at the most to two-material problems, and therefore only one LSF is used at any instance. Although the current work makes use of the LSM for tracking the geometry, it is also applicable to other approaches mentioned above for defining the design geometry.

1.4.2 Geometry mapping and modeling the physical response

Mapping the material geometry to a mechanical model is performed through either a Lagrangian (deforming mesh) or an Eulerian (fixed mesh) approach. Most popular ways to map the geometry using an LSM include conforming discretization (Lagrangian approach), density-based mapping (Eulerian approach), and immersed boundary methods (Eulerian approach). Figure 1.2 provides a comparison of different mapping approaches as the design domain undergoes a shape change. A key advantage of Eulerian approaches [40, 101, 120] over a Lagrangian approach is that the finite element mesh does not need to be updated to track the material geometry. Density-based mapping suffer from challenges of smeared and jagged material geometry, e.g. as shown in Figure 1.2. Therein the material geometry is projected onto a finite element mesh using a density distribution with the material geometry represented by jagged gray elements. In contrast immersed boundary approaches use Lagrangian markers (also referred to as intersection points) for a clear representation of the material geometry as shown in Figure 1.2.

From a modeling standpoint immersed boundary approaches are attractive when treat-

ing discontinuities in the problem domain (e.g. cracks, holes, or interface between two materials) or when the material geometry is dynamically evolving and requires frequent re-meshing which can be computationally expensive. As a result immersed boundary methods have found widespread use in applications such as multiphase problems [75, 138] and topology optimization [28, 76, 129]. Furthermore, immersed boundary methods have been shown to converge to the classical FEM solution upon spatial refinement [40].

This thesis adopts the eXtended Finite element Method (XFEM), an immersed boundary method developed in [88] based on the partition of unity method [8], to map the material geometry and model the physical response of the mechanical problem.

The XFEM uses an enrichment function to locally capture the non-smooth solution of state variable fields along the material interface, without requiring a conforming mesh. Depending on the type of discontinuity various enrichment strategies have been developed as described in [40]. Following the work in [52, 124] we adopt a generalized Heaviside enrichment strategy with multiple enrichment levels. The use of multiple enrichment levels ensures that the solution field is interpolated in a consistent manner, and avoids any artificial coupling in the presence of disconnected phases as discussed in [82, 126]. The Heaviside enrichment is a step enrichment and is discontinuous by construction, making it preferable for problems involving strong discontinuities such as material-void problems. For C^0 -continuous problems, the continuity in the solution is enforced through stabilized Lagrange or Nitsche methods [118]. Intuitively the discontinuous nature of the Heaviside enrichment function is expected to affect the smoothness of the physical response and corresponding shape sensitivities as further discussed in Chapter 3.

For a two-phase problem the approximation of a solution field, $\mathbf{u}(\mathbf{x})$, denoted as $\hat{\mathbf{u}}(\mathbf{x})$, using the Heaviside-enriched XFEM is given by

$$\hat{\mathbf{u}}(\mathbf{x}) = \begin{cases} \sum_{e=1}^{\Psi} \left(\sum_{i \in I} \mathcal{N}_i(\mathbf{x}) \mathbf{u}_{i,e}^1 \delta_{el}^{1,i} \right) & \text{if } \mathbf{x} \in \Omega^1 \\ \sum_{e=1}^{\Psi} \left(\sum_{i \in I} \mathcal{N}_i(\mathbf{x}) \mathbf{u}_{i,e}^2 \delta_{el}^{2,i} \right) & \text{if } \mathbf{x} \in \Omega^2, \end{cases} \quad (1.4)$$

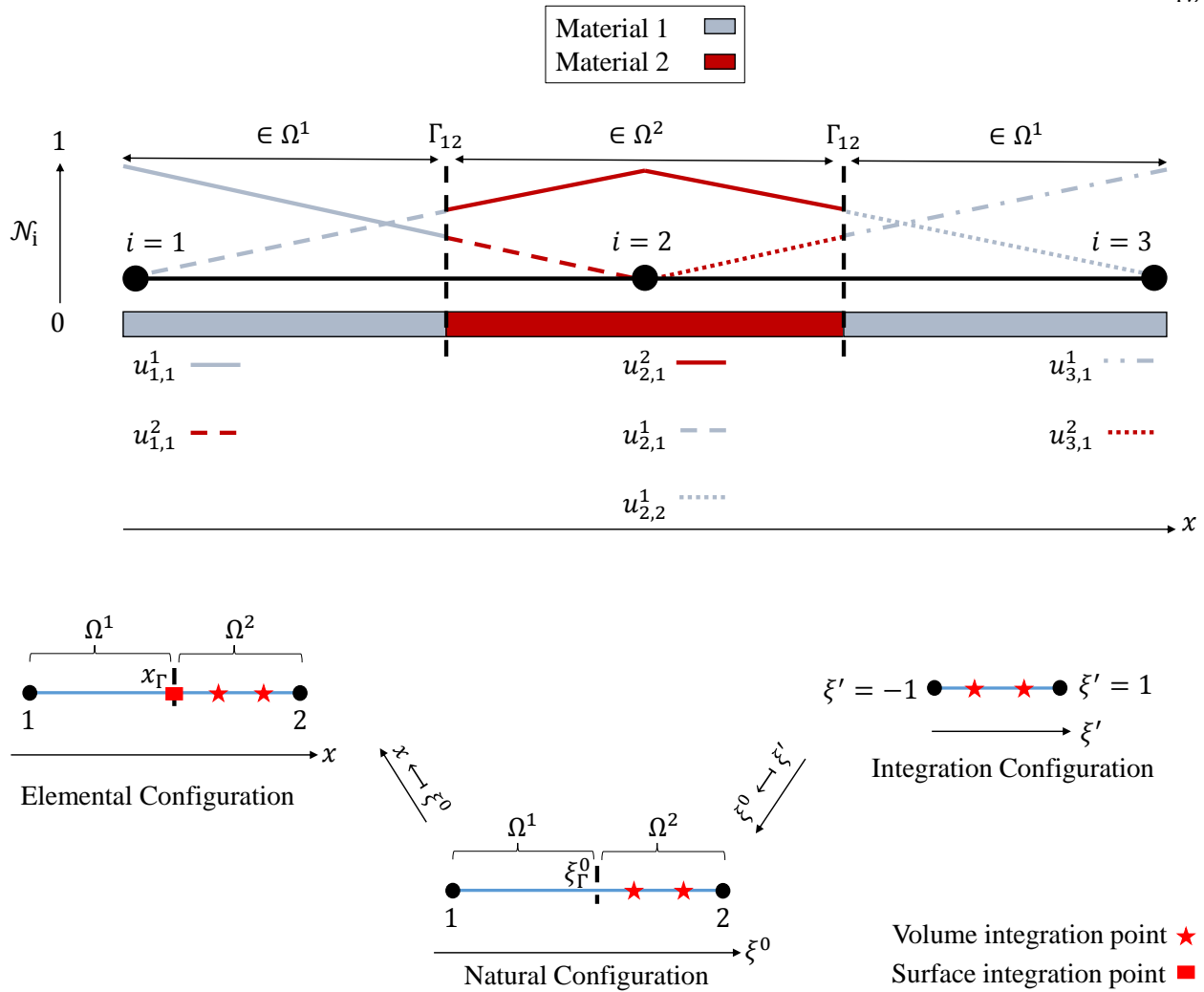


Figure 1.6: Heaviside-enriched XFEM framework in 1D: Interpolation of solution field using generalized Heaviside enrichment (top); Mapping of integration domains for an intersected element (bottom).

where I is the set of all nodes in the finite element mesh, $\mathcal{N}_i(\mathbf{x})$ is the nodal basis function associated with node i , Ψ is the maximum number of enrichment levels and $\mathbf{u}_{i,e}^m$ is the vector of degrees of freedom at node i for phase $m \in (1, 2)$. The Kronecker delta $\delta_{el}^{m,i}$ selects the active enrichment level, l , for node i and material phase m such that only one set of degrees of freedom is used for interpolating the solution at any given point, \mathbf{x} in Ω , thereby satisfying the partition of unity principle.

Figure 1.6 presents an intersection configuration comprising of two linear finite elements

in 1D. Basis functions, \mathcal{N}_i , have been plotted over each element. Below each node, the active set of degrees of freedom have been stated corresponding to (1.4). Nodes 1 and 3 belong to material phase 1 whereas node 2 belongs to material phase 2. Nodes 1 and 3 interpolate in each material phase using only one degree of freedom per phase. Node 2 interpolates in material phase 2 using one degree of freedom. For a consistent interpolation in phase 1, node 2 requires two degrees of freedom as the support of \mathcal{N}_2 includes two disconnected regions of material phase 1. Figure 1.8 presents an intersection configuration depicting the active set of degrees of freedom corresponding to a single finite element in 2D. For a more comprehensive understanding of the adopted enrichment strategy the reader is referred to the study in [82].

The Heaviside-enriched XFEM requires integrating the weak form of the governing equations separately in each material phase. Thus an element intersected by the zero level set contour is subdivided as shown in Figure 1.6. In 2D and 3D we perform this subdivision using Delaunay triangulation [59]. Integration over these subdivisions requires identification of three distinct configurations. Figure 1.6 presents the mapping between these configurations for an intersected element in 1D. An element in the global coordinate system (Elemental Configuration) is mapped to an element in its natural coordinate system (Natural Configuration) with coordinates ranging between $\xi_1^0 = -1$ and $\xi_2^0 = 1$. The subdivided elements in the Natural Configuration are further mapped to integration subdomains (Integration Configuration) with coordinates for each subdomain ranging between $\xi' = -1$ and $\xi' = 1$. The solution field, \hat{u} , can then be approximated using 1D maps based on e.g. a linear interpolation scheme as detailed in Section 3 of Appendix B. Figure 1.8 presents a mapping of intersection configuration domains in 2D.

The generalized Heaviside enrichment strategy requires that the material interface does not intersect a node. This is achieved by shifting the material interface, x_Γ , when the interface comes within a critical distance of a node, referred to as the critical shift distance, x_{Γ_c} . The interface is shifted such that the new interface position is at a distance, x_{Γ_c} from the node. Various options for shifting the material interface are possible as presented in Section 3 of

Appendix B. In this thesis we perform a Phase 1 Shift (P1S), such that upon shifting x_Γ , the previously intersected node lies in phase 1. Figure 1.7 presents a schematic depicting the change in intersection configuration when performing the interface shift. The shape sensitivities are then evaluated taking the material shift into account. Effects of shifting the material interface on the physical response and its sensitivities are examined in detail in Section 5.1.2 of Appendix B.

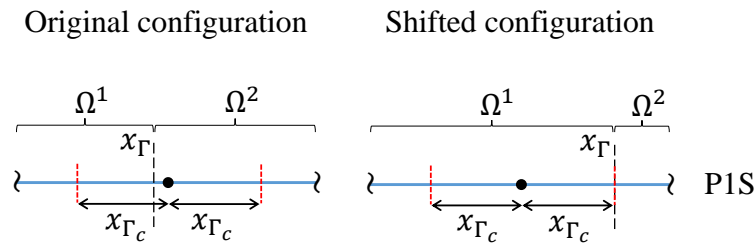


Figure 1.7: Interface shift schematic.

The LSF is mapped onto the XFEM mesh by evaluating the parametrized LSF at the nodes. Standard bilinear and trilinear shape functions, in 2D and 3D respectively, are used to interpolate the level set value in an element. These shape functions permit an element edge to be intersected by the material interface, i.e. $\phi(\mathbf{x}) = 0$, at most once. Lines and faces in 2D and 3D respectively, connecting the edge intersection points, \mathbf{x}_Γ , define the material interface within a finite element as shown in Figure 1.8.

In the physical modeling community the XFEM has previously been used in [42, 86, 109] among others to model multiphase problems. In the topology optimization community the LSM-XFEM approach is often classified as a generalized shape optimization approach [32]. As mentioned earlier, this classification stems from the fact that the approach allows for topology modifications resulting from merging or disappearing of holes. The LSM-XFEM approach has been used in the context of shape and topology optimization in [47, 65, 76, 133] among others.

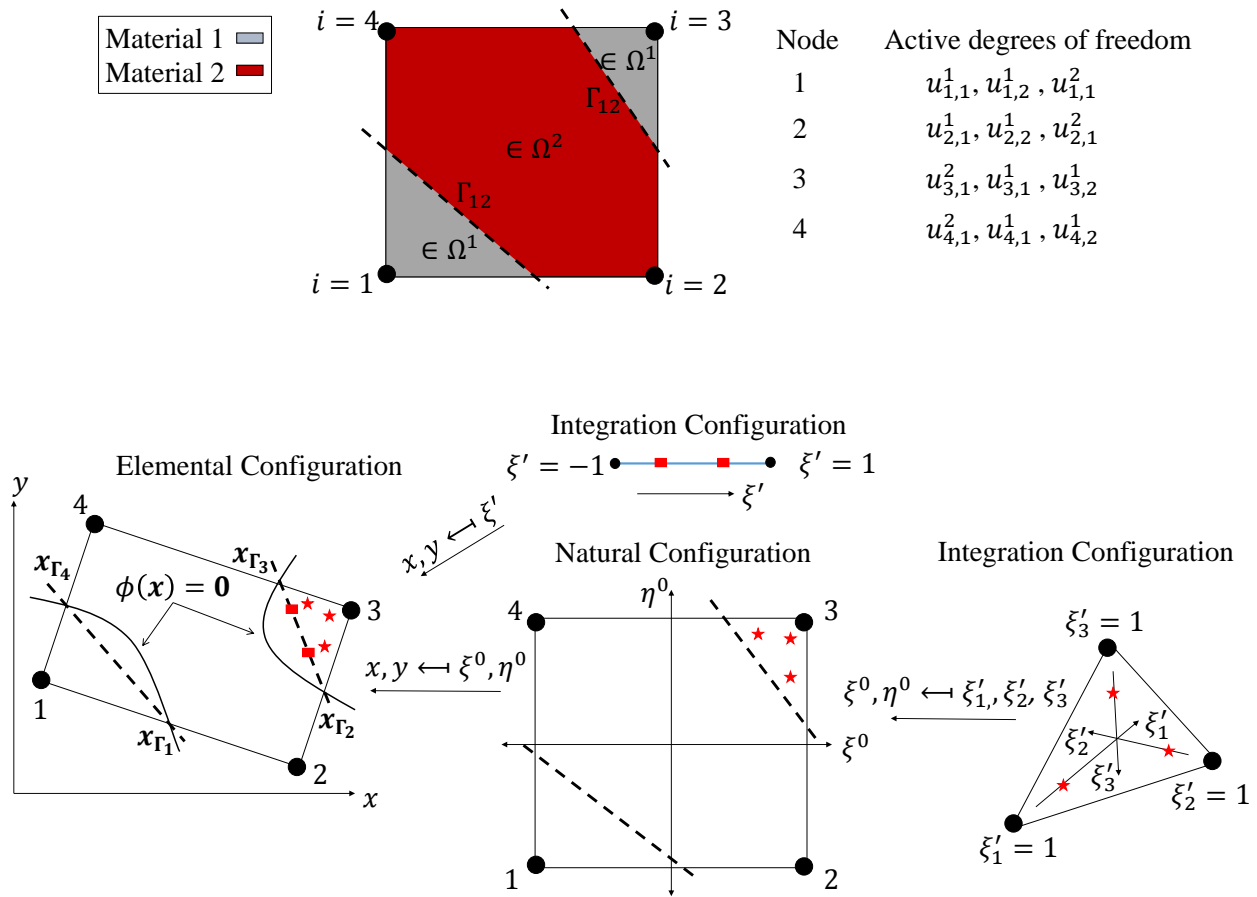


Figure 1.8: Heaviside-enriched XFEM framework in 2D: Interpolation of solution field using generalized Heaviside enrichment (top); Mapping of integration domains for an intersected element (bottom).

1.5 Physical models of interest

This section presents the physical models used for performing the numerical studies discussed in Chapters 2, 3, and 4. Namely, the variational form of the governing equations for unsteady diffusion, thermo-coupled static linear elasticity, and static hyperelasticity are presented. All materials are assumed to be isotropic. We use the model problem depicted in Figure 1.9 to present the variational form of the governing equations.

We adopt the standard Galerkin approach in defining the solution spaces $\mathcal{U} = \mathcal{U}^1 \times \mathcal{U}^2$,

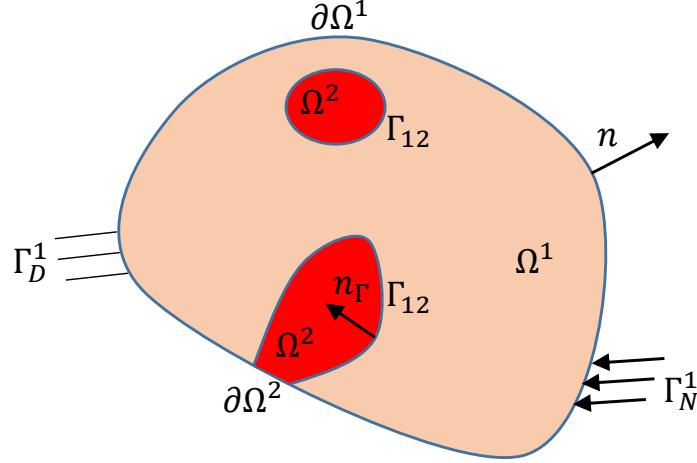


Figure 1.9: Schematic of the model problem.

$\mathbf{u} = \mathbf{u}^1 \times \mathbf{u}^2$ and the weighting spaces $\mathcal{V} = \mathcal{V}^1 \times \mathcal{V}^2$, $\boldsymbol{\mathcal{V}} = \boldsymbol{\mathcal{V}}^1 \times \boldsymbol{\mathcal{V}}^2$, such that

$$\begin{aligned}
 \mathcal{U}^m &= \{T^m \in H^1(\Omega^m); T^m = T_D \text{ on } \Gamma_D^m\}, \\
 \mathcal{V}^m &= \{\zeta^m \in H^1(\Omega^m); \zeta^m = 0 \text{ on } \Gamma_D^m\}, \\
 \boldsymbol{\mathcal{U}}^m &= \{\mathbf{u}^m \in H^1(\Omega^m); \mathbf{u}^m = \mathbf{u}_D \text{ on } \Gamma_D^m\}, \\
 \boldsymbol{\mathcal{V}}^m &= \{\mathbf{v}^m \in H^1(\Omega^m); \mathbf{v}^m = \mathbf{0} \text{ on } \Gamma_D^m\},
 \end{aligned} \tag{1.5}$$

where T^m and \mathbf{u}^m , are the restriction of the temperature and displacement field respectively to Ω^m . Further, ζ^m and \mathbf{v}^m are the temperature and displacement weighting functions respectively. The spaces \mathcal{U} and \mathcal{V} are Hilbert manifolds consisting of scalar functions with square integrable first derivatives, whereas the spaces $\boldsymbol{\mathcal{U}}$ and $\boldsymbol{\mathcal{V}}$ are Hilbert manifolds consisting of vector functions with square integrable first derivatives.

The weak form for the unsteady heat diffusion equations augmented with Nitsche's method [60, 118] to satisfy continuity of temperature and flux across the interface, is: Find $T^m \in \mathcal{U}^m$

$$\mathcal{R}^D = \mathcal{R}_\Omega^D + \mathcal{R}_{\Gamma_N}^D + \mathcal{R}_{\Gamma_{12}}^D = 0 \quad \forall \zeta^m \text{ in } \mathcal{V}^m, \tag{1.6}$$

where \mathcal{R}_Ω^D is the residual of the volumetric contribution, $\mathcal{R}_{\Gamma_N}^D$ is the residual contribution from the Neumann boundary, and $\mathcal{R}_{\Gamma_{12}}^D$ is the residual contribution from the interface conditions.

These residual contributions are given by

$$\begin{aligned}\mathcal{R}_\Omega^D &= \sum_{m=1,2} \int_{\Omega^m} \left(\rho C \frac{\partial T^m}{\partial t} - \nabla \zeta^m \cdot (k^m \nabla T^m) \right) d\mathbf{x}, \\ \mathcal{R}_{\Gamma_N}^D &= \sum_{m=1,2} \int_{\Gamma_N^m} \zeta^m q_N d\mathbf{x}', \\ \mathcal{R}_{\Gamma_{12}}^D &= - \int_{\Gamma_{12}} \llbracket \zeta \rrbracket \{k \nabla T\} \cdot \mathbf{n}_\Gamma d\mathbf{x}' - \int_{\Gamma_{12}} \{k \nabla \zeta\} \cdot \mathbf{n}_\Gamma \llbracket T \rrbracket d\mathbf{x}' + \int_{\Gamma_{12}} \gamma_\Gamma \llbracket \zeta \rrbracket \llbracket T \rrbracket d\mathbf{x}',\end{aligned}\tag{1.7}$$

where ρ , C and k^m are the density, heat capacity, and isotropic thermal conductivity respectively. A heat flux, q_N , is specified on the Neumann boundary, $\partial\Omega_N^m$, with an outward normal \mathbf{n} . The integrals $\int_\chi d\mathbf{x}$ and $\int_\chi d\mathbf{x}'$ denote operation on $\chi \subset \mathbb{R}^d$ and $\chi \subset \mathbb{R}^{d-1}$ respectively.

In this thesis we consider numerical examples based on linear elasticity as well as thermo-elastic coupling. For brevity we present only the weak form for thermo-coupled static linear elasticity. The weak form herein is also augmented with the Nitsche's method, to satisfy continuity of displacement and traction across the interface in material-material problems. The weak form is stated as: Find $\mathbf{u} \in \mathcal{U}^m$ such that

$$\mathcal{R}^E = \mathcal{R}_\Omega^E + \mathcal{R}_{\Gamma_N}^E + \mathcal{R}_{\Gamma_{12}}^E = 0 \quad \forall \mathbf{v} \in \mathcal{V}.\tag{1.8}$$

The above residual contributions are given by

$$\begin{aligned}\mathcal{R}_\Omega^E &= \sum_{m=1,2} \int_{\Omega^m} \boldsymbol{\epsilon}(\mathbf{v}^m) : \boldsymbol{\sigma}(\mathbf{u}^m, T^m) d\mathbf{x}, \\ \mathcal{R}_{\Gamma_N}^E &= - \sum_{m=1,2} \int_{\Gamma_N^m} \mathbf{v}^m \mathbf{t}_N d\mathbf{x}', \\ \mathcal{R}_{\Gamma_{12}}^E &= - \int_{\Gamma_{12}} (\llbracket \mathbf{v} \rrbracket \{ \boldsymbol{\sigma}(\mathbf{u}), T^m \} \cdot \mathbf{n}_\Gamma - \{ \boldsymbol{\sigma}(\mathbf{v}) \} \cdot \mathbf{n}_\Gamma \llbracket \mathbf{u} \rrbracket + \gamma_\Gamma \llbracket \mathbf{v} \rrbracket \llbracket \mathbf{u} \rrbracket) d\mathbf{x}'.\end{aligned}\tag{1.9}$$

The traction, \mathbf{t}_N , is specified on the Neumann boundary, Γ_N^m . The Cauchy stress tensor, $\boldsymbol{\sigma}^m$, accounting for thermal expansion is defined using the constitutive model

$$\boldsymbol{\sigma}^m = \mathbf{D}^m \boldsymbol{\epsilon}^m = \mathbf{D}^m \left(\frac{1}{2} (\nabla \mathbf{u}^m + (\nabla \mathbf{u}^m)^T) - \alpha^m (T^m - T_{ref}) \right),\tag{1.10}$$

where \mathbf{D}^m is the fourth order constitutive tensor for the isotropic material belonging to material phase m , and $\boldsymbol{\epsilon}^m$ is the infinitesimal strain tensor. The thermal expansion is accounted

for based on the reference temperature T_{ref} , for a coefficient of thermal expansion given by α^m .

The jump and averaging operators in (1.7) and (1.9) are defined as $\llbracket \cdot \rrbracket = (\cdot)^2 - (\cdot)^1$ and $\{\cdot\} = \gamma^1\{\cdot\}^1 + \gamma^2\{\cdot\}^2$ respectively. The constants γ^1 , and γ^2 are referred to as weighting parameters. The definition of the penalty parameter, γ_Γ , is associated with definition of the weighting parameters so as to provide stability to the method [5]. The weighting parameters along with the penalty parameter determine the accuracy with which the interface conditions are satisfied. Various approaches for defining the weighting parameters have been proposed in literature. The classical Nitsche's method involves using an equal weighting [30] such that,

$$\gamma^1 = \gamma^2 = 0.5. \quad (1.11)$$

However, in presence of small intersections or large values of k^m (or E^m) this approach will result in unusually large estimates of the penalty parameter γ_Γ [5]. An extremely high penalty can lead to poor conditioning of the underlying system of equations. To increase robustness by varying the weighting parameter with the element size, in [6] a volume weighted definition of the weighting parameters was suggested such that,

$$\gamma^m = \frac{meas(\Omega^m)}{meas(\Omega^1) + meas(\Omega^2)}. \quad (1.12)$$

A smarter choice for weights was presented in [5] where the weighting parameters assumed the form,

$$\gamma^m = \frac{meas(\Omega^m)/\Xi^m}{meas(\Omega^1)/\Xi^1 + meas(\Omega^2)/\Xi^2}, \quad (1.13)$$

where Ξ is the thermal conductivity in (1.7) and Young's modulus in (1.9). The above formulation in addition to accounting for the small intersection areas, further accounts for material differences across the material interface. Following the work in [5] we define the penalty parameter as

$$\gamma_\Gamma = 2 c_\Gamma \frac{meas(\Gamma_{AB})}{meas(\Omega^1)/\Xi^1 + meas(\Omega^2)/\Xi^2}. \quad (1.14)$$

The user defined penalty c_Γ determines how strongly the interface constraints are enforced. A high value of c_Γ ensures better enforcement of the interface conditions, but as mentioned above may lead to poor conditioning of the underlying system of equations. The influence of c_Γ on the shape sensitivities is discussed in Section 5.1.1. of Appendix B. The operator $meas(\cdot)$ refers to the Lebesgue measure of the respective quantity.

We also consider solid-void problems considering finite strains using the Saint Venant-Kirchhoff hyperelastic model. The hyperelastic model involves solving for the vector displacement field, $\mathbf{u}(\mathbf{x})$, in Ω^1 . Phase 2 is void of any material. Within the context of material nonlinearity, equilibrium is formulated with respect to a reference undeformed configuration and the weak form is stated as: $\mathbf{u}^1 \in \mathbf{U}^1$ such that

$$\mathcal{R}^H = \mathcal{R}_\Omega^H + \mathcal{R}_{\Gamma_N}^H \quad \forall \mathbf{v}^1 \in \mathbf{V}^1. \quad (1.15)$$

Here \mathcal{R}_Ω^H is the residual of the volumetric contribution and $\mathcal{R}_{\Gamma_N}^H$ is the residual contribution from the Neumann boundary. These contributions are given by:

$$\begin{aligned} \mathcal{R}_\Omega^H &= \int_{\Omega^1_0} \mathbf{F}(\mathbf{v}^1) : \mathbf{P}(\mathbf{u}^1) d\mathbf{x}, \\ \mathcal{R}_{\Gamma_N}^H &= - \int_{\Gamma^1_{N_0}} \mathbf{v}^1 \mathbf{t}_N d\mathbf{x}'. \end{aligned} \quad (1.16)$$

The traction, \mathbf{t}_N , is specified on the Neumann boundary, $\Gamma^1_{N_0}$. The subscript ‘0’ refers to entities defined in the undeformed configuration. The deformation gradient, \mathbf{F} , accounts for the motion of the spatial coordinate in the deformed configuration, \mathbf{x}^1 , with respect to the spatial coordinate in the undeformed configuration, \mathbf{x}^1_0 . We consider single-phase hyperelastic problems wherein the displacement or traction are not required to be continuous across the material-void interface. Hence no interface conditions are enforced.

1.5.1 Topology optimization

Topology optimization is a well established computational approach to mathematically optimize the layout and the geometry of a body based on a physical design problem. The

method is popular for its ability to generate lightweight mechanical components for the automotive, aerospace, and medical industries, and has emerged as a promising approach to utilize the benefits of additive manufacturing [16, 83, 89]. Topology optimization allows radical changes in both the shape of the body and the material geometry within the body as shown in Figure 1.10. This chapter provides an introduction involving the basic concepts surrounding topology optimization.

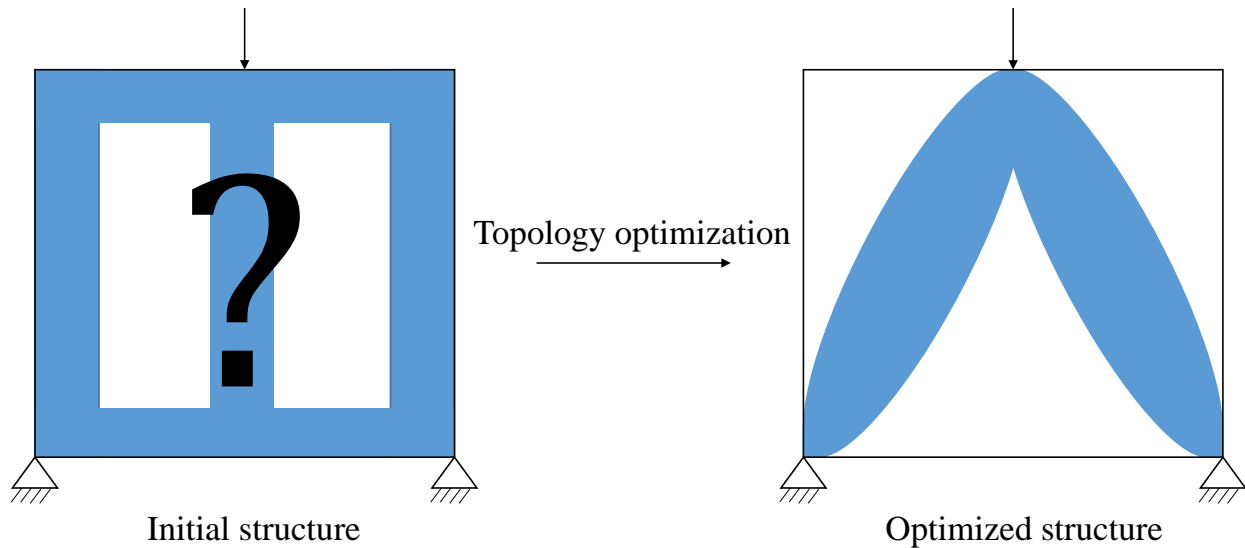


Figure 1.10: A structure undergoing topology optimization to increase stiffness of the structure subject to volume constraint.

Topology optimization problems considered in this thesis, for instance for static linear elasticity, are mathematically expressed as:

$$\begin{aligned} & \underset{\mathbf{s}}{\text{minimize}} && \mathcal{Z}(\mathbf{u}(\mathbf{s}), \mathbf{s}) \\ & \text{subject to} && g_i(\mathbf{u}(\mathbf{s}), \mathbf{s}) \leq 0; \quad \forall i = 1, \dots, n_g \end{aligned} \quad (1.17)$$

where \mathcal{Z} , g_i define the objective and inequality constraints respectively. The vectors \mathbf{u} and \mathbf{s} represent the vector of state and design variables respectively. In addition to the constraints listed in (1.17) we make use of box constraints to bound the design variables such that $s_k^{\min} \leq s_k \leq s_k^{\max}$ for k -th design variable. A formulation such as the one in (1.17) where only the design variables are independent, is referred to as Nested Analysis and

Design (NAND) approach [7]. In this case the vector of state variables \mathbf{u} is computed for a given vector of design variables \mathbf{s} obtained by solving the vector of residuals of the governing equations (Section 1.5) $\mathcal{R} = 0$ of the underlying physics.

The choice of design variables \mathbf{s} is highly problem and framework dependent. For instance density-based methods employ artificial elemental densities as design variables. The material properties are then parametrized using material interpolation functions such that most of the intermediate density values are penalized [115]. Downsides associated with density-based topology optimization include fuzzy boundaries and inaccurate response along material boundaries as discussed in Section 1.1. Level set methods on the other hand employ the material boundary [4, 132, 133] or nodal level set values [90, 129] as design variables. Similar to density-based methods [116] LSMs also require regularization techniques to obtain a well-posed optimization problem, to remove numerical artifacts and to improve the convergence of the optimization problem [27, 82, 132]. A relatively new class of topology optimization problems involve the use of geometric primitives as design variables. These geometric design variables are mapped to a density field [93] or an LSF [47] for defining the material layout during the optimization process. Compared to the traditional element or node-based design optimization framework, the proposed approach can incorporate more geometry information into topology optimization with the shape sensitivities directly related to the definition of the geometric primitives. In the context of LSM-XFEM-based topology optimization, this thesis focuses on the use of nodal level set values (Section 4.1) and geometric primitives (Section 4.2) as design variables.

The update of the design variables in LSM-based topology optimization can be distinguished using two major categories. The first category treats the optimization process as a quasi-temporal process involving the solution of a Hamilton-Jacobi equation [122] for describing the evolution of the LSF based on a design velocity field, e.g. in [1, 137]. The velocity at the material boundary is typically derived from variational shape sensitivity analysis, and then extended to the rest of the domain [28]. The second category for updating

design variables involves mathematical programming wherein shape sensitivities are related directly to the optimization variables \mathbf{s} , e.g. in [90, 129]. This work uses the latter approach to avoid the unnecessary cost of solving an additional partial differential equation in the form of the Hamilton-Jacobi equation.

1.5.1.1 Optimization algorithms

Optimization algorithms can be grouped into categories of gradient-free (black-box) and gradient-based methods. As implied by the name, the former do not rely on gradient information and therefore have no requirement for continuity/differentiability of \mathcal{Z} or g_i . This makes them well-suited for discrete problems, i.e. problems where the design variable can only have discrete values such as the number of hinges in a structure. Some of the popular gradient-free optimization algorithms are simulated annealing [81], genetic algorithms [84], and branch and bound methods [67]. Although easy to implement gradient-free methods are restrictive with respect to the dimension of the design space i.e. a large number of design variables lead to a rapid escalation of computational costs [63]. Given the possibility of high number of design variables in topology optimization [35] gradient-free methods are not the preferred choice.

In contrast gradient-based algorithms are a more viable tool given their efficiency in handling large number of design variables [149]. These algorithms use the derivative information to guide the search process. As a result, the optimization studies presented in this thesis are restricted to problems with continuous and differentiable objective and constraint functions. Most physical phenomena are modeled by a set of partial differential equations resulting in nonlinear objective functions and constraints. Consequently this work employs gradient-based algorithms for continuous nonlinear constrained optimization. Some of the most popular optimization algorithms in this class include interior point methods [134] and sequential quadratic programming (SQP) [43]. In the current study the globally convergent method of moving asymptotes (GCMMA) [123] is employed, which was developed

with structural optimization in sight. In the current thesis the GCMMA parameters values controlling the adaptation of the initial, lower and upper asymptotes are 0.5, 0.7, and 1.43 respectively.

1.5.1.2 Sensitivity analysis

When using gradient-based algorithms for optimization problems, the implementation of a sensitivity analysis is imperative. Ways to calculate the shape sensitivities include finite difference, the direct, and the adjoint method. The main advantage of the finite difference method lies in its trivial implementation. However finite differences gets very costly as it requires solving the system of equation twice (assuming central finite difference) for every design variable s_k . The computational cost of finite differences can turn out to be very high as several analyses of the physical problems are necessary. We thus shift our focus to sensitivities computed using the direct and adjoint approach.

The derivative of the objective function \mathcal{Z} in (1.17) can be decomposed using the chain rule to give

$$\frac{d\mathcal{Z}(\mathbf{u}(\mathbf{s}), \mathbf{s})}{ds_k} = \frac{d\mathcal{Z}}{ds_k} + \left(\frac{\partial \mathcal{Z}}{\partial \mathbf{u}} \right)^T \frac{\partial \mathbf{u}}{\partial s_k}. \quad (1.18)$$

Similarly the derivative of the residual of governing equations can be decomposed using the chain rule to give

$$\frac{d\mathcal{R}(\mathbf{u}(\mathbf{s}), \mathbf{s})}{ds_k} = \frac{\partial \mathcal{R}}{ds_k} + \frac{\partial \mathcal{R}}{\partial \mathbf{u}} \frac{\partial \mathbf{u}}{\partial s_k}. \quad (1.19)$$

Solving for $\partial \mathbf{u} / \partial s_k$ in (1.19) we have,

$$\frac{\partial \mathbf{u}}{\partial s_k} = - \left(\frac{\partial \mathcal{R}}{\partial \mathbf{u}} \right)^{-1} \frac{d\mathcal{R}}{ds_k}. \quad (1.20)$$

Solving (1.20), followed by substitution in (1.18) gives us the direct approach to computing sensitivities

$$\frac{d\mathcal{Z}(\mathbf{u}(\mathbf{s}), \mathbf{s})}{ds_k} = \frac{d\mathcal{Z}}{ds_k} - \left(\frac{\partial \mathcal{Z}}{\partial \mathbf{u}} \right)^T \left(\frac{\partial \mathcal{R}}{\partial \mathbf{u}} \right)^{-1} \frac{d\mathcal{R}}{ds_k}. \quad (1.21)$$

In contrast the adjoint approach avoids direct evaluation of the implicit part in (1.18):

$$\frac{d\mathcal{Z}(\mathbf{u}(\mathbf{s}), \mathbf{s})}{ds_k} = \frac{d\mathcal{Z}}{ds_k} - \boldsymbol{\lambda}^T \frac{d\mathcal{R}}{ds_k}; \quad \left(\frac{\partial \mathcal{R}}{\partial \mathbf{u}} \right)^T \boldsymbol{\lambda} = \frac{\partial \mathcal{Z}}{\partial \mathbf{u}}. \quad (1.22)$$

As is evident from (1.21) the direct method requires number of linear solves equal to the number of design variables while the adjoint method requires number of solves equal to the number of objective and constraint functions. If the number of design variables is small relative to the number of objective and constraints, the direct method is preferred. If the number of design variables is large relative to the number of objectives and constraints the adjoint method is computationally more efficient. As topology optimization problems typically have a large number of design variables the adjoint method is employed in this thesis for the computation of sensitivities. For transient problems not reaching a steady state, sensitivity analysis can be thought of as an extension of (1.22) wherein the adjoint states are computed by integrating the adjoint equations backward in time as detailed in [24]. The topic of shape sensitivities in context to Heaviside-enriched XFEM is further discussed in Chapter 3.

1.6 Structure of the thesis

The rest of the thesis is organized as follows: Chapter 2 presents the contributions made towards advances in design using the XFEM; Chapter 3 analyses the behavior of shape sensitivities using Heaviside-enriched XFEM; in Chapter 4 we present topology optimization problems using the XFEM, employing nodal level set values and geometric primitives as design variables. Appendix A, B, and C present the publications resulting from the work in this thesis. Appendix D discusses the implementation of certain computational algorithms relevant to the work in this thesis.

The chapters in the main body present moderately detailed highlights of the contributions of this thesis. The reader is appropriately referred to the publications in the Appendix for further details and numerical examples as and when deemed necessary. Suggestions on

future research are provided at the end of the discussion on every contribution along with a brief outlook of the contribution made. It is important to point out that notations might differ from one paper to another. Hence to maintain readability notations have been kept consistent throughout the main body of the thesis. As a result notations in the main body of the thesis may or may not be consistent with notations in the respective publications from the Appendix.

Chapter 2

Advances in Design

This chapter presents the advances made towards making the XFEM a more viable and reliable tool for modeling real world physical phenomenon. Specifically, i) The longstanding problem of inaccurate prediction of stresses in the context of immersed boundary methods is addressed. ii) A framework is developed for modeling of heterogeneous materials with uncertain inclusion geometry.

2.1 Gradient-stabilized stresses

Stress-based design optimization is integral to designing structures that take the strength of materials into account. As a result over the past decade, there has been a growing interest in the study of shape and topology optimization problems considering stress-based objectives and constraints. For instance, recent advances in additive manufacturing has generated immense interest for accurately modeling the process. Predicting residual stresses in additive manufacturing is an integral part of the modeling process. Thus there has been immense interest in computational modeling of residual stresses [29, 78, 85, 148]. Researchers have simultaneously been focusing on developing optimization frameworks to introduce designs that minimize development of undesirable residual stresses during the manufacturing process. Immersed boundary methods such as the XFEM are naturally associated with additive manufacturing given their ability to accurately model physics along the material interface without the need for re-meshing. However as discussed in Section 1.2 the XFEM has a

longstanding issue of overestimation of stresses. A material interface too close to a node can lead to small intersection areas. These small regions present vanishing zones of influence for certain degrees of freedom which can adversely affect the condition number of the system, result in uncontrolled displacement gradients across element edges, and for a nonlinear model may affect the stability of the system of equations. An overview of the efforts made to resolve the issue of overestimation of stresses using the XFEM has been provided in Section 1.2.

Low-order finite elements, given their simplicity and ease of implementation are the most popular choice of interpolation for topology optimization problems. The influence of small intersection areas on the accuracy of spatial gradients is aggravated when using low-order elements. To maintain stability of the system and ensure the convergence of stress prediction with mesh refinement, we adopt the ghost penalty approach presented in [18] for Stokes flow, and adapt it for linear and hyperelasticity.

2.1.1 Ghost penalty for stabilizing displacement gradients

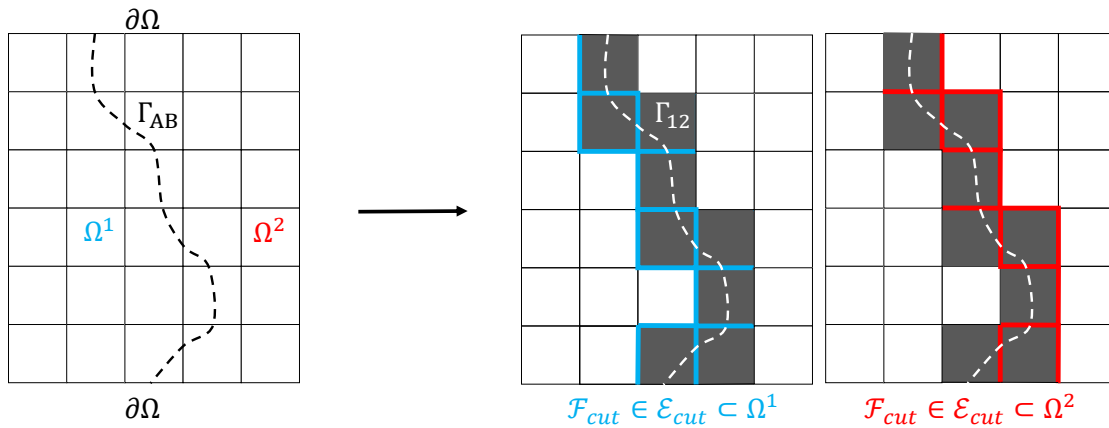


Figure 2.1: Stabilized faces in a two-phase problem.

We consider the set of element faces, \mathcal{F}_{cut} , belonging to intersected elements, \mathcal{E}_{cut} , as shown in Figure 2.1. For each face, $F \in \mathcal{F}_{cut}$, there exist two elements (one of which is the intersected element itself), \mathcal{E}^A and \mathcal{E}^B , such that $F = \mathcal{E}^A \cap \mathcal{E}^B$. The jump in the displacement

gradients across this face is then penalized by augmenting the left hand side of (1.8) and (1.15) with the following term.

$$\mathcal{R}_F^E = \mathcal{R}_F^H = \sum_{F \in \mathcal{F}_{cut}} \sum_{m=1,2} \int_F \gamma_u h E^m [\nabla \mathbf{v}^m] [\nabla \mathbf{u}^m] d\mathbf{x}', \quad (2.1)$$

where E^m is the elastic modulus of phase m , and γ_u is a penalty parameter that determines how strongly the gradients are penalized. The jump in the displacement gradient is defined as $[\nabla \mathbf{u}^m] = \mathbf{n}_F \cdot \nabla \mathbf{u}^m|_{\mathcal{E}^A} - \mathbf{n}_F \cdot \nabla \mathbf{u}^m|_{\mathcal{E}^B}$, where \mathbf{n}_F denotes the unit normal to the face, F . For faces that are intersected jump in the displacement gradients is penalized for both material phases. Note that only the jump of the displacement gradients in normal direction is penalized. Alternatively the jump in the stresses (including presence of thermal expansion) can directly be penalized by augmenting the left hand side of (1.8) and (1.15) with the following term.

$$\mathcal{R}_F^E = \mathcal{R}_F^H = \sum_{F \in \mathcal{F}_{cut}} \sum_{m=1,2} \int_F \gamma_u h [\boldsymbol{\epsilon}(\mathbf{v}^m)] [\boldsymbol{\sigma}(\mathbf{u}^m, T^m)] d\mathbf{x}', \quad (2.2)$$

The implementation of (2.2) for hyperelastic materials is not straightforward. This is due to the complexity involved in the computation of the stiffness matrix associated with (2.2) for a hyperelastic model. Furthermore (2.2) has not been studied formally in literature for error and convergence properties unlike (2.1) was studied in [18]. We hence use (2.1) for all stress stabilization studies in this thesis.

This face oriented stabilization of spatial gradients presents two advantages - i) Smooth displacement gradients are obtained along the material interface. ii) The zone of influence of degrees of freedom no longer vanishes because (2.1) requires integration over the entire face independent of the location of the intersection. A drawback is that the framework results in a non-smooth behavior of stresses as the material interface transitions from one element to another. This is a result of the on/off nature of (2.1), and is discussed in detail in Section 5.1.3 of Appendix C. Since $F = \mathcal{E}^A \cap \mathcal{E}^B$, by definition faces along the boundary of the mesh are excluded from the set \mathcal{F}_{cut} . A solution to this issue is padding the domain of interest with dummy void phase elements as discussed in Section 4.1.

2.1.2 XFEM informed smoothing of stresses

In addition to stabilizing the displacement gradients, in the current study we introduce a scalar stress field, τ , using an XFEM informed smoothing procedure. Using the solution of the displacement field we solve the following equation to obtain a gradient stabilized scalar stress field in a Heaviside-enriched XFEM framework.

$$\begin{aligned} \mathcal{R}_\Omega^S + \mathcal{R}_F^S = 0 \quad \forall \eta \in \mathcal{V} \implies \\ \sum_{m=1,2} \int_{\Omega^m} \eta^m (\tau^m - \mathcal{S}(\mathbf{u}^m)) \, d\mathbf{x} + \sum_{F \in \mathcal{F}_{cut}} \sum_{m=1,2} \int_F \gamma_\tau h [\nabla \eta^m] [\nabla \tau^m] \, d\mathbf{x}' = 0. \end{aligned} \quad (2.3)$$

Here \mathcal{S} is a scalar function of the components of the Cauchy stress tensor, e.g. axial stress, principal stress, and von Mises stress, computed using the displacement fields, \mathbf{u}^m . In the present study \mathcal{S} is the von Mises stress function. In presence of thermal expansion, \mathcal{S} is also a function of T^m . The smoothed scalar stress field is denoted by τ^m , with η^m being the corresponding weighting function. The functions τ^m and η^m belong to Hilbert manifolds, \mathcal{U} and \mathcal{V} respectively, consisting of scalar functions with square integrable first derivatives. Note, the scalar stress field is computed using the displacement field subjected to ghost penalty. Thus the ghost penalty terms in (2.3) provide a second level of spatial gradient stabilization.

In comparison with an area weighted smoothing [90], the XFEM informed smoothing ensures the avoidance of overestimation of stresses by penalizing the stresses across the entire elemental face. However, like the area weighted smoothing the XFEM informed smoothing is just a post-processing step. Section 2.1.3 provides comparison of the two approaches through a numerical example.

2.1.3 Application to cantilever beam problem

Through this example we compare the accuracy of stresses computed using the proposed approach. Comparisons are drawn against stresses computed using a body fitted mesh as well as stresses computed using an area weighted smoothing. The problem setup consists

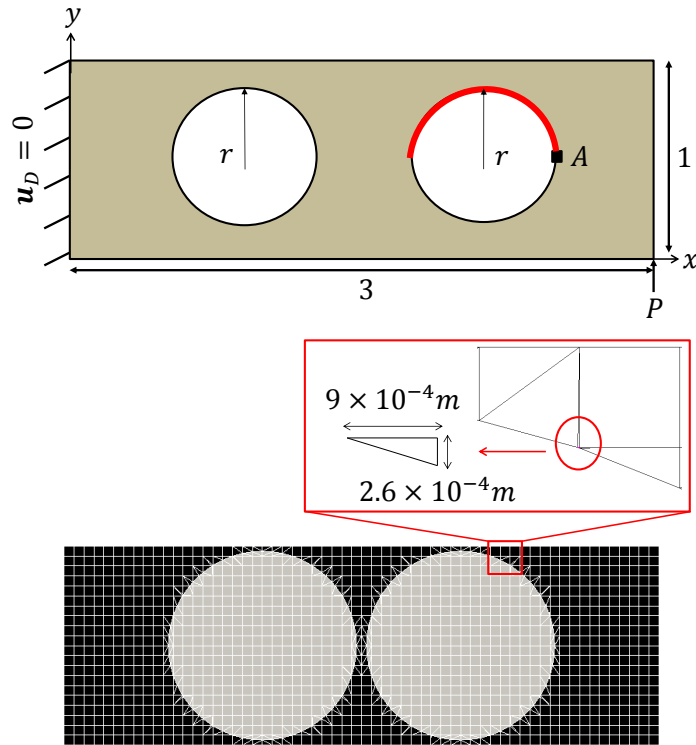


Figure 2.2: Cantilever beam setup (top), and mesh $h = 0.05m$ (bottom). Stresses are monitored along the highlighted region. All dimensions are in m.

of a material-void 2D cantilever beam as shown in Figure 2.2. The beam is assumed linear elastic with a Young's modulus, $E = 10^4 N/m^2$, and Poisson's ratio, $\nu = 0.3$. The beam is fixed along its left edge. A point load of $P = 10N$ is applied at the bottom right corner of the beam. Within the beam are two circular inclusions, each of radius r , centers of which lie at $\mathbf{x} = (1, 0.5)$ and $\mathbf{x} = (2, 0.5)$. We monitor the stresses along the upper-half interface of the circular inclusion centered at $\mathbf{x} = (2, 0.5)$.

With $r = 0.4742m$ we investigate the accuracy of stresses along the material interface. The value of r is chosen such that the interface configuration results in small intersection areas for all mesh sizes used in the current example. Figures 2.3 and 2.4 plot the von Mises stress, σ_{vM} , as a function of the central angle, θ , measured in degrees counterclockwise from point A in Figure 2.2. The stresses are plotted for various mesh sizes, h , for different values of stabilization penalty parameters, γ_u and γ_τ . These stresses are compared against a reference

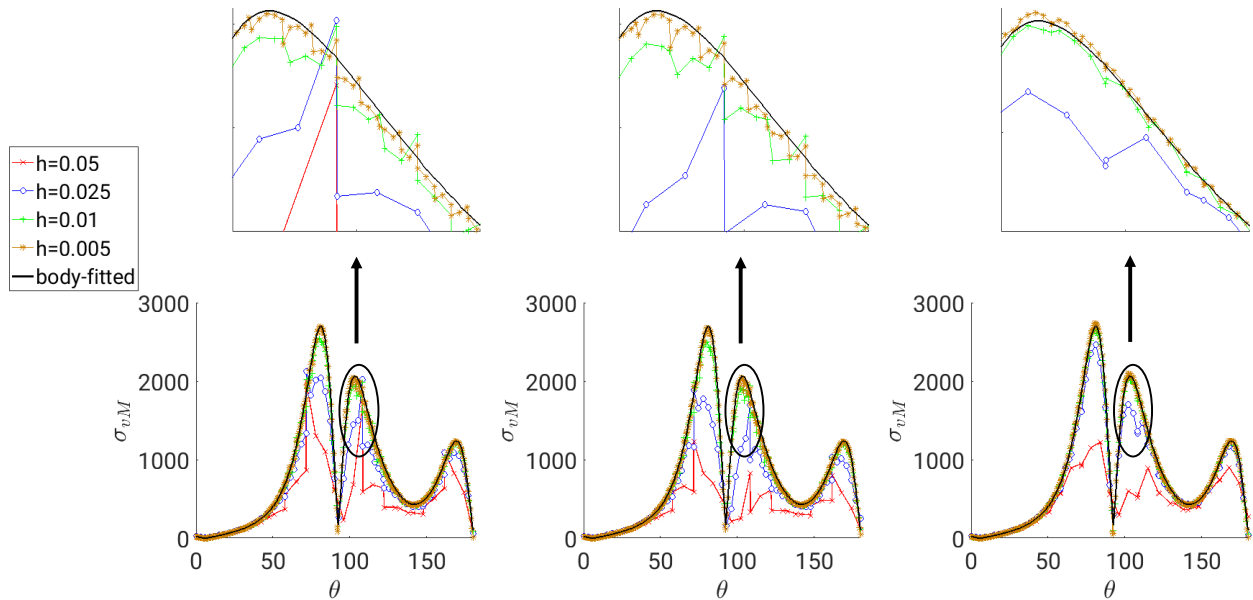


Figure 2.3: Stress (N/m^2) profile along the material interface: Area weighted smoothing (left), Area weighted smoothing with $\gamma_u = 0.1$ (middle), XFEM informed smoothing with $\gamma_u = 0, \gamma_\tau = 0$ (right).

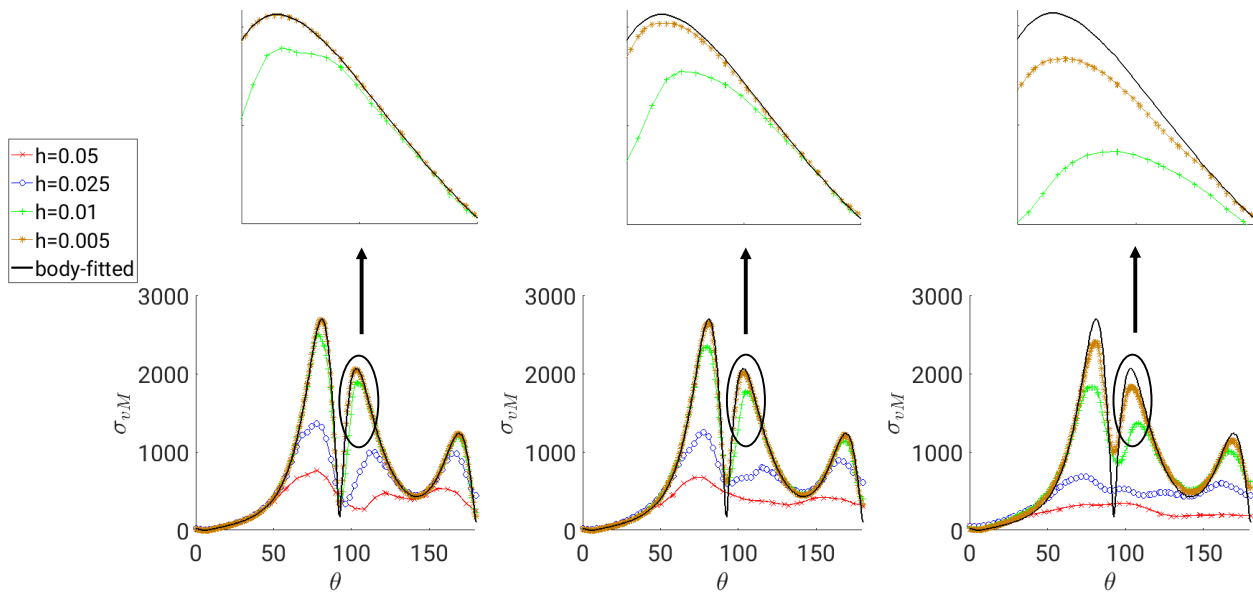


Figure 2.4: Stress (N/m^2) profile along the material interface: XFEM informed smoothing with $\gamma_u = 0.1, \gamma_\tau = 10^{-4}$ (left), $\gamma_u = 0.1, \gamma_\tau = 10^{-3}$ (middle), and $\gamma_u = 1.0, \gamma_\tau = 10^{-2}$ (right).

plot obtained using a body-fitted mesh of size $h = 0.005m$. The body-fitted solution was converged for this mesh size. Area weighted smoothing with and without ghost penalty, as well as XFEM informed smoothing without ghost penalty, i.e. $\gamma_u = 0$ and $\gamma_\tau = 0$, result in oscillatory stresses. Upon mesh refinement, these stresses do not converge to the body-fitted solution as shown in Figure 2.3. In contrast stresses obtained using XFEM informed smoothing of stress with ghost penalty (Figure 2.4) have a smoother profile along the interface and converge with refinement in mesh. However, one should be careful with their choice of gradient stabilization parameters. As expected and as shown in Figure 2.4 a large value of the ghost penalty parameter smooths out the stresses extensively resulting in loss of stress profile capturing ability. Based on results presented in Figures 2.3 and 2.4, for all stress-based optimization studies performed in this thesis we chose $\gamma_u = 0.1$ and $\gamma_\tau = 10^{-4}$. Figure 2.5 further presents a comparison of stress field distribution for the intersection configuration in Figure 2.2, between area weighted stresses and XFEM informed smoothed stresses with $\gamma_u = 0.1, \gamma_\tau = 10^{-4}$.

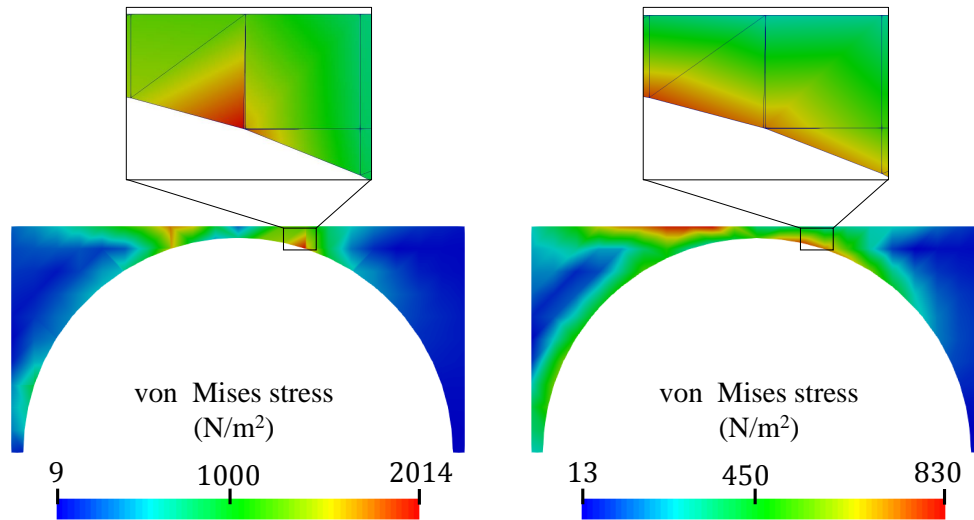


Figure 2.5: Stress field distribution using: Area weighted smoothing (left) and XFEM informed smoothing with $\gamma_u = 0.1, \gamma_\tau = 10^{-4}$ (right).

The effect of XFEM informed smoothing of stress on the sensitivity of stresses is

discussed in Section 3.3. A detailed analysis of the stresses for the current problem setup is performed in Section 5.1 of Appendix C wherein the robustness of the proposed approach for computing stresses using immersed boundary methods with low order finite elements is established.

2.1.4 Galerkin Gradient Least Squares Stabilization

High gradients within the same material phase may cause oscillations in the scalar stress field. An example of such a scenario is the two-phase problem setup presented in Section 5.4 of Appendix C. Therein to simulate a void the Young's modulus of the material is set to a very low value in the desired region. This change in Young's modulus is not gradual and happens over the span of a single element.

Employment of the Galerkin least squares (GLS) method does not resolve the above issue since the least-squares form of (2.3) only contributes to L_2 -stability which is already present in the Galerkin method. The Galerkin Gradient Least Squares Stabilization presented in [37] adds stability in the H_1 -seminorm thus providing control over the gradient of the scalar stress field within the same material phase. Applying the GGLS requires adding the following term to the left hand side of (2.3).

$$\mathcal{R}_{GGLS}^E = \mathcal{R}_{GGLS}^H = \sum_{m=1,2} \int_{\Omega^m} \nabla \eta^m \gamma_{GGLS} \cdot \nabla (\tau^m - \mathcal{S}(\mathbf{u}^m)) d\mathbf{x}; \quad \gamma_{GGLS} = \frac{h^2}{6}, \quad (2.4)$$

where h is the background mesh size. Figure 2.6 presents a scenario wherein oscillations occur in the scalar stress field resulting in -ve von Mises stresses away from the material interface. The scenarios correspond to the stress distribution in Fig. 27b of Appendix C. Applying the GGLS stabilization helped diminish these oscillations in the stress field. Note, results presented in Appendix C are not influenced by stress field oscillations because they occur in the dummy void region of the problem domain which is not a part of the optimization process. Hence GGLS was not used for any of the results presented in Appendix C.

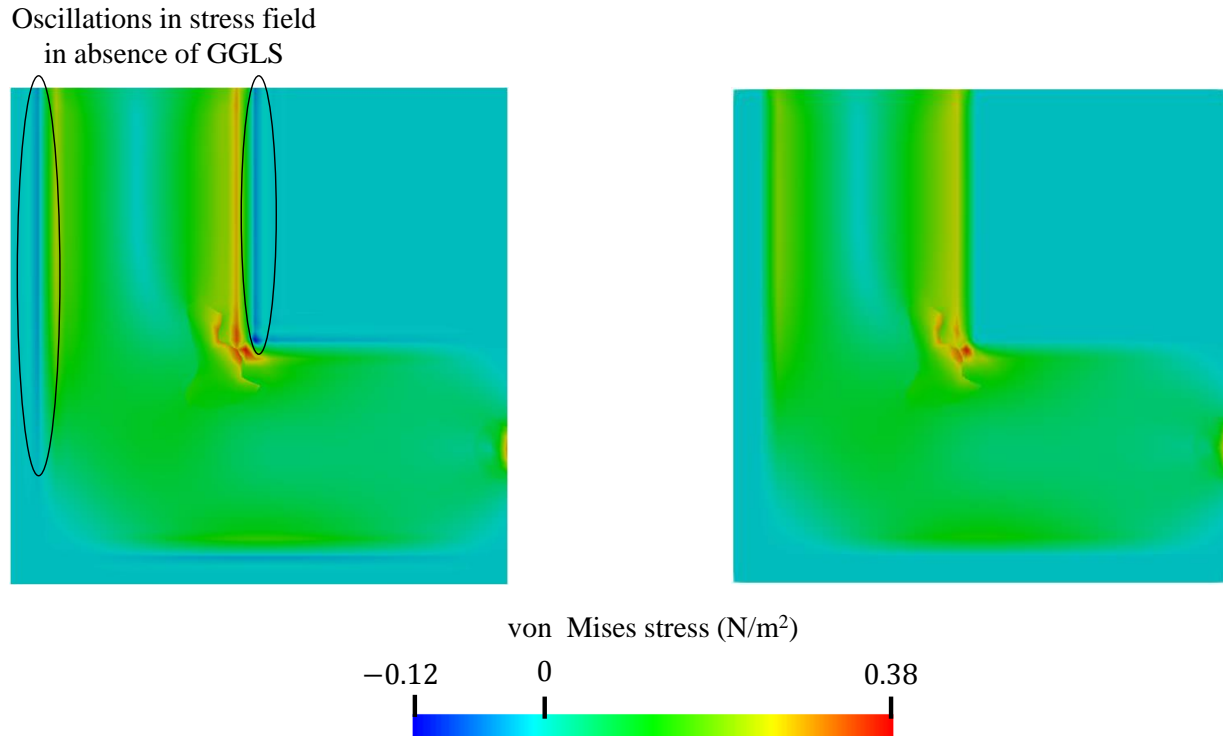


Figure 2.6: Stress field distribution in absence (left) and in presence (right) of GGLS.

2.1.5 Outlook and future work

The issue of overestimation of stresses resulting from small intersection areas following vanishing zone of influence of degrees of freedom is addressed. The ghost penalty method prevents the influence of degrees of freedom from vanishing and provides stability to the system of equations. However as shown through a numerical study, ghost penalty alone was not sufficient in obtaining convergence of stresses along the material interface with refinement in mesh. An XFEM informed smoothing in combination with ghost penalty provides a second level of spatial gradient stabilization which was shown to be effective in eliminating stress peaks and attain convergence with mesh refinement.

The proposed method for computation of stresses is an improvement over existing methods. In its current framework stresses are non-differentiable as the material interface transitions an element (see Section 5.1.3 of Appendix C). Future studies should focus on

resolving this issue.

2.2 Modeling uncertainty in material geometry

Concerning XFEM-based design, this work pertains to the concept of the extended stochastic finite element method (X-SFEM) which extends the XFEM to the stochastic domain using a polynomial chaos expansion (PCE) to approximate the degrees of freedom based on the random parameters characterizing the geometry. Section 1.2 provides an overview of research aimed towards modeling uncertainty in material geometry. As mentioned in Section 1.2 the work presented in this section constitutes only a part of the research on XFEM-based design of geometric uncertainty presented in [69]. The specific contribution of this thesis pertains to the development of "active stochastic subdomains" discussed in Section 2.2.1. Following the development of active stochastic subdomains we investigate the application of X-SFEM for problems with either a weakly or strongly discontinuous solution at the random material interface using the Heaviside enrichment function.

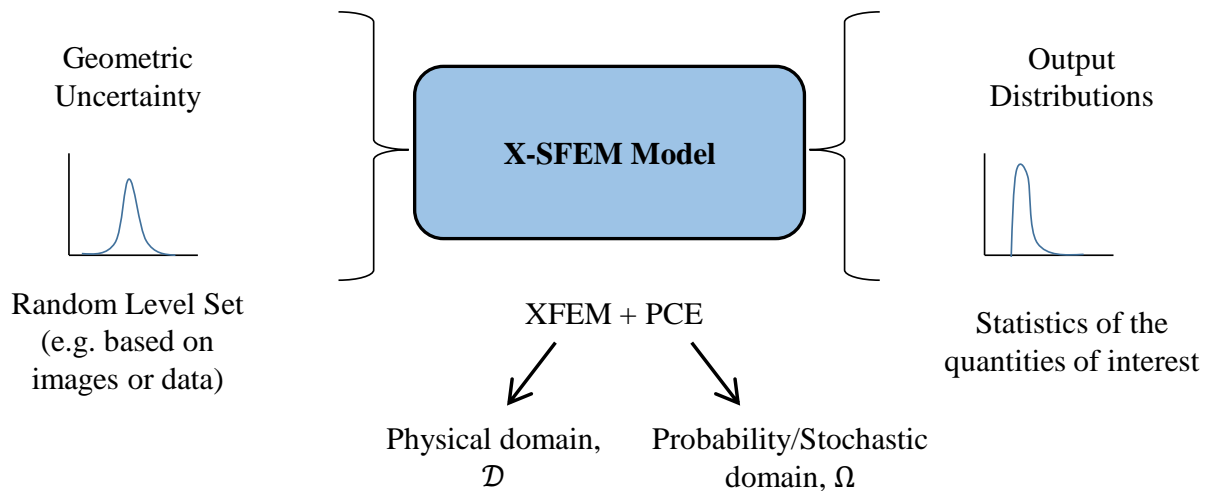


Figure 2.7: X-SFEM model.

The proposed X-SFEM approach is illustrated with a stochastic version (Figure 2.8) of the model problem depicted in Figure 1.9. The model problem contains an inclusion with uncertain geometry embedded in a matrix. The governing equations are solved over the

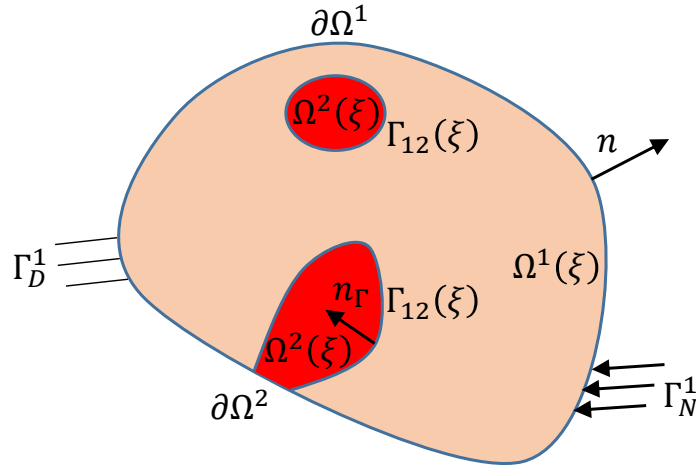


Figure 2.8: Schematic of the stochastic model problem.

spatial domain Ω as discussed in Section 1.5. The probability space is denoted by (Σ, \mathcal{B}, P) . Here, Σ is the set of elementary events, \mathcal{B} is the σ -algebra of events, and P is the probability measure. This work considers random variables with uniform distributions. The random inclusion geometry is characterized by a finite set of random parameters, $\xi : \Sigma \rightarrow \mathcal{X} \subseteq \mathbb{R}^d$. The random interface location, $\Gamma_{12}(\xi)$, is defined by the zero contour of a stochastic version of the LSF (1.1) denoted by $\phi(\mathbf{x}, \xi) : \Omega \times \mathcal{X} \rightarrow \mathbb{R}$. The random LSF like its deterministic counterpart is mapped onto the XFEM mesh by evaluating the parametrized level set function at the nodes.

The approximation of the solution field in the presence of uncertain material geometry, using the XFEM (1.4) is defined as,

$$\hat{\mathbf{u}}(\mathbf{x}, \xi) = \begin{cases} \sum_{e=1}^{\Psi} \left(\sum_{i \in I} \mathcal{N}_i(\mathbf{x}) \mathbf{u}_{i,e}^1(\xi) \delta_{el}^{1,i} I_{i,e}^1(\xi) \right) & \text{if } \mathbf{x} \in \Omega^1(\xi) \\ \sum_{e=1}^{\Psi} \left(\sum_{i \in I} \mathcal{N}_i(\mathbf{x}) \mathbf{u}_{i,e}^2(\xi) \delta_{el}^{2,i} I_{i,e}^2(\xi) \right) & \text{if } \mathbf{x} \in \Omega^2(\xi), \end{cases} \quad (2.5)$$

where the indicator function I restricts the approximation of the degrees of freedom $\mathbf{u}_{i,e}^m(\xi)$ to the active stochastic subdomain $\hat{\mathcal{X}}_{i,e}^m$, construction of which is discussed in Section 2.2.1. The active enrichment level is denoted by l in $\delta_{el}^{m,i}$ and depends on ξ . The indicator function

is defined as

$$I_{i,e}^m(\boldsymbol{\xi}) = \begin{cases} 1 & \text{if } \boldsymbol{\xi} \in \hat{\mathcal{X}}_{i,e}^m \\ 0 & \text{otherwise} \end{cases}. \quad (2.6)$$

The degrees of freedom, $\mathbf{u}_{i,e}^m(\boldsymbol{\xi})$, are approximated in the stochastic space using a PCE of order p . The stochastic approximation for a degree of freedom is defined by

$$\mathbf{u}_{i,e}^m(\boldsymbol{\xi}) = \sum_{j=1}^{M_{PC}} L_{i,e,j}^m(\boldsymbol{\xi}) a_{i,e,j}^m, \quad (2.7)$$

where $a_{i,e,j}^m$ are the stochastic coefficients to be determined and $L_{i,e,j}^m$ are Legendre polynomials defined on $\hat{\mathcal{X}}_{i,e}^m$. While random variables with uniform distributions are considered in this work, local orthogonal polynomial bases for other distributions may be constructed numerically. The proposed approach to construct $L_{i,e,j}^m$ follows the multi-element generalized PCE [130] wherein a single element in \mathcal{X} is defined by $\hat{\mathcal{X}}_{i,e}^m$. The stochastic approximation is restricted to a single element to minimize the number of expansion coefficients to be determined by the system of equations. Section 4.2 of Appendix A provides further details for the construction of the Legendre polynomials in the current work.

2.2.1 Active stochastic subdomain

The active stochastic subdomain for each degree of freedom, denoted as $\mathcal{X}_{i,e}^m \subseteq \mathcal{X}$, defines the stochastic subdomain where the degrees of freedom $\mathbf{u}_{i,e}^m$ are nonzero. The active stochastic subdomain for each degree of freedom is constructed based on $\phi_j(\boldsymbol{\xi}) = 0$ computed for all nodes of every element sharing node i . Each degree of freedom at node i is active for one or more regions created by $\phi_j(\boldsymbol{\xi}) = 0$. Typically each degree of freedom is active over a single connected subdomain. However a degree of freedom may be active over disconnected regions depending on the discretization. In this case additional enrichment levels are added such that each degree of freedom is active over a single connected subdomain. The variation of the degrees of freedom is smooth over the active stochastic subdomain.

A minimum bounding hyperrectangle approximates the active stochastic subdomain,

such that $\hat{\mathcal{X}}_{i,e}^m = [a_j, b_j] \subseteq [-1, 1]^d$ where $j = 1, \dots, d$. For $d = 1$, $\hat{\mathcal{X}}_{i,e}^m = \mathcal{X}_{i,e}^m$. The basis polynomials in the stochastic approximation are transformed and normalized onto this hyperrectangle. Figure 2.9 is used to illustrate the concept of active stochastic subdomains for $d = 1$. The bar has length $L = 1$ and is modeled using 5 elements. The interface position r depends on one random parameter such that $r = 0.2\xi + 0.5$. The random LSF is given as $\phi(\xi) = x - r(\xi)$. The active stochastic subdomain for $u_{3,1}^2$ is then defined by the interval $[-1, 0.5]$. Here the intersection point $\xi = 0.5$ is computed from $\phi_4(\xi) = 0$.

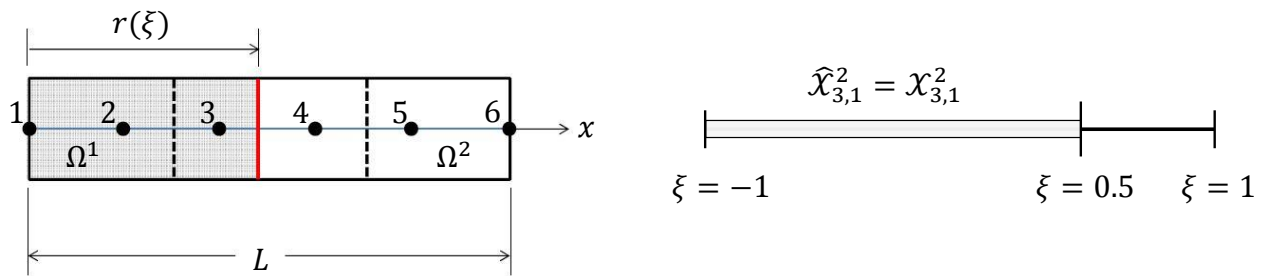


Figure 2.9: 1D spatial intersection configuration example (left) and corresponding active stochastic subdomain for $u_{3,1}^2$ (right) .

For $d > 1$, if the minimum bounding hyperrectangle and the active stochastic subdomain do not have similar volumes an ill-conditioned system may result. For instance if the active stochastic subdomain for $d = 2$ is a sliver as depicted in Figure 2.10, the area of the minimum bounding hyperrectangle does not closely match the area of the active stochastic subdomain. A rotated coordinate system is then required for the bounding rectangle to closely approximate the active stochastic subdomain as shown in Figure 2.10. Upon rotation the minimum bounding rectangle matches the active stochastic subdomain using the rotated coordinate system. The transformed basis, $L_{i,e,j}^m$, is then computed using the rotated coordinate system. The rotated coordinate system is applied for the numerical examples in this work when the ratio of the minimum bounding rectangle area to the active area is greater than 2. The influence of such a rotation of the stochastic subdomain on the Legendre polynomial bases is discussed in detail in Section 4.2 of Appendix A.

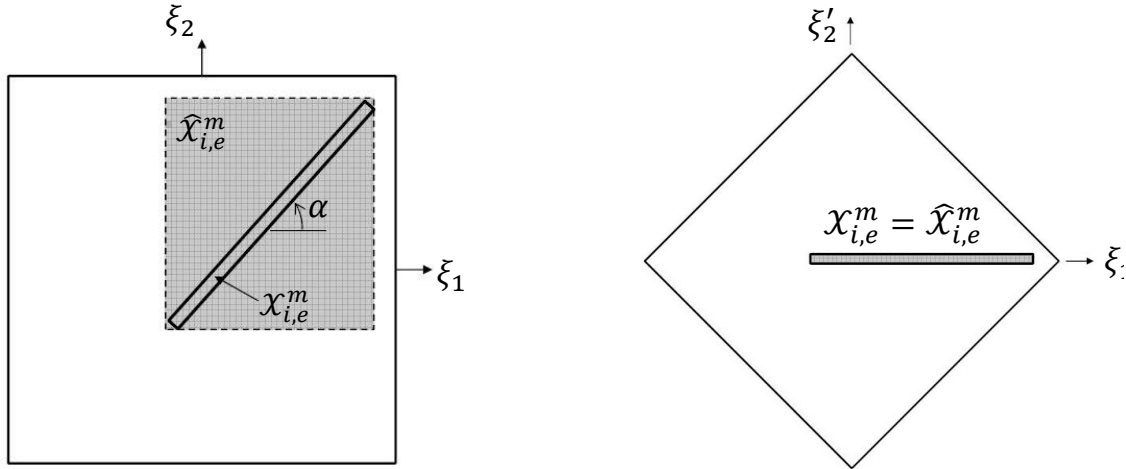


Figure 2.10: Example of a sliver configuration of an active stochastic subdomain in 2D (left), and minimum bounding rectangle defined using a rotated coordinate system (right).

2.2.2 Application to linear elastic bimaterial plate

The effectiveness of the proposed approach is demonstrated using the linear elastic bimaterial plate problem shown in Figure 2.11. A circular plate of radius $b = 2m$ has a centered circular inclusion of radius r . The geometry of the inclusion is random with the radius defined as $r = 1.26 + 0.54\xi$. The elastic modulus and Poisson's ratio of the plate are $E_1 = 10N/m^2$ and $\nu_1 = 0.3$. The elastic modulus and Poisson's ratio of the inclusion are given by $E_2 = 1N/m^2$, $\nu_2 = 0.25$. This problem is studied using the proposed Heaviside enrichment in X-SFEM as well as the C^0 -continuous enrichment proposed in [94]. This work does not use the ghost penalty approach discussed in 2.1.1, and thus to mitigate issues with ill-conditioning caused by an extremely small (or large) ratio of intersected areas in an intersected element, we use the geometric preconditioning scheme introduced in [68].

The degrees of freedom for the x-displacement at $\mathbf{x} = (0.9, 0)$ is shown in Figures 2.12 and 2.13 using the C^0 -continuous [94] and Heaviside enrichment functions, respectively. The variation of the degrees of freedom using the C^0 -continuous enrichment is not smooth with respect to ξ . The peaks correspond to the intersection of the interface with a node. Therefore more peaks occur as the spatial mesh is refined. Using the Heaviside enrichment

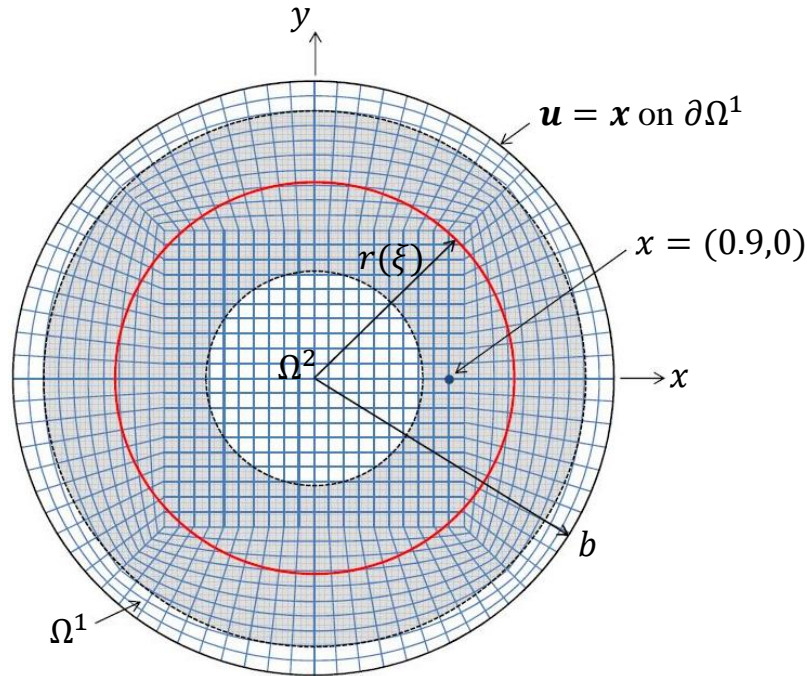


Figure 2.11: Problem setup for a bimaterial plate with mesh size $h = 0.1m$.

the behavior of the degrees of freedom is piecewise smooth in the stochastic domain for any spatial mesh size, as depicted in Figure 2.13 for different spatial mesh sizes. The value of ξ at which the degree of freedom becomes active changes with mesh size.

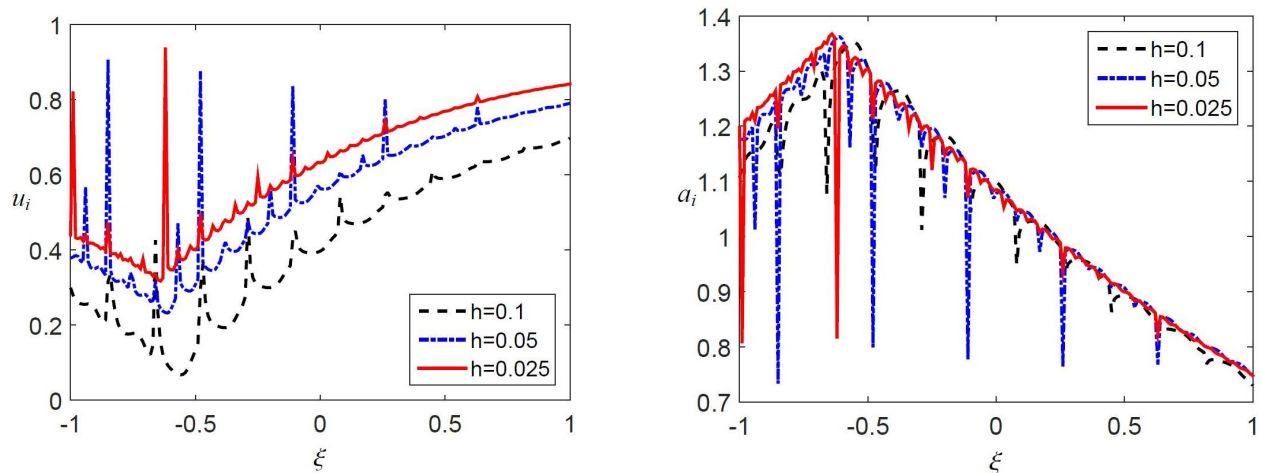


Figure 2.12: Regular (left) and enriched (right) degree of freedom using the C^0 enrichment function [94] for the x-displacement at $\mathbf{x} = (0.9, 0)$ as a function of ξ with spatial mesh refinement.

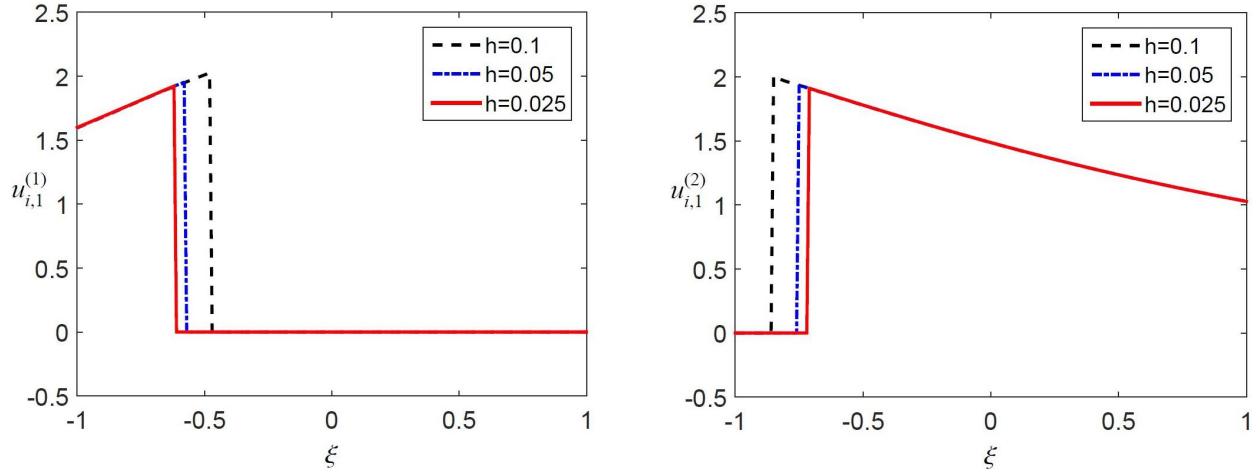


Figure 2.13: Level 1 degrees of freedom for phase 1 (left) and phase 2 (right) using the generalized Heaviside enrichment strategy for the x-displacement at $\mathbf{x} = (0.9, 0)$ as a function of ξ with spatial mesh refinement.

An analytical solution to the current problem exists [121] and is used to compute the relative error in the X-SFEM solution. A comparison of the solution error using the C^0 -continuous and Heaviside enrichment functions is shown in Figure 2.14. A higher convergence rate is achieved using the Heaviside enrichment. This higher convergence rate can be attributed to the smoother degrees of freedom obtained using the Heaviside enrichment as discussed above.

Section 5 of Appendix A presents three more numerical examples to study the convergence and accuracy of the proposed Heaviside enriched X-SFEM. Examples with one and two random parameters are studied in detail. Problems with continuous as well as discontinuous solution across the material interface are studied

2.2.3 Outlook and future work

The convergence and accuracy of the proposed method was demonstrated for example problems with continuous and discontinuous solutions at the interface. The degrees of freedom are smooth with respect to the random parameters regardless of the spatial mesh size.

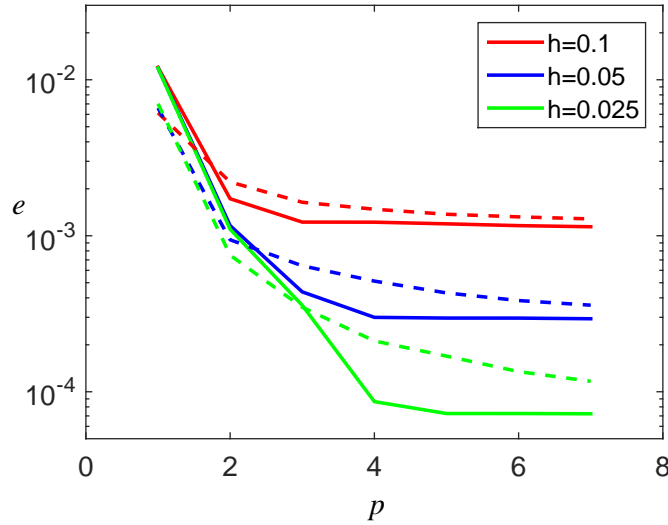


Figure 2.14: Error convergence using the X-SFEM with respect to p . Solid and dashed lines represent the Heaviside and C^0 -continuous enrichment functions, respectively.

Due to the smoothness of the degrees of freedom convergence in the stochastic space occurs with low orders of the polynomial approximation.

Although good precision approximate solutions have been obtained using the proposed X-SFEM framework, at the stochastic level integration becomes more and more expensive as the dimension (number of random parameters) in the stochastic domain increases. With an increase in the stochastic dimensionality stochastic partitions get more and more complex with presence of regions in the stochastic domain with small areas and the non-triviality involved in monitoring stochastic partitions for such regions. This constitutes the main disadvantage associated with the current intrusive framework requiring integration in the stochastic domain. Hence future work should focus on non-intrusive approaches such as construction of response surfaces for predicting the response of physical systems with uncertain material geometry.

Note, ever since the publication of the above work [71] there has been limited work surrounding the concept of modeling uncertainty using the XFEM with particular applica-

tions to magneto-active heterogeneous materials with random microstructure [105], and to fracture analysis of laminated composite plate with a central crack [66].

Chapter 3

Behavior of Shape Sensitivities

Based on (1.22), shape sensitivities depend on: i) variation of the response function, \mathcal{Z} , with respect to the design variables and ii) the variation of the residual of the system of equations, \mathcal{R} , with respect to the design variables. The dependency of \mathcal{R} on a single design variable s can be decomposed into explicit and implicit parts such that,

$$\frac{\partial \mathcal{R}}{\partial s} = \frac{\partial \mathcal{R}}{\partial s} + \frac{\partial \mathcal{R}}{\partial \mathbf{x}_\Gamma} \frac{\partial \mathbf{x}_\Gamma}{\partial s}. \quad (3.1)$$

The above can be decomposed on an elemental level to obtain the discretized residual derivatives such that

$$\frac{\partial \hat{\mathcal{R}}}{\partial s} = \sum_{e \in N_e} \frac{\partial \hat{\mathcal{R}}_e}{\partial s} + \sum_{e \in N_e} \sum_{k=1}^{N_\Gamma} \frac{\partial \hat{\mathcal{R}}_e}{\partial \mathbf{x}_\Gamma^k} \mathbf{V}^k; \quad \mathbf{V}^k = \frac{\partial \mathbf{x}_\Gamma^k}{\partial s}, \quad (3.2)$$

where N_e is the set of all elements that constitute the finite element mesh, and N_Γ is the number of interfaces present within the element e . The boundary velocity \mathbf{V} may or may not be of constant magnitude along the material interface. Note that $\partial \hat{\mathcal{R}}_e / \partial \mathbf{x}_\Gamma^k$ vanishes for elements not intersected by the material interface. Furthermore, unless the governing equations depend explicitly on the design variables the first term in 3.2 vanishes. As a result often only the second term needs to be computed. This however is not the case if using a C^0 -continuous enrichment wherein the enrichment function itself depends explicitly on the design variables [92]. While it is straightforward to determine the explicit dependency of the response function on the design variable, it is less obvious how the residual behaves with respect to the design variable within the context of the Heaviside-enriched XFEM.

The generalized Heaviside enrichment strategy used in this thesis allows for each disconnected region of the same phase to be approximated by an independent set of nodal degrees of freedom. If the support of a nodal basis function is intersected by the interface as in Figure 1.6, by construction the solution is discontinuous across the interface. The presence of such a discontinuity presents the primary motivation to investigate the behavior of shape sensitivities within the context of Heaviside-enriched XFEM. To better demonstrate the discontinuity across the material interface we plot the degrees of freedom and $\partial\mathcal{R}/\partial s$ as a function of s , in Figures 3.1 and 3.2 respectively, corresponding to a node belonging to one of the intersected elements from Section 3.1.

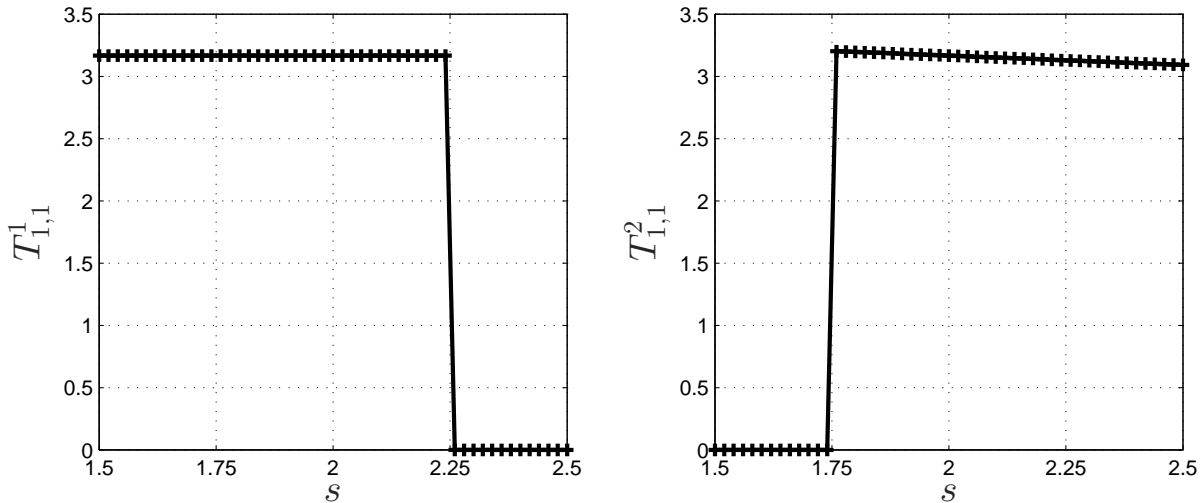


Figure 3.1: Degrees of freedom for node located at $\mathbf{x} = (16.75, 3)$, in Figure 3.4

Section 4 of Appendix B presents detailed derivations of $\partial\mathcal{R}/\partial s$ using both continuum (differentiate, then discretize) and discrete (discretize, then differentiate) approaches. The choice of approach for computing $\partial\mathcal{R}/\partial s$ depends largely on the system of equations that needs to be solved as well as the generality and ease of implementation. Both the discretized and continuum approach present limitations in their application to a generic framework irrespective of the physics involved as also discussed in Section 4 of Appendix B. As the preferred option in the current study we adopt a semi-analytical approach wherein great

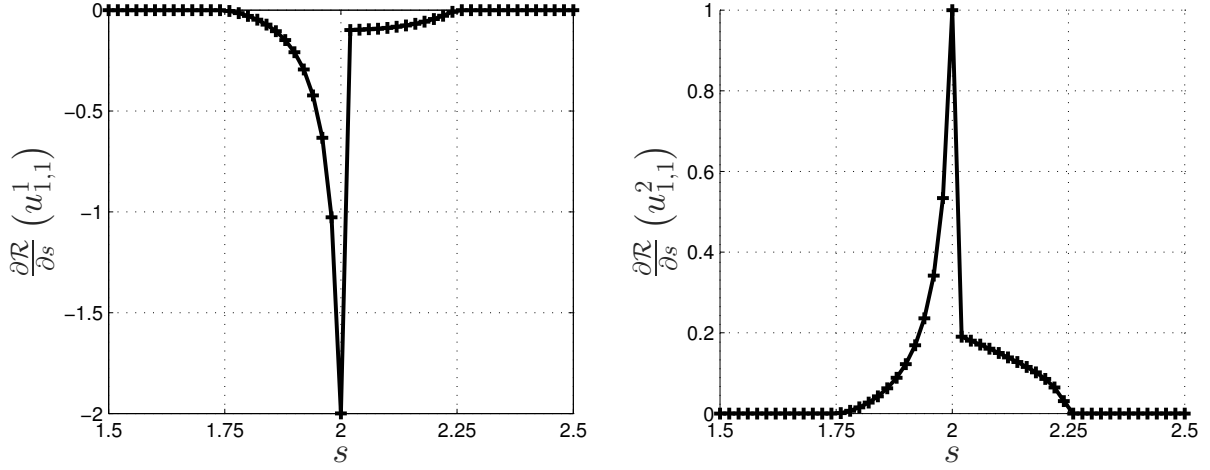


Figure 3.2: $\partial R/\partial s$ for degrees of freedom plotted in Figure 3.1

ease of implementation is achieved by finite differencing the term $\partial \hat{\mathcal{R}}_e / \partial \mathbf{x}_\Gamma^k$ in (3.2) using a design perturbation size Δ_{FD} :

$$\frac{\partial \hat{\mathcal{R}}}{\partial s} = \sum_{e \in N_e} \sum_{k=1}^{N_\Gamma} \sum_{i=1}^{N_{\mathbf{x}_\Gamma}} \left(\frac{\hat{\mathcal{R}}_e \Big|_{\mathbf{x}_{\Gamma_i}^k + \Delta_{FD}} - \hat{\mathcal{R}}_e \Big|_{\mathbf{x}_{\Gamma_i}^k - \Delta_{FD}}}{2\Delta_{FD}} \right) \mathbf{V}_{\mathbf{x}_{\Gamma_i}}. \quad (3.3)$$

where $N_{\mathbf{x}_\Gamma}$ is the number of intersection points.

Alternatively, a hybrid scheme may be adopted wherein a continuum approach (derived in Section 4 of Appendix B) may be used for volumetric terms while the material boundary terms are subjected to finite differencing to give,

$$\begin{aligned} \frac{\partial \mathcal{R}}{\partial s} &= \int_{\Omega^m} \frac{\partial \mathcal{F}}{\partial s} d\mathbf{x} + \int_{\partial\Omega^m} \mathcal{F} \mathbf{V} \cdot \tilde{\mathbf{n}} d\mathbf{x}' \\ &+ \sum_{e \in N_e} \sum_{k=1}^{N_\Gamma} \sum_{i=1}^{N_{\mathbf{x}_\Gamma}} \left(\frac{\hat{\mathcal{R}}_{e_\Gamma} \Big|_{\mathbf{x}_{\Gamma_i}^k + \Delta_{FD}} - \hat{\mathcal{R}}_{e_\Gamma} \Big|_{\mathbf{x}_{\Gamma_i}^k - \Delta_{FD}}}{2\Delta_{FD}} \right) \mathbf{V}_{\mathbf{x}_{\Gamma_i}}. \end{aligned} \quad (3.4)$$

Here \mathcal{F} can take the form of any of the integrands in (1.7), (1.9) or (1.16), defined in Ω^m . The finite differencing in (3.3) and (3.4) is carried out by perturbing the individual edge intersection points, \mathbf{x}_{Γ_i} , belonging to every intersected finite element as shown in Figure 3.3.

Such a perturbation helps account for the arc length change capturing the curvature of the interface too. In contrast a global finite differencing is performed by perturbing the entire interface geometry via the design variable such that

$$\frac{\partial \mathcal{Z}}{\partial s} = \frac{\int_{\Omega^m} \mathcal{G}|_{s+\Delta_{FD}} - \int_{\Omega^m} \mathcal{G}|_{s-\Delta_{FD}}}{2\Delta_{FD}} d\mathbf{x} + \frac{\int_{\partial\Omega^m} \mathcal{G}'|_{s+\Delta_{FD}} - \int_{\partial\Omega^m} \mathcal{G}'|_{s-\Delta_{FD}}}{2\Delta_{FD}} d\mathbf{x}'. \quad (3.5)$$

The continuous function, \mathcal{G} , is defined over the material subdomain Ω^m (e.g. strain energy). The continuous function, \mathcal{G}' exists only on the material boundaries (e.g. interface stress measure).

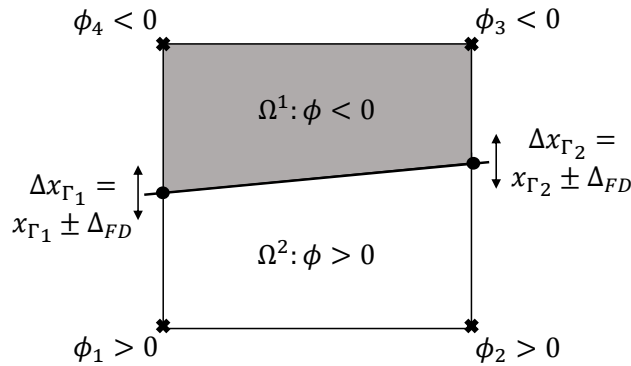


Figure 3.3: Perturbing intersection points for finite differencing in (3.3).

3.1 Verification of shape sensitivities

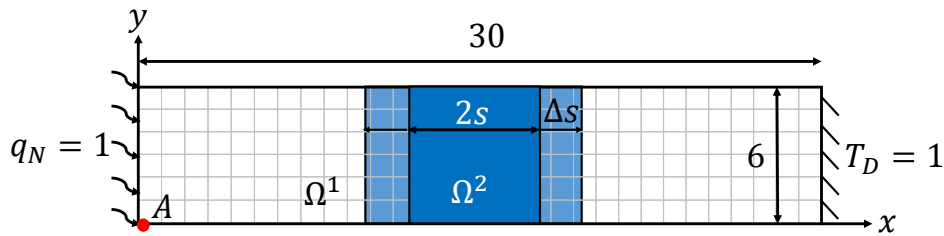


Figure 3.4: Heat diffusion problem setup with strip inclusion. All dimensions in m

We consider a two-phase steady state diffusion problem shown in Figure 3.4. A vertical strip inclusion of conductivity $k_2 = 10W/(mK)$ is embedded into a rectangular matrix of conductivity $k_1 = 1W/(mK)$. The center location of the strip is maintained constant at

$\mathbf{x} = (15, 6)$. A Neumann boundary condition of $q_N = 1Wm^{-2}$ is applied along the left edge. A Dirichlet boundary condition of $T_D = 1K$ is applied to the right edge. The top and bottom edges are adiabatic. The problem domain is discretized using a mesh size of $h = 1.0m$. The design variable, s , is half the width of the strip inclusion, measured parallel to the horizontal axis. Shape sensitivities are recorded for every configuration as the design variable is varied between $s = 1.5$ and $s = 2.5$, in constant increments of $\Delta s = 0.02$. The response function, \mathcal{Z} , is the temperature measured at node A located at $\mathbf{x} = (0, 0)$. Shape sensitivities are recorded for every configuration as the design variable is varied between $s = 1.5$ and $s = 2.5$, in constant increments of $\Delta s = 0.02$. The response function, \mathcal{Z} , is the temperature measured at node A located at $\mathbf{x} = (0, 0)$. This work does not use the ghost penalty approach discussed in 2.1.1, and thus to mitigate issues with ill-conditioning caused by an extremely small (or large) ratio of intersected areas within an intersected element, we use the geometric preconditioning scheme introduced in [68].

The current problem setup is a 2D approximation of a 1D model with the analytical solution given by

$$T_A = T_D + \left(\frac{30 - 2s}{k_1} + \frac{2s}{k_2} \right) \frac{q_N}{6}, \quad (3.6)$$

$$\frac{\partial T_A}{\partial s} = -0.3.$$

The analytical solution in (3.6) shows a linear dependency of \mathcal{Z} on the width of the vertical strip inclusion. As a result the corresponding shape sensitivities are constant as computed in (3.6). A perturbation size of $\Delta_{FD} = 10^{-6}h/2$ was chosen. The shape sensitivities obtained using the different approaches discussed above are presented in Figure 3.5. The relative difference in sensitivities between the three approaches was insignificant (approximately 10^{-8}) except at $s = 2.0$ which resulted in an intersection configuration wherein the material interface coincides with finite element mesh nodes. Here the finite differenced sensitivities vanish. This behavior is a result of the material interface shift depicted in Figure 1.7 and is discussed in detail in Section 5.1.2 of Appendix B. To maintain accuracy of the shape sensitivities it is important that the finite difference perturbations in Figure 3.3 do not undergo any

interface shift within the critical shift distance. While finite differencing $\partial\hat{\mathcal{R}}_e/\partial\hat{\mathbf{x}}_\Gamma^k$, design perturbations may result in the material interface crossing over to a neighboring element. To ensure central finite differencing of $\partial\hat{\mathcal{R}}_e/\partial\hat{\mathbf{x}}_\Gamma^k$, the finite difference perturbation size is chosen to be less than the critical shift distance. Inaccurate sensitivities are obtained via global finite differencing (3.5) because finite differencing $\partial\mathcal{Z}/\partial s$ at a global level provides no control over the elemental interface shift, i.e. $\mathcal{G}'|_{s+\Delta_{FD}}$, $\mathcal{G}'|_{s-\Delta_{FD}}$, $\mathcal{G}|_{s+\Delta_{FD}}$ and $\mathcal{G}|_{s-\Delta_{FD}}$ in (3.5) are evaluated based on design configurations subjected to the material interface shift. For various values of Δ_{FD} between $10^{-3}h$ and $10^{-10}h$, the relative difference (with respect to $\Delta_{FD} = 10^{-6}h/2$) in the XFEM-based shape sensitivities was measured to be approximately 10^{-5} , thus proving the robustness of the proposed semi-analytical approach.

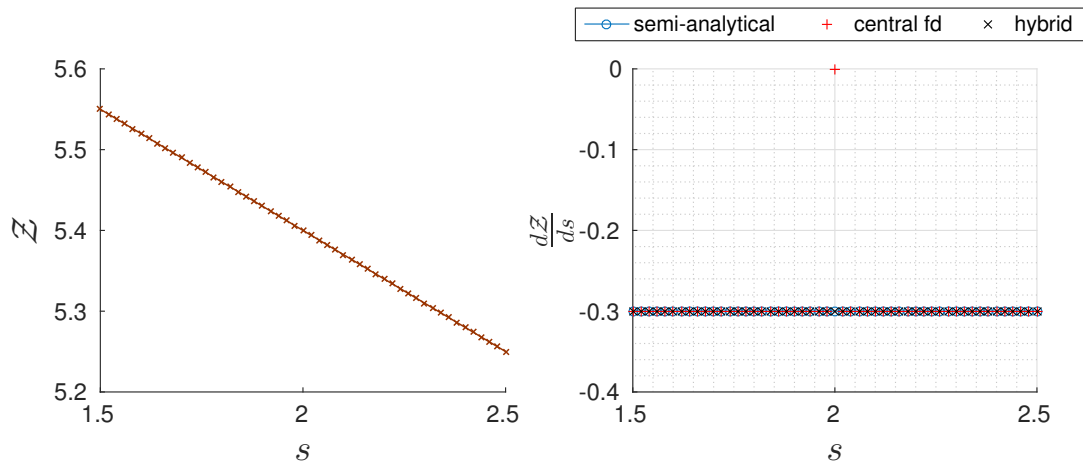


Figure 3.5: Accuracy of semi-analytical shape sensitivities: Response function (left) and corresponding shape sensitivities (right).

3.2 Effect of geometry discretization and LSF on shape sensitivities

Since we use the LSM to describe our interface geometry we note an implication of computing the design velocity, $\mathbf{V} = \partial\mathbf{x}_\Gamma/\partial s$ using the level set field. Referring to Figure

1.6, the interface position can be expressed in terms of the level set field such that

$$x_\Gamma = x_1 - \frac{x_2 - x_1}{\phi_2 - \phi_1} \phi_1. \quad (3.7)$$

The design velocity is then given by,

$$\frac{\partial \mathbf{x}_\Gamma}{\partial s} \delta s = \frac{x_2 - x_1}{(\phi_2 - \phi_1)^2} \left(\phi_1 \frac{\partial \phi_2}{\partial s} \delta s - \phi_2 \frac{\partial \phi_1}{\partial s} \delta s \right). \quad (3.8)$$

Based on (3.8) the gradient of the level set field $|\nabla \phi| \approx |(\phi_2 - \phi_1)/(x_2 - x_1)|$ may have a strong influence on the shape sensitivities.

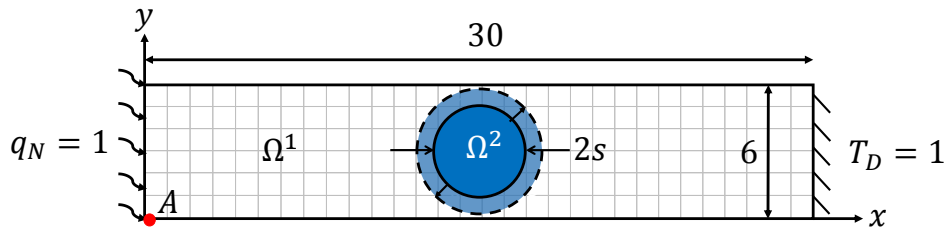


Figure 3.6: Heat diffusion problem setup with circular inclusion. All dimensions in m

Through a numerical example we investigate the dependency of the shape sensitivities on the discretization of the design geometry as well as the gradient of the LSF, $|\nabla \phi|$. We consider a two-phase steady state diffusion problem shown in Figure 3.6. A circular inclusion of conductivity $k_2 = 10W/(mK)$, is embedded into a rectangular matrix of conductivity $k_1 = 1W/(mK)$. The circular inclusion is centered at $\mathbf{x} = (15, 3)$. A Neumann boundary condition of $q_N = 1Wm^{-2}$ is applied to the left edge. A Dirichlet boundary condition of $T_D = 1K$ is applied to the right edge. The top and bottom edges are adiabatic. The design variable, s , is the radius of the circular inclusion. Shape sensitivities are recorded for every configuration as the design variable is varied between $s = 1.5$ and $s = 2.5$, in constant increments of $\Delta s = 0.02$. The response function, \mathcal{Z} , is the temperature measured at node A located at $\mathbf{x} = (0, 0)$. In this example, we also focus on the sensitivities for the perimeter (*per*) of the inclusion. The circular inclusion has a perimeter of $2\pi s$. Consequently, the analytical solution for the sensitivity of the perimeter is 2π .

We consider four LSFs, all of which represent a circular geometry but vary in the gradient of their function:

$$\begin{aligned}
 LSF_1 &\implies \phi(\mathbf{x}) = s - |\mathbf{x} - \mathbf{x}^c|, \\
 LSF_2 &\implies \phi(\mathbf{x}) = \frac{LSF_1}{10}, \\
 LSF_3 &\implies \phi(\mathbf{x}) = LSF_1 * 10, \\
 LSF_4 &\implies \phi(\mathbf{x}) = LSF_1 * (0.1 \sin^2(\omega\theta) + 10(1 - \sin^2(\omega\theta))),
 \end{aligned}
 \tag{3.9}$$

where ω is the frequency and θ is the angle measured in radians. The function LSF_1 possesses sign distance property. Figure 3.7 present the four level set fields discussed in 3.9. Although they represent the same geometry, it is evident their gradients differ significantly.

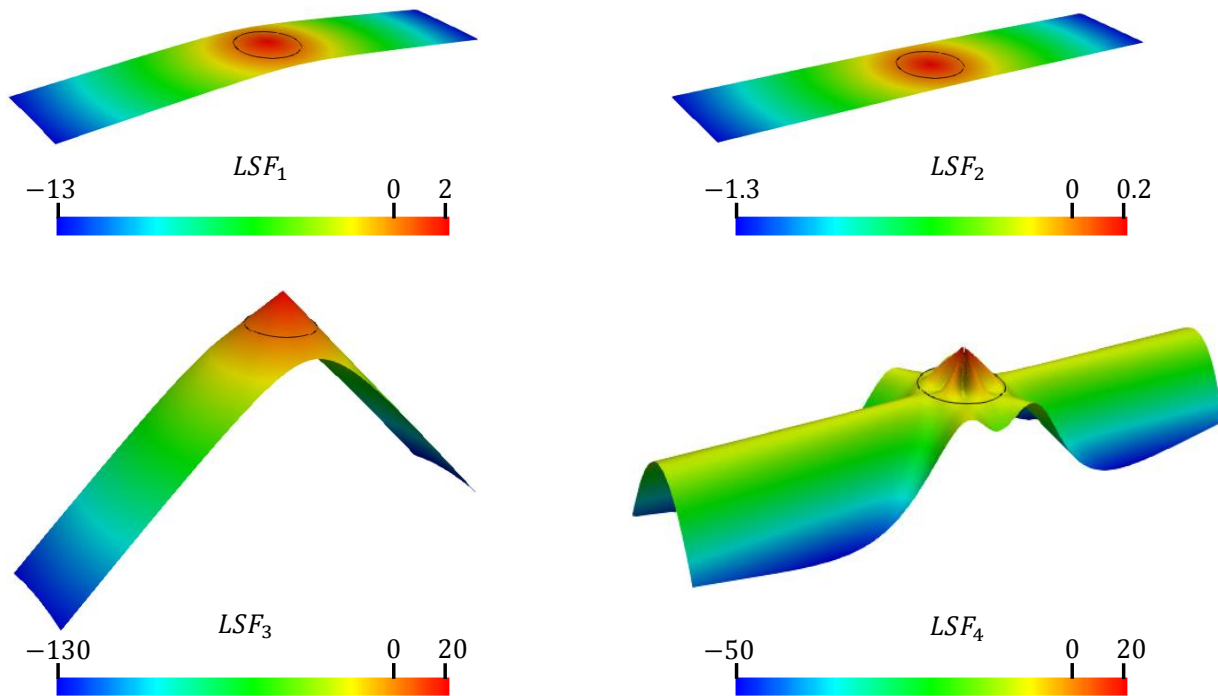


Figure 3.7: Level set functions described in (3.9) with zero level set contour.

We use the sign distance function (LSF_1) to study the influence of geometry discretization on the shape sensitivities. The response function and the corresponding shape sensitivities for a mesh sizes of $h = 0.25$ and $h = 0.05$ are plotted in Figure 3.8. A visibly

smooth response function is obtained. However, the shape sensitivities for $h = 0.25$ obtained are not smooth. Plotted alongside the sensitivities for the response function are the sensitivities for the perimeter of the circular inclusion. With mesh refinement the sensitivities for the inclusion interface perimeter approach the constant value of 2π indicating a more accurate approximation of the interface geometry. The improved approximation of the interface geometry leads to a smoother behavior of the shape sensitivities. Thus implying influence of the discretization of the design geometry on the computation of the shape sensitivities.

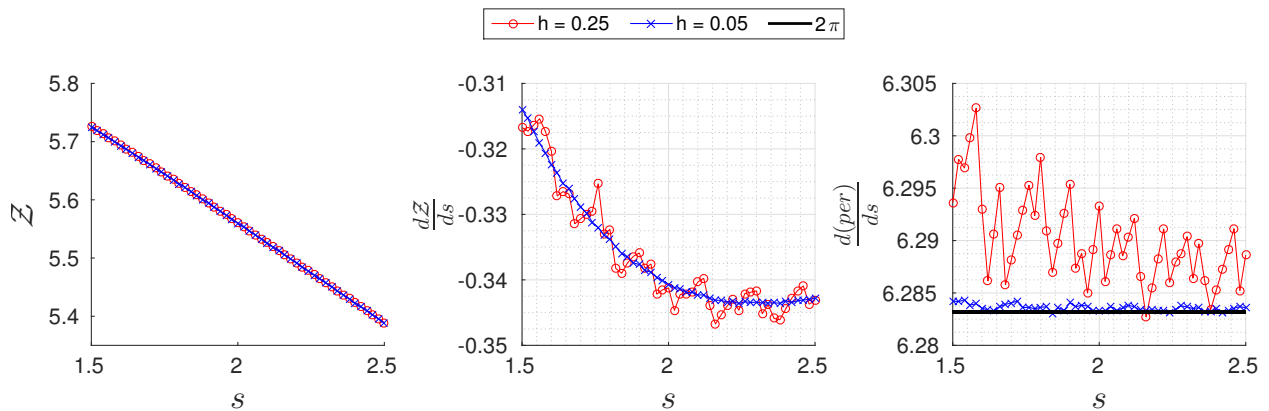


Figure 3.8: Dependence of shape sensitivities on geometry discretization: Response function (left), and sensitivities corresponding to response function (middle) and perimeter (right) using LSF_1 .

Since the smoothness of shape sensitivities depends on the discretization of the geometry, the levels of mesh refinement required to obtain smoother shape sensitivities is geometry dependent. As a result finer meshes are required to better approximate the geometries of smaller feature sizes. Alternatively the order of the geometry description can be increased. Instead of using polygons in 2D and facets in 3D to approximate the material interface within an element as done in this study, higher-order approximations could be used. It is important to note, the smoothness of the shape sensitivities is not entirely dependent on the discretization of the geometry. This is observed from the sensitivity plots in Fig. 12 of Appendix B where the design geometry consists of only straight lines. The fluctuations

observed there are attributed to the change in triangulation patterns as the interface moves through the background mesh. Recall from Figure 1.8, the integration subdomains in the current study are constructed via Delaunay triangulation.

We now study the effect of $|\nabla\phi|$ on the behavior of shape sensitivities. We use a mesh with $h = 0.05$ to eliminate errors in sensitivity resulting from geometry discretization. Figure 3.10 plots the response functions and the corresponding sensitivities for the different LSFs as a function of the design variable s . The response function for the different LSFs match closely with relative differences of less than 10^{-5} . However the sensitivities computed using LSF_4 present significant deviation from the sensitivities computed using rest of the LSFs. The objective sensitivities computed using LSF_4 although oscillatory reproduce the overall behavior produced by other LSFs. However, the perimeter sensitivity computed using LSF_4 present significant oscillations and deviate from the expected value of 2π . Considering the accurate sensitivities obtained using LSF_2 and LSF_3 it can be inferred that the uniformity (or non-uniformity) of $|\nabla\phi|$ plays a significant role in determining the accuracy (or lack of) of the sensitivities as compared to the slope alone of $|\nabla\phi|$. Regardless of oscillations in sensitivities, for all LSFs considered here the shape sensitivities were accurate in regards to the respective LSF, as determined by verification against finite differenced sensitivities.

It should be further pointed out that the shape sensitivities for LSF_2 and LSF_3 are equal to the shape sensitivities for LSF_1 owing to the chain rule in (3.8). This would not be the case if the design variables were nodal level set values. In such a scenario the shape sensitivities scale with the respective LSF although still mimicking the overall behavior of shape sensitivities corresponding to the sign distance function LSF_1 . The shape sensitivities for nodal level set values as design variables are plotted in Figure 3.9 corresponding to $s = 1.5$ in Figure 3.6. As discussed earlier, in the context of the XFEM shape sensitivities exist only for intersected element. Hence for clarity, Figure 3.6 plots only the domain in the vicinity of the circular inclusion.

In order to track the origin of oscillations in shape sensitivities for LSF_4 we further

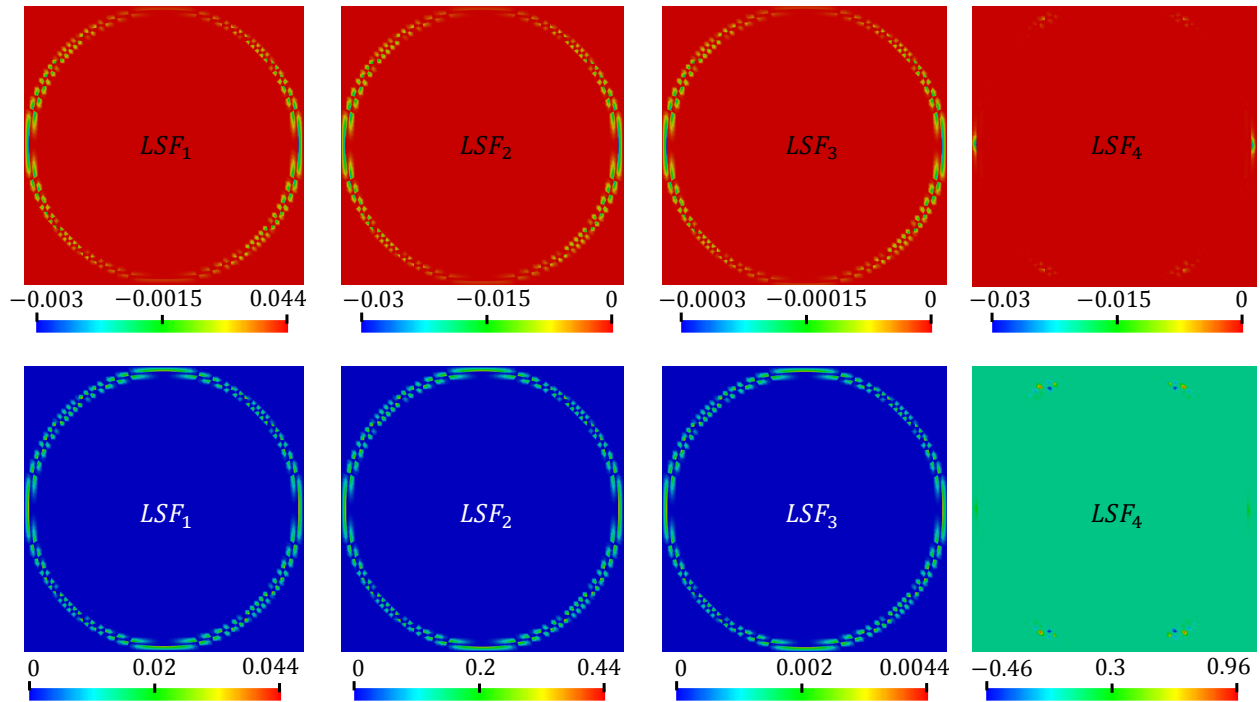


Figure 3.9: dZ/ds (top) and $d(per)/ds$ (bottom) for nodal level set design variables.

draw comparisons against two more LSFs as defined below.

$$\begin{aligned}
 LSF_5 &\implies \phi(\mathbf{x}) = LSF_1 * (0.60 \sin^2(\omega\theta) + 9.50 (1 - \sin^2(\omega\theta))) \\
 LSF_6 &\implies \phi(\mathbf{x}) = LSF_1 * (2.05 \sin^2(\omega\theta) + 8.05 (1 - \sin^2(\omega\theta)))
 \end{aligned} \tag{3.10}$$

As is evident from (3.10) LSF_4 , LSF_5 , and LSF_6 differ in their amplitudes which is directly proportional to the curvature of the LSFs in \mathbb{R}^{d+1} . Figure 3.11 presents a comparison of the shape sensitivities between LSF_1 , LSF_4 , LSF_5 , and LSF_6 . Clearly as the curvature decreases from LSF_4 to LSF_5 to LSF_6 the shape sensitivities become less oscillatory in that order. This shows a strong influence of the curvature of an LSF and shape sensitivities.

Section 5 of Appendix B uses various numerical studies to establish the accuracy and robustness of computing shape sensitivities using the proposed semi-analytical approach within the framework of Heaviside-enriched XFEM. Examples in 2D and 3D using linear and nonlinear physics are studied.

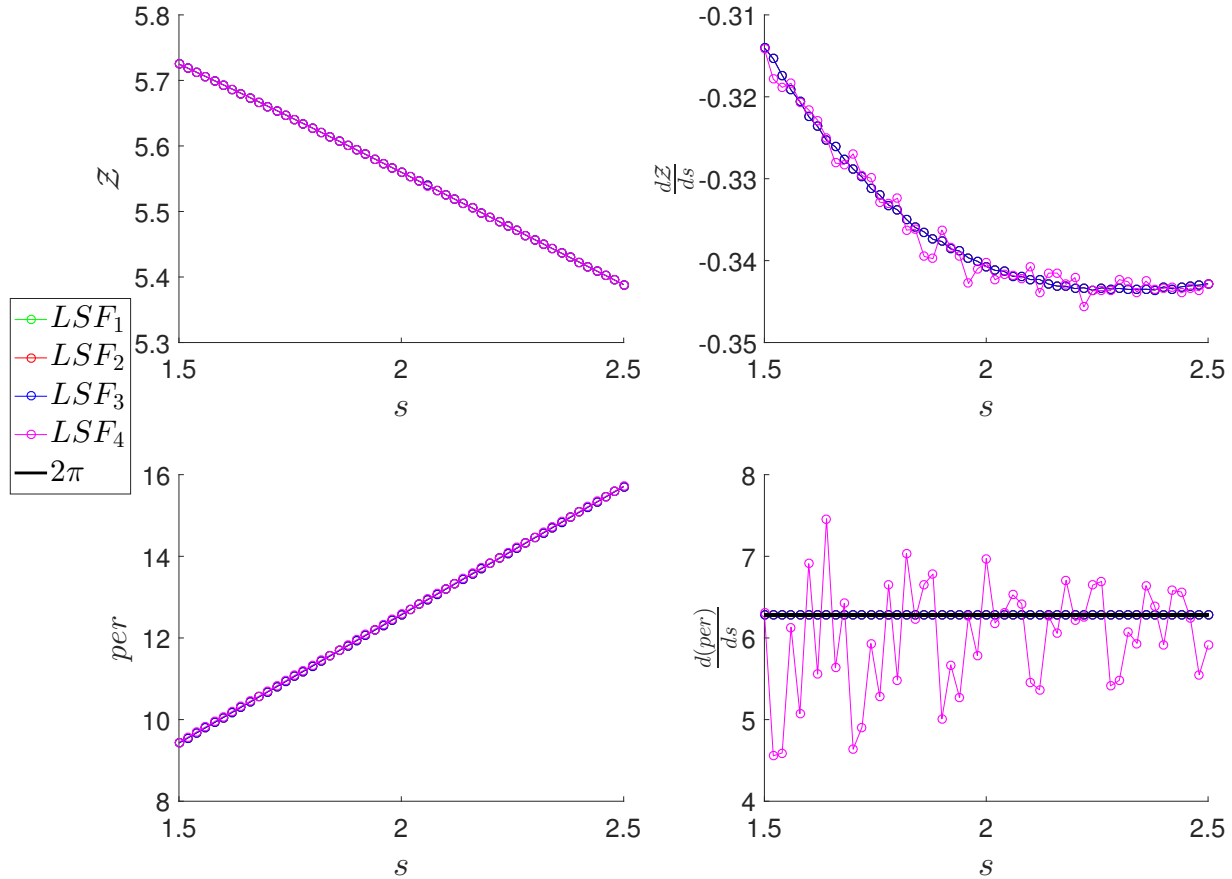


Figure 3.10: Influence of $|\nabla\phi|$ on the response function and corresponding shape sensitivities

3.3 Effect of XFEM informed smoothing of stresses on sensitivities

We further investigate the accuracy of the stress sensitivities using the XFEM informed smoothing approach presented in Section 2.1.2. The stress sensitivities are computed with respect to the inclusion radius, r , of the problem setup in Section 2.1.3. Figure 3.12 plots the stress sensitivities for different mesh sizes of $h = 0.025m$ and $h = 0.005m$. Reference sensitivities are obtained using a body-fitted mesh. Area weighted smoothing and XFEM informed smoothing without ghost penalty result in oscillatory sensitivities. Mesh refinement further aggravates the oscillations. In contrast sensitivities corresponding to XFEM informed smoothing with $\gamma_u = 0.1$ and $\gamma_\tau = 10^{-4}$ are smooth and converge with refinement in mesh.

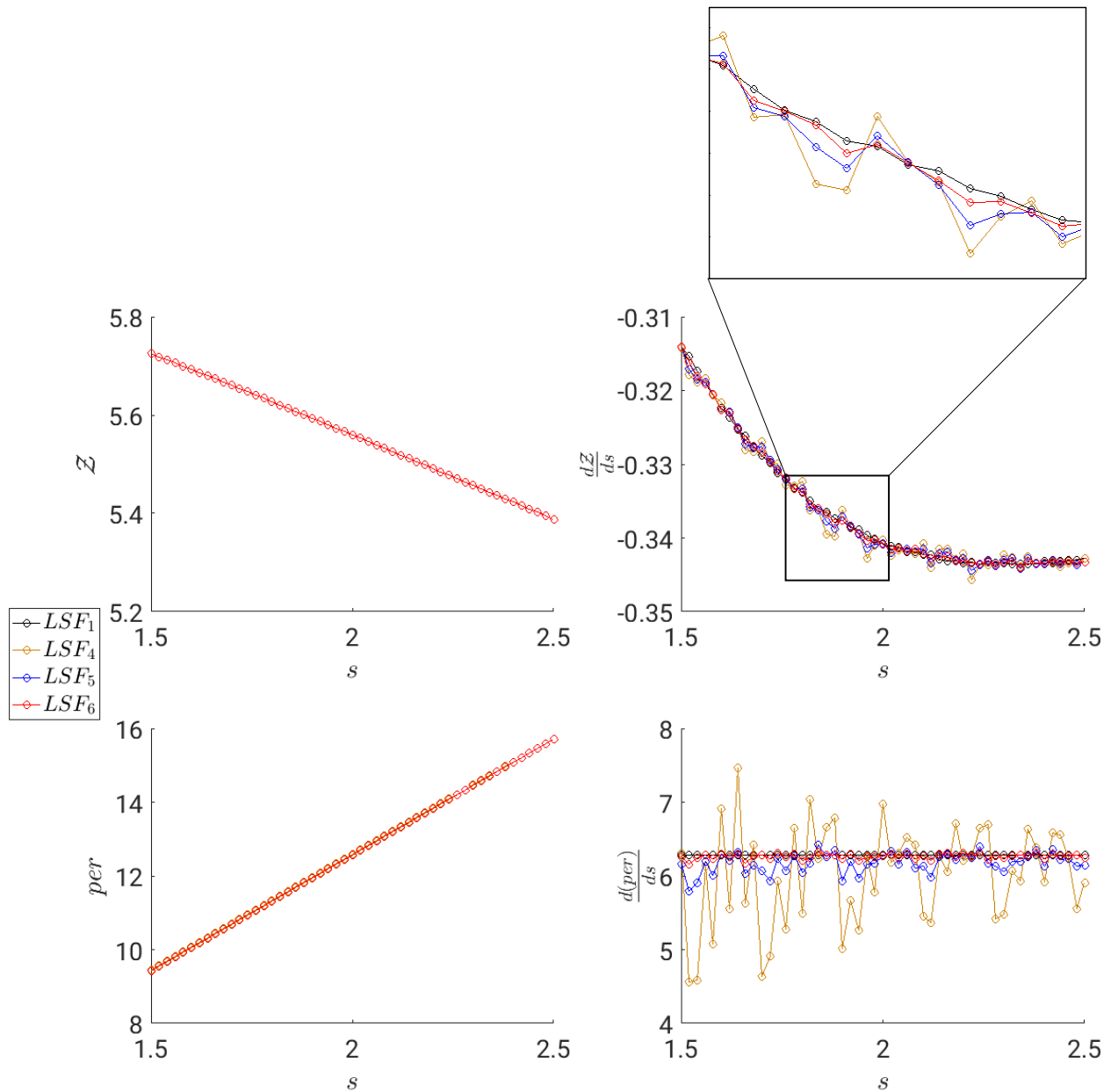


Figure 3.11: Influence of variation of $|\nabla\phi|$ (curvature) on the response function and corresponding shape sensitivities

Using larger values of γ_u and γ_τ results in smoother stress profiles. Consequently XFEM informed smoothing with $\gamma_u = 1.0$ and $\gamma_\tau = 10^{-2}$ results in diminished sensitivities especially on coarse meshes as can be seen for $h = 0.025m$.

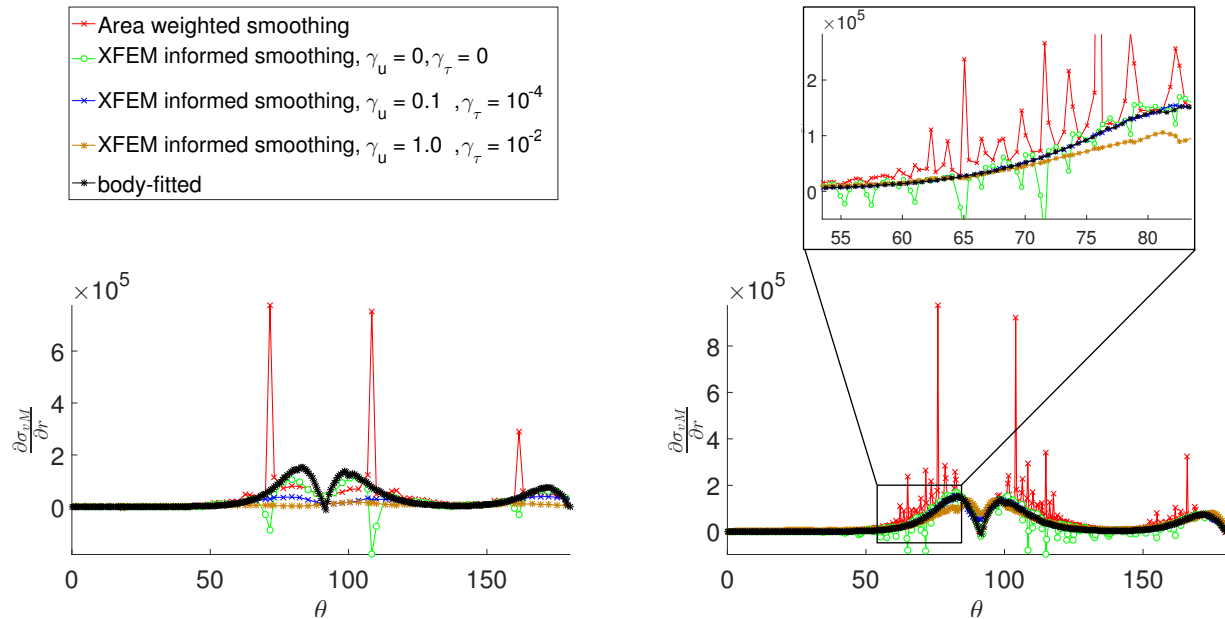


Figure 3.12: Comparison of stress sensitivities along material interface for $h = 0.025m$ (left) and $h = 0.005m$ (right).

3.4 Outlook and future work

We proposed an XFEM informed semi-analytical approach to computing shape sensitivities. Accuracy and robustness of the semi-analytical shape sensitivities was established via comparisons against body-fitted and finite differenced shape sensitivities. One disadvantage of the Heaviside-enriched XFEM is the need for interface conditions to enforce continuity in solution across the material interface. The accuracy (relative to a body-fitted mesh) of the shape sensitivities was found to be influenced by how strongly the interface conditions are enforced as discussed in Section 5.1.1 of Appendix B. Furthermore we illustrated the dependency of the smoothness of shape sensitivities on the discretization of the design geometry. With refinement in mesh and an accurate description of the material geometry smoother sensitivities were obtained.

As a topic of future work we bring to light a possible issue with the current framework

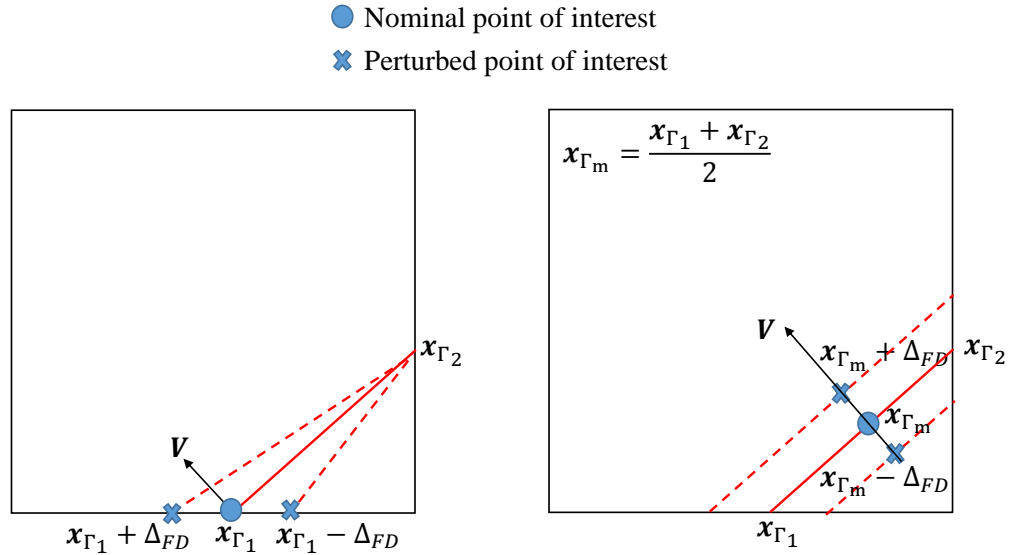


Figure 3.13: Discretized consistent (left) and continuum consistent (right) approach for perturbing points of interest for computation of semi-analytical sensitivities (3.3).

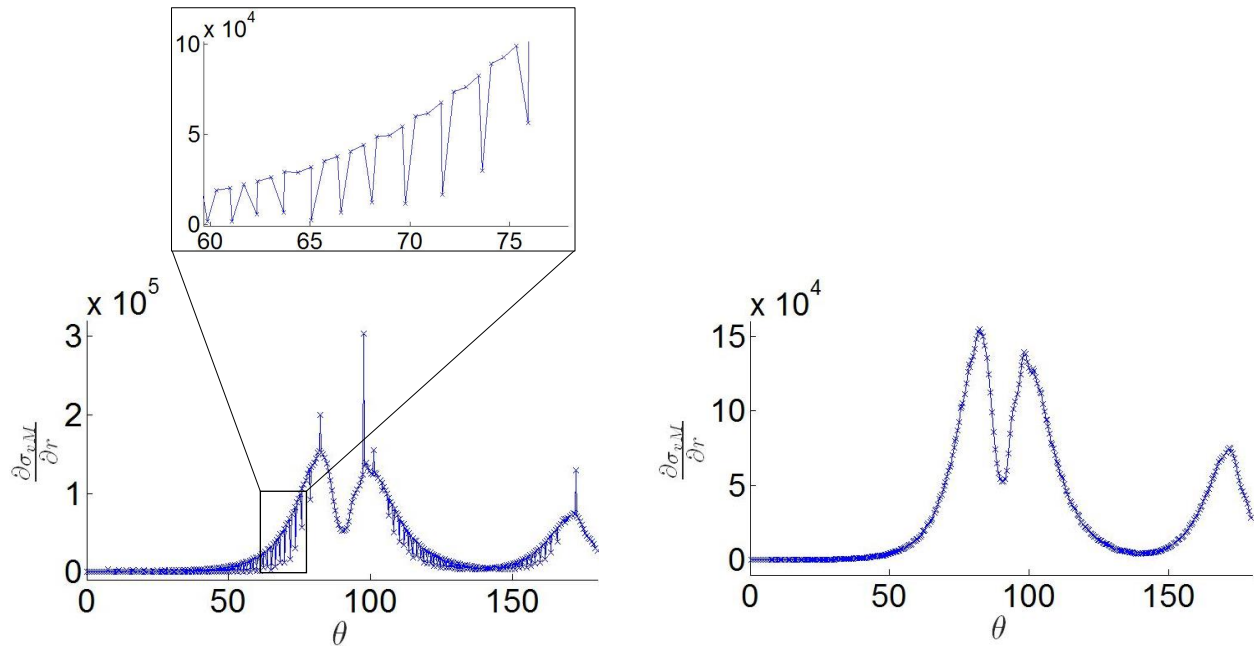


Figure 3.14: Stress sensitivities using discretized consistent (left) and continuum consistent (right) approach for XFEM informed smoothing with $\gamma_u = 0.1$ and $\gamma_\tau = 10^{-4}$.

of evaluating shape sensitivities in a discretized setting. From Figure 3.13 we see that the shape sensitivities are computed in the direction of the element edge as opposed to

the direction of the motion of the interface. This approach although consistent with the immersed boundary framework, is inconsistent with the continuum concept according to which shape sensitivities depend only on the normal component of the deformation of the material boundary [26]. So to say, in a discretized setting the intersection points along material edges compute only a component of the actual material interface velocity. If this component is almost tangential to the material interface boundary, naturally the velocity at that intersection point will be a reduced version of the actual velocity leading to diminished shape sensitivities. This effect is observed in Figure 3.14 which shows a comparison of shape sensitivities for XFEM informed smoothing with $\gamma_u = 0.1$ and $\gamma_\tau = 10^{-4}$ in Figure 3.12, using discretized consistent and continuum consistent approaches. For demonstrative purposes the shape sensitivities using the continuum consistent approach in the current example are evaluated at \mathbf{x}_{Γ_m} as shown in Figure 3.13. The discrepancy in the discretized consistent and continuum consistent approach has not formed the basis of any study yet and presents a great avenue for future work. It is not clear how the continuum consistent approach should be implemented in an XFEM-based framework. Furthermore, it is also not yet clear how, if at all, the continuum consistent approach would influence design criteria integrated over the entire domain or away from the interface, in comparison to the discretized consistent approach. In the author's experience, the sensitivity of a global or far away design criteria using the discretized consistent approach are not influenced significantly by the locally diminished sensitivities, if any. However, a more systematic study investigating this issue needs to be performed.

Chapter 4

Advances in Design Optimization

As mentioned in Section 1.5.1 the current work focuses on level set based topology optimization using nodal level set values or geometric primitives as design variables. The description of the LSF $\phi(\mathbf{x})$ significantly depends on the choice of the design variables \mathbf{s} . Following the discussion in Section 3.2 an oscillatory LSF can heavily influence the shape sensitivities which may further affect convergence of the optimization process. Furthermore an oscillatory material boundary is known to promote convergence to local minima [28], and is unattractive from a design and manufacturing standpoint. An oscillatory material boundary can also influence the analysis of the physical system, introducing unwanted noise in the XFEM-based approximation of the solution. Hence regularizing the LSF so as to control its smoothness and limit the amount of spatial variations of the LSF is important. Common regularization schemes for doing so, include: i) As discussed in [4], perimeter regularization is closely related to the mean curvature of the material boundary. Hence controlling the perimeter to produce non-oscillatory material boundaries is a common option [27, 82, 137]. ii) Use of a filtering/averaging scheme to reduce fluctuations in the material boundary. Applying a filter to an LSF is usually straightforward and does not involve toying with the objective or constraints [1, 82]. In contrast, a relatively complicated approach was adopted in [61] wherein a Helmholtz PDE-based filtering technique was used to smoothen the LSF.

For nodal level set values as design variables a perimeter penalty (4.3) prevents emergence of small geometric features and helps get rid of oscillations in an LSF along the material

boundary as shown in [82]. The intensity of the perimeter penalization needs to be carefully managed as too high a magnitude may result in loss of structurally significant geometric features. For geometric primitives as design variables the shape of the material boundary is made smooth by using a simple anisotropic filter which presents certain advantages over penalizing the perimeter (see Section 4.2.2).

It is a well known fact that LSM-based optimization methods suffer from slow design evolution resulting from localization of the shape sensitivities. Geometric primitive-based optimization alleviates this issue due to lack of localized shape sensitivities. For nodal level set values as design variables, slow convergence is alleviated by adopting the isotropic filtering approach of [44] as discussed in [82]. The LSF value, ϕ_i , for node i is then defined through an explicit function of the optimization variables as follows:

$$\phi_i = \frac{\sum_{j=1}^{N_n} w_{ij} s_j}{\sum_{j=1}^{N_n} w_{ij}}, \quad (4.1)$$

where

$$w_{ij} = \max(0, r_\phi - \|\mathbf{x}_i - \mathbf{x}_j\|). \quad (4.2)$$

Here N_n is the number of nodes in the finite element mesh and r_ϕ is the smoothing filter radius. The linear filter (4.1) widens the zone of influence of the design variable on the level set field resulting in enhanced convergence of the optimization process [65]. The filter in 4.1 is known to have a smoothing effect too, although the control over geometry is not very reliable [82]. In the absence of a level set filter $\phi_i = s_i$. To avoid inconsistencies in the optimization process all filtering schemes should be accounted for in (3.8) through chain rule.

4.1 Stress-based optimization

To make stress-based topology optimization compatible with recent advances in additive manufacturing, robust and reliable prediction of stresses and corresponding shape sensitivities is important. Following the discussion in Sections 2.1 and 3.3 we apply the

proposed framework of spatially stabilized stresses to the benchmark topology optimization problem of an L-beam.

The majority of previous work on stress constrained optimization considers volume minimization problems subject to stress constraints. For a material-void problem such a formulation is ill-posed with the optimal solution being a structure with zero volume. We thus formulate the optimization problem as a compliance minimization problem subject to stress and volume constraints. While compliance minimization leads to an overall decrease in stresses, stress constraints are required to eliminate designs with stress peaks. To promote smooth shapes and discourage the formation of small geometric features we augment the objective with a measure of the interface perimeter [50, 82]. The optimization problem is formulated as follows.

$$\begin{aligned} \min_{\mathbf{s}} \quad & c_J \mathcal{J}(\mathbf{u}(\mathbf{s})) + c_P \mathcal{P}(\mathbf{s}) \\ \text{s.t.} \quad & \begin{cases} g(\sigma_V(\tau(\mathbf{s})) \leq 0 \\ g(\sigma_T(\tau(\mathbf{s})) \leq 0 \\ \frac{V^1(\mathbf{s})}{V(\mathbf{s})} - c_V \leq 0 \end{cases}, \end{aligned} \quad (4.3)$$

where \mathcal{J} is the compliance integrated over the complete domain, and \mathcal{P} is the perimeter corresponding to the material domain boundary. The penalties c_J and c_P are associated with the compliance and perimeter respectively. These are chosen such that the terms constituting the objective function are of similar order throughout the optimization process. The volume ratio of the material phase, V^1 , with respect to the total volume, V , is constrained to be less than or equal to c_V . Section 4 of Appendix C discusses the optimization formulation adopted for material-material problems wherein the objective is to minimize the volume fraction of phase 1. In contrast to a material-void setting, such a problem formulation is not ill-posed because the design domain consists of at least one material leading to a structural design with finite volume at all times during the optimization process. In addition to the constraints listed in (4.3) we make use of box constraints to bound the design variables such

that $-h \leq \mathbf{s} \leq +h$ for mesh size h .

The stress constraints in this thesis are implemented using the global constraints approach of [99]. It is easy to implement and sufficient to study the primary goal of this work, which strictly pertains to the applicability of spatially stabilized stresses to stress-based optimization. Consequently the findings of the current work are applicable to any of the other numerous approaches available in literature ranging from local stress measures (e.g. [25, 31, 33, 45]) to global measures (e.g. [3, 55, 77, 103, 106]) to block aggregation methods (e.g. [73, 100]). The global stress constraints approach implies the use of one constraint that represents all local constraints. Given a maximum allowable stress value, σ_{max} , the global stress constraints are defined as,

$$\begin{aligned} g(\sigma_V(\tau(\mathbf{s}))) &= \frac{1}{\beta_V} \log \int_{\Omega} e^{\beta_V \left(\frac{\tau - \sigma_{max}}{\sigma_{max}} \right)} d\mathbf{x} - \frac{1}{\beta_V} \log \int_{\Omega} d\mathbf{x}, \\ g(\sigma_{\Gamma}(\tau(\mathbf{s}))) &= \frac{1}{\beta_{\Gamma}} \log \int_{\Gamma} e^{\beta_{\Gamma} \left(\frac{\tau - \sigma_{max}}{\sigma_{max}} \right)} d\mathbf{x}' - \frac{1}{\beta_{\Gamma}} \log \int_{\Gamma} d\mathbf{x}'. \end{aligned} \quad (4.4)$$

The stress constraints in (4.4) are formulated using the smoothed stresses of (2.3). The parameters β_V and β_{Γ} are tuning coefficients which penalize the failure to satisfy the stress constraint. As they tend to infinity the stress constraints become equal to $(\tau - \sigma_{max})/\sigma_{max}$. However, a large value of β_V or β_{Γ} renders the optimization problem unstable and difficult to solve due to the increasing nonlinearity and badly scaled sensitivities of the stress constraints. Selection of the parameters β_V and β_{Γ} thus involves a trade-off between accuracy of the global stress capturing capability and stability of the optimization problem. Figure 4.1 plots the variation of the stress constraints in (4.4) as a function of the tuning coefficients. Sensitivities are computed using the adjoint approach discussed in Section 1.5.1.2, and detailed in Section 4.2 of Appendix C.

4.1.1 Application to L-beam

Through this example we demonstrate the applicability of the proposed approach to the benchmark problem of an L-beam in 3D. A vertical load of $P = 0.1N$ is applied along

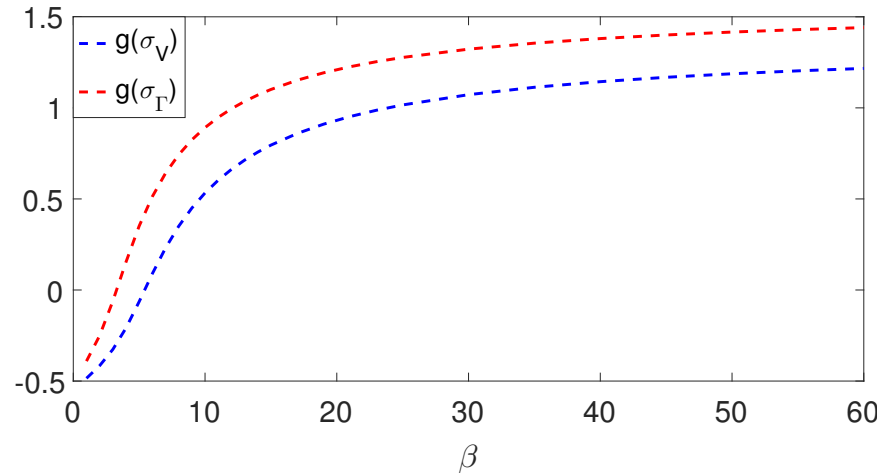


Figure 4.1: Variation of stress constraints as a function of the tuning coefficient β .

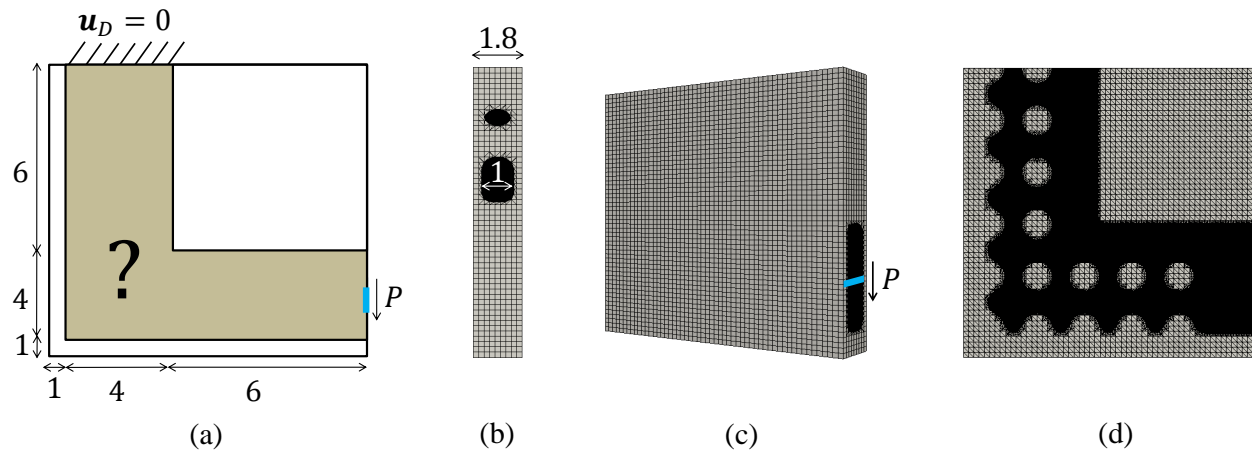


Figure 4.2: (a) Cross-sectional view of the L-beam problem setup; Finite element mesh, $h = 0.2m$, with initial seeding in 3D for load case RE: (b) Top view; (c) Perspective view; (d) Slice along the thickness. All dimensions are in m .

the middle of the right vertical edge, distributed over two elements along the height. The beam is made of an isotropic elastic material with Young's modulus, $E = 100N/m^2$, and a Poisson's ratio, $\nu = 0.3$. The problem domain is discretized using a mesh size of $h = 0.2m$. A list of relevant problem parameters is presented in Table 4.1. Figure 4.2 shows the problem setup alongside the finite element mesh with the initial seeding of the design domains using circular inclusions of radius $0.7m$. The black regions are occupied by the elastic material

Table 4.1: Parameter list for topology optimization of single-phase 3D linear elastic L-beam.

Parameter	Value
σ_{max}	$0.3N/m^2$
r_ϕ	$2.4 h$
c_J	10^2
c_P	0.006
c_v	0.48
β_V (up till iteration 360)	15
β_V (iteration 360 onward)	18
β_Γ	6
GCMMA step size (up till iteration 360)	0.002
GCMMA step size (iteration 360 onward)	0.005
GCMMA constraint penalty	10^4

(phase A). The void regions (phase B) are depicted in grey. As mentioned in Section 2.1.1 faces lying on the boundary of the mesh are not stabilized. To ensure that gradients across all material faces are stabilized we expand the domain along the original boundary of the beam including, along the thickness of the structure. In Figure 4.2a the extended boundary is represented by the unshaded region.

Figures 4.3 and 4.4 present the evolution of the normalized compliance and constraints, respectively. The initial design violates every constraint. The compliance of the structure rises initially while the stress reduces. As a result, the re-entrant corner profile has a lower curvature. Subsequently a decrease in the compliance of the structure and presence of active stress constraints result in a completely inclined flange. During the optimization process it was observed that the structure near the application of the load gets very thin as the volume is reduced and develops a tendency to break off completely. This phenomenon is represented by a spike in the evolution plots of Figure 4.3 and 4.4. To prevent the structure from completely breaking off we adopt a continuation strategy for the GCMMA step size, starting with a small value and as the volume constraint is close to being satisfied the step size is increased. Reducing the volume of a structure is counteractive to reducing the stress.

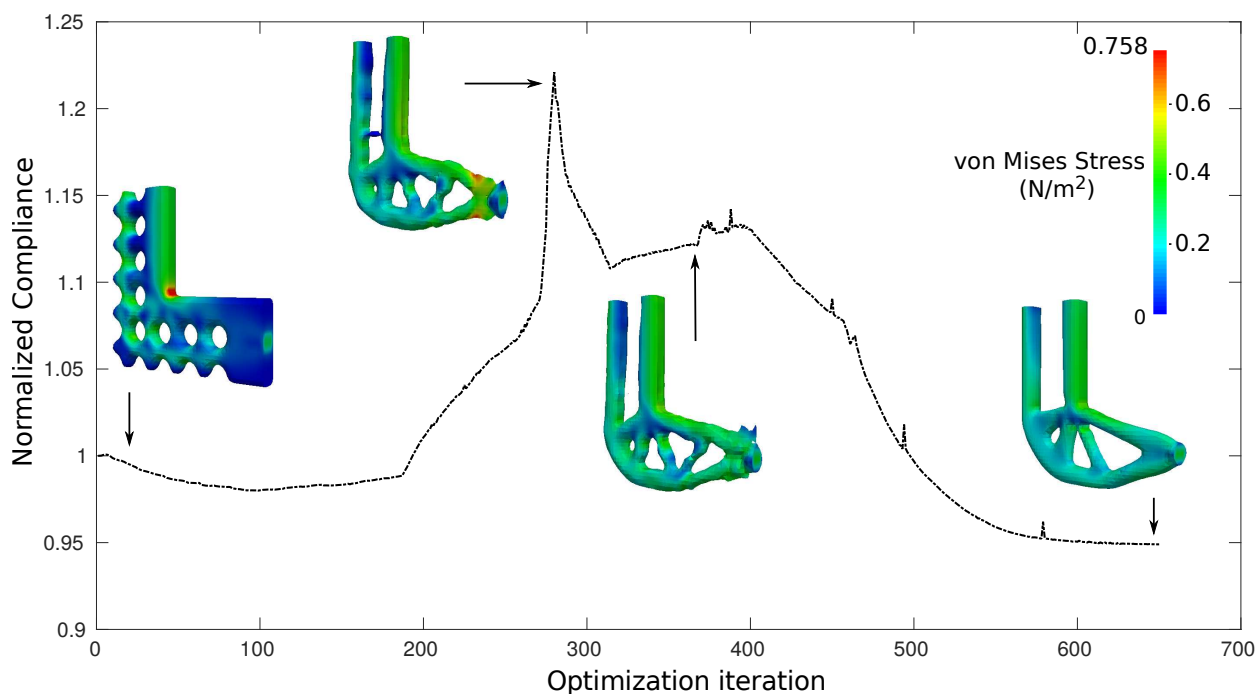


Figure 4.3: Evolution of normalized compliance for 3D linear elastic L-beam.

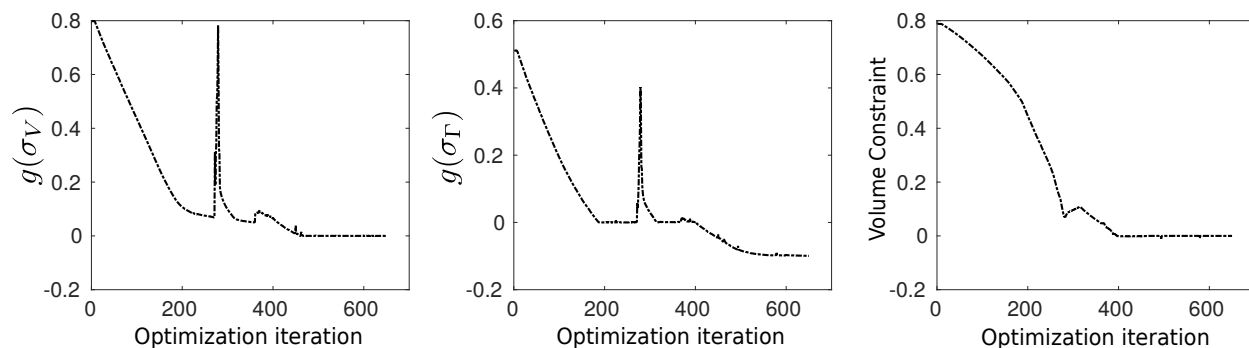


Figure 4.4: Evolution of stress and volume constraints for 3D linear elastic L-beam.

Thus, to facilitate smooth convergence of the optimization problem a continuation strategy is also adopted for the KS tuning coefficient, β_V . Figure 4.5 presents a comparison of the final designs obtained with and without stress constraints. In the absence of stress constraints the re-entrant corner is retained resulting in localized high stresses. Ignoring stress constraints although resulted in a design with 3.8% lower compliance, the increase in peak stresses was

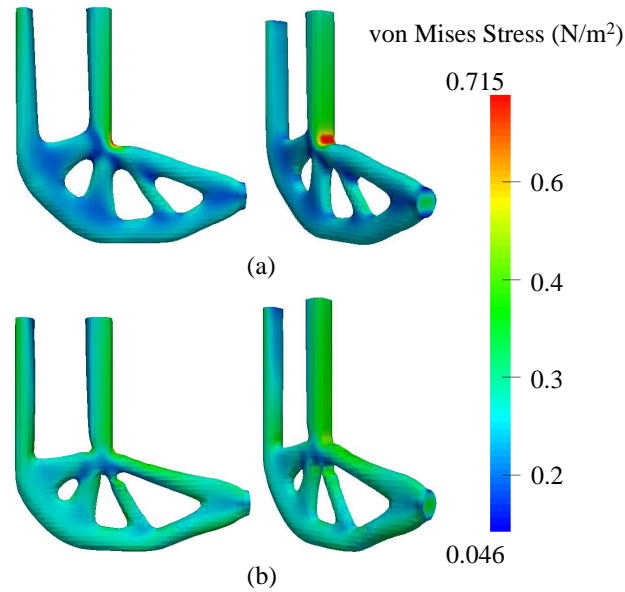


Figure 4.5: Stress distribution in optimized design for 3D linear elastic L-beam: (a) Without stress constraints; (b) With stress constraints

61.9% compared to the optimized design using stress constraints..

Section 5 of Appendix C presents various other examples relevant to the current discussion. Applicability of the proposed approach to topology optimization under different load cases is shown for a material-void L-shaped beam using an elastic material in 2D. We also apply the proposed approach to optimizing the design of a material-void L-shaped beam using a hyperelastic material in 2D and 3D. Furthermore arguments are made in favor of using a hyperelastic material outside the small strain limit for stress-based optimization. Finally the proposed optimization approach is extended to a material-material 2D L-beam using linear elastic materials. A comparison is drawn between designs optimized for different allowable maximum stress values. For all optimization problems considered smooth convergence of stress constraints was reported based on the evolution plots presented.

4.1.2 Outlook and future work

We established the applicability of spatially stabilized stresses to stress-based optimization for material-void and material-material problems. Linear elastic and hyperelastic problems in 2D and 3D were considered. Future studies should focus on more accurate measures for stress constraints such as the regional measure in [73] should be employed for better control of local stress levels. In addition, multiphase problems involving more than two materials should be considered.

4.2 Topology Optimization using Geometric Primitives

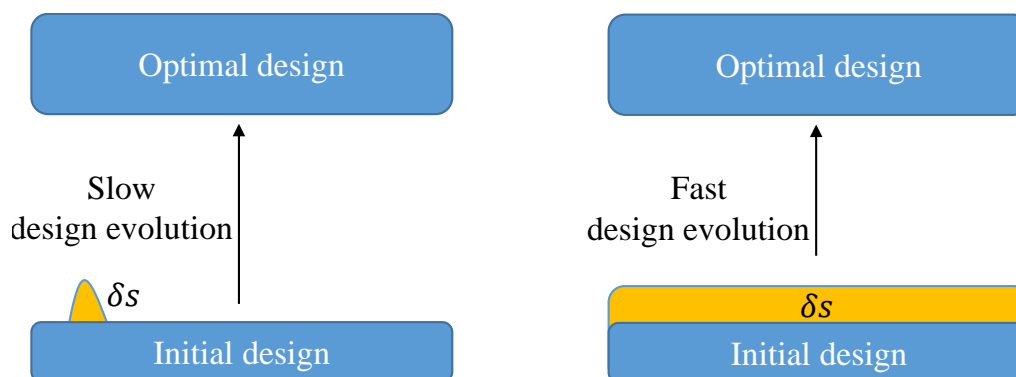


Figure 4.6: Design evolution resulting from localized sensitivities in traditional LSM (left) and more universal sensitivities using geometric primitives (right).

Compared to the more popular element or node-based design optimization frameworks, the concept of geometric primitives as design variables allows for geometry information to be directly incorporated into the topology optimization framework. With crisp definition of material geometries and accurate physical response along material boundaries, immersed boundary methods present a great platform for geometric primitive-based topology optimization. As a result immense possibilities are presented for making the optimization process more flexible from a geometric standpoint [93, 143]. Moreover, geometric primitives as design variables are independent of mesh size, and thus do not scale with the number of elements

in the mesh. Hence the topology optimization process is rendered computationally less expensive. Furthermore, LSM-based topology optimization is known to suffer from slow design evolution resulting from extremely localized sensitivities. The concept of geometric primitives alleviates this issue as shown in Figure 4.6. Therein, the initial design comprises of a thin block. Assuming the optimal design is a thicker version of the thin block, an approach using nodal level set values as design variables results in slow design evolution resulting from localized perturbations of the design corresponding to every nodal design variable. In contrast, using a geometric primitive such as a rectangle with its height as the design variable will lead to a faster design evolution resulting from a universal perturbation of the design.

Work on geometric primitives as design variables in topology optimization has gained contribution from primary two research groups. The first group of researchers, with the aim of establishing a direct link between topology optimization and CAD systems developed a new computational framework for minimum compliance optimization based on the concept of moving morphable components (MMC) [47]. Structural topology optimization was performed using super-ellipses describing rectangular components in 2D. The finite element problem was evaluated using the XFEM. This work was extended to allow for components with variable thicknesses in [144] and curved members in [46]. The work in [144] was performed using the Ersatz material model with the material layout described by projecting an aggregated min/max topological description function describing the MMCs. The framework presented in [144] was extended to 3D problems in [142]. Recently in [145] the MMC approach was used to control the structural complexity of the optimized design based on the number of components forming the structure. The second group of researchers have consistently used geometry projection techniques mapping geometric primitives to density fields for performing topology optimization. The idea was first presented in [9] where the stiffness of structures was maximized using rectangular bars of fixed width. As a more comprehensive extension to the previous study, in [93] the out-of-plane thickness was penalized similar to density in SIMP such that the resulting design is made of bars of a specified thickness, and

of bars with zero thickness. Furthermore the geometry projection functions of the individual bars were aggregated using a p-norm function. This work was extended to optimize structures made of plates (in 3D) with constant thickness [141]. Therein a composition of the density resulting from the geometric projection of the plates and a free density field was performed to allow for the creation of holes and modification of plate boundaries to assume non-rectangular shapes. This results in a hybrid between geometric primitives and density-based methods. Recently a framework for stress-based topology optimization of structures using bars and plates was presented in [140]. Therein a global stress measure aggregating the stress at the centroid of every geometric primitive was used to generate optimized design without stress singularities.

All of aforementioned work has been restricted to linear elasticity. Furthermore use of immersed boundary methods for geometric primitives-based topology optimization has been restricted to 2D problems. Through this contribution of the thesis we aim at addressing these gaps in literature. We further present an anisotropic filter in combination with explicit penalization of design variables to promote smooth LSFs and smooth material boundaries which are attractive from a convergence (avoiding local minima), analysis, and manufacturing point of view.

4.2.1 Ribs as geometric primitives for topology optimization

In this thesis we use ribs in 2D and 3D as discrete building components. Figure 4.7 presents an example of a rib in 3D. The level set field of a rib in 3D is defined using the LSF for a superellipsoid such that

$$\phi_{rib} = \left(\left(\frac{r - r_c}{a} \right)^p + \left(\frac{s - s_c}{b} \right)^p + \left(\frac{t - t_c}{c} \right)^p \right)^{1/p} - 1. \quad (4.5)$$

The length, width, and height of the rib are assumed along x , y and z direction respectively given by $2a$, $2b$, and $2c$. The parameter p controls the 'rectangle-ness' of the rib with $p = 2$ representing a circle. In the current study $p = 10$ was found to satisfactorily represent a rib.

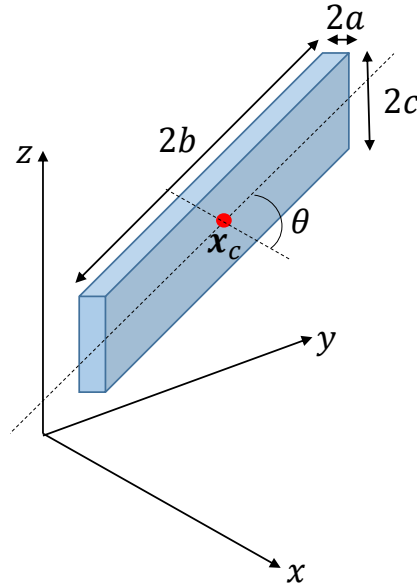


Figure 4.7: Example of a 3D rib as a geometric primitive.

The rib is free to rotate about the z -axis. Thereby the local coordinate system of the rib is oriented at an angle θ measured in radians w.r.t. to the Cartesian coordinate system, as shown in Figure 4.7. This transformation is straight forward and defined as

$$\begin{bmatrix} r - r_c \\ s - s_c \\ t - t_c \end{bmatrix} = \begin{bmatrix} \cos\theta & -\sin\theta & 0 \\ \sin\theta & \cos\theta & 0 \\ 0 & 0 & 1 \end{bmatrix} \begin{bmatrix} x - x_c \\ y - y_c \\ z - z_c \end{bmatrix}. \quad (4.6)$$

The design variables of a rib in 3D are its position (x_c, y_c, z_c) , dimension (a, b, c) and orientation θ . The definition of the design variables remain unchanged in 2D in absence of z_c and c . Multiple ribs can be represented using a single LSF by, e.g. using the Kreisselmeier-Steinhauser function [64] to present a differentiable approximation of the minimum operator:

$$\phi_{KS} = -\frac{1}{\beta} \ln \left(\sum_{i=1}^{i=n_{rib}} e^{-\beta \phi_{rib}^i} \right) \quad (4.7)$$

where n_{rib} is the number of ribs in the design domain, and β is a parameter controlling the sharpness of the approximating function. This thesis uses a value of $\beta = 20$.

4.2.2 Anisotropic smoothing

The goal here is to regularize the LSF to produce smooth material boundaries in the in-plane directions of the structure. Consequently we propose an anisotropic filter wherein the LSF value, ϕ_i , for node i is defined as follows:

$$\phi_i = \frac{\sum_{j=1}^{N_n} w_{ij} \phi_{KS_j}}{\sum_{j=1}^{N_n} w_{ij}}, \quad (4.8)$$

where

$$w_{ij} = \max(0, \mathbf{r}_\phi - \|(\mathbf{x}_i - \mathbf{x}_j)'\|). \quad (4.9)$$

The transformed distance $(\mathbf{x}_i - \mathbf{x}_j)'$ is obtained by rotating the Cartesian coordinate system to align with the material boundary's local coordinate system such that

$$(\mathbf{x}_i - \mathbf{x}_j)' = \begin{bmatrix} \mathbf{t}_1 \\ \mathbf{t}_2 \\ \mathbf{n} \end{bmatrix}_i (\mathbf{x}_i - \mathbf{x}_j); \quad \mathbf{n}_i = \frac{\nabla \phi_{KS_j}}{\|\nabla \phi_{KS_j}\|}. \quad (4.10)$$

Here \mathbf{n} is the unit normal assumed to align with the rotated y-axis in 2D and rotated z-axis in 3D at node i , and \mathbf{t}_1 and \mathbf{t}_2 are unit tangent vectors at node i . Together, these three vectors form an orthonormal basis. Naturally in 2D the transformation vector consists of \mathbf{t}_1 and \mathbf{n} which form an orthonormal basis in 2D. The smoothing radius vector \mathbf{r}_ϕ is chosen to include the influence of nodes lying in the plane of the tangent vectors and exclude points lying along the normal vector. However since this operation is performed on a fixed background mesh it is important that the smoothing radius in the normal direction is greater than the mesh size to ensure inclusion of enough nodes in the support domain as shown in Figure 4.8.

Note, there currently exist smoothing filters such as the isotropic filter in (4.1). Figure 4.8 presents a comparison between the support domains for isotropic and anisotropic smoothing. An isotropic smoothing when using geometric primitives would result in extreme undesirable mass loss as further confirmed by comparisons made in 2D and 3D in Figure 4.9. There is however some unavoidable mass loss using anisotropic smoothing too. This

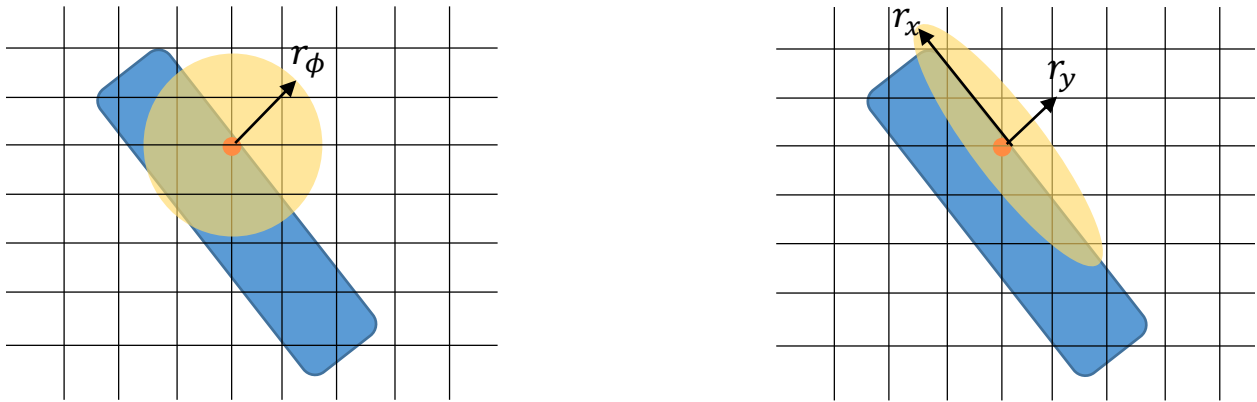


Figure 4.8: Support domain for isotropic smoothing (left) and anisotropic smoothing (right).

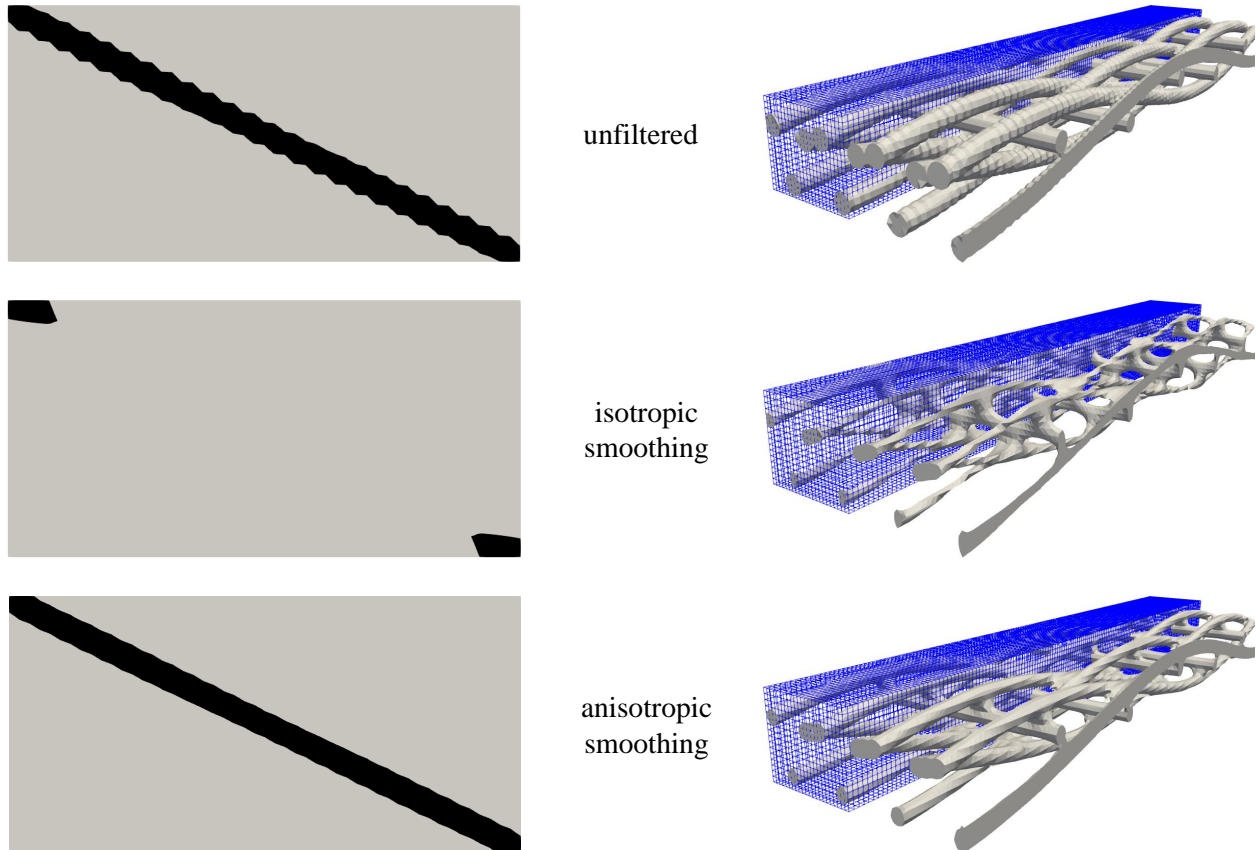


Figure 4.9: Material boundaries in 2D (left) and 3D (right).

is a result of the requirement of having a smoothing radius in the normal direction greater

than the mesh size, as discussed above. The anisotropic smoothing is successful in producing smooth boundaries analogous to the perimeter penalty in (4.3). However compared to the perimeter penalty the anisotropic smoothing does not suffer from possible non-convexity issues. One such scenario is depicted in Figure 4.10 wherein the perimeter of the structure may be reduced by either breaking it off or straightening out the boundary. When using the perimeter penalty there is no way to control how (in what direction) the perimeter is regulated. This is not the case with anisotropic smoothing.

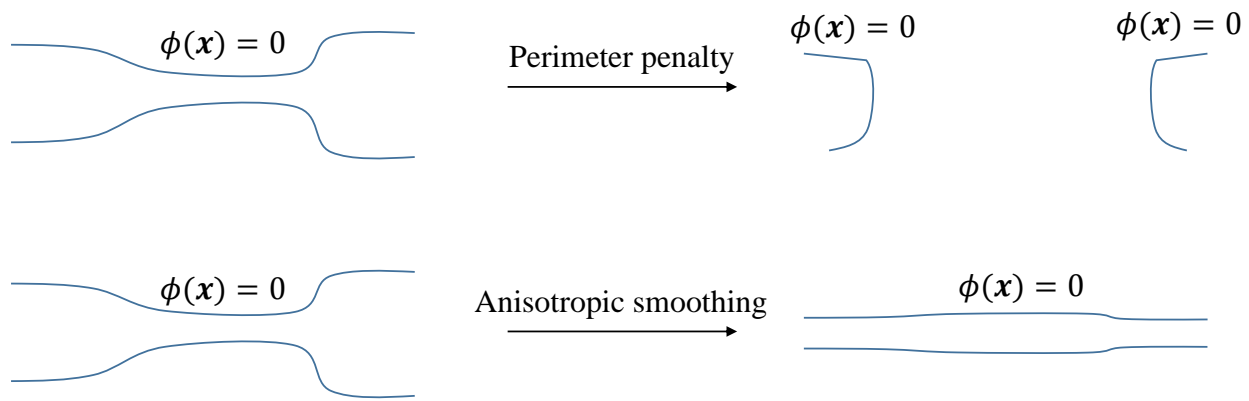


Figure 4.10: Difference in affect of perimeter penalty (left) and anisotropic smoothing (right).

Generating an LSF requires mapping the geometric design variables to (4.7) which are in turned mapped to (4.8). As can be imagined ϕ_{KS_j} belonging to a particular node may affect the value of ϕ_i in (4.8) at multiple nodes. This would require repeated computation of (4.7) and (4.5) for every such node. Depending on the mesh size such an approach to updating (4.8) based on the geometric design variables can quickly get very expensive. We thus propose a multilevel filter framework for parallel computing in order to save computational time and memory when employing multiple levels of filter/functions for computing an LSF, details of which are provided in Appendix D.1. Such a framework also opens many avenues for testing various combinations of filter schemes for regularizing an LSF.

It is common for modular research-based optimization frameworks to not have knowledge about the connectivity of the finite element mesh. Such a code was the basis of the

research in this thesis. Consequently the gradient of the level set field required for evaluating the normal to a surface is computed using a point cloud as in meshfree methods [79], details of which have been provided in Appendix D.2.

4.2.3 Numerical examples

The proposed approach for performing topology optimization using geometric primitives is applied to 2D static linear elastic and 3D steady and unsteady thermo-elastic systems. Due to the fairly simple nature of the configuration of geometric primitives in the 3D problems studied in this thesis, a need for anisotropic smoothing was not observed. Consequently the 3D examples presented do not make use of (4.8). This work does not use the ghost penalty approach discussed in 2.1.1, and thus to mitigate issues with ill-conditioning caused by an extremely small (or large) ratio of intersected areas within an intersected element, we use the geometric preconditioning scheme introduced in [68].

4.2.3.1 Application to linear elasticity

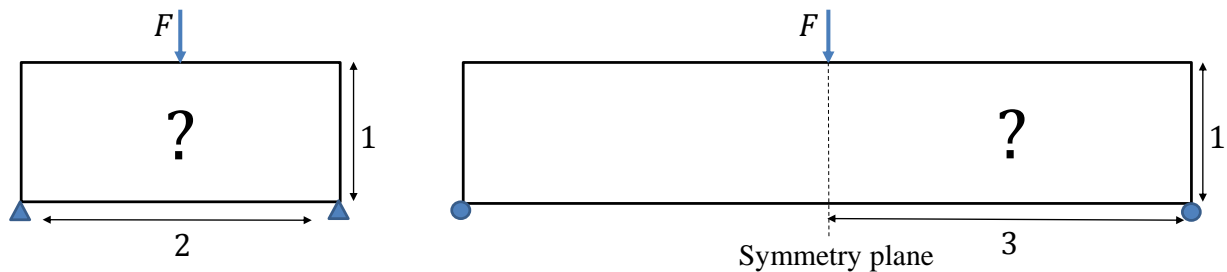


Figure 4.11: Problem setup for two-bar truss problem (left) and MBB beam problem (right). All dimensions in m.

We solve the benchmark topology optimization problems of two-bar truss and Messerschmitt - Bölkow-Blohm (MBB) beam in 2D to verify the applicability of the proposed approach. The problem setup of these benchmark problems is presented in Figure 4.11. The problem domain is discretized using a mesh size of $h = 0.02m$. For both problems

the load applied is $F = 1N$. The linear elastic material considered has a Young's modulus of $E = 1N/m^2$ and a Poisson's ratio of $\nu = 0.3$. For the MBB problem we model half of the domain, and symmetry boundary conditions are imposed along the plane $x = 3$. The optimization problem involves minimizing the compliance of the structure subject to a constraint on the structural volume, V^1 . Often the number of ribs required to form the optimized structure is lower than the number of ribs present in the initial design. For instance only 2 ribs should be sufficient to form the optimized structure in the two-bar truss optimization problem. However, to start from a non-biased design we populate the initial design with 12 ribs as shown in Figure 4.12. In such a scenario some ribs tend to disappear. If disconnected from the structure these ribs no longer add information to the shape sensitivities and thus are left unattended by the optimizer. However the presence of such partially disappearing ribs introduces oscillations in the LSF especially on coarser meshes as shown in Figure 4.13. Hence as a part of the objective we penalize the area of the ribs that fall below a certain threshold. The optimization problem formulation is then stated as

$$\begin{aligned} \min_{\mathbf{s}} \quad & \mathcal{J}(\mathbf{u}(\mathbf{s})) + c_s \sum_{i=1}^{i=n_{rib}} I(A_i)4a_i b_i \\ \text{s.t.} \quad & \left\{ \begin{array}{l} \frac{V^1(\mathbf{s})}{V(\mathbf{s})} - c_V \leq 0 \end{array} \right. \end{aligned} \quad (4.11)$$

where the indicator function for penalizing the area of the ribs, $I(A_i)$, is defined as

$$I(A_i) = \begin{cases} 1 & \text{if } 4a_i b_i \leq A_{th} \\ 0 & \text{otherwise} \end{cases} \quad (4.12)$$

The weight of penalty on the area of the ribs is given by c_s . In addition to the constraints listed in (4.11) we make use of box constraints to bound the geometric design variables such that $s_k^{min} \leq s_k \leq s_k^{max}$ for k -th design variable. The complete list of parameters for the two-bar truss and MBB beam optimization problems is presented in Table 4.2.

The initial design for both problems consists of 12 ribs, 6 placed horizontally and 6 vertically to form a 2D grid of ribs. Figure 4.12 presents the evolution of the design for both

Table 4.2: Parameter list for topology optimization of two-bar truss problem. All dimensions in m.

Parameter	Two-bar truss	MBB beam
r_x, r_y	$2.4 h, 1.04 h$	$4.8 h, 1.2 h$
c_s	1000	0
A_{th}	$9 h^2$	-
c_v	0.3	0.5
x_c^{min}, x_c^{max}	0, 2	0, 3
y_c^{min}, y_c^{max}	0, 1	0, 1
a^{min}, a^{max}	0, 2.24	0, 3.2
b^{min}, b^{max}	0, 0.2	0, 0.1
$\theta^{min}, \theta^{max}$	0, 3.15	0, 3.15
GCMMA step size	0.005	0.002
GCMMA constraint penalty	10^2	10^2

problems. A final structure confirming to the node-based topology optimization solution of these problems is obtained, with non-oscillatory boundaries. The number of independent ribs in the final design is less than 12 as some ribs were deemed useless in regards to their contribution to the structural design and thus completely removed by the optimizer. In the absence of penalizing the design variables, small ribs are found to be leftover from the optimization process which was the case for the MBB beam optimization problem. These ribs however do not cause oscillations in the LSF as they are completely overlapped by a larger rib. Convergence is achieved in a reasonable number of optimization steps for both problems as demonstrated by convergence plots for the two-bar truss problem and the MBB beam problem in Figures 4.14 and 4.15 respectively. The volume constraint for the MBB beam problem remains inactive throughout the optimization process.

Note, the two bar truss problem is a symmetric problem. However as can be observed in Figure 4.12, the design evolves in an asymmetrical manner. In the author's experience such an asymmetric design evolution is a combination of, choice of optimization algorithm, as well as numerical noise which depending on the optimization problem may significantly influence the shape sensitivities.

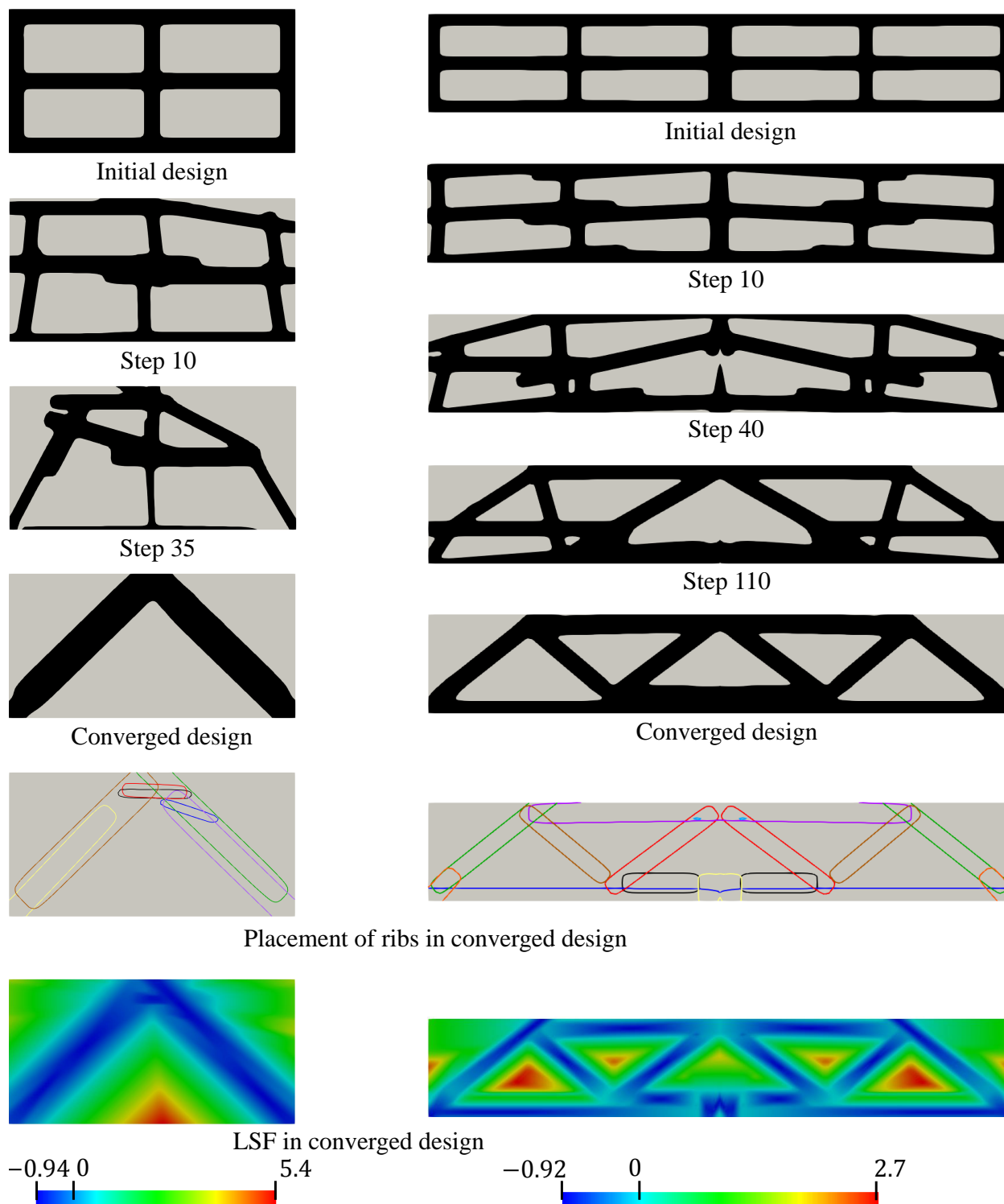


Figure 4.12: Evolution of ribs for two-bar truss problem (left) and MBB beam problem (right).

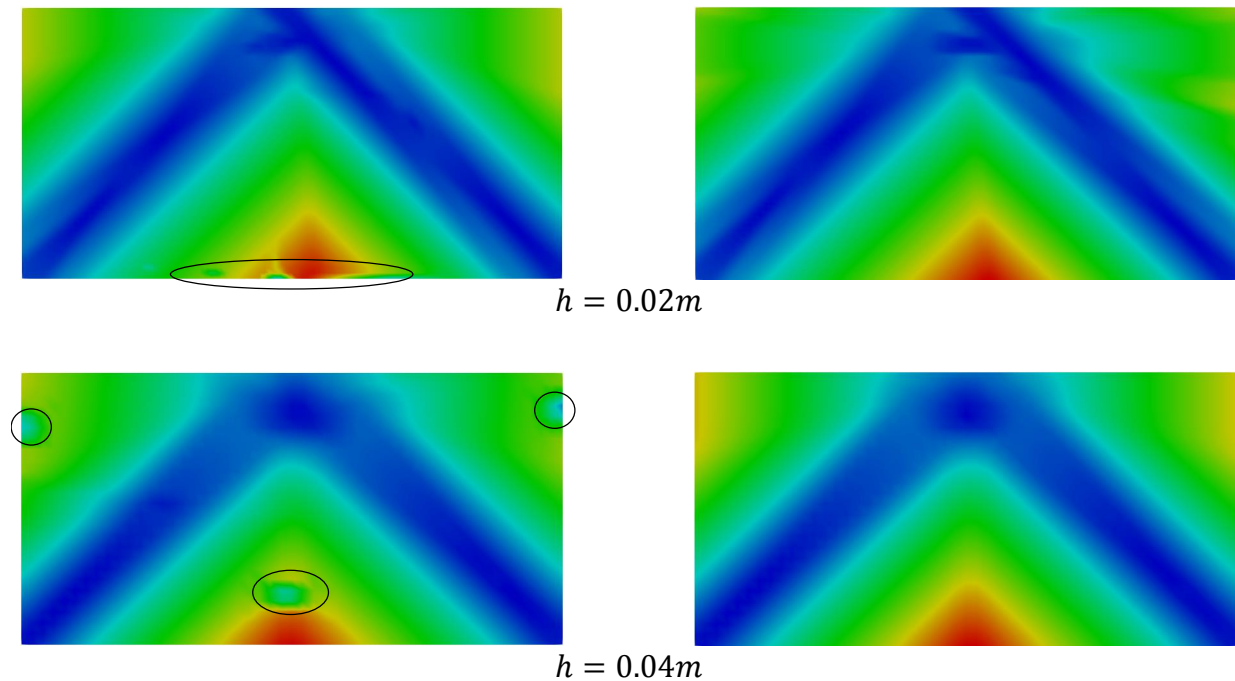


Figure 4.13: Oscillations in LSF for two-bar truss problem caused by partially disappearing ribs (left), and elimination of oscillations in LSF upon penalization of area of ribs (right).

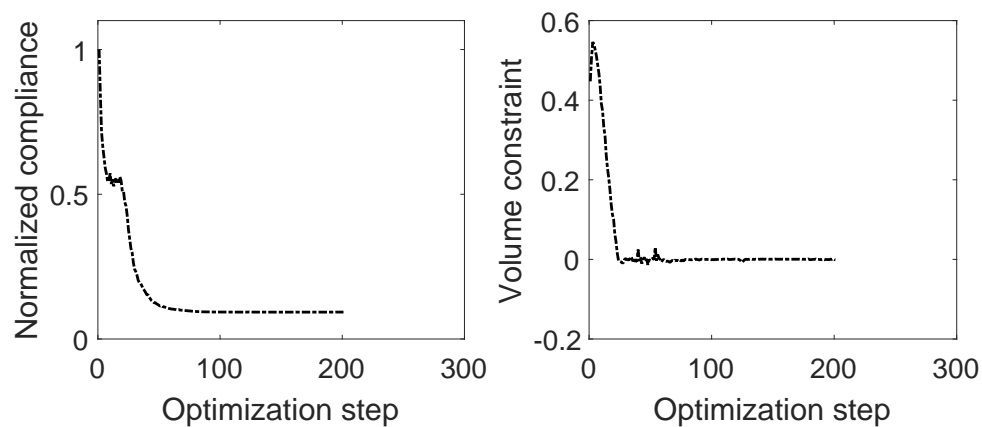


Figure 4.14: Convergence plots for two-bar truss problem.

4.2.3.2 Application to thermo-elastic systems

We extend the proposed framework for topology optimization using geometric primitives to steady and unsteady thermo-elastic systems. To verify the applicability of the

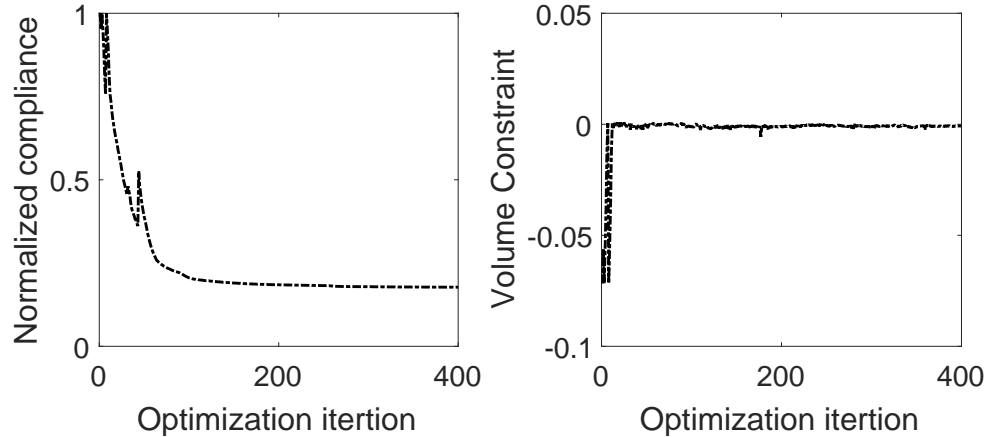


Figure 4.15: Convergence plots for MBB beam problem.

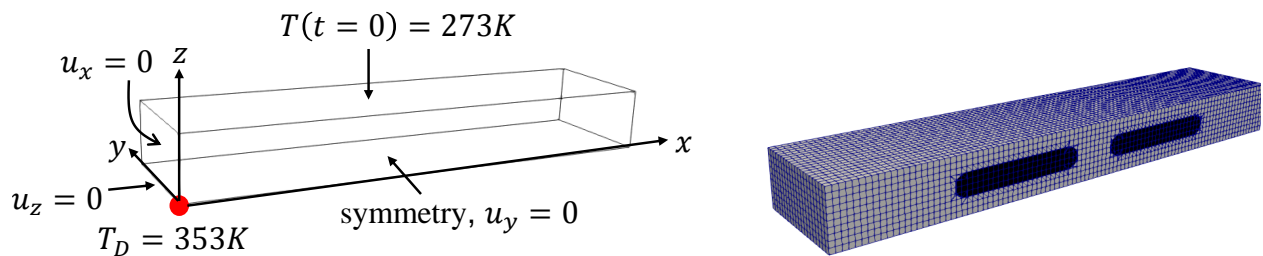


Figure 4.16: Passive thermo-elastic problem setup (left) and mesh with fiber inclusions (right).

proposed framework to thermo-elastic systems we first study a passive optimization problem setup wherein high conductive and low expanding stiff fibers are placed in a low conductive and high expanding soft matrix. Figure 4.16 presents the problem setup along with relevant boundary conditions and initial placement of fiber inclusions in the matrix. The problem domain is 30mm by 6mm by 3mm . A mesh size of $h = 0.3\text{mm}$ is used. The goal of the optimization problem is to find the optimal position of fiber inclusions given a target displacement profile subject to a constraint on the fiber volume V^1 . The optimization problem is then stated as

$$\begin{aligned} \min_s \quad & \sqrt{\int_{z=3} (U_{target} - u_z)^2 d\mathbf{x}'} \\ \text{s.t.} \quad & \left\{ \begin{array}{l} \frac{V^1(s)}{V(s)} - c_V \leq 0 \end{array} \right. \quad ; \quad U_{target} = 0.024x - 0.0022x^2 \end{aligned} \quad (4.13)$$

The target displacement was chosen knowing that such a profile can be obtained using the passive thermo-elastic problem setup. Choosing an obtainable profile serves as a good verification test. The material properties associated with the fiber and matrix, and other problem parameters are presented in Table 4.3.

Table 4.3: Parameter list for topology optimization of steady passive thermo-elastic problem. All dimensions in mm.

Parameter	Value
E_f, E_m	$69 \times 10^3, 13 \text{ N/mm}^2$
ν_f, ν_m	0.3, 0.45
α_f, α_m	$2.1 \times 10^{-5}, 2.7 \times 10^{-4} \text{ K}^{-1}$
k_f, k_m	0.205, $2 \times 10^{-4} \text{ W/(mm K)}$
c_v	0.3
x_c^{min}, x_c^{max}	0, 30
y_c^{min}, y_c^{max}	0, 6
z_c^{min}, z_c^{max}	0, 3
a^{min}, a^{max}	0, 30
b^{min}, b^{max}	0, 6
c^{min}, c^{max}	0, 3
$\theta^{min}, \theta^{max}$	0, 3.15
GCMMA step size (up to 50 iterations)	0.005
GCMMA step size (50-th iteration onward)	0.0025
GCMMA constraint penalty	10^2

Figure 4.17 presents the evolution of the design for select iterations, alongside the corresponding u_z plots. The matrix having a higher thermal expansion coefficient has a tendency to expand more than the fiber inclusions. Thus the optimizer places one of the fiber inclusions lower than the other in order to achieve the desired curved displacement profile. A comparison between the target displacement and displacement profile of the converged design is presented in Figure 4.18. Figure 4.19 presents the convergence of the objective. Oscillations were noticed in convergence after 50 optimization steps. Hence inner iterations were performed using the GCMMA from iteration 50 onward. Inner iterations in the GCMMA are MMA subproblems wherein the objective and constraint functions are

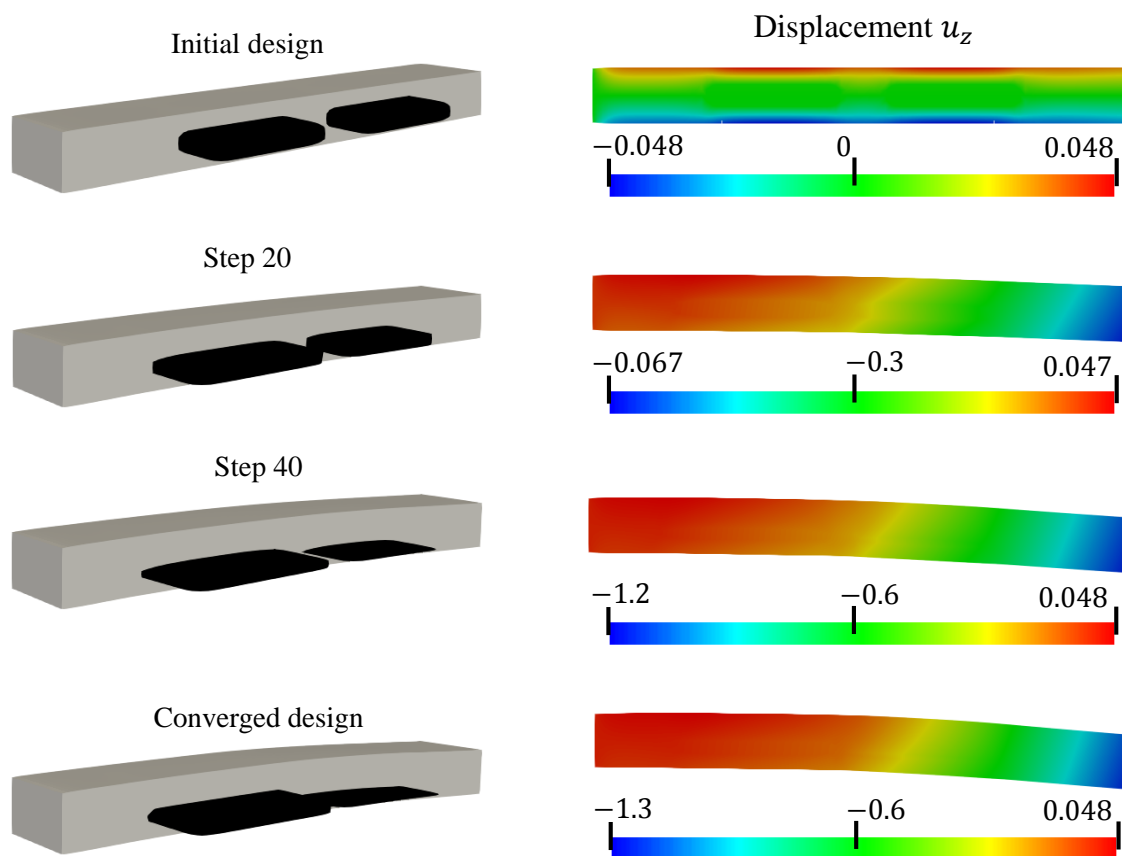


Figure 4.17: Deformed cross-sectional view with fibers reflected about axis of symmetry (left) and u_z plotted on cross-sectional view of deformed design (right).

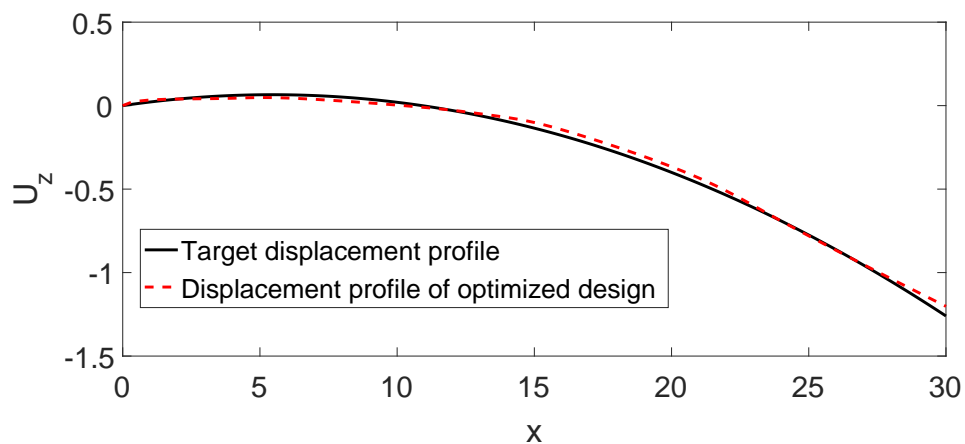


Figure 4.18: Comparison of displacement profile against target displacement.

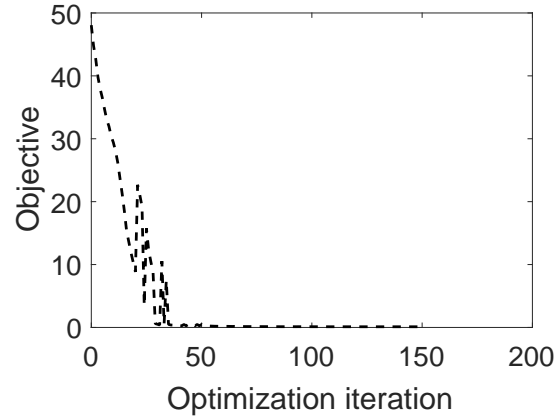


Figure 4.19: Convergence plots for steady passive thermo-elastic optimization problem.

replaced by certain convex separable functions [123]. The optimal solution to the subproblem produces a lower objective value than the previous step thus guaranteeing convergence to some local minima. The volume constraint remained inactive throughout the optimization process. Since the current problem is solved to steady state the temperature throughout the domain remains constant at $353K$. The fiber inclusions essentially act as stiff inserts in a soft surrounding. Hence the problem is described as passive.

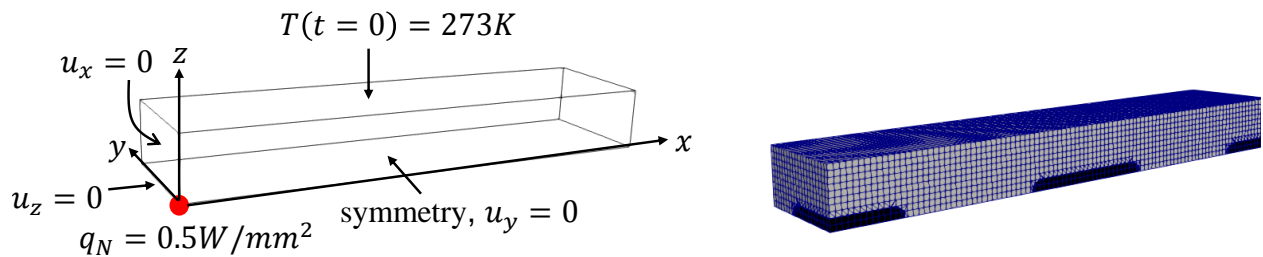


Figure 4.20: Active thermo-elastic problem setup (left) and mesh with fiber inclusions (right).

We now apply the proposed optimization framework to study an unsteady optimization problem setup wherein high conductive and low expanding stiff fibers are placed in a low conductive and high expanding soft matrix. Figure 4.20 presents the problem setup along with relevant boundary conditions and initial placement of fiber inclusions in the matrix.

Problem domain is $30mm$ by $6mm$ by $3mm$. A mesh size of $h = 0.3mm$ is used. The heat

flux, q_N is applied for 3 seconds with $\Delta t = 1$. The goal of the optimization problem is to find the optimal position of fiber inclusions given a target displacement profile at $t = 3s$ subject to a constraint on the fiber volume V^1 . The optimization problem is then stated as

$$\begin{aligned} \min_s \quad & \sqrt{\int_{z=3} (U_{target} - u_z(t=3))^2 d\mathbf{x}'} \\ \text{s.t.} \quad & \begin{cases} \frac{V^1(\mathbf{s})}{V(\mathbf{s})} - c_V \leq 0 \\ U_{target} = ax; a = \begin{cases} 10^{-4} & \forall x \leq 15mm \\ 10^{-3} & \forall x > 15mm \end{cases} \end{cases} \end{aligned} \quad (4.14)$$

Problem parameters from Table 4.3 are used. Any additional problem parameter or parameters inconsistent with the previous example are listed in Table 4.4.

Table 4.4: Parameter list for topology optimization of unsteady active thermo-elastic problem. All dimensions in mm.

Parameter	Value
$(\rho C)_f, (\rho C)_m$	$2.5 \times 10^{-3}, 1.3 \times 10^{-3} J/(mm^3 K)$
GCMMA step size	0.005

Figure 4.21 presents the evolution of the design for select iterations. Figure 4.22 present a comparison of the temperature and displacement plots between the initial and converged designs. One of the fiber inclusions is connected to the heat source. This fiber inclusion having a high conductivity heats up faster than the surrounding matrix. The fiber inclusion owing to it's stiffness does not bend. However the surrounding matrix upon heating deforms greatly causing the rest of the structure, including the disconnected fiber inclusions, to bend upwards in a straight line. Thus minimizing the objective requires the optimizer to adjust the slope of the deformed section of the structure which is in turn controlled by the size of the fiber inclusion connected to the hear source. Figure 4.23 presents the convergence of the objective. As in the previous example oscillations (not visible in Figure 4.23) were noticed in convergence after 70 optimization steps. Hence inner iterations were performed using the GCMMA from iteration 70 onward. The volume constraint remained inactive throughout the optimization process. In the current problem the fiber inclusion connected to the heat

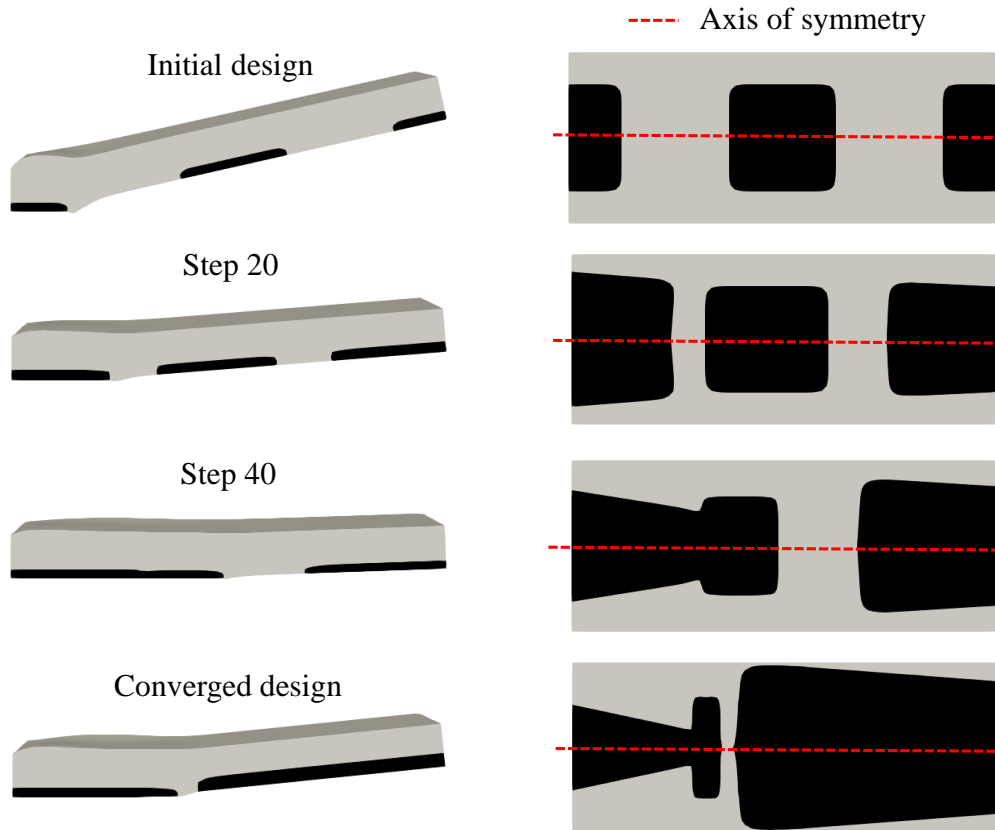


Figure 4.21: Deformed cross-sectional view with fibers reflected about axis of symmetry (left) and u_z plotted on cross-sectional view of deformed design (right). Deformation of design amplified by a factor of 75.

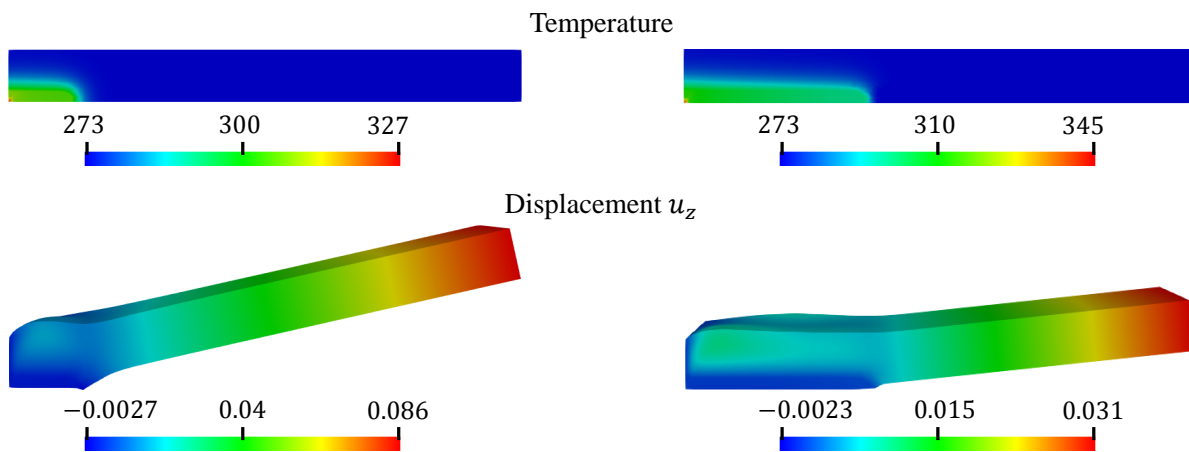


Figure 4.22: Comparison of the temperature and displacement plots between the initial (left) and converged (right) designs. Deformation of design amplified by a factor of 75.

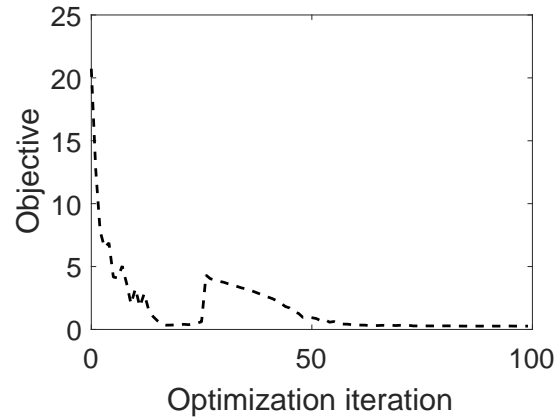


Figure 4.23: Convergence plots for unsteady active thermo-elastic optimization problem.

source acts as an actuator controlling the deformation of the rest of the structure based on its shape and size. Hence the problem is described as active.

4.2.4 Outlook and future work

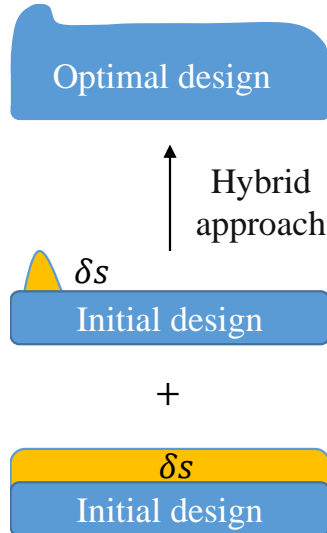


Figure 4.24: Future work should focus on a hybrid approach.

We extended the concept of geometric primitive-bases topology optimization using immersed boundary methods in 3D. We further introduced the concept of a localized anisotropic

filter for obtaining geometric primitives with smooth surfaces by filtering the LSF only in the in-place directions of the structure. The anisotropic filter presents a solution to the non-convexity issue presented by the concept of penalizing the perimeter for smoother geometries. The anisotropic filter was shown to successfully remove oscillations from the material boundary. The proposed framework was successfully applied to two benchmark problems in linear elasticity. We further applied the proposed framework to steady and unsteady thermo-elastic systems in 3D. Smooth convergence of objective and constraints was observed for all examples presented. Inner iterations with the GCMMA were required to achieve convergence of design in 3D. The issue of extremely localized sensitivities resulting in slow design evolution is alleviated through the use of geometric primitives.

For future work a hybrid approach should be considered wherein the design variables comprise of nodal level set values as well as geometric primitives, as shown in Figure 4.24. It is expected that such an approach will render immense flexibility to the topology optimization process. While the geometric primitives will aid in the fast evolution of the overall design, the nodal design variables will help provide a local control over the material geometry, thus combining the best of both worlds. However special treatment of the optimization process as well as additional regularization may be required based on the resultant LSF.

Chapter 5

Summary

This thesis has introduced certain advances made towards making the XFEM a more viable and reliable design and optimization tool. This section summarizes the overall contributions and their implications on future research.

- (i) We presented a robust semi-analytical approach to computing the shape sensitivities using the XFEM. Advantages and challenges of the proposed approach in the context of Heaviside-enriched XFEM were discussed. We further studied the dependency of the shape sensitivities on spatial resolution, interface conditions, and smoothness of the LSF. In addition a possible issue with computing continuum shape sensitivities using a discretized consistent approach was brought to light. Future research should be aware of the implications when using the discretized consistent approach. Consequently studies should focus on ways to incorporating the continuum consistent approach in the XFEM framework.
- (ii) The issue of overestimation of stresses using the XFEM was addressed using the ghost penalty method combined with a novel XFEM informed stabilization scheme. Accurate and robust computation of stresses and stress sensitivities was reported. The proposed approach is a significant improvement over preexisting approaches. Researchers should feel confident about using the XFEM for stress-based optimization. Furthermore researchers should look at exploring the concept of ghost penalty for other physics in the context of topology optimization.

- (iii) Building on some recent studies we demonstrated 3D static and transient XFEM-based topology optimization using geometric primitives. We further presented a regularization approach in the context of geometric primitives-based topology optimization wherein non-smooth boundaries were eliminated using an anisotropic filter. It is expected that future studies will develop hybrid approaches wherein the design variables are a combination of nodal level set values as well as geometric primitives. Such an approach will render immense flexibility to the topology optimization process using the LSM-XFEM, in terms of possessing fast convergence rates as well as local control of the material geometry.
- (iv) Unrelated to topology optimization, as a contribution to design using the XFEM, we developed the concept of active stochastic subdomains which is integral to modeling problems with either a weak or a strong discontinuity across a random material interface. The convergence and accuracy of the proposed method is demonstrated using problems with continuous and discontinuous solutions in the problem domain. However the approach was found to be too expensive given its intrusive nature. It would be unrealistic to expect future studies to extend the proposed approach to 3D for multiple uncertain parameters. Non-intrusive approaches might be more practical.

In conclusion, the LSM-XFEM approach for designing and optimizing coupled multi-physics problems has shown great promise, as is evident by the variety of physics it has been applied to in the literature. The limited research in LSM-XFEM-based topology optimization is a result of the non-intuitive implementation of an XFEM-based framework in research codes. Moreover XFEM suffers from stabilization issues, and LSM from regularization issues. Regardless, the advantages of the approach (such as crisp geometry and accurate resolution of physics) outweigh the drawbacks. Furthermore, most issues surrounding stabilization in XFEM have solutions in the literature, and research on LSM-based topology optimization is

on the rise with new papers being published on a weekly basis.

Bibliography

- [1] Kazuhisa Abe, Shunsuke Kazama, and Kazuhiro Koro. A boundary element approach for topology optimization problem using the level set method. International Journal for Numerical Methods in Biomedical Engineering, 23(5):405–416, 2007.
- [2] Joe Alexandersen, Niels Aage, Casper Schousboe Andreasen, and Ole Sigmund. Topology optimisation for natural convection problems. International Journal for Numerical Methods in Fluids, 76(10):699–721, 2014.
- [3] G. Allaire and F. Jouve. Minimum stress optimal design with the level set method. Engineering analysis with boundary elements, 32(11):909–918, 2008.
- [4] Gregoire Allaire, Francois Jouve, and Anca-Maria Toader. Structural optimization using sensitivity analysis and a level-set method. Journal of Computational Physics, 194(1):363–393, 2004.
- [5] Chandrasekhar Annavarapu, Martin Hautefeuille, and John E Dolbow. A robust Nitsche’s formulation for interface problems. Computer Methods in Applied Mechanics and Engineering, 225–228:44–54, 2012.
- [6] Chandrasekhar Annavarapu, Martin Hautefeuille, and John E Dolbow. Stable imposition of stiff constraints in explicit dynamics for embedded finite element methods. International Journal for Numerical Methods in Engineering, 92(2):206–228, 2012.
- [7] JS Arora and Q Wang. Review of formulations for structural and mechanical system optimization. Structural and Multidisciplinary Optimization, 30(4):251–272, 2005.
- [8] I. Babuška and J. M. Melenk. The partition of unity method. International Journal for Numerical Methods in Engineering, 40(4):727–758, 1997.
- [9] Bryan Bell, Julian Norato, and Daniel Tortorelli. A geometry projection method for continuum-based topology optimization of structures. In 14th AIAA/ISSMO Multidisciplinary Analysis and Optimization Conference, 2012.
- [10] Ted Belytschko, Yun Yun Lu, and Lei Gu. Element-free galerkin methods. International journal for numerical methods in engineering, 37(2):229–256, 1994.

- [11] Martin P Bendsøe. Optimal shape design as a material distribution problem. Structural and multidisciplinary optimization, 1(4):193–202, 1989.
- [12] Martin P Bendsøe, Ole Sigmund, Martin P Bendsøe, and Ole Sigmund. Topology optimization by distribution of isotropic material. Springer, 2004.
- [13] Martin Philip Bendsøe and Noboru Kikuchi. Generating optimal topologies in structural design using a homogenization method. Computer methods in applied mechanics and engineering, 71(2):197–224, 1988.
- [14] Kai-Uwe Bletzinger, Stefan Kimmich, and Ekkehard Ramm. Efficient modeling in shape optimal design. Computing Systems in Engineering, 2(5–6):483–495, 1991.
- [15] Thomas Borrvall and Joakim Petersson. Topology optimization of fluids in stokes flow. International journal for numerical methods in fluids, 41(1):77–107, 2003.
- [16] D Brackett, I Ashcroft, and R Hague. Topology optimization for additive manufacturing. In Proceedings of the solid freeform fabrication symposium, Austin, TX, pages 348–362. Springer, 2011.
- [17] M. Burger, B. Hackl, and W. Ring. Incorporating topological derivatives into level set methods. Journal of Computational Physics, 194(1):344–362, 2004.
- [18] Erik Burman and Peter Hansbo. Fictitious domain methods using cut elements: III. A stabilized nitsche method for stokes problem. ESAIM: Mathematical Modelling and Numerical Analysis, 48(3):859–874, 2014.
- [19] Shouyu Cai, Weihong Zhang, Jihong Zhu, and Tong Gao. Stress constrained shape and topology optimization with fixed mesh: a b-spline finite cell method combined with level set function. Computer Methods in Applied Mechanics and Engineering, 278:361–387, 2014.
- [20] V.J. Challis and J.K. Guest. Level set topology optimization of fluids in stokes flow. International Journal for Numerical Methods in Engineering, 79(10):1284–1308, 2009.
- [21] Shikui Chen, Michael Yu Wang, and Ai Qun Liu. Shape feature control in structural topology optimization. Computer-Aided Design, 40(9):951–962, 2008.
- [22] Jack Chessa and Ted Belytschko. An extended finite element method for two-phase fluids. Journal of Applied Mechanics, 70(1):10–17, 2003.
- [23] Jack Chessa and Ted Belytschko. Arbitrary discontinuities in space–time finite elements by level sets and x-fem. International Journal for Numerical Methods in Engineering, 61(15):2595–2614, 2004.
- [24] Peter Coffin and Kurt Maute. A level-set method for steady-state and transient natural convection problems. Structural and Multidisciplinary Optimization, 53(5):1047 – 1067, 2016.

- [25] G. A. da Silva, A. T. Beck, and E. L. Cardoso. Topology optimization of continuum structures with stress constraints and uncertainties in loading. International Journal for Numerical Methods in Engineering, pages n/a–n/a. nme.5607.
- [26] Michel C Delfour and J. P. Zolésio. Structure of shape derivatives for nonsmooth domains. Journal of Functional Analysis, 104(1):1–33, 1992.
- [27] NP Dijk, M Langelaar, and F Keulen. Explicit level-set-based topology optimization using an exact heaviside function and consistent sensitivity analysis. International Journal for Numerical Methods in Engineering, 91(1):67–97, 2012.
- [28] N.P. Dijk, K. Maute, M. Langelaar, and F. Keulen. Level-set methods for structural topology optimization: a review. Structural and Multidisciplinary Optimization, 48(3):437–472, 2013.
- [29] J. Ding, P. Colegrove, J. Mehnen, S. Ganguly, P.M. Sequeira Almeida, F. Wang, and S. Williams. Thermo-mechanical analysis of wire and arc additive layer manufacturing process on large multi-layer parts. Computational Materials Science, 50(12):3315–3322, 2011.
- [30] John Dolbow and Isaac Harari. An efficient finite element method for embedded interface problems. International journal for numerical methods in engineering, 78(2):229–252, 2009.
- [31] P. Duysinx and M. P. Bendsøe. Topology optimization of continuum structures with local stress constraints. International Journal for Numerical Methods in Engineering, 43(8):1453–1478, 1998.
- [32] Pierre Duysinx, Laurent Van Miegroet, Thibault Jacobs, and Claude Fleury. Generalized shape optimization using X-FEM and level set methods. In IUTAM Symposium on Topological Design Optimization of Structures, Machines and Materials, pages 23–32. Springer, 2006.
- [33] Hélio Emmendoerfer and Eduardo Alberto Fancello. Topology optimization with local stress constraint based on level set evolution via reaction–diffusion. Computer Methods in Applied Mechanics and Engineering, 305:62–88, 2016.
- [34] H.A. Eschenauer, V.V. Kobelev, and A. Schumacher. Bubble method for topology and shape optimization of structures. Structural and Multidisciplinary Optimization, 8(1):42–51, 1994.
- [35] Hans A Eschenauer and Niels Olhoff. Topology optimization of continuum structures: a review. Applied Mechanics Reviews, 54(4):331–390, 2001.
- [36] Matthias Firl, Roland Wüchner, and Kai-Uwe Bletzinger. Regularization of shape optimization problems using fe-based parametrization. Structural and Multidisciplinary Optimization, 47(4):507–521, 2013.

- [37] Leopoldo Penna Franca and Eduardo Gomes Dutra Do Carmo. The galerkin gradient least-squares method. Computer Methods in Applied Mechanics and Engineering, 74(1):41–54, 1989.
- [38] Gilles A Francfort and François Murat. Homogenization and optimal bounds in linear elasticity. Archive for Rational mechanics and Analysis, 94(4):307–334, 1986.
- [39] Thomas-Peter Fries and Andreas Zilian. On time integration in the XFEM. Int. J. Numer. Meth. Engng., 79(1):69–93, 2009.
- [40] T.P. Fries and T. Belytschko. The extended/generalized finite element method: an overview of the method and its applications. International Journal for Numerical Methods in Engineering, 84(3):253–304, 2010.
- [41] P. Fulmański, A. Laurain, J.F. Scheid, and J. Sokołowski. Level set method with topological derivatives in shape optimization. International Journal of Computer Mathematics, 85(10):1491–1514, 2008.
- [42] Axel Gerstenberger and Wolfgang A Wall. An extended finite element method/lagrange multiplier based approach for fluid–structure interaction. Computer Methods in Applied Mechanics and Engineering, 197(19):1699–1714, 2008.
- [43] Philip E Gill, Walter Murray, and Michael A Saunders. Snopt: An sqp algorithm for large-scale constrained optimization. SIAM review, 47(1):99–131, 2005.
- [44] James K Guest, Jean H Prévost, and T Belytschko. Achieving minimum length scale in topology optimization using nodal design variables and projection functions. International journal for numerical methods in engineering, 61(2):238–254, 2004.
- [45] Xu Guo, Weisheng Zhang, Michael Yu Wang, and Peng Wei. Stress-related topology optimization via level set approach. Computer Methods in Applied Mechanics and Engineering, 200(47-48):3439–3452, 2011.
- [46] Xu Guo, Weisheng Zhang, Jian Zhang, and Jie Yuan. Explicit structural topology optimization based on moving morphable components (mmc) with curved skeletons. Computer Methods in Applied Mechanics and Engineering, 310:711–748, 2016.
- [47] Xu Guo, Weisheng Zhang, and Wenliang Zhong. Doing topology optimization explicitly and geometrically a new moving morphable components based framework. Journal of Applied Mechanics, 81(8):081009, 2014.
- [48] Xu Guo, Weisheng Zhang, and Wenliang Zhong. Explicit feature control in structural topology optimization via level set method. Computer Methods in Applied Mechanics and Engineering, 272:354–378, 2014.
- [49] G. Haasemann, M. Kästner, S. Prüger, and V. Ulbricht. Development of a quadratic finite element formulation based on the XFEM and NURBS. International Journal for Numerical Methods in Engineering, 86(4–5):698–617, 2011.

- [50] R.B. Haber, C.S. Jog, and M.P. Bendsøe. A new approach to variable-topology shape design using a constraint on perimeter. Structural Optimization, 11(1):1–12, 1996.
- [51] Raphael T Haftka and Ramana V Grandhi. Structural shape optimizationa survey. Computer Methods in Applied Mechanics and Engineering, 57(1):91–106, 1986.
- [52] Anita Hansbo and Peter Hansbo. A finite element method for the simulation of strong and weak discontinuities in solid mechanics. Computer Methods in Applied Mechanics and Engineering, 193(33-35):3523–3540, 2004.
- [53] F Henke, M Winklmaier, V Gravemeier, and WA Wall. A semi-lagrangean time-integration approach for extended finite element methods. International Journal for Numerical Methods in Engineering, 98(3):174–202, 2014.
- [54] Badri Hiriyur, Haim Waisman, and George Deodatis. Uncertainty quantification in homogenization of heterogeneous microstructures modeled by xfem. International Journal for Numerical Methods in Engineering, 88(3):257–278, 2011.
- [55] Kai A James, Edmund Lee, and Joaquim RRA Martins. Stress-based topology optimization using an isoparametric level set method. Finite Elements in Analysis and Design, 58:20–30, 2012.
- [56] Nicholas Jenkins and Kurt Maute. Level set topology optimization of stationary fluid-structure interaction problems. Structural and Multidisciplinary Optimization, 52(1):179–195, 2015.
- [57] Jakob Søndergaard Jensen and Ole Sigmund. Topology optimization for nanophotonics. Laser & Photonics Reviews, 5(2):308–321, 2011.
- [58] Long Jiang and Shikui Chen. Parametric structural shape & topology optimization with a variational distance-regularized level set method. Computer Methods in Applied Mechanics and Engineering, 321:316–336, 2017.
- [59] Barry Joe. Geompacka software package for the generation of meshes using geometric algorithms. Advances in Engineering Software and Workstations, 13(5-6):325–331, 1991.
- [60] M. Juntunen and R. Stenberg. Nitsche’s method for general boundary conditions. Mathematics of Computation, 78(267):1353–1374, 2009.
- [61] Atsushi Kawamoto, Tadayoshi Matsumori, Shintaro Yamasaki, Tsuyoshi Nomura, Tsuguo Kondoh, and Shinji Nishiwaki. Heaviside projection based topology optimization by a pde-filtered scalar function. Structural and Multidisciplinary Optimization, 44(1):19–24, 2011.
- [62] Gaetan K.W. Kenway, Graeme J. Kennedy, and Joaquim R.R.A. Martins. A CAD-free approach to high-fidelity aerostructural optimization. In 13th AIAA/ISSMO Multidisciplinary Analysis Optimization Conference, 13-15 September 2010, Fort Worth, Texas, 2010.

- [63] Oliver Kramer, David Echeverría Ciaurri, and Slawomir Koziel. Derivative-free optimization. In Computational optimization, methods and algorithms, pages 61–83. Springer, 2011.
- [64] G. Kreisselmeier and R. Steinhauser. Application of vector performance optimization to a robust control loop design for a fighter aircraft. Int. J. of Control, 37:251–284, 1983.
- [65] Sebastian Kreissl and Kurt Maute. Levelset based fluid topology optimization using the extended finite element method. Structural and Multidisciplinary Optimization, 46(3):311–326, 2012.
- [66] Achchhe Lal, Shailesh P Palekar, Sameer B Mulani, and Rakesh K Kapania. Stochastic extended finite element implementation for fracture analysis of laminated composite plate with a central crack. Aerospace Science and Technology, 60:131–151, 2017.
- [67] Ailsa H Land and Alison G Doig. An automatic method of solving discrete programming problems. Econometrica: Journal of the Econometric Society, pages 497–520, 1960.
- [68] C. Lang, D. Makhija, A. Doostan, and K. Maute. A simple and efficient preconditioning scheme for heaviside enriched XFEM. Comput. Mech., 54:1357–1374, 2014.
- [69] Christopher Lang. An XFEM Approach to Modeling Material Interface Uncertainty. PhD thesis, University of Colorado at Boulder, 2015.
- [70] Christopher Lang, Alireza Doostan, and Kurt Maute. Extended stochastic fem for diffusion problems with uncertain material interfaces. Computational Mechanics, 51(6):1031–1049, 2013.
- [71] Christopher Lang, Ashesh Sharma, Alireza Doostan, and Kurt Maute. Heaviside enriched extended stochastic fem for problems with uncertain material interfaces. Computational Mechanics, 56(5):753–767, 2015.
- [72] Matthew Lawry and Kurt Maute. Level set shape and topology optimization of finite strain bilateral contact problems. International Journal for Numerical Methods in Engineering.
- [73] Chau Le, Julian Norato, Tyler Bruns, Christopher Ha, and Daniel Tortorelli. Stress-based topology optimization for continua. Structural and Multidisciplinary Optimization, 41(4):605–620, 2010.
- [74] Christoph Lehrenfeld. The nitsche xfem-dg space-time method and its implementation in three space dimensions. SIAM Journal on Scientific Computing, 37(1):A245–A270, 2015.
- [75] Christoph Lehrenfeld and Arnold Reusken. Nitsche-xfem with streamline diffusion stabilization for a two-phase mass transport problem. SIAM journal on scientific computing, 34(5):A2740–A2759, 2012.

- [76] L. Li, M.Y. Wang, and P. Wei. XFEM schemes for level set based structural optimization. Frontiers of Mechanical Engineering, 7(4):335–356, 2012.
- [77] Haojie Lian, Asger N Christiansen, Daniel A Tortorelli, Ole Sigmund, and Niels Aage. Combined shape and topology optimization for minimization of maximal von mises stress. Structural and Multidisciplinary Optimization, 55(5):1541–1557, 2017.
- [78] Lars-Erik Lindgren, Andreas Lundbäck, and Martin Fisk. Thermo-mechanics and microstructure evolution in manufacturing simulations. Journal of Thermal Stresses, 36(6):564–588, 2013.
- [79] Gui-Rong Liu. Meshfree methods: moving beyond the finite element method. Taylor & Francis, 2009.
- [80] Jikai Liu and Yongsheng Ma. A survey of manufacturing oriented topology optimization methods. Advances in Engineering Software, 100:161–175, 2016.
- [81] M Locatelli. Simulated annealing algorithms for continuous global optimization: convergence conditions. Journal of Optimization Theory and applications, 104(1):121–133, 2000.
- [82] David Makhija and Kurt Maute. Numerical instabilities in level set topology optimization with the extended finite element method. Structural and Multidisciplinary Optimization, 49(2):185–197, 2014.
- [83] Kurt Maute, Anton Tkachuk, Jiangtao Wu, H Jerry Qi, Zhen Ding, and Martin L Dunn. Level set topology optimization of printed active composites. Journal of Mechanical Design, 137(11):111402, 2015.
- [84] John McCall. Genetic algorithms for modelling and optimisation. Journal of Computational and Applied Mathematics, 184(1):205–222, 2005.
- [85] Peter Mercelis and Jean-Pierre Kruth. Residual stresses in selective laser sintering and selective laser melting. Rapid Prototyping Journal, 5(12):254–265, 2006.
- [86] R. Merle and J. Dolbow. Solving thermal and phase change problems with the extended finite element method. Computational Mechanics, 28, 2002.
- [87] Rajat Mittal and Gianluca Iaccarino. Immersed boundary methods. Annu. Rev. Fluid Mech., 37:239–261, 2005.
- [88] N. Moës, J. Dolbow, and T. Belytschko. A finite element method for crack growth without remeshing. International Journal for Numerical Methods in Engineering, 46(1):131–150, 1999.
- [89] Xin Ning and Sergio Pellegrino. Design of lightweight structural components for direct digital manufacturing. 2012.

- [90] Lise Noël and Pierre Duysinx. Shape optimization of microstructural designs subject to local stress constraints within an xfm-level set framework. Structural and Multidisciplinary Optimization, 55(6):2323–2338, 2017.
- [91] Lise Noël, Pierre Duysinx, and Kurt Maute. Level set topology optimization considering damage. Structural and Multidisciplinary Optimization, 56(4):737–753, 2017.
- [92] Lise Noël, Laurent Van Miegroet, and Pierre Duysinx. Analytical sensitivity analysis using the extended finite element method in shape optimization of bimaterial structures. International Journal for Numerical Methods in Engineering, 107(8):669–695, 2016.
- [93] JA Norato, BK Bell, and DA Tortorelli. A geometry projection method for continuum-based topology optimization with discrete elements. Computer Methods in Applied Mechanics and Engineering, 293:306–327, 2015.
- [94] A. Nouy and A. Clément. Extended stochastic finite element method for the numerical simulation of heterogeneous materials with random material interfaces. Int. J. Numer. Meth. Engng., 83:1312–1344, 2010.
- [95] A. Nouy, F. Schoefs, and N. Moës. X-SFEM, a computational technique based on X-FEM to deal with random shapes. Eur. J. Comput. Mech., 16:277–293, 2007.
- [96] Anthony Nouy, Alexandre Clement, Franck Schoefs, and N Moës. An extended stochastic finite element method for solving stochastic partial differential equations on random domains. Computer Methods in Applied Mechanics and Engineering, 197(51):4663–4682, 2008.
- [97] Stanley Osher and Ronald Fedkiw. Implicit functions. In Level Set Methods and Dynamic Implicit Surfaces, pages 3–16. Springer, 2003.
- [98] Stanley J. Osher and J. A. Sethian. Fronts propagating with curvature dependent speed: algorithms based on Hamilton-Jacobi formulations. Journal of Computational Physics, 79(1):12–49, 1988.
- [99] J. París, F. Navarrina, I. Colominas, and M. Casteleiro. Topology optimization of continuum structures with local and global stress constraints. Structural and Multidisciplinary Optimization, 39(4):419–437, 2008.
- [100] J. París, F. Navarrina, I. Colominas, and M. Casteleiro. Block aggregation of stress constraints in topology optimization of structures. Advances in Engineering Software, 41(3):433–441, 2010.
- [101] Jamshid Parvizian, Alexander Düster, and Ernst Rank. Finite cell method. Computational Mechanics, 41(1):121–133, 2007.
- [102] Charles S Peskin. Flow patterns around heart valves: a numerical method. Journal of computational physics, 10(2):252–271, 1972.

- [103] R. Picelli, S. Townsend, C. Brampton, J Norato, and H.A. Kim. Stress-based shape and topology optimization with the level set method. Computer Methods in Applied Mechanics and Engineering, 2017.
- [104] Alfredo Pinelli, IZ Naqavi, Ugo Piomelli, and Julien Favier. Immersed-boundary methods for general finite-difference and finite-volume navier–stokes solvers. Journal of Computational Physics, 229(24):9073–9091, 2010.
- [105] Dmytro Pivovarov and Paul Steinmann. On stochastic fem based computational homogenization of magneto-active heterogeneous materials with random microstructure. Computational Mechanics, 58(6):981–1002, 2016.
- [106] Miha Polajnar, Franc Kosel, and Radovan Drazumeric. Structural optimization using global stress-deviation objective function via the level-set method. Structural and Multidisciplinary Optimization, 55(1):91–104, 2017.
- [107] Juan Jose Ródenas, Octavio Andrés González-Estrada, José Enrique Tarancón, and Francisco Jose Fuenmayor. A recovery-type error estimator for the extended finite element method based on singular+ smooth stress field splitting. International Journal for Numerical Methods in Engineering, 76(4):545–571, 2008.
- [108] George IN Rozvany. Structural design via optimality criteria: the Prager approach to structural optimization, volume 8. Springer Science & Business Media, 2012.
- [109] Henning Sauerland and Thomas-Peter Fries. The stable xfem for two-phase flows. Computers & Fluids, 87:41–49, 2013.
- [110] Dimitris Savvas, George Stefanou, Manolis Papadrakakis, and George Deodatis. Homogenization of random heterogeneous media with inclusions of arbitrary shape modeled by xfem. Computational mechanics, 54(5):1221–1235, 2014.
- [111] LA Schmit Jr. Structural synthesis 1959-1969-a decade of progress. 1971.
- [112] B Schott and WA Wall. A new face-oriented stabilized xfem approach for 2d and 3d incompressible navier–stokes equations. Computer Methods in Applied Mechanics and Engineering, 276:233–265, 2014.
- [113] Ashesh Sharma and Kurt Maute. Stress-based topology optimization using spatial gradient stabilized xfem. Structural and Multidisciplinary Optimization, pages 1–22, 2017.
- [114] Ashesh Sharma, Hernan Villanueva, and Kurt Maute. On shape sensitivities with heaviside-enriched xfem. Structural and Multidisciplinary Optimization, 55(2):385–408, 2017.
- [115] Ole Sigmund and Kurt Maute. Topology optimization approaches. Structural and Multidisciplinary Optimization, 48(6):1031–1055, 2013.

- [116] Ole Sigmund and Joakim Petersson. Numerical instabilities in topology optimization: a survey on procedures dealing with checkerboards, mesh-dependencies and local minima. Structural and Multidisciplinary Optimization, 16(1):68–75, 1998.
- [117] J. Sokolowski and A. Zochowski. Topological derivatives for elliptic problems. Inverse problems, 15:123, 1999.
- [118] Rolf Stenberg. On some techniques for approximating boundary conditions in the finite element method. Journal of Computational and Applied Mathematics, 63(1-3):139–148, 1995.
- [119] Theofanis Strouboulis, Ivo Babuška, and Kevin Copps. The design and analysis of the generalized finite element method. Computer methods in applied mechanics and engineering, 181(1):43–69, 2000.
- [120] Theofanis Strouboulis, Kevin Copps, and Ivo Babuška. The generalized finite element method. Computer methods in applied mechanics and engineering, 190(32):4081–4193, 2001.
- [121] N. Sukumar, D. Chopp, N. Moës, and T. Belytschko. Modeling holes and inclusions by level sets in the extended finite element method. Comput. Methods Appl. Mech. Eng., 190:6183–6200, 2001.
- [122] Mark Sussman, Peter Smereka, and Stanley Osher. A level set approach for computing solutions to incompressible two-phase flow. Journal of Computational physics, 114(1):146–159, 1994.
- [123] Krister Svanberg. A class of globally convergent optimization methods based on conservative convex separable approximations. SIAM journal on optimization, 12(2):555–573, 2002.
- [124] Kenjiro Terada, Mitsuteru Asai, and Michihiro Yamagishi. Finite cover method for linear and non-linear analyses of heterogeneous solids. International Journal for Numerical Methods in Engineering, 58(9):1321–1346, 2003.
- [125] Andrea Toselli and Olof B Widlund. Domain decomposition methods: algorithms and theory, volume 34. Springer, 2005.
- [126] AB Tran, Julien Yvonnet, Q-C He, C Toulemonde, and J Sanahuja. A multiple level set approach to prevent numerical artefacts in complex microstructures with nearby inclusions within XFEM. International Journal for Numerical Methods in Engineering, 85(11):1436–1459, 2011.
- [127] Laurent Van Miegroet and Pierre Duysinx. Stress concentration minimization of 2D filets using X-FEM and level set description. Structural and Multidisciplinary Optimization, 33(4-5):425–438, 2007.

- [128] Luminita A Vese and Tony F Chan. A multiphase level set framework for image segmentation using the mumford and shah model. International journal of computer vision, 50(3):271–293, 2002.
- [129] Carlos H. Villanueva and Kurt Maute. Density and level set-XFEM schemes for topology optimization of 3-D structures. Comput. Mech., 54(1):133–150, 2014.
- [130] X. Wan and G. Karniadakis. Multi-element generalized polynomial chaos for arbitrary probability measures. SIAM J. Sci. Comput., 28:901–928, 2006.
- [131] Michael Yu Wang and Xiaoming Wang. color level sets: a multi-phase method for structural topology optimization with multiple materials. Computer Methods in Applied Mechanics and Engineering, 193(6):469–496, 2004.
- [132] Michael Yu Wang, Xiaoming Wang, and Dongming Guo. A level set method for structural topology optimization. Computer methods in applied mechanics and engineering, 192(1):227–246, 2003.
- [133] P. Wei, M.Y. Wang, and X. Xing. A study on X-FEM in continuum structural optimization using a level set model. Computer-Aided Design, 42(8):708–719, 2010.
- [134] Stephen J Wright. Primal-dual interior-point methods. SIAM, 1997.
- [135] Qi-Zhi Xiao and Bhushan Lal Karihaloo. Improving the accuracy of xfem crack tip fields using higher order quadrature and statically admissible stress recovery. International Journal for Numerical Methods in Engineering, 66(9):1378–1410, 2006.
- [136] D. Xiu and G. Karniadakis. The Wiener-Askey polynomial chaos for stochastic differential equations. SIAM J. Sci. Comput., 24:619–644, 2002.
- [137] Shintaro Yamasaki, Tsuyoshi Nomura, Atsushi Kawamoto, Kazuo Sato, Kazuhiro Izui, and Shinji Nishiwaki. A level set based topology optimization method using the discretized signed distance function as the design variables. Structural and Multidisciplinary Optimization, 41(5):685–698, 2010.
- [138] Nicholas Zabaras, Baskar Ganapathysubramanian, and Lijian Tan. Modelling dendritic solidification with melt convection using the extended finite element method. Journal of Computational Physics, 218(1):200–227, 2006.
- [139] J. Zhang, W.H. Zhang, J.H. Zhu, and L. Xia. Integrated layout design of multi-component systems using XFEM and analytical sensitivity analysis. Computer Methods in Applied Mechanics and Engineering, 245-246(15):75–89, 2012.
- [140] Shanglong Zhang, Arun L Gain, and Julián A Norato. Stress-based topology optimization with discrete geometric components. Computer Methods in Applied Mechanics and Engineering, 325:1–21, 2017.

- [141] Shanglong Zhang, Julián A Norato, Arun L Gain, and Naesung Lyu. A geometry projection method for the topology optimization of plate structures. Structural and Multidisciplinary Optimization, 54(5):1173–1190, 2016.
- [142] Weisheng Zhang, Dong Li, Jie Yuan, Junfu Song, and Xu Guo. A new three-dimensional topology optimization method based on moving morphable components (mmcs). Computational Mechanics, 59(4):647–665, 2017.
- [143] Weisheng Zhang, Dong Li, Jian Zhang, and Xu Guo. Minimum length scale control in structural topology optimization based on the moving morphable components (mmc) approach. Computer Methods in Applied Mechanics and Engineering, 311:327–355, 2016.
- [144] Weisheng Zhang, Jie Yuan, Jian Zhang, and Xu Guo. A new topology optimization approach based on moving morphable components (mmc) and the ersatz material model. Structural and Multidisciplinary Optimization, 53(6):1243–1260, 2016.
- [145] Weisheng Zhang, Jianhua Zhou, Yichao Zhu, and Xu Guo. Structural complexity control in topology optimization via moving morphable component (mmc) approach. Structural and Multidisciplinary Optimization, 56(3):535–552, 2017.
- [146] Benliang Zhu, Xianmin Zhang, and Sergej Fatikow. Structural topology and shape optimization using a level set method with distance-suppression scheme. Computer Methods in Applied Mechanics and Engineering, 283:1214–1239, 2015.
- [147] Olgierd Cecil Zienkiewicz and Jian Zhong Zhu. The superconvergent patch recovery and a posteriori error estimates. part 1: The recovery technique. International Journal for Numerical Methods in Engineering, 33(7):1331–1364, 1992.
- [148] T. I. Zohdi. Modeling and simulation of cooling-induced residual stresses in heated particulate mixture depositions in additive manufacturing. Computational Mechanics, 56(4):613–630, 2015.
- [149] Kong-Tian Zuo, Li-Ping Chen, Yun-Qing Zhang, and Jingzhou Yang. Study of key algorithms in topology optimization. The International Journal of Advanced Manufacturing Technology, 32(7-8):787–796, 2007.

Appendix A

Publication 1: Heaviside enriched extended stochastic FEM for problems with uncertain material interfaces [71]



Heaviside enriched extended stochastic FEM for problems with uncertain material interfaces

Christopher Lang¹ · Ashesh Sharma² · Alireza Doostan² · Kurt Maute²

Received: 23 April 2015 / Accepted: 21 August 2015 / Published online: 5 September 2015
© Springer-Verlag Berlin Heidelberg 2015

Abstract This paper is concerned with the modeling of heterogeneous materials with uncertain inclusion geometry. The eXtended stochastic finite element method (X-SFEM) is a recently proposed approach for modeling stochastic partial differential equations defined on random domains. The X-SFEM combines the deterministic eXtended finite element method (XFEM) with a polynomial chaos expansion (PCE) in the stochastic domain. The X-SFEM has been studied for random inclusion problems with a C^0 -continuous solution at the inclusion interface. This work proposes a new formulation of the X-SFEM using the Heaviside enrichment for modeling problems with either continuous or discontinuous solutions at the uncertain inclusion interface. The Heaviside enrichment formulation employs multiple enrichment levels for each material subdomain which allows more complex inclusion geometry to be accurately modeled. A PCE is applied in the stochastic domain, and a random level set function implicitly defines the uncertain interface geometry. The Heaviside enrichment leads to a discontinuous solution in the spatial and stochastic domains. Adjusting the support of the stochastic approximation according to the active stochastic subdomain for each degree of freedom is proposed. Numerical examples for heat diffusion and linear elasticity are studied to illustrate convergence and accuracy of the scheme under spatial and stochastic refinements. In addition to problems with discontinuous solutions, the Heaviside enrichment is applicable to problems with C^0 -continuous solutions by enforcing continuity at the interface. A higher

convergence rate is achieved using the proposed Heaviside enriched X-SFEM for C^0 -continuous problems when compared to using a C^0 -continuous enrichment.

Keywords X-SFEM · Level set method · Heaviside enrichment · Polynomial chaos · Uncertainty quantification

1 Introduction

Computational methods for the propagation of uncertainties through models governed by partial differential equations are powerful tools for the prediction of a system's response, model validation, and engineering design. For heterogeneous composite materials, the material layout has uncertainty due to fabrication techniques. In order to relate the effective properties to the material layout, the uncertainty in geometry requires methods that account for the random material interfaces. This work proposes an approach to model problems with either a weak or a strong discontinuity across a random material interface. Examples from the first class of problems include perfectly bonded interfaces, while examples from the latter class of problems include imperfectly bonded interfaces, crack analysis, and the phonon Boltzmann transport model for heat diffusion at the submicron scale. The proposed approach introduces the Heaviside enrichment function in the eXtended stochastic finite element method (X-SFEM) [12], which extends the eXtended finite element method (XFEM) [10] to the stochastic domain using a polynomial chaos expansion (PCE) [25] to approximate the degrees of freedom based on the random parameters characterizing the interface position.

Following the work by Hansbo and Hansbo [4], the Heaviside enriched XFEM is a deterministic approach for solving problems with strong discontinuities across an embedded

✉ Alireza Doostan
doostan@colorado.edu

¹ Structural Mechanics and Concepts Branch, NASA Langley Research Center, Hampton, VA, USA

² Aerospace Engineering Sciences, University of Colorado, Boulder, CO, USA

interface without requiring a mesh which conforms to the interface geometry. The Heaviside enrichment strategy is also applicable to problems with a weak discontinuity across the material interface but requires the enforcement of the continuity of the solution by an interface constraint method such as the stabilized Lagrange multiplier and Nitsche methods [5, 18]. The XFEM formulation in this work implements multiple enrichment levels to consistently approximate the solution in all disconnected regions of the same phase [8, 21]. The use of additional enrichment levels accurately models neighboring intersected elements as well as elements intersected more than once. This implementation of the XFEM is particularly useful for modeling problems with a varying interface geometry, as mesh regeneration is avoided and robustness is added for more complex interface configurations.

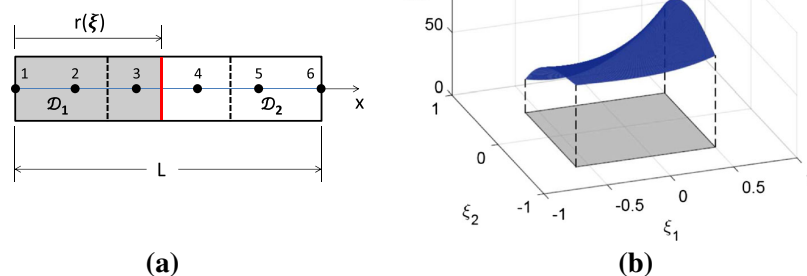
A Monte Carlo (MC) simulation combined with the XFEM may be utilized to solve the stochastic problem. In Savvas et al. [14], the homogenization of random media with varying inclusion geometry is studied using the XFEM coupled with MC simulation. While the XFEM avoids remeshing for each realization of the inclusion geometry, numerous XFEM analyses may be required for sampling the varying inclusion geometry. An alternative is the X-SFEM [11], which requires a single solution of a larger system of equations. The X-SFEM was recently introduced for modeling problems with C^0 -continuous solutions at random material interfaces. The spatial domain is discretized by the XFEM and extended to the stochastic domain by a PCE based on the random parameters characterizing the uncertain interface geometry. The dimension of the stochastic domain is determined by the finite set of random parameters chosen to characterize the interface geometry. Each spatial degree of freedom is approximated in the stochastic space using a PCE, and a Galerkin projection leads to a finite system of equations to be solved for the expansion coefficients. The Wiener-Askey PCE [25] defines polynomial sets which are orthogonal with respect to the probability density function of the random parameters. The application of PCE may lead to exponential convergence rates if the degrees of freedom vary smoothly with

respect to the random parameters. However, for non-smooth behavior of the degrees of freedom in the stochastic domain, the PCE may converge slowly or fail to converge. The X-SFEM was studied for problems with C^0 -continuous solutions at the random material interface with various enrichment functions in [6]. This work proposes a new formulation of the X-SFEM in order to solve problems with either a weakly or strongly discontinuous solution at the random material interface using the Heaviside enrichment function.

Building on the work in [6, 9], a method for extending the Heaviside enriched XFEM to the stochastic domain using a PCE is proposed. A random level set function is utilized to implicitly define the interface position, which depends on a set of random parameters. The Heaviside enrichment allows modeling of weak and strong discontinuities across the material interface, and leads to degrees of freedom that are discontinuous in the stochastic domain. Here a degree of freedom refers to an unknown in the XFEM discretization. Each degree of freedom is a function of the random inputs and is approximated by a PCE in the stochastic domain. The discontinuous behavior in the stochastic domain results from each degree of freedom being nonzero for only a portion of the stochastic domain. To illustrate this discontinuous behavior, consider the bimaterial bar example in Fig. 1a. The two material subdomains are given as \mathcal{D}_1 and \mathcal{D}_2 , and the uncertain interface location is defined by $r(\xi)$ where ξ is a vector of random parameters. Each degree of freedom is nonzero (active) over part of the stochastic subdomain depending on the variation of the interface. An example of a degree of freedom (*dof*) variation for 2 random parameters is shown in Fig. 1b in which the active subdomain is a rectangle in the stochastic domain.

The X-SFEM generally uses a set of polynomial basis defined globally over the stochastic space for the approximation of the spatial degrees of freedom. Due to the non-smooth behavior and possibly local behavior of the degrees of freedom in the stochastic domain, such a global basis is not well suited. This work proposes adjusting the support of the PCE basis functions for the approximation of each spatial

Fig. 1 **a** Bar example with an uncertain interface. **b** An active stochastic subdomain for 2 random parameters



degree of freedom. The support of the PCE basis functions are adjusted to match the active stochastic subdomain, e.g., the gray region in the ξ_1 - ξ_2 plane in Fig. 1b. The adjustment of the PCE basis functions depends on the characterization of the interface geometry and is determined by the spatial mesh as well as the random level set function. Adjusting the support of the PCE basis functions increases accuracy, and the system remains well-conditioned for higher approximation orders of the PCE.

The focus of this study is on discontinuous and C^0 -continuous example problems in heat diffusion and linear elasticity. While the proposed method is designed to solve problems with a strong discontinuity, C^0 -continuous problems are included in order to compare the performance of the proposed approach with existing methods. The remainder of the paper is organized as follows: Sect. 2 defines the model problem and random level set function. The Heaviside enriched XFEM is presented in Sect. 3. The extension of the XFEM to the stochastic domain is described in Sect. 4. Four numerical examples are presented in Sect. 5 to describe and examine the performance of the proposed method.

2 Model problems

The proposed X-SFEM approach is illustrated with the model problem depicted in Fig. 2 for heat diffusion and linear elasticity. The model problem contains an inclusion embedded in a matrix, and the geometry of the inclusion is uncertain. While the model problem consists of a material with a single random inclusion for simplicity, the proposed method is applicable to multiple inclusions. The level set method is used to define the random interface geometry. This section describes the setup and the governing equations for the model problem.

2.1 Domain description

The governing equations are solved over the spatial domain $\mathcal{D} \subset \mathbb{R}^n$, and the probability space is denoted by (Σ, \mathcal{B}, P) .

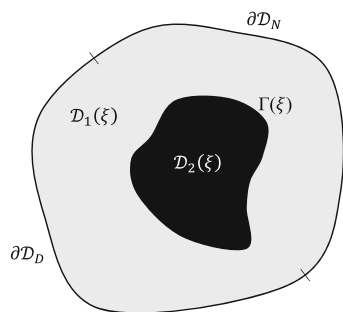


Fig. 2 Schematic of the model problem with a single random inclusion

Here, Σ is the set of elementary events, \mathcal{B} is the σ -algebra of events, and P is the probability measure. The random inclusion geometry is characterized by a finite set of random parameters, $\xi : \Sigma \rightarrow \Omega \subseteq \mathbb{R}^d$. The spatial domain is comprised of two non-overlapping material subdomains, such that $\mathcal{D} = \mathcal{D}_1(\xi) \cup \mathcal{D}_2(\xi)$. The material interface has zero thickness and is defined as $\Gamma(\xi) = \mathcal{D}_1(\xi) \cap \mathcal{D}_2(\xi)$. The boundary of \mathcal{D} is comprised of a Dirichlet boundary, $\partial\mathcal{D}_D$, and a Neumann boundary, $\partial\mathcal{D}_N$.

2.2 Random level set

The level set method [15] is used to implicitly define the random interface geometry. This approach is frequently used in the XFEM to define geometric features [2, 19, 20, 23]. A random level set function is introduced to define the random interface geometry for the model problem. The random interface location, $\Gamma(\xi)$, is defined by the zero contour of a random level set function $\phi(\mathbf{x}, \xi) : \mathcal{D} \times \Omega \rightarrow \mathcal{R}$. The properties of $\phi(\mathbf{x}, \xi)$ are given by

$$\begin{aligned} \phi(\mathbf{x}, \xi) &< 0 && \text{if } \mathbf{x} \in \mathcal{D}_1(\xi) \\ \phi(\mathbf{x}, \xi) &> 0 && \text{if } \mathbf{x} \in \mathcal{D}_2(\xi) \\ \phi(\mathbf{x}, \xi) &= 0 && \text{if } \mathbf{x} \in \Gamma(\xi). \end{aligned} \quad (1)$$

Consider a finite element mesh, \mathcal{T}_h , for \mathcal{D} consisting of elements with edges that do not necessarily coincide with Γ . The random level set function is discretized according to \mathcal{T}_h ,

$$\phi(\mathbf{x}, \xi) = \sum_{i \in I} M_i(\mathbf{x}) \phi_i(\xi), \quad (2)$$

where $M_i(\mathbf{x})$ are the nodal basis functions, I is the set of all nodes in the mesh, and $\phi_i(\xi)$ is the value of the random level set function at node i . For this work, the basis functions used to interpolate the level set function, $M_i(\mathbf{x})$, are the same as the basis functions used to interpolate the solution, $N_i(\mathbf{x})$, introduced in Sect. 3.2.

In this work, the characterization of the random interface geometry is assumed to be known. For realistic problems, the random interface characterization often requires a collection of measurement data for numerous outcomes of the interface geometry [16, 17]. The measurement data may be collected from various experimental approaches, such as optical images and micrographs. The approach used in this work to define the random level set function is by computing $\phi_i(\xi)$ as realizations of the interface geometry. An example of this approach uses the signed distance function, defined as

$$\phi(\mathbf{x}_i, \xi) = \pm \min \|\mathbf{x}_i - \mathbf{x}_\Gamma(\xi)\| \quad (3)$$

where $\mathbf{x}_\Gamma(\xi)$ is the interface location, \mathbf{x}_i is the spatial coordinate at node i , and $\|\cdot\|$ denotes the L^2 -distance. With

this approach, the random level set function is constructed by defining the interface location as a function of ξ . Another example of defining the random level set function is discussed in Sect. 5.4.

2.3 Heat diffusion with random geometry

The stationary heat diffusion equation is solved for a single inclusion with random interface geometry. The model heat diffusion problem consists of finding the random temperature field, $u(\mathbf{x}, \xi)$, such that the following holds almost surely in Ω for phase $i = 1, 2$,

$$\begin{aligned} -\nabla \cdot (k \nabla u_i) &= f & \text{in } \mathcal{D}_i(\xi) \\ (k \nabla u_i) \cdot \mathbf{n}_i &= q_T & \text{on } \partial \mathcal{D}_i \cap \partial \mathcal{D}_N \\ u_i &= u_T & \text{on } \partial \mathcal{D}_i \cap \partial \mathcal{D}_D, \end{aligned} \quad (4)$$

where k is the thermal conductivity of an isotropic material, f is the volumetric heat source, and u_i denotes the restriction of u to \mathcal{D}_i . A temperature u_T is specified on $\partial \mathcal{D}_D$, and a heat flux q_T is specified on $\partial \mathcal{D}_N$ with an outward unit normal to \mathcal{D}_i denoted by \mathbf{n}_i . The conductivity is defined as

$$k(\mathbf{x}, \xi) = \begin{cases} 0 < k_{\min} < k_1 < k_{\max} < \infty & \text{if } \mathbf{x} \in \mathcal{D}_1(\xi) \\ 0 < k_{\min} < k_2 < k_{\max} < \infty & \text{if } \mathbf{x} \in \mathcal{D}_2(\xi) \end{cases}, \quad (5)$$

with constants k_1 and k_2 . For well-posedness, k_1 and k_2 are bounded by a minimum and maximum value. A thermal resistance is assumed to exist at the interface, which may be due to imperfect contact or a thin coating, leading to a discontinuous solution. The flux at the interface for the discontinuous solution is defined as

$$\begin{aligned} q_1 &= \alpha(u_1 - u_2) & \text{on } \Gamma^-(\xi) \\ q_2 &= -\alpha(u_1 - u_2) & \text{on } \Gamma^+(\xi), \end{aligned} \quad (6)$$

where q_1 and q_2 are the heat flux at the interface in the phase 1 and phase 2 domains, respectively, and α is the unit thermal conductance at the interface. The phase 1 side of the interface is denoted by Γ^- , and the phase 2 side of the interface is denoted by Γ^+ . For imperfect contact, α represents the conductivity across the interface with $\alpha = 0$ representing no conduction. For a thin layer, $\alpha = k_\Gamma/t_\Gamma$, where k_Γ and t_Γ are the conductivity and thickness of the interface layer. The solution is C^0 -continuous for perfect thermal contact at the interface. In this case, continuity of the solution and flux across the random interface is enforced by the following interface conditions:

$$\begin{aligned} \llbracket u \rrbracket &= u_1 - u_2 = 0 & \text{on } \Gamma(\xi) \\ k_1 \nabla u_1 \cdot \mathbf{n}_1 + k_2 \nabla u_2 \cdot \mathbf{n}_2 &= 0 & \text{on } \Gamma(\xi). \end{aligned} \quad (7)$$

2.4 Linear elasticity with random geometry

The model linear elasticity problem consists of finding the random displacement field, $\mathbf{u}(\mathbf{x}, \xi)$, such that the following holds almost surely in Ω for $i = 1, 2$,

$$\begin{aligned} -\nabla \cdot (\boldsymbol{\sigma}_i) &= \mathbf{b} & \text{in } \mathcal{D}_i(\xi) \\ \boldsymbol{\sigma}_i \cdot \mathbf{n}_i &= \mathbf{t}_d & \text{on } \partial \mathcal{D}_i \cap \partial \mathcal{D}_N \\ \mathbf{u}_i &= \mathbf{u}_d & \text{on } \partial \mathcal{D}_i \cap \partial \mathcal{D}_D \end{aligned} \quad (8)$$

where $\boldsymbol{\sigma}_i$ is the stress tensor and \mathbf{u}_i is the displacement solution restricted to \mathcal{D}_i . The applied body forces are denoted by \mathbf{b} , and prescribed displacements \mathbf{u}_d and tractions \mathbf{t}_d are imposed on $\partial \mathcal{D}_D$ and $\partial \mathcal{D}_N$, respectively. The constitutive relation for a linear elastic material is defined as

$$\boldsymbol{\sigma}_i = \mathbf{C}_i : \boldsymbol{\varepsilon}(\mathbf{u}_i) \quad \text{in } \mathcal{D}_i(\xi), \quad (9)$$

where \mathbf{C}_i is the elasticity tensor and $\boldsymbol{\varepsilon}$ is the strain tensor. Assuming small strains and displacements, the kinematics model is defined as

$$\boldsymbol{\varepsilon} = \frac{1}{2}(\nabla \mathbf{u}_i + \nabla \mathbf{u}_i^T). \quad (10)$$

A crack or other imperfect bond at the interface leads to a discontinuous displacement. Zero traction at the crack interface is assumed, defined as

$$\begin{aligned} \boldsymbol{\sigma}_1 \mathbf{n}_1 &= \mathbf{0} & \text{on } \Gamma^-(\xi) \\ \boldsymbol{\sigma}_2 \mathbf{n}_2 &= \mathbf{0} & \text{on } \Gamma^+(\xi). \end{aligned} \quad (11)$$

For a perfect bond at the interface, which gives a C^0 -continuous solution, continuity of the displacement and normal stress across the random interface require

$$\begin{aligned} \llbracket \mathbf{u} \rrbracket &= \mathbf{u}_1 - \mathbf{u}_2 = \mathbf{0} & \text{on } \Gamma(\xi) \\ \boldsymbol{\sigma}_1 \mathbf{n}_1 + \boldsymbol{\sigma}_2 \mathbf{n}_2 &= \mathbf{0} & \text{on } \Gamma(\xi). \end{aligned} \quad (12)$$

3 Heaviside enriched X-FEM

The XFEM [10, 19] uses an enrichment function to locally capture the non-smooth solution at the interface without requiring a mesh which conforms to Γ . Following the work by Hansbo and Hansbo [4] and Terada [21], a generalized Heaviside enrichment strategy is adopted which employs multiple enrichment levels [7–9]. The generalized Heaviside enrichment provides great flexibility in solving a broad range of partial differential equations with multiple phases for any choice of nodal basis functions. An advantage to using the Heaviside enrichment is that there are no issues with blending elements, which may exist for C^0 -continuous

enrichments. Also, neighboring intersected elements and elements intersected more than once can be modeled accurately using the generalized Heaviside enrichment strategy. This section defines the weak form of the governing Eqs. (4)–(8) and the generalized Heaviside enrichment approach for solving the deterministic forms of the model problem.

3.1 Weak form

The weak form of the governing equations for heat diffusion and linear elasticity are constructed by multiplying (4) and (8) by a set of admissible test functions and integrating over \mathcal{D} . The space $V = H^1(\mathcal{D})$ is the Hilbert space consisting of scalar functions with square integrable first derivatives and $V_0 = \{v \in V : v|_{\partial\mathcal{D}_D} = 0\}$. Let $u \in V$ be the solution and $v \in V_0$ be an admissible test function. The weak form of the deterministic heat diffusion problem is stated as: Find $u \in V$ such that $u = u_t$ on $\partial\mathcal{D}_D$ and

$$\int_{\mathcal{D}} (\kappa \nabla u) \cdot \nabla v dx - \int_{\mathcal{D}} f v dx - \int_{\partial\mathcal{D}_N} q_t v ds + R_\Gamma = 0 \quad \forall v \in V_0, \tag{13}$$

where s denotes the boundary of \mathcal{D} and R_Γ includes the interface conditions from either (6) or (7) depending on whether the solution is discontinuous or continuous across the interface. For the discontinuous problem in which a thermal resistance exists at the interface,

$$R_\Gamma = \int_{\Gamma^-} q_1 v_1 d\Gamma - \int_{\Gamma^+} q_2 v_2 d\Gamma, \tag{14}$$

where v_i denotes the restriction of v to \mathcal{D}_i for phase $i = 1, 2$, and the fluxes q_1 and q_2 are defined in (6). For a C^0 -continuous solution at the interface, an interface constraint method [1, 5, 18] is used to enforce the solution continuity across the interface. Two common constraint formulations for enforcing continuity across material interfaces are the stabilized Lagrange and Nitsche methods, which are defined in [7, 8] for application to heat diffusion and linear elasticity.

The space $W = H^1(\mathcal{D})$ is the Hilbert space consisting of vector functions with square integrable first derivatives and $W_0 = \{\mathbf{w} \in W : \mathbf{w}|_{\partial\mathcal{D}_D} = 0\}$. Let $\mathbf{u} \in W$ be the displacement and $\mathbf{w} \in W_0$ be an admissible test function. The weak form of the deterministic elasticity problem is stated as: Find $\mathbf{u} \in W$ such that $\mathbf{u} = \mathbf{u}_d$ on $\partial\mathcal{D}_D$ and

$$\int_{\mathcal{D}} \boldsymbol{\sigma} : \boldsymbol{\varepsilon}(\mathbf{w}) dx - \int_{\mathcal{D}} \mathbf{b} \cdot \mathbf{w} dx - \int_{\partial\mathcal{D}_N} \mathbf{t}_d \cdot \mathbf{w} ds + R_\Gamma = 0 \quad \forall \mathbf{w} \in W_0, \tag{15}$$

where R_Γ includes the interface conditions from (11) or (12) for problems with a discontinuous or continuous solution

across the interface, respectively. For discontinuous problems with a zero traction at the interface,

$$R_\Gamma = 0. \tag{16}$$

For C^0 -continuous problems in which a perfect bond exists at the interface, the stabilized Lagrange and Nitsche methods can be used to enforce solution continuity at the interface [7, 8].

3.2 Approximation

The finite element mesh for \mathcal{D} , \mathcal{T}_h , consists of elements with edges that do not necessarily coincide with Γ . For a two phase problem with one level set function, an intersected element has a region corresponding to each of the two phases. The support of a nodal basis function includes multiple elements. If the support of a nodal basis function is intersected by the interface, there may be regions of the same phase which are not connected. A Heaviside enrichment function is implemented in the XFEM formulation, such that each disconnected region of the same phase is approximated by an independent set of nodal basis functions. The space V and W are comprised of the spaces for all disconnected regions and written as $V = \{v : v_i \in H^1(\mathcal{D})\}$ and $W = \{\mathbf{w} : \mathbf{w}_i \in H^1(\mathcal{D})\}$. Here, the subscript i represents the set of disconnected regions for each phase. The approximation of $u(\mathbf{x})$, denoted by $u^h(\mathbf{x})$, for two phases is defined as

$$u^h(\mathbf{x}) = \sum_{m=1}^M \left(H(-\phi(\mathbf{x})) \sum_{i \in I} N_i(\mathbf{x}) u_{i,m}^{(1)} \delta_{mr}^{(1),i} + H(\phi(\mathbf{x})) \sum_{i \in I} N_i(\mathbf{x}) u_{i,m}^{(2)} \delta_{mr}^{(2),i} \right), \tag{17}$$

where I is the set of all nodes in \mathcal{T}_h , $N_i(\mathbf{x})$ is the nodal basis function, M is the maximum number of enrichment levels, and $u_{i,m}^{(q)}$ is the degree of freedom at node i for phase $q \in \{1, 2\}$. The Kronecker delta $\delta_{mr}^{(q),i}$ selects the active enrichment level r for node i and phase q such that only one set of degrees of freedom are used for interpolating the solution at the point \mathbf{x} , therefore satisfying the partition of unity principle. The Heaviside function is given by

$$H(z) = \begin{cases} 1 & z > 0 \\ 0 & z \leq 0 \end{cases}. \tag{18}$$

In this formulation, a single basis function, $N_i(\mathbf{x})$, is used at each node. Additional nodal degrees of freedom are added for each phase and enrichment level. Although (17) is written using the maximum possible number of enrichment levels, the specific number of enrichment levels at each node is determined by the spatial mesh and *a priori* knowledge of the



interface location. The number of enrichment levels required depends on the number of disconnected regions of the same phase included in the support of $N_i(\mathbf{x})$. A key advantage of employing multiple enrichment levels using the Heaviside enrichment is that accurate solutions can be determined for neighboring intersected elements and elements intersected more than once using a single level set function, adding robustness for problems involving moving or changing interface geometry. Further details of this enrichment strategy are provided in [7,8].

4 Extended stochastic FEM

The extended stochastic FEM (X-SFEM) [13] extends the XFEM to a stochastic framework using a PCE to model problems defined on random domains. The X-SFEM for C^0 -continuous problems with random inclusions was introduced in [11]. The X-SFEM was studied for heat diffusion with a single random inclusion [6], specifically focusing on the accuracy and the smoothness of the degrees of freedom as a function of the random variables using various C^0 -continuous enrichment functions. Requirements for a successful enrichment function were presented as well as a partitioning strategy for accurate integration in the probability domain. Here, the X-SFEM is studied for both continuous and discontinuous problems with random inclusions by extending the Heaviside enriched formulation described in Sect. 3 to the stochastic domain using a PCE. The PCE approximates the variation of the spatial degrees of freedom with respect to the random parameters ξ . In this work, a degree of freedom refers to the unknowns in the XFEM system of equations, and stochastic or expansion coefficients refer to the unknowns in the X-SFEM system of equations as described in Sect. 4.3. A PCE with global basis is well suited for a C^0 -continuous enrichment function when the variation of the degrees of freedom is smooth and defined over the entire stochastic domain. However, a PCE with global basis is not well suited when using the Heaviside enrichment function in the X-SFEM. For the Heaviside enrichment, each degree of freedom is discontinuous as it is defined only on a subdomain of Ω . This subdomain is referred to as the active stochastic subdomain. Instead of a PCE with global support in the stochastic domain, adjusting the support of the PCE basis functions to account for the variation in the active stochastic subdomains is proposed. This section defines the active stochastic subdomains, adjustment of the PCE basis functions, and construction of the system of equations.

4.1 Active stochastic subdomains

The active stochastic subdomain for each degree of freedom, denoted as $\Omega_{i,m}^{(q)} \subseteq \Omega$, defines the stochastic subdomain

where the degree of freedom $u_{i,m}^{(q)}$ is nonzero. The active stochastic subdomain for each degree of freedom is determined by the intersection of $\phi(\xi) = 0$ and the support of the nodal basis function in the XFEM approximation. For the linear basis functions used in this work, $\phi_j(\xi) = 0$ is computed for the nodes of the elements sharing node i to determine the active stochastic subdomains. Each degree of freedom at node i is active for one or more regions created by $\phi_j(\xi) = 0$. Typically, each degree of freedom is active over a single connected subdomain. However, a degree of freedom may be active over disconnected regions depending on the discretization. In this case, additional enrichment levels are added such that each degree of freedom is active over a single connected subdomain.

The variation of the degrees of freedom is smooth over the active stochastic subdomain for which a polynomial approximation is well suited. As will be described, a PCE is constructed on the active stochastic subdomain using polynomial functions. For $d = 1$ and when $\xi : \Omega \rightarrow [-1, 1]$, $\Omega_{i,m}^{(q)}$ is defined by the interval $[a, b] \subseteq [-1, 1]$. For $d > 1$, the active stochastic subdomain is approximated by a hyperrectangle, $\hat{\Omega}_{i,m}^{(q)}$, and the product of one-dimensional polynomials are used to construct the PCE on $\hat{\Omega}_{i,m}^{(q)}$. A minimum bounding rectangle approximates the active stochastic subdomain, such that $\hat{\Omega}_{i,m}^{(q)} = [a_j, b_j] \subseteq [-1, 1]^d$ where $j = 1, \dots, d$. For $d = 1$, $\hat{\Omega}_{i,m}^{(q)} = \Omega_{i,m}^{(q)}$. An example illustration of an approximate active stochastic subdomain for $d = 1$ and $d = 2$ is depicted in Fig. 3a and b. As discussed in the next section, a rotated $\hat{\Omega}_{i,m}^{(q)}$ may be required to closely approximate the area of the active stochastic subdomain, which is depicted in Fig. 3c.

The simple bar example of Fig. 1 is used to illustrate the active stochastic subdomains for $d = 1$. The bar has

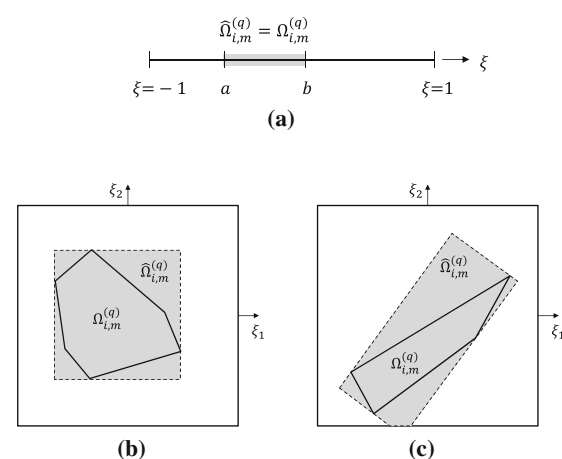


Fig. 3 Active stochastic subdomain for a $d = 1$, b $d = 2$, and c rotated in $d = 2$

length $L = 1$ and is modeled using 5 elements. Let the interface position depend on one random parameter $r = 0.2\xi + 0.5$, where ξ is distributed uniformly over $[-1, 1]$, i.e., $\xi \sim U[-1, 1]$. The random level set function is given as $\phi(\xi) = x - r(\xi)$. The active stochastic subdomain for the degree of freedom interpolating the phase 2 solution at node 3, denoted $\Omega_{3,1}^{(2)}$, is defined by the interval $[-1, 0.5]$, and $\Omega_{4,1}^{(1)}$ is defined by the interval $[-0.5, 1]$. The intersection points $\xi = 0.5$ and $\xi = -0.5$ are computed from $\phi_4(\xi) = 0$ and $\phi_3(\xi) = 0$, respectively. Note that the other two active stochastic subdomains for nodes 3 and 4, $\Omega_{3,1}^{(1)}$ and $\Omega_{4,1}^{(2)}$ are defined by the interval $[-1, 1]$. The example in Sect. 5.1 further illustrates the active subdomains for $d = 1$ and depicts the variation of the degrees of freedom.

4.2 Approximation

In the X-SFEM, the Heaviside enrichment function and the degrees of freedom in (17) are functions of the random variables ξ . For the Heaviside enriched formulation, the X-SFEM approximation of $u(x, \xi)$ is defined as

$$u^h(x, \xi) = \sum_{m=1}^M \left(H(-\phi(x, \xi)) \sum_{i \in I} N_i(x) u_{i,m}^{(1)}(\xi) \delta_{mr}^{(1),i} I_{i,m}^{(1)}(\xi) + H(\phi(x, \xi)) \sum_{i \in I} N_i(x) u_{i,m}^{(2)}(\xi) \delta_{mr}^{(2),i} I_{i,m}^{(2)}(\xi) \right), \quad (19)$$

where the indicator function I restricts the approximation of each degree of freedom $u_{i,m}^{(q)}(\xi)$ to the active stochastic subdomain $\hat{\Omega}_{i,m}^{(q)}$. The active enrichment level is denoted by r in $\delta_{mr}^{(q),i}$ and depends on ξ . The indicator function is defined as

$$I_{i,m}^{(q)}(\xi) = \begin{cases} 1 & \text{if } \xi \in \hat{\Omega}_{i,m}^{(q)} \\ 0 & \text{otherwise} \end{cases}. \quad (20)$$

Each degree of freedom, $u_{i,m}^{(q)}(\xi)$, is approximated in the stochastic space using a PCE of order p . A compact notation is introduced to define the set of degrees of freedom as $u_n(\xi)$, where n is an index to the set $\{i, m, q\}$ which consists of all nodes, enrichment levels, and phases. The stochastic approximation for a degree of freedom is defined by

$$u_n(\xi) = \sum_{j=1}^{M_{PC}} L_j^n(\xi) a_j^n, \quad (21)$$

where a_j^n are the stochastic coefficients to be determined and L_j^n are polynomials defined on $\hat{\Omega}^n$. For random variables with the independent uniform distributions considered in this work, multi-dimensional Legendre polynomials form

an orthogonal basis with respect to the uniform measure, such that

$$\langle L_i, L_j \rangle = \int_{[-1,1]^d} L_i(\xi) L_j(\xi) P(\xi) d\xi = \langle L_i^2 \rangle \delta_{ij}, \quad (22)$$

where δ_{ij} denotes the Kronecker delta and $\langle \cdot \rangle$ denotes the mathematical expectation operator. The uniform measure is given as $P(\xi) = (\frac{1}{2})^d I_{[-1,1]^d}$, where $I_{[-1,1]^d}$ is the indicator set of the hypercube $[-1, 1]^d$ with d random variables. The Legendre polynomials in (22) are the standard basis defined on Ω . The polynomials L_j^n in the PCE (21) are defined on $\hat{\Omega}^n$, and are constructed by transforming the standard Legendre polynomials. While random variables with uniform distributions are considered in this work, local orthogonal polynomial bases for other distributions may be constructed numerically [22].

The proposed approach to construct L_j^n follows the multi-element generalized PCE [22], in which a single element in Ω is defined by $\hat{\Omega}^n$. The stochastic approximation is restricted to a single element to minimize the number of expansion coefficients to be determined by the system of equations. The L_j are scaled by a linear transformation from Ω to $\hat{\Omega}^n$ and normalized to construct L_j^n . The uniform random parameter ξ is defined on $[-1, 1]$, and $\tilde{\xi}$ is a uniform random parameter defined on $[a, b]$. For $d = 1$, constructing the L_j^n on the active stochastic subdomain uses the linear transformation

$$\tilde{\xi}_i = \frac{b_i - a_i}{2} \xi_i + \frac{b_i + a_i}{2} \quad \text{for } i = 1, \dots, d. \quad (23)$$

Since $\langle L_i, L_j \rangle = \frac{1}{2i+1} \delta_{ij}$, the normalization constant is given as $\sqrt{2i+1}$. The transformed and normalized polynomials are defined on $\hat{\Omega}^n$ by

$$L_j^n(\tilde{\xi}) = \sqrt{2j+1} L_j(\xi(\tilde{\xi})), \quad (24)$$

and the L_j^n are zero outside of $\hat{\Omega}^n$. For $d > 1$, the multi-dimensional set of polynomials is constructed by the tensor product of one-dimensional polynomials with total order up to p [24]. The number of stochastic coefficients required in (21) is defined as

$$M_{PC} = \frac{(p+d)!}{p!d!}. \quad (25)$$

A comparison of the one-dimensional Legendre polynomials on $[-1, 1]$ and the transformed and normalized Legendre polynomials on $[a, b] = [-0.75, 0]$ is shown in Fig. 4 for $p = 3$. The transformed basis, L_j^n , is computed for each degree of freedom and avoids poorly conditioned systems resulting from small active stochastic subdomains.

Additionally for $d > 1$, the minimum bounding hyperrectangle and the active stochastic subdomain should have

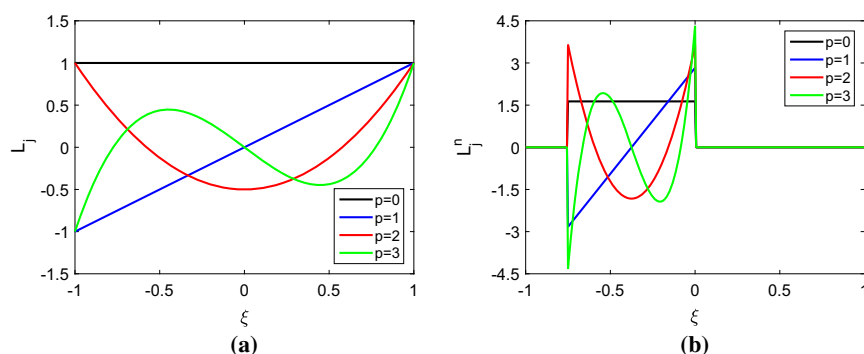


Fig. 4 **a** Legendre polynomials on $[-1, 1]$, and **b** transformed and normalized Legendre polynomials on $[-0.75, 0]$

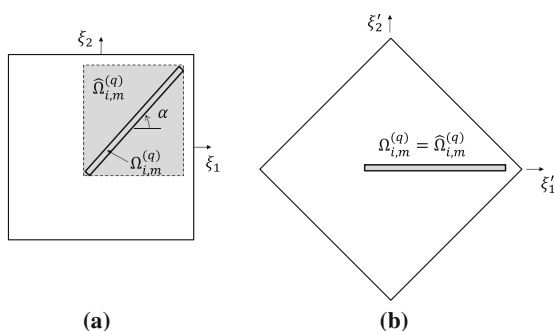


Fig. 5 **a** Example sliver configuration of an active stochastic subdomain for $d = 2$, and **b** the rotated coordinate system for defining the minimum bounding rectangle

similar volumes. Otherwise an ill-conditioned system may result. Here, the focus is on $d = 2$, in which a minimum bounding rectangle is defined for the active stochastic subdomain. If the active stochastic subdomain for $d = 2$ is a sliver, as depicted in Fig. 5a, the area of the minimum bounding rectangle does not closely match the area of the active stochastic subdomain. A rotated coordinate system is required in order for the bounding rectangle to closely approximate the active stochastic subdomain. The rotation for $d = 2$ is defined by the angle α , and the rotated coordinate system is $\xi' = T\xi$. With α specified as the angle from the positive ξ_1 axis to the longest bounding box edge, the rotation to the reference coordinate system is defined as

$$T = \begin{bmatrix} \cos(-\alpha) & -\sin(-\alpha) \\ \sin(-\alpha) & \cos(-\alpha) \end{bmatrix}. \tag{26}$$

The rotated coordinate system for the example sliver configuration is shown in Fig. 5b. In this case, the minimum bounding rectangle matches the active stochastic subdomain using the rotated coordinate system. The transformed basis, L_j^n , is computed using the rotated coordinate system. While

the rotation is needed for defining the active stochastic subdomain for some degrees of freedom, ξ is used throughout the rest of the paper without reference to ξ' . The rotated coordinate system is applied for the numerical examples in this work when the ratio of the minimum bounding rectangle area to the active area is greater than 2 for $d = 2$.

The uniform distribution of ξ is not preserved under a rotation, therefore the Legendre basis in ξ' is not orthogonal with respect to the measure of ξ' on $\hat{\Omega}^n$ when the rotation is utilized. However, it is straightforward to see that this basis is orthogonal with respect to the uniform density over $\hat{\Omega}^n$. In the subsequent formulations, the expectations are therefore taken with respect to the uniform density over $\hat{\Omega}^n$ when a coordinate rotation is performed. Additionally, the rotation may lead to an active stochastic subdomain which extends beyond Ω , as illustrated in Fig. 3c. Since $\hat{\Omega}^n \subseteq \Omega$, the L_j^n are computed only within Ω .

Finally, active stochastic subdomains with small areas may lead to an ill-conditioned system. In order to avoid the ill-conditioning, the area of the active stochastic subdomain, A_Ω , is required to be greater than a minimum value. A tolerance is implemented such that the coefficients of the PCE for degrees of freedom with $A_\Omega < A_{tol}$ are constrained to zero. By doing so, the variation of the degree of freedom in Ω is neglected. A tolerance value of $A_{tol} = 10^{-6}$ was implemented for the numerical examples in this work, for which degrees of freedom were constrained only in Example 3.

4.3 System of equations

In this section, the system of equations that results from the spatial and stochastic discretizations is described. The semi-discretized system of equations defined in (13) and (15) can be written in matrix form as

$$K(\xi)u(\xi) - f(\xi) = 0, \tag{27}$$

where \mathbf{K} is the conduction or stiffness matrix, \mathbf{f} is the load vector, and \mathbf{u} represents the vector of nodal degrees of freedom. The number of spatial degrees of freedom is denoted by N_{FE} , and the dependency on the random inclusion geometry is included by the random vector ξ . Following the approach outlined in [6], the system of equations is constructed to solve for the expansion coefficients in (21). However, the transformed polynomial basis L_j^n is specific to each spatial degree of freedom in this work. The polynomial expansion of each degree of freedom (21) is introduced into (27), and the Galerkin projection of the residual leads to a coupled system of equations for the vector of coefficients, \mathbf{a}_j , i.e.,

$$\sum_{k=1}^{M_{PC}} \langle \mathbf{K}_{ij}(\cdot) L_k^i(\cdot) L_l^j(\cdot) \rangle \mathbf{a}_k - \langle \mathbf{f}_i(\cdot) L_l^i(\cdot) \rangle = 0, \quad l = 1, \dots, M_{PC}. \quad (28)$$

The $(M_{PC} \cdot N_{FE}) \times (M_{PC} \cdot N_{FE})$ system of equations is written in compact form as

$$\mathbf{K}_s \hat{\mathbf{a}} - \mathbf{f}_s = \mathbf{0}, \quad (29)$$

where \mathbf{K}_s and \mathbf{f}_s are assembled from each spatial element integrated over Ω . The vector $\hat{\mathbf{a}}$ collects all of the expansion coefficients for the vector $\mathbf{u}(\xi)$ as defined in (21). Each l^{th} sub-vector component of the element vector \mathbf{f}_s^e is defined as

$$(\mathbf{f}_s^e)_l = \langle \mathbf{f}_i^e(\cdot) L_l^i(\cdot) \rangle \quad \text{for } l = 1, \dots, M_{PC}, \quad (30)$$

and each (k, l) block of the element matrix \mathbf{K}_s^e is defined as

$$(\mathbf{K}_s^e)_{kl} = \langle \mathbf{K}_{ij}^e(\cdot) L_k^i(\cdot) L_l^j(\cdot) \rangle \quad \text{for } k, l = 1, \dots, M_{PC}. \quad (31)$$

Here, (i, j) are indices for the degrees of freedom belonging to the nodes of element e in the finite element mesh, and (i, j) are not summed. The polynomial basis L^i is defined on $\hat{\Omega}^i$.

The element quantities \mathbf{K}_s^e and \mathbf{f}_s^e are computed by integrating over the spatial and stochastic domains. The spatial domain is partitioned for an intersected element for accurate integration over \mathcal{D} , which is standard practice in the XFEM. The partition is constructed to align with the interface, as described in [2, 7]. The integration over Ω also requires a partition for accuracy, since $\mathbf{K}^e(\xi)$ and $\mathbf{f}^e(\xi)$ vary piecewise smoothly with ξ . Partitioning of Ω is also standard practice for the X-SFEM. However, the proposed approach for using the Heaviside enrichment requires a specific partitioning technique, which is described as follows. The domain in which the response varies smoothly is bounded by the intersection of $\phi_i(\xi) = 0$ with the support of the basis functions. Therefore, $\phi_i(\xi) = 0$ for the degrees of freedom at the nodes of the element and its neighbors are used to define the

stochastic partition. Additionally, $\hat{\Omega}_i$ is considered in the construction of the stochastic partition, as it defines the nonzero subdomain for the PCE. The element stochastic partition is constructed using the union of $\phi_i(\xi) = 0$ for the nodes of the element and its neighbors, as well as $\hat{\Omega}_i$ for the nodes of the element. Each element stochastic partition is potentially different, as well as each $\hat{\Omega}_i$, which leads to increased computational costs. However, constructing the element stochastic partition and performing the element integration are well suited for efficient parallel processing.

In this work, a triangulation is used for the partition of the 2D spatial domain. The level set field is interpolated by linear shape functions. For integration in the spatial domain, the triangular partition of an intersected element aligns with the interface. Therefore the numerical integration in the spatial domain is exact for a properly chosen integration rule determined by the weak form of the governing equation. For $d = 1$, the partition of the stochastic domain is constructed using points according to $\phi_i(\xi) = 0$ where i is the set of nodes of the element and its neighbors. For $d = 2$, the stochastic partition is constructed using a triangulation of the bounding rectangle edges of the active stochastic subdomains for the element nodes as well as $\phi_i(\xi) = 0$, where i is again the set of nodes of the element and its neighbors. An example partition of the stochastic domain is illustrated in Fig. 6a for $d = 1$ with 4 points for $\phi_i(\xi) = 0$. Figure 6b depicts a triangulated stochastic partition for $d = 2$ with 2 edges for $\phi_i(\xi) = 0$ and 2 minimum bounding rectangles for Ω^n . For integration in the stochastic domain, a local error is introduced from solving $\phi_i(\xi) = 0$ for $d = 1$ and $d = 2$. Additionally, the zero level set curves are assumed to be linear for $d = 2$. Note that the integration rule for the stochastic domain depends on the chosen order of the PCE.

5 Numerical examples

Four numerical examples are presented to study the convergence and accuracy of the proposed Heaviside enriched X-SFEM. The first two numerical examples have one random parameter and an analytical solution for investigating the convergence of the method. The inclusion geometry in the third and fourth numerical examples is characterized by two random parameters in order to demonstrate the proposed method for problems with a two-dimensional stochastic domain. Example problems with continuous and discontinuous solutions are studied in this section. Solving problems with continuous solutions using the Heaviside enriched X-SFEM allows a comparison with the X-SFEM using a C^0 -continuous enrichment [11]. The first three examples have C^0 -continuous solutions while the solution is discontinuous in the fourth numerical example. The C^0 -continuous enrichment used in the following examples was proposed in [11].

Fig. 6 Example stochastic partition for **a** $d = 1$ and **b** $d = 2$. The triangulation for $d = 2$ is denoted by the dashed red lines

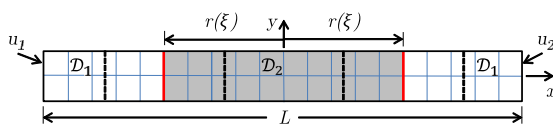
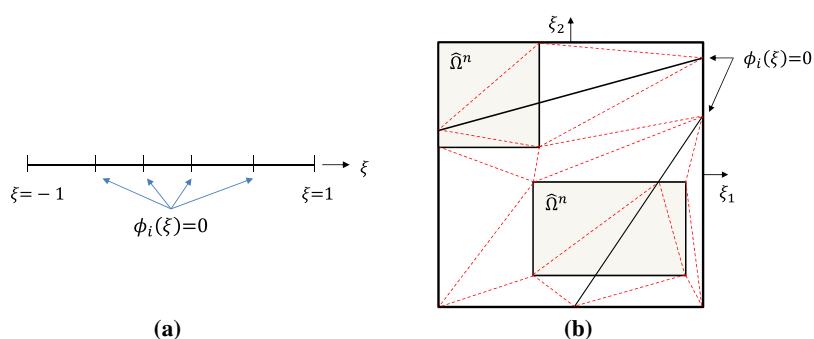


Fig. 7 Problem description for Example 1, shown with mesh size $h = 1$

5.1 Example 1: diffusion in a two-material bar

The first numerical example solves the heat diffusion problem (4) for the two-material bar shown in Fig. 7. The bar has length $L = 20$ with a centered inclusion of length $2r(\xi)$. The material interface is described by one random parameter, such that $r(\xi) = 5 + 2.5\xi$ and ξ has a uniform distribution $U(-1, 1)$. The inclusion geometry for $r = 5$ is shaded in Fig. 7, and the dashed lines represent the variation of the inclusion geometry. The material conductivity in \mathcal{D}_1 and \mathcal{D}_2 is $k_1 = 2$ and $k_2 = 20$, respectively. The temperature at the left boundary is specified as $u_1 = 0$, and the temperature at the right boundary is specified as $u_2 = 100$. While the problem is one-dimensional in the physical domain, this example is modeled using 20 quadrilateral elements. The stabilized Lagrange and Nitsche methods with a constraint factor of $k_1 + k_2$ are used to enforce solution continuity at Γ . The solutions using these methods were nearly identical for the example problem, and the results shown use the stabilized Lagrange method. The solution in the spatial domain for a specific value of ξ is piecewise linear over three subdomains. The chosen spatial discretization reproduces the exact solution and contributes zero error to the approximation.

Two studies are performed for this example. First, the degree of freedom approximation as a function of ξ is examined and compared to solving multiple XFEM solutions for different interface positions. Second, the convergence of the solution error with respect to the stochastic approximation order p is determined. This example problem was studied in [6] using the X-SFEM with the C^0 -continuous enrichment.

In order to show the variation of the degrees of freedom as a function of ξ , the deterministic solution is solved for

$\xi = -1$ to $\xi = 1$ in steps of $\Delta\xi = 0.01$. The deterministic solution is computed using the XFEM by solving multiple problems for various interface positions defined by $r(\xi)$. It is noted that a preconditioner is required in the XFEM for varying interface positions in order to avoid an ill-conditioned system of equations due to possible element intersections with a small ratio of volumes on either side of the interface [7]. A preconditioner was not used in the X-SFEM. The variation of the degrees of freedom for the node located at $\mathbf{x} = (5, 0)$ are shown in Fig. 8. The X-SFEM approximation for $p = 1$ is shown for comparison. The support of the PCE basis for the stochastic approximation is defined by the active subdomain. Note that the stabilized Lagrange (and Nitsche) interface constraint formulation couples the phase 1 and 2 degrees of freedom. Increasing the order of the PCE reduces the error in the X-SFEM solution, as shown in the second part of this numerical example.

The accuracy of the X-SFEM solution is measured by the relative error defined by

$$e = \frac{\|u - \hat{u}\|_{L^2(\Omega; L^2(\mathcal{D}))}}{\|u\|_{L^2(\Omega; L^2(\mathcal{D}))}}, \quad (32)$$

where u denotes the analytical solution and \hat{u} denotes the X-SFEM solution. The relative error is computed for each stochastic approximation order, p , and the convergence of the error is shown in Fig. 9. The error convergence for the proposed Heaviside enriched X-SFEM is compared with the X-SFEM using the C^0 -continuous enrichment. While the error for the Heaviside enriched X-SFEM is higher, the convergence rate for both approaches is the same. The difference in the magnitude of the error occurs because the C^0 -continuous enrichment leads to an approximation which is one polynomial degree higher in Ω than the Heaviside enrichment.

5.2 Example 2: linear elastic bimaterial plate

The second numerical example solves the linear elasticity problem (8) for the circular inclusion shown in Fig. 10.

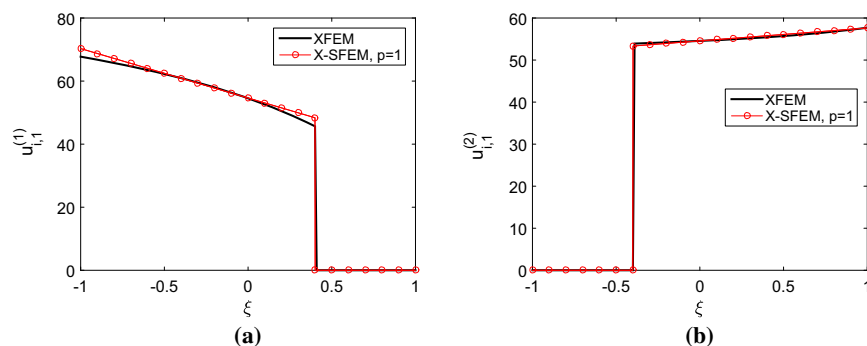


Fig. 8 The a phase 1 and b phase 2 degree of freedom values as a function of ξ for the node located at $x = (5, 0)$ using the XFEM and X-SFEM

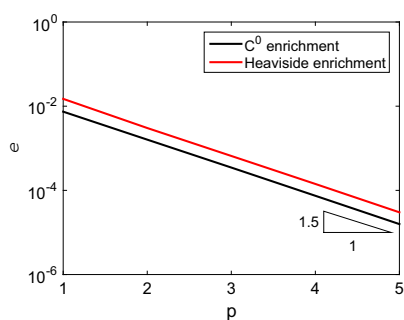


Fig. 9 Convergence of the relative error for the X-SFEM with the C^0 and Heaviside enrichment

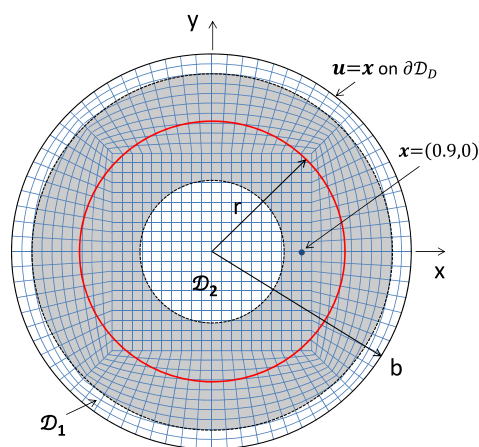


Fig. 10 Problem description for Example 2, shown with mesh size $h = 0.1$

This problem was presented in [11] using a C^0 -continuous enrichment function. A circular plate of radius $b = 2$ has a centered circular inclusion of radius r . The radius of the inclusion is determined by a single random parameter with a uniform distribution $U(-1, 1)$. The inclusion radius is given by $r = 1.26 + 0.54\xi$. The elastic modulus and Poisson’s ratio of the plate are $E_1 = 10$ and $\nu_1 = 0.3$. The elastic modulus and Poisson’s ratio of the inclusion are given by $E_2 = 1$, $\nu_2 = 0.25$. A radial displacement is prescribed at the boundary of the plate, such that $u_d = x$. The stabilized Lagrange method [8] is used to enforce continuity at the interface with a constraint factor of $100(E_1 + E_2)$. This problem is studied using the proposed Heaviside enrichment in X-SFEM as well as the C^0 -continuous enrichment proposed in [11].

Two studies are performed for this example. First, the behavior of the degrees of freedom in the stochastic domain is compared using the C^0 -continuous and Heaviside enrichment function for a deterministic sweep. The second study examines the accuracy of the X-SFEM solution and compares the convergence for the Heaviside and C^0 -continuous enrichment functions.

As in the first example, the XFEM solution is determined for numerous values of ξ in order to examine the behavior of

the degrees of freedom in the stochastic domain. The deterministic problem is solved for $\xi = -1$ to $\xi = 1$ with steps of $\Delta\xi = 0.01$. The degrees of freedom for the x-displacement at $x = (0.9, 0)$ is shown in Figs. 11 and 12 using the C^0 -continuous and Heaviside enrichment functions, respectively. As discussed in [6] and shown here, the variation of the degrees of freedom using the C^0 -continuous enrichment is not smooth with respect to ξ . The peaks correspond to the intersection of the interface with a node, therefore more peaks occur as the spatial mesh is refined. While some improvement in smoothness occurs with spatial mesh refinement, a smooth behavior of the degrees of freedom depends on a converged spatial mesh for the C^0 -continuous enrichment. Using the Heaviside enrichment, the behavior of the degrees of freedom is piecewise smooth in the stochastic domain for any spatial mesh size, as depicted in Fig. 12 for three spatial mesh sizes. The value of ξ at which the degree of freedom becomes active changes with mesh size. A second level degree of freedom exists at this node for phase 2 using the Heaviside enrichment,

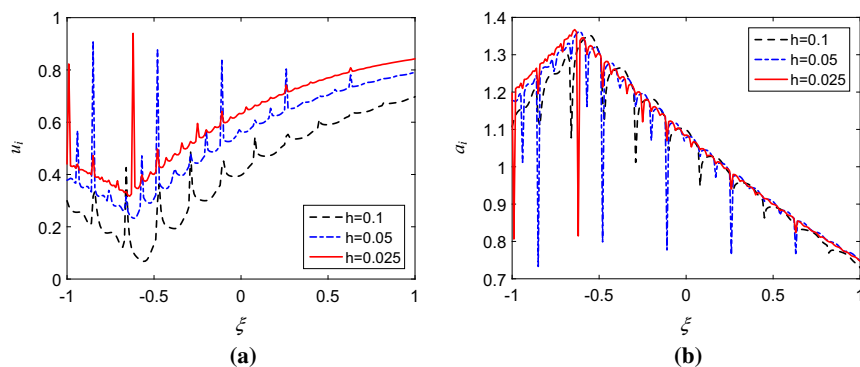


Fig. 11 **a** The regular and **b** enriched degree of freedom using the C^0 enrichment function for the x-displacement at $x = (0.9, 0)$ as a function of ξ with spatial mesh refinement

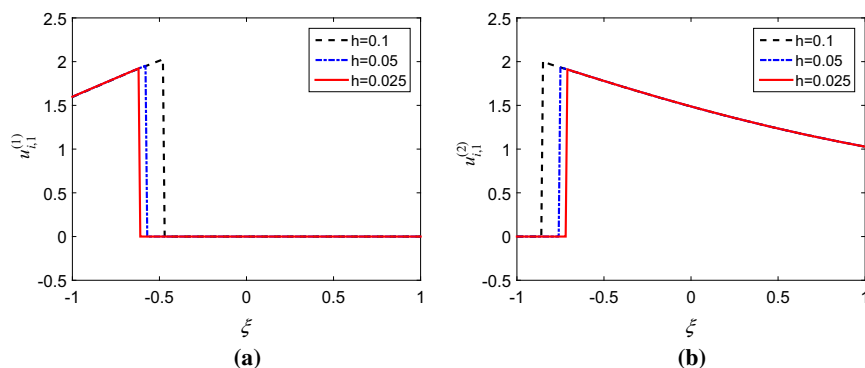


Fig. 12 The level 1 degrees of freedom for **a** phase 1 and **b** phase 2 using the Heaviside enrichment function for the x-displacement at $x = (0.9, 0)$ as a function of ξ with spatial mesh refinement

which is due to disconnected regions of phase 2 occurring for $-0.667 \leq \xi \leq -0.656$. The additional degree of freedom varies smoothly over this small active stochastic subdomain and is zero elsewhere. A description of why additional enrichment levels may be required for the same phase is provided in [7].

The analytical solution [19] is used to compute the relative error (32) in the X-SFEM solution. A comparison of the solution error using the C^0 -continuous and Heaviside enrichment functions is shown in Fig. 13 for three spatial mesh sizes. A higher convergence rate is achieved using the Heaviside enrichment. The spatial error dominates as each curve flattens as p is increased using the Heaviside enrichment.

5.3 Example 3: two parameter material inclusion

The third numerical example studies the proposed Heaviside enriched X-SFEM for an inclusion geometry defined by two random parameters, resulting in a two-dimensional stochastic domain. The example problem solves the heat diffusion

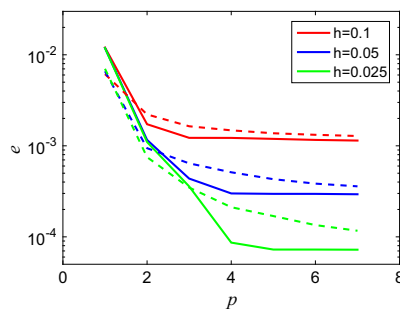


Fig. 13 Error convergence using the X-SFEM with respect to p for Example 2. *Solid and dashed lines* represent the Heaviside and C^0 -continuous enrichment functions, respectively

problem (4) for the random material inclusion with $d = 2$ depicted in Fig. 14. This problem was presented in [6] using a C^0 -continuous enrichment function. A square domain with a side length of 20 has a random inclusion with radius $r(\theta, \xi)$ defined by two random parameters with independent uniform distributions $U(-1, 1)$. The thermal conductivity of \mathcal{D}_1 and \mathcal{D}_2 are $k_1 = 2$ and $k_2 = 20$, respectively. The stabilized

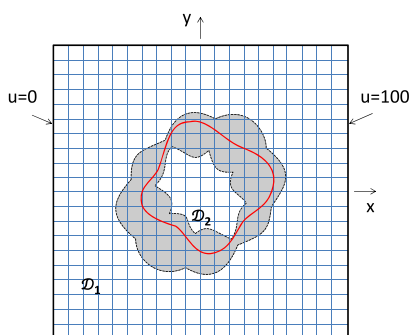


Fig. 14 Problem description for Example 3, shown with mesh size $h = 1$

Lagrange method is used for enforcing continuity at the interface with a constraint factor of $k_1 + k_2$. The temperature on the left and right side is specified as $u_T = 0$ and $u_T = 100$. A tolerance of $A_{tol} = 10^{-6}$ is used for constraining to zero the coefficients of the PCE for degrees of freedom with small active stochastic subdomains. The radius of the inclusion is given by

$$r(\theta, \xi) = \bar{r} + \sigma \sum_{k=1}^2 \frac{1}{k} \xi_k [\cos(k^2\theta) + \sin(k^2\theta)], \quad (33)$$

where $\bar{r} = 4$ and $\sigma = 1$. The angle θ is measured counter-clockwise from the positive x-axis.

The convergence of the X-SFEM solution with spatial and stochastic refinement is studied. Since an analytical solution does not exist for this problem, the expectation of the solution is computed and compared with a reference solution. The expectation of the X-SFEM solution is defined by

$$\|u\|_E^2 = \left\langle \int_{\mathcal{D}} (k\nabla u)^T \nabla u dx \right\rangle. \quad (34)$$

The Monte Carlo (MC) reference solution is computed from a set of XFEM solutions using a random sampling of ξ . A least-squares polynomial chaos regression [3] is used to determine the reference energy norm using the XFEM for the interface geometry generated by 50,000 random samples of ξ with 4 mesh sizes ($h = \{1, 0.5, 0.25, 0.125\}$). For $h = 0.125$, which was the smallest mesh size used for a MC reference solution, the mean energy norm of the reference solution is 157.523 with a 95 % confidence interval of ± 0.00402 . The comparison of the X-SFEM energy norm and the reference solution is shown in Fig. 15 for 3 spatial mesh sizes ($h = \{1, 0.5, 0.25\}$). For each spatial mesh size, the Heaviside enriched X-SFEM solution converges quickly to the reference solution as the order of the PCE is increased. A higher convergence rate for each spatial mesh size is achieved when compared to the C^0 -continuous enrichment functions explored in [6]. The

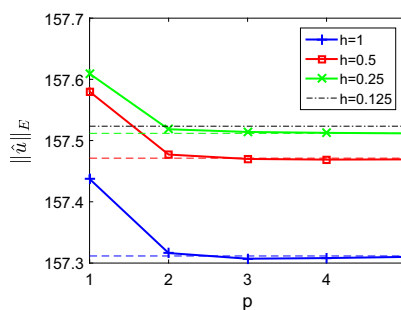


Fig. 15 Energy norm of the approximate solution for Example 3. The X-SFEM approximation and reference solution are represented by *solid* and *dashed* lines, respectively, for $h = \{1, 0.5, 0.25\}$

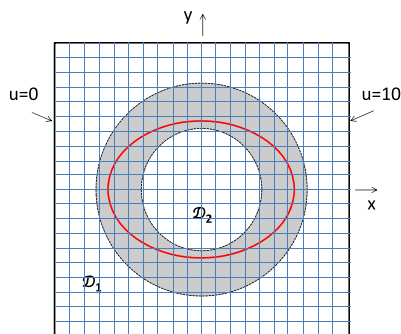


Fig. 16 Problem description for Example 4, shown with mesh size $h = 1$

stochastic approximation converges for order $p = 2$. Additionally, convergence to the reference solution is seen with spatial mesh refinement.

5.4 Example 4: two parameter ellipsoidal inclusion

The Heaviside enriched X-SFEM for a problem with a discontinuous solution across the random material interface with a two-dimensional stochastic domain is studied. The fourth numerical example solves the heat diffusion problem (4) for a material with an ellipsoidal inclusion shown in Fig. 16. A square domain with a side length of 20 has a single random ellipsoidal inclusion. The inclusion geometry is characterized by two random parameters, and the solution at the interface is discontinuous due to a thin interface layer with a thermal conductance of $\alpha = 10$. The flux at the interface is defined according to (6). The thermal conductivity of \mathcal{D}_1 and \mathcal{D}_2 are $k_1 = 2$ and $k_2 = 20$, respectively. The temperature on the left and right side of the domain is specified as $u_T = 0$ and $u_T = 100$. The random inclusion geometry is defined by the implicit representation of an ellipse and two random parameters with independent uniform distributions $U(-1, 1)$. Using the equation of an ellipse, the level set function is defined as

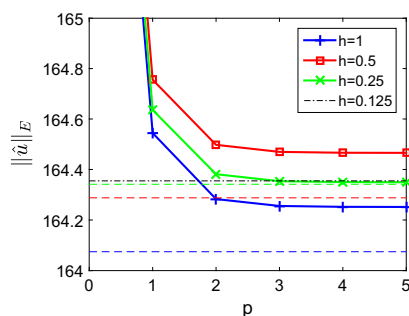


Fig. 17 Energy norm of the approximate solution for Example 4. The X-SFEM approximation and reference solution are represented by *solid* and *dashed lines*, respectively, for $h = \{1, 0.5, 0.25\}$

$$\phi(\mathbf{x}, \boldsymbol{\xi}) = r^2 - a(\xi_1)x_1^2 - b(\xi_2)x_2^2. \quad (35)$$

where $r = 5$ and $a(\xi_1) = 1 + 0.5\xi_1$ and $b(\xi_2) = 1 + 0.5\xi_2$. Using this definition instead of the signed distance function, the level set function is linear with respect to $\boldsymbol{\xi}$. As a consequence, the partition for stochastic integration exactly aligns with $\phi_i(\boldsymbol{\xi})$.

The convergence of the Heaviside enriched X-SFEM solution with increasing p is studied using a reference solution. The reference solution is computed with a least-squares polynomial chaos regression using the XFEM solutions for 50,000 samples of $\boldsymbol{\xi}$ with 4 spatial mesh sizes ($h = \{1, 0.5, 0.25, 0.125\}$). The mean energy norm for the XFEM reference for $h = 0.125$ is 164.355 with a 95 % confidence interval of ± 0.0606 . The mean energy norm of the X-SFEM solution (34) is compared with the reference solution in Fig. 17 for the three spatial mesh sizes of ($h = \{1, 0.5, 0.25\}$). The additional mesh size of $h = 0.125$ is included for the XFEM reference solution to show convergence. The X-SFEM energy norm converges quickly. Similar to Example 3, the stochastic approximation converges at approximately $p = 2$. However, the X-SFEM solution does not converge to the corresponding reference solution for each spatial mesh size. When compared with Example 3, the reference energy norm has a larger variability as indicated by the confidence interval. The spatial error is dominating for the coarser mesh sizes of $h = 1$ and $h = 0.5$ with $p > 2$. A certain spatial resolution is required for convergence with a low order of the stochastic approximation. A similar requirement was identified in [6] using the C^0 -continuous enrichment function for continuous problems.

6 Conclusions

A Heaviside enriched extended stochastic FEM has been developed for solving problems with uncertain inclusion geometry which have either a continuous or discontinuous

solution across the material interface. The Heaviside enrichment leads to a discontinuous solution in the stochastic domain, such that the degrees of freedom are nonzero (or active) on a subdomain of the stochastic domain. The active stochastic subdomain for each degree of freedom is determined by the spatial mesh and the random level set function. The stochastic approximation is constructed on the active stochastic subdomain for each degree of freedom, which leads to an accurate solution and well-conditioned system of equations. A minimum bounding hyperrectangle approximates the active stochastic subdomain, and the basis polynomials in the stochastic approximation are transformed and normalized onto the hyperrectangle. The proposed X-SFEM is best suited for a low number of random parameters due to the computational cost associated with construction of the polynomial bases. Approximations of high dimensional stochastic functions with discontinuities is a challenging and active area of research.

The convergence and accuracy of the proposed method was demonstrated for example problems with continuous and discontinuous solutions at the interface. Studying problems with continuous solutions allowed a comparison to an existing approach. The proposed Heaviside enriched X-SFEM leads to a higher convergence rate for problems with continuous solutions when compared to using a C^0 -continuous enrichment function. The degrees of freedom are smooth with respect to the random parameters regardless of the spatial mesh size. Due to the smoothness of the degrees of freedom, convergence in the stochastic space occurs with low orders of the polynomial approximation. Additional advantages of using the proposed Heaviside enrichment approach for problems with an uncertain interface configuration are that neighboring intersected elements and elements intersected more than once can be modeled accurately, and there are no issues with blending elements.

Acknowledgments The first author acknowledges the support of the NASA Fundamental Aeronautics Program Fixed Wing Project, and the second, third, and fourth author acknowledges the support of the National Science Foundation under Grant CMMI-1201207. The third author acknowledges the support of the U.S. Department of Energy Office of Science, Office of Advanced Scientific Computing Research, under Award Number DE-SC0006402 and the National Science Foundation under Grant CMMI-1454601. The opinions and conclusions presented are those of the authors and do not necessarily reflect the views of the sponsoring organizations.

References

1. Fernández-Méndez S, Huerta A (2004) Imposing essential boundary conditions in mesh-free methods. *Comput Methods Appl Mech Eng* 193:1257–1275
2. Fries TP, Belytschko T (2010) The extended/generalized finite element method: an overview of the method and its applications. *Int J Numer Methods Eng* 84:253–304

3. Hampton J, Doostan A (2015) Coherence motivated sampling and convergence analysis of least-squares polynomial chaos regression. *Comput Methods Appl Mech Eng* 290:73–97
4. Hansbo A, Hansbo P (2004) A finite element method for the simulation of strong and weak discontinuities in solid mechanics. *Comput Methods Appl Mech Eng* 193:3523–3540
5. Juntunen M, Stenberg R (2009) Nitsche's method for general boundary conditions. *Math Comput* 78:1353–1374
6. Lang C, Doostan A, Maute K (2013) Extended stochastic FEM for diffusion problems with uncertain material interfaces. *Comput Mech* 51:1031–1049
7. Lang C, Makhija D, Doostan A, Maute K (2014) A simple and efficient preconditioning scheme for heaviside enriched XFEM. *Comput Mech* 54:1357–1374
8. Makhija D, Maute K (2014) Numerical instabilities in level set topology optimization with the extended finite element method. *Struct Multidiscip Optim* 49:185–197
9. Makhija D, Maute K (2015) Level set topology optimization of scalar transport problems. *Struct Multidiscip Optim* 51:267–285
10. Moës N, Dolbow J, Belytschko T (1999) A finite element method for crack growth without remeshing. *Int J Numer Methods Eng* 46:131–150
11. Nouy A, Clément A (2010) Extended stochastic finite element method for the numerical simulation of heterogeneous materials with random material interfaces. *Int J Numer Methods Eng* 83:1312–1344
12. Nouy A, Schoefs F, Moës N (2007) X-SFEM, a computational technique based on X-FEM to deal with random shapes. *Eur J Comput Mech* 16:277–293
13. Nouy A, Clément A, Schoefs F, Moës N (2008) An extended stochastic finite element method for solving stochastic partial differential equations on random domains. *Comput Methods Appl Mech Eng* 197:4663–4682
14. Savvas D, Stefanou G, Papadrakakis M, Deodatis G (2014) Homogenization of random heterogeneous media with inclusions of arbitrary shape modeled by xfem. *Comput Mech* 54:1221–1235
15. Sethian J (1999) *Level set methods and fast marching methods: evolving interfaces in computational geometry, fluid mechanics, computer vision, and materials science*. Cambridge University Press, New York
16. Stefanou G (2009) The stochastic finite element method: past, present, and future. *Comput Methods Appl Mech Eng* 198:1031–1051
17. Stefanou G, Nouy A, Clément A (2009) Identification of random shapes from images through polynomial chaos expansion of random level set functions. *Int J Numer Methods Eng* 79:127–155
18. Stenberg R (1995) On some techniques for approximating boundary conditions in the finite element method. *J Comput Appl Math* 63:139–148
19. Sukumar N, Chopp D, Moës N, Belytschko T (2001) Modeling holes and inclusions by level sets in the extended finite element method. *Comput Methods Appl Mech Eng* 190:6183–6200
20. Tan L, Zabarav N (2006) A level set simulation of dendritic solidification with combined features of front-tracking and fixed-domain methods. *J Comput Phys* 211:36–63
21. Terada K, Asai M, Yamagishi M (2003) Finite cover method for linear and non-linear analyses of heterogeneous solids. *Int J Numer Methods Eng* 58:1321–1346
22. Wan X, Karniadakis G (2006) Multi-element generalized polynomial chaos for arbitrary probability measures. *SIAM J Sci Comput* 28:901–928
23. Wang M, Wang X, Guo D (2003) A level set method for structural topology optimization. *Comput Methods Appl Mech Eng* 192:227–246
24. Xiu D (2010) *Numerical methods for stochastic computations: a spectral method approach*. Princeton University Press, Princeton
25. Xiu D, Karniadakis G (2002) The Wiener–Askey polynomial chaos for stochastic differential equations. *SIAM J Sci Comput* 24:619–644

Appendix B

Publication 2: On shape sensitivities with heaviside-enriched XFEM [114]



RESEARCH PAPER

On shape sensitivities with heaviside-enriched XFEM

Ashesh Sharma¹ · Hernan Villanueva² · Kurt Maute¹Received: 24 August 2016 / Revised: 14 October 2016 / Accepted: 5 December 2016 / Published online: 24 December 2016
© Springer-Verlag Berlin Heidelberg 2016

Abstract This paper investigates the behavior of shape sensitivities within the context of the eXtended Finite Element Method (XFEM) using a Heaviside enrichment strategy, wherein the shape derivative is computed by the adjoint method. The Heaviside function is discontinuous by construction. This feature of the enrichment function presents advantages as well as challenges in the computation of shape sensitivities, both of which are discussed in detail in this paper. Using continuum and discrete approaches, we present the derivation of analytical shape sensitivities with respect to the design variables which define the design geometry. We propose a robust semi-analytical approach to computing the shape sensitivities, which provides great ease of implementation as compared to fully analytical approaches. The behavior of the XFEM-based shape sensitivities is analyzed using linear heat diffusion examples in 2D, and an incompressible fluid flow example in 3D. We compare XFEM-based shape sensitivities against shape sensitivities obtained through the classical approach of using a body-fitted mesh. It is found that the former are not as smooth as those obtained using a comparable body-fitted mesh. This discrepancy is shown to be an outcome of the

discretization error of the design geometry on a background mesh and is not a consequence of the approach by which the XFEM-based shape sensitivities are computed.

Keywords Shape sensitivity · Adjoint method · Generalized shape optimization · Heaviside enrichment · eXtended finite element method

1 Introduction

Shape sensitivities quantify the effect that a change in shape has on the response of the design. Shape sensitivity analysis in general comprises of computing the derivative of a response function (e.g. strain energy, stress, perimeter, etc.) with respect to parameters that describe the corresponding domain geometry. The classical method of computing shape sensitivities, also referred to as boundary variations, has been extensively studied, for example, by Simon (1980), Jameson (1988) and Sokolowski and Zolésio (1992). One important application of shape sensitivity analysis is gradient computation for design optimization. The scope of improving the performance of designs due to changes in shape led to the development of shape optimization methods; see, for example, Sokolowski and Zolésio (1992) and Mohammadi and Pironneau (2001). In shape optimization, the position of each point on the material boundaries is a function of the shape design variables. Shape optimization of internal and external boundaries is of great importance to improving the detailed design of engineering systems against many criteria, such as stiffness or buckling in structural mechanics, or fluid drag and lift forces in fluid dynamics.

Over the years, researchers used various strategies to define the geometry of material domains. Classical

✉ Kurt Maute
maute@colorado.edu

Ashesh Sharma
ashesh.sharma@colorado.edu

Hernan Villanueva
carlos.villanueva@colorado.edu

¹ Department of Aerospace Engineering Sciences, University of Colorado at Boulder, Boulder, CO 80309-0429, USA

² Department of Mechanical Engineering, University of Colorado at Boulder, Boulder, CO 80309-0427, USA

approaches for parametrization of shapes were either based on CAD models or were CAD-free, both of which provide an explicit representation of the material geometry. CAD models include the use of Bézier curves, B-splines and NURBS for the representation of material geometry (cf. Bletzinger et al. 1991, Haasemann et al. 2011). CAD-free parametrization involves describing the material geometry directly using finite element meshes as described by Kenway et al. (2010) and Firl et al. (2013). In contrast, Osher and Sethian (1988) introduced the concept of Level Set Methods (LSM) for defining the material boundaries implicitly by iso-contours of a level set field. As with explicit approaches mentioned above, this implicit function allows for a crisp description of the boundaries as discussed by Dijk et al. (2013). Mapping the geometry to a mechanical model is performed through either a Lagrangian (deforming mesh) or an Eulerian (fixed mesh) approach. Figure 1 provides a comparison of different mapping approaches as the design domain undergoes a shape change.

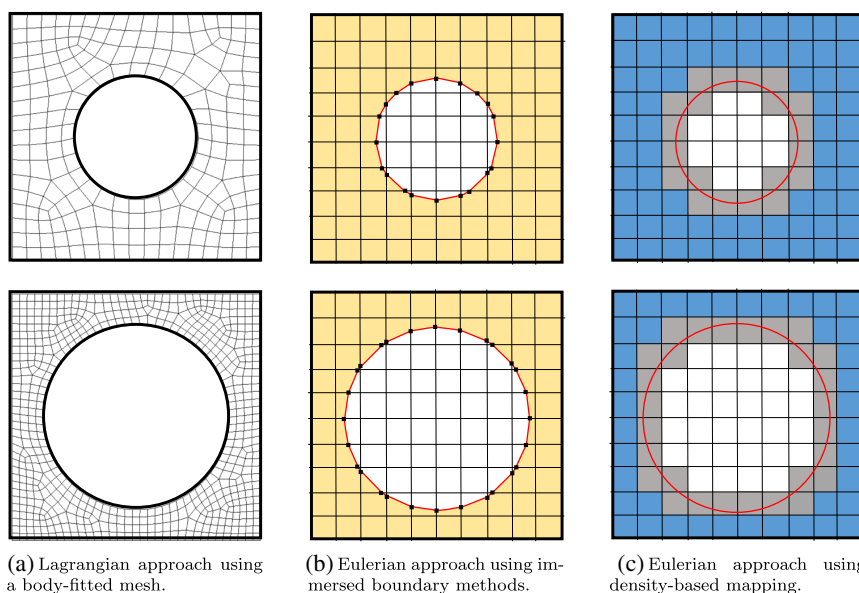
The computation of shape sensitivities using Lagrangian approaches has been studied in detail. Initial studies used nodal coordinates of a finite element mesh as the design variables, as discussed by Haftka and Grandhi (1986). A disadvantage of this approach, as pointed out by Chen and Tortorelli (1997), was the large number of design variables and mesh degradation. Methods involving mesh parameterizations (Tortorelli et al. 1994) and filtering techniques (Firl et al. 2013) were studied to overcome these issues (see also Azegami et al. 1997 and Mohammadi and Pironneau 2004). However, these Lagrangian-based approaches still face drawbacks with the primary issues being that the

finite element mesh cannot deform much and that topological changes are not possible. Re-meshing overcomes these issues, but it increases the overall complexity and computational costs. Furthermore, Schleupen et al. (2000) showed that adapting the finite element mesh during the optimization process leads to an inconsistent sensitivity analysis and may affect the convergence rate of the optimization process.

In contrast to Lagrangian methods, recently developed Eulerian approaches formulate shape sensitivity problems by projecting the design onto a fixed mesh. Examples of such approaches include density based methods (cf. Wang et al. 2003; Allaire et al. 2004, 2005), fictitious domain methods (cf. Haslinger et al. 2001 and Kim and Chang 2005), and immersed boundary methods (cf. Duysinx et al. 2006, Wei et al. 2010, Najafi et al. 2015). These techniques have shown to mitigate the issues associated with Lagrangian-based methods.

In this paper we adopt an Eulerian approach that utilizes the eXtended Finite element Method (XFEM), developed by Moës et al. (1999), to model the physical response of the mechanical problem. The XFEM is an immersed boundary technique that uses an enrichment function to locally capture the non-smooth solution of state variable fields along the material interface, without requiring a conforming mesh. Depending on the type of discontinuity various enrichment strategies have been developed as described by Fries and Belytschko (2010). The design geometry in the current work is defined using the LSM. This combination is referred to as the LSM-XFEM approach, and is often classified as a generalized shape optimization approach (Duysinx et al. 2006). This classification stems from the fact that

Fig. 1 Examples of geometry mapping undergoing shape change



the approach allows for topology modifications as existing holes can merge or disappear. The LSM-XFEM approach has been used in the context of shape and topology optimization by Duysinx et al. (2006), Wei et al. (2010), Kreissl and Maute (2012), and Li et al. (2012), among others. Note that although the current work makes use of the LSM, it is also applicable to other methods of defining the design geometry.

The majority of previous XFEM-based studies on shape sensitivities make use of C^0 -continuous enrichment functions, such as the one introduced by Moës et al. (2003) which do not allow for strong discontinuities within the solution field. A recent study in the context of C^0 -continuous enrichment functions was performed by Noël et al. (2016), on developing analytical sensitivity analysis for shape optimization of bi-material structures. Some of the first studies considering strong discontinuities were presented by Duysinx et al. (2006) who adopt a semi-analytical approach for the computation of the sensitivities in material-void problems. When perturbing the level set field in the vicinity of a node, they ignore the contribution of newly intersected elements. This special treatment of intersected elements is bound to degrade the accuracy of the computed shape sensitivities. An analytical sensitivity study to address material-material interface problems in multi-component system was presented by Zhang et al. (2012) wherein the sensitivities are derived from a material-material interface model. As a consequence for material-void problems, their approach requires an approximation of the voids by a weak material which increases the overall computational cost. In contrast, Wei et al. (2010) use a Heaviside function in the form of a standard discontinuous enrichment strategy for 2D material-void problems. However, this enrichment strategy is not guaranteed to consistently approximate the state variable fields for configurations with complex intersection patterns as discussed by Makhija and Maute (2014).

Following the work of Terada et al. (2003) and Hansbo and Hansbo (2004), we adopt a generalized Heaviside enrichment strategy with multiple enrichment levels. The use of multiple enrichment levels ensures that the solution field is interpolated in a consistent manner, and avoids artificial coupling in the presence of disconnected phases as discussed by Tran et al. (2011) and Makhija and Maute (2014). The Heaviside enrichment is a step enrichment and is discontinuous by construction, making it preferable for problems involving strong discontinuities such as material-void problems. For C^0 -continuous problems, the continuity in the solution is enforced through stabilized Lagrange or Nitsche methods (Stenberg 1995). Intuitively, the discontinuous nature of the Heaviside enrichment function is expected to affect the smoothness of shape sensitivities. Heaviside-enriched XFEM for shape and topology optimization has been used by Wei et al. (2010), Li et al. (2012),

Villanueva and Maute (2014), Lawry and Maute (2015), Jeong et al. (2016) and Liu et al. (2016), among others.

None of the aforementioned studies provide an in-depth discussion on the numerical behavior of the shape sensitivities. Filling this gap in the literature is the primary goal of this paper. We investigate in detail the advantages and challenges that the Heaviside-enriched XFEM poses to the computation of shape sensitivities via the adjoint method, for both material-void and material-material problems. Analytical shape sensitivities are derived using both continuum (differentiate, then discretize) and discrete (discretize, then differentiate) approaches. Numerical examples on steady heat diffusion in 2D and steady incompressible Navier-Stokes flow in 3D are presented for discussion of the numerical behavior of shape sensitivities. Through these examples we investigate the dependency of the shape sensitivities on spatial resolution and interface conditions. Furthermore we compare both numerically and analytically, the XFEM-based shape sensitivities against shape sensitivities obtained by the classical Lagrangian approach using a body-fitted mesh.

The remaining part of this manuscript is organized as follows: Section 2 introduces a model problem alongside the governing equations and their variational forms for the heat diffusion and incompressible fluid flow studies; Section 3 discusses the details of the adopted Heaviside-enriched XFEM; Section 4 presents the shape sensitivities using the adjoint approach in the context of variational calculus; in Section 5, numerical examples are presented to analyze and validate the proposed approach; finally, a summary and concluding remarks are presented in Section 6. Appendix A presents a 1D analytical example to draw comparisons between shape sensitivities obtained using Heaviside-enriched XFEM and shape sensitivities obtained using a body-fitted mesh.

2 Model problem

The current study is illustrated using the model problem depicted in Fig. 2. Our model problem consists of one or more stationary inclusions (material or void) embedded in a matrix. The LSM is used to define the material geometry. This section describes the problem setup, the governing equations for the model problem and their corresponding variational form.

2.1 Domain description

The governing equations presented in Sections 2.2 and 2.3 are solved over the spatial domain $\Omega \subset \mathbb{R}^d$, for d topological dimensions. This spatial domain is composed of two non-overlapping material subdomains (also referred to as

material phases), Ω^1 and Ω^2 , such that $\Omega = \Omega^1 \cup \Omega^2$. The external boundaries for the material domains Ω^1 and Ω^2 are expressed as $\partial\Omega^1$ and $\partial\Omega^2$ respectively. The outward vector to these boundaries is denoted by \mathbf{n} . The Dirichlet and Neumann boundaries are denoted by $\Gamma_D = \partial\Omega^m \cap \partial\Omega_D$ and $\Gamma_N = \partial\Omega^m \cap \partial\Omega_N$ respectively, where $m = 1, 2$. We consider a sharp material interface, $\Gamma \subset \mathbb{R}^{d-1}$, defined as $\Gamma_{12} = \partial\Omega^1 \cap \partial\Omega^2$. The outward normal along the material interface Γ_{12} , with respect to $\partial\Omega^1$, is denoted by \mathbf{n}_Γ .

The material interface geometry is defined using a set of design variables, s . Within the context of the XFEM, the material interface geometry can be defined in several manners. In the seminal work on the XFEM by Moës et al. (1999), cracks in 2D domains were parameterized explicitly using polygons. Recently, Haasemann et al. (2011) used B-splines to improve the accuracy of interface approximation. The LSM, due to its ability to handle complex shapes along with its ease of implementation, has been naturally associated with the XFEM; see, for example, Sukumar et al. (2001), Wang et al. (2003), Zabaras et al. (2006), and Fries and Belytschko (2010). Any of the aforementioned approaches for defining the design geometry are applicable to the current study and can be used to construct a set of points, $\mathbf{x}_\Gamma(s)$, that defines the material interface geometry, Γ_{12} .

We make use of the LSM to describe our model geometry. The material distribution in Fig. 2 can be interpreted in terms of a level set field, $\phi(\mathbf{x}, s)$, such that

$$\begin{aligned} \phi(\mathbf{x}, s) &< 0 \quad \forall \mathbf{x} \in \Omega^1|_s, \\ \phi(\mathbf{x}, s) &> 0 \quad \forall \mathbf{x} \in \Omega^2|_s, \\ \phi(\mathbf{x}, s) &= 0 \quad \forall \mathbf{x} \in \Gamma_{12}|_s. \end{aligned} \tag{1}$$

The level set field is mapped onto the XFEM mesh by evaluating the parametrized level set field at the nodes. Standard bilinear and trilinear shape functions, in 2D and 3D respectively, are used to interpolate the level set value within an element. These shape functions permit that an element edge can be intersected by the material interface, i.e. $\phi(\mathbf{x}, s) = 0$, at most once. Lines and faces in 2D and

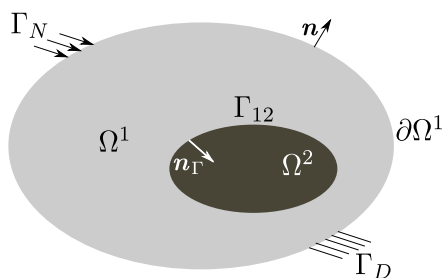


Fig. 2 Schematic of the model problem, with a single inclusion

3D respectively, connecting the edge intersection points, $\mathbf{x}_\Gamma(s) (= \mathbf{x}_\Gamma(\phi(\mathbf{x}, s)))$, define the material interface within a finite element as shown in Fig. 3.

An example of defining the level set field as a function of the design variable is given in (2) wherein the level set field describes a sphere centered at \mathbf{x}_c

$$\phi(\mathbf{x}, s) = s - |\mathbf{x} - \mathbf{x}_c| \tag{2}$$

where $|\cdot|$ denotes the L^2 norm, and the design variable, s , assumes the role of the radius of the sphere. Thus, changes in the design variable lead to changes in the shape of the domain. For a detailed discussion on the LSM within the context of shape and topology optimization, the reader may refer to the comprehensive reviews by Dijk et al. (2013) and Gain and Paulino (2013).

2.2 Steady heat diffusion

The model for the heat diffusion problem involves solving for the scalar temperature field, $u(\mathbf{x})$, in Ω for material phases $m = 1, 2$. The two-phase domain is governed by

$$\begin{aligned} -\nabla \cdot (\boldsymbol{\kappa}^m \nabla u^m) &= 0 \quad \text{in } \Omega^m, \\ u^m &= u_D \quad \text{on } \Gamma_D, \\ (\boldsymbol{\kappa}^m \nabla u^m) \cdot \mathbf{n} &= q_N \quad \text{on } \Gamma_N, \end{aligned} \tag{3}$$

where $\boldsymbol{\kappa}$ is the thermal conductivity tensor, and u^m is the restriction of u to Ω^m . The temperature, u_D , is specified on the Dirichlet boundary, Γ_D , and a heat flux, q_N , is specified on the Neumann boundary, Γ_N . The materials are assumed to be isotropic, i.e. $\boldsymbol{\kappa}^m = k^m \mathbf{I}$, with k^1 and k^2 being constant over their respective material phases. Additionally, continuity of the solution and flux across the material interface, Γ_{12} , must be ensured such that

$$\begin{aligned} u^1 - u^2 &= 0 \quad \text{on } \Gamma_{12}, \\ k^1 \nabla u^1 \cdot \mathbf{n}_\Gamma - k^2 \nabla u^2 \cdot \mathbf{n}_\Gamma &= 0 \quad \text{on } \Gamma_{12}. \end{aligned} \tag{4}$$

2.3 Incompressible Navier-Stokes flow model

We also consider a Newtonian fluid governed by the steady incompressible Navier-Stokes equations for a single phase

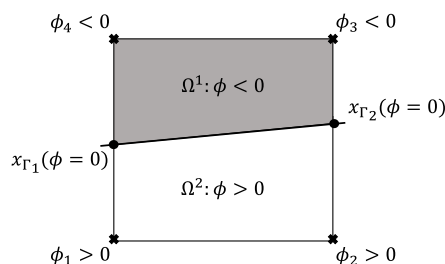


Fig. 3 Construction of interface geometry for an intersected element in 2D

flow problem. The inclusion is void of any material. As a result, fluid flow exists only in material phase 1 of our model problem. The model problem involves solving for the vector velocity field, $\mathbf{v}(\mathbf{x})$, and pressure field, $p(\mathbf{x})$, in Ω^1 . The fluid flow is governed by

$$\begin{aligned} \rho^1 \mathbf{v}^1 \cdot \nabla \mathbf{v}^1 - \nabla \cdot \boldsymbol{\sigma} &= \mathbf{0} \quad \text{in } \Omega^1, \\ \nabla \cdot \mathbf{v}^1 &= \mathbf{0} \quad \text{in } \Omega^1, \end{aligned} \tag{5}$$

where $\boldsymbol{\sigma}(\mathbf{v}^1, p^1) = -p^1 \mathbf{I} + 2\mu^1 \boldsymbol{\epsilon}(\mathbf{v}^1)$ represents the Cauchy-stress tensor. The density and dynamic viscosity of the fluid are given by ρ^1 and μ^1 respectively, and are assumed to be constant throughout Ω^1 . The rate of deformation tensor is given by $\boldsymbol{\epsilon}(\mathbf{v}^1) = (\nabla \mathbf{v}^1 + (\nabla \mathbf{v}^1)^T)/2$. The Dirichlet and Neumann boundary conditions are given by

$$\begin{aligned} \mathbf{v}^1 &= \mathbf{v}_D \quad \text{on } \Gamma_D, \\ \boldsymbol{\sigma}(\mathbf{v}^1, p^1) \cdot \mathbf{n} &= \mathbf{t}_N \quad \text{on } \Gamma_N. \end{aligned} \tag{6}$$

The velocity, \mathbf{v}_D , is specified on the Dirichlet boundary, Γ_D , and the traction, \mathbf{t}_N , is specified on the Neumann boundary, Γ_N .

Assuming mass conservation across the material interface, and no-slip conditions along the stationary material-void interface, the velocity field at the interface is prescribed to

$$\mathbf{v}^1 = \mathbf{0} \quad \text{on } \Gamma_{12}. \tag{7}$$

2.4 Variational form of the governing equations

The weak form of the governing equations is constructed by multiplying the governing equations with a set of admissible test functions and integrating over the domain, Ω . We adopt the standard Galerkin approach in defining the solution spaces $\mathcal{U} = \mathcal{U}^1 \times \mathcal{U}^2$, $\mathcal{U} = \mathcal{U}^1 \times \mathcal{U}^2$ and the weighting spaces $\mathcal{V} = \mathcal{V}^1 \times \mathcal{V}^2$, $\mathcal{V} = \mathcal{V}^1 \times \mathcal{V}^2$, such that

$$\begin{aligned} \mathcal{U}^m &= \{u^m, p^m \in H^1(\Omega^m); u^m = u_D \text{ on } \Gamma_D\}, \\ \mathcal{V}^m &= \{v^m, \eta^m \in H^1(\Omega^m); v^m = 0 \text{ on } \Gamma_D\}, \\ \mathcal{U}^m &= \{v^m \in H^1(\Omega^m); v^m = \mathbf{v}_D \text{ on } \Gamma_D\}, \\ \mathcal{V}^m &= \{\omega^m \in H^1(\Omega^m); \omega^m = \mathbf{0} \text{ on } \Gamma_D\}, \end{aligned} \tag{8}$$

where v^m , η^m , and ω^m are the temperature, pressure, and velocity weighting functions respectively. The spaces \mathcal{U} and \mathcal{V} are Hilbert spaces consisting of scalar functions with square integrable first derivatives, whereas the spaces \mathcal{U} and \mathcal{V} are Hilbert spaces consisting of vector functions with square integrable first derivatives.

The weak form for the heat diffusion equations (3), augmented with Nitsche's method (Stenberg 1995; Juntunen

and Stenberg 2009) to satisfy the interface conditions (4), is: Find $u^m \in \mathcal{U}^m$ such that $u^m = u_D$ on Γ_D and

$$\mathcal{R}^D = \mathcal{R}_\Omega^D + \mathcal{R}_{\Gamma_N}^D + \mathcal{R}_{\Gamma_{12}}^D = 0 \quad \forall v^m \text{ in } \mathcal{V}^m, \tag{9}$$

where \mathcal{R}_Ω^D is the residual of the volumetric contribution from (3), $\mathcal{R}_{\Gamma_N}^D$ is the residual contribution from the Neumann boundary, and $\mathcal{R}_{\Gamma_{12}}^D$ is the residual contribution from the interface conditions presented in (4). These residual contributions are given by

$$\begin{aligned} \mathcal{R}_\Omega^D &= (\nabla v^m, (\boldsymbol{\kappa} \nabla u^m))_{\Omega^m}, \\ \mathcal{R}_{\Gamma_N}^D &= -(v^m, q_N)_{\Gamma_N}, \\ \mathcal{R}_{\Gamma_{12}}^D &= -(\llbracket v \rrbracket, \{k \nabla u\} \cdot \mathbf{n}_\Gamma)_{\Gamma_{12}} \\ &\quad - (\{k \nabla v\} \cdot \mathbf{n}_\Gamma, \llbracket u \rrbracket)_{\Gamma_{12}} \\ &\quad + (\llbracket v \rrbracket, \gamma_u \llbracket u \rrbracket)_{\Gamma_{12}}, \end{aligned} \tag{10}$$

where $(a, b)_X = \int_X a b \, dx$ denotes the L^2 inner product on $X \subset \mathbb{R}^d$, and $\langle a, b \rangle_X = \int_X a b \, dx'$ denotes the L^2 inner product on $X \subset \mathbb{R}^{d-1}$. The jump and averaging operators are defined as $\llbracket \cdot \rrbracket = (\cdot)^2 - (\cdot)^1$ and $\{ \cdot \} = \gamma^1 (\cdot)^1 + \gamma^2 (\cdot)^2$ respectively. The constants γ_u , γ^1 , and γ^2 determine the accuracy with which the interface conditions are satisfied. Following the work by Annavarapu et al. (2012), we define these constants as

$$\begin{aligned} \gamma_u &= 2 c_{\Gamma_u} \frac{\text{meas}(\Gamma_{12})}{\text{meas}(\Omega^1)/k^1 + \text{meas}(\Omega^2)/k^2}, \\ \gamma^m &= \frac{\text{meas}(\Omega^m)/k^m}{\text{meas}(\Omega^1)/k^1 + \text{meas}(\Omega^2)/k^2}, \end{aligned} \tag{11}$$

where c_{Γ_u} is a user-defined constant and determines how strongly the interface constraints in (4) are enforced. A high penalty on c_{Γ_u} may ensure more accuracy but at the cost of system stability. The operator $\text{meas}(\cdot)$ refers to the magnitude of the respective quantity.

For the steady incompressible Navier-Stokes equations (5–6), we follow the approach of Schott and Wall (2014) to satisfy the interface conditions (7). Thus, the weak form is stated as: Find $\mathbf{v}^1 \in \mathcal{U}^1$, $p^1 \in \mathcal{U}^1$ such that, $\mathbf{v}^1 = u_D$ on Γ_D and

$$\begin{aligned} \mathcal{R}^{NS} &= \mathcal{R}_\Omega^{NS} + \mathcal{R}_{\Gamma_N}^{NS} + \mathcal{R}_{\Gamma_{12}}^{NS} = 0, \\ \forall \boldsymbol{\omega}^1 \in \mathcal{V}^1, \forall \eta^1 \in \mathcal{V}^1. \end{aligned} \tag{12}$$

Here, \mathcal{R}_Ω^{NS} is the residual of the volumetric contribution from (5), $\mathcal{R}_{\Gamma_N}^{NS}$ is the residual contribution from the Neumann boundary, and $\mathcal{R}_{\Gamma_{12}}^{NS}$ is the residual contribution from



the interface conditions presented in (6). These residual contributions are given by

$$\begin{aligned}\mathcal{R}_{\Omega^S}^{NS} &= \left(\boldsymbol{\omega}^1, \rho^1 \mathbf{v}^1 \cdot \nabla \mathbf{v}^1\right)_{\Omega^1} \\ &\quad + \left(\boldsymbol{\epsilon} \left(\boldsymbol{\omega}^1\right), 2\mu^1 \boldsymbol{\epsilon} \left(\mathbf{v}^1\right)\right)_{\Omega^1} - \left(\nabla \cdot \boldsymbol{\omega}^1, p^1\right)_{\Omega^1} \\ &\quad + \left(\boldsymbol{\eta}^1, \nabla \cdot \mathbf{v}^1\right)_{\Omega^1}, \\ \mathcal{R}_{\Gamma_N}^{NS} &= -\left(\boldsymbol{\omega}^1, \mathbf{t}_N\right)_{\Gamma_N}, \\ \mathcal{R}_{\Gamma_{12}}^{NS} &= -\left(\boldsymbol{\omega}^1, \boldsymbol{\sigma} \left(\mathbf{v}^1, p^1\right) \cdot \mathbf{n}_{\Gamma}\right)_{\Gamma_{12}} \\ &\quad - \left(\boldsymbol{\sigma} \left(\boldsymbol{\omega}^1, p^1\right) \cdot \mathbf{n}_{\Gamma}, \mathbf{v}^1\right)_{\Gamma_{12}} \\ &\quad + \gamma_v \left(\boldsymbol{\omega}^1, \mathbf{v}^1\right)_{\Gamma_{12}}.\end{aligned}\quad (13)$$

The constant γ_v determines the accuracy with which the interface condition is satisfied. Following the work by Schott and Wall (2014), we define γ_v as

$$\gamma_v = c_{\Gamma_v} \frac{\mu^1}{h}, \quad (14)$$

where h is the element size, and c_{Γ_v} is a user-defined constant and determines how strongly the interface constraints in (4) are enforced. A high penalty on c_{Γ_v} may ensure more accuracy but at the cost of system stability.

The convective term in (5) is known to cause node to node oscillations in the velocity field. Furthermore, we interpolate the velocity and pressure field using trilinear (in 3D) basis functions. This equal order interpolation gives rise to instability in the pressure field. To increase the stability of the system of equations, we augment (13) with SUPG (streamline-upwind/Petrov-Galerkin) and PSPG (pressure stabilizing/Petrov-Galerkin) terms introduced by Tezduyar et al. (1992).

3 Heaviside-enriched XFEM

In order to accurately capture non-smooth solutions across material interfaces, the traditional finite element method requires a mesh that conforms to the design geometry. The XFEM eliminates this requirement by augmenting the standard finite element interpolation by additional enrichment functions to capture discontinuities in either the state variables or their spatial gradients within an element. Following the work by Terada et al. (2003), Hansbo and Hansbo (2004), and Makhija and Maute (2014), a generalized Heaviside enrichment strategy with multiple enrichment levels is adopted to ensure that the solution field is interpolated in a consistent manner, and to avoid any artificial coupling due to disconnected material phases. This enrichment strategy has been successfully applied to incompressible Navier-Stokes problems by Kreissl and Maute (2012), to

heat diffusion by Lang et al. (2014), to linear elasticity by Makhija and Maute (2014), Villanueva and Maute (2014) and Lang et al. (2015), to fluid-structure interaction problems by Jenkins and Maute (2015), and to convection problems by Coffin and Maute (2016a, b).

For a two-phase problem, the approximation of solution field, $u(\mathbf{x})$, denoted as $\hat{u}(\mathbf{x})$, using the Heaviside-enriched XFEM is given by

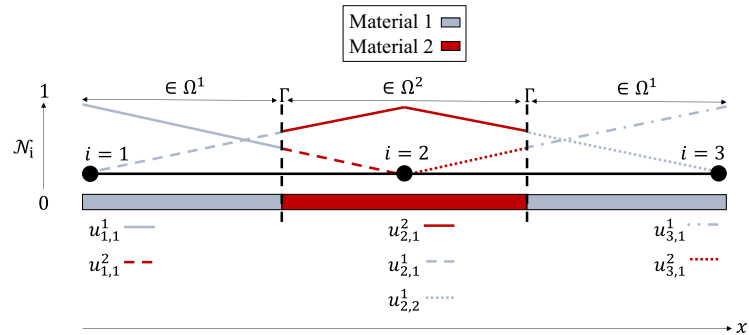
$$\hat{u}(\mathbf{x}) = \begin{cases} \sum_{e=1}^{\Psi} \left(\sum_{i \in I} \mathcal{N}_i(\mathbf{x}) u_{i,e}^1 \delta_{el}^{1,i} \right) & \text{if } \mathbf{x} \in \Omega^1 \\ \sum_{e=1}^{\Psi} \left(\sum_{i \in I} \mathcal{N}_i(\mathbf{x}) u_{i,e}^2 \delta_{el}^{2,i} \right) & \text{if } \mathbf{x} \in \Omega^2, \end{cases} \quad (15)$$

where I is the set of all nodes within the finite element mesh, $\mathcal{N}_i(\mathbf{x})$ is the nodal basis function associated with node i , Ψ is the maximum number of enrichment levels and $u_{i,e}^m$ is the degree of freedom at node i for phase $m \in (1, 2)$. The Kronecker delta $\delta_{el}^{m,i}$ selects the active enrichment level, l , for node i and material phase m such that only one set of degrees of freedom is used for interpolating the solution at any given point, \mathbf{x} in Ω , thereby satisfying the partition of unity principle introduced by Babuška and Melenk (1997).

Figure 4 presents an intersection configuration comprising of two finite elements in 1D. Linear nodal basis functions, \mathcal{N}_i , have been plotted over each element. Below each node, the active set of degrees of freedom have been stated corresponding to (15). Nodes 1 and 3 belong to material phase 1 whereas node 2 belongs to material phase 2. Nodes 1 and 3 interpolate in each material phase using only one degree of freedom per phase. Node 2 interpolates in material phase 2 using one degree of freedom. However, for a consistent interpolation in phase 1, node 2 requires two degrees of freedom as the support of \mathcal{N}_2 includes two disconnected regions of material phase 1. For a more comprehensive understanding of the adopted enrichment strategy, the reader is referred to the study by Makhija and Maute (2014).

The Heaviside-enriched XFEM requires integrating the weak form of the governing equations separately in each material phase. To this end, an element intersected by the zero level set contour is subdivided as shown in Fig. 5. In 2D and 3D, this subdivision is typically carried out using Delaunay triangulation. Integration over these subdivisions require the identification of three distinct configurations. Figure 5 presents the mapping between three different configurations for an intersected element in 1D. An element in the global coordinate system (Elemental Configuration) is mapped to an element in its natural coordinate system (Natural Configuration) with coordinates ranging between $\xi_A^0 = -1$ and $\xi_B^0 = 1$. The subdivided elements in the Natural Configuration are further mapped to integration subdomains (Integration Configuration) with coordinates for each subdomain ranging between $\xi' = -1$ and $\xi' = 1$. Using a linear

Fig. 4 Interpolation of solution field using generalized Heaviside enrichment



interpolation scheme for approximation, the solution field, \hat{u} , is defined through the following 1D maps:

$$\hat{u}(x_k) = \mathcal{N}_A(\xi_k^0)u_A + \mathcal{N}_B(\xi_k^0)u_B, \tag{16}$$

with

$$\xi_k^0 = \begin{cases} \mathcal{N}_A(\xi_i')\xi_A^0 + \mathcal{N}_B(\xi_i')\xi_\Gamma^0 & x \in \Omega^1 \\ \mathcal{N}_A(\xi_j')\xi_\Gamma^0 + \mathcal{N}_B(\xi_j')\xi_B^0 & x \in \Omega^2. \end{cases} \tag{17}$$

The maps presented in (16) and (17) are revisited for deriving shape sensitivities in Section 4.2.

The generalized Heaviside enrichment strategy allows for each disconnected region of the same phase to be approximated by an independent set of nodal degrees of freedom. If the support of a nodal basis function is intersected by the interface as in Fig. 4, by construction, the solution (15) is discontinuous across the interface. Figure 6 presents an example of variation in the degrees of freedom leading to a strong discontinuity in the solution field, $\hat{u}(x)$. The presence of such a discontinuity presents the primary motivation to investigate the behavior of shape sensitivities within the context of Heaviside-enriched XFEM.

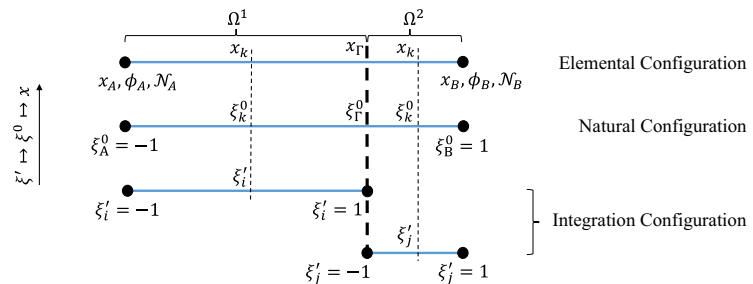
The generalized Heaviside enrichment strategy requires that the material interface does not intersect a node. This is achieved by shifting the material interface, x_Γ , when the interface comes within a critical distance of a node, referred to as the critical shift distance, x_{Γ_c} . The interface is shifted

such that the new interface position is at a distance, x_{Γ_c} from the node. The different options for shifting the material interface include: i) Phase 1 Shift (P1S), such that upon shifting x_Γ , the previously intersected node lies in phase 1, ii) Phase 2 Shift (P2S), such that upon shifting x_Γ , the previously intersected node lies in phase 2, and iii) Phase Maintaining Shift (PMS), wherein upon shifting x_Γ , the node retains its phase. In the scenario when x_Γ lies exactly on a node, we resort to P1S. Figure 7 presents a schematic depicting the change in intersection configuration when performing the various shifts. Effects of shifting the material interface on the response function and its sensitivities are further discussed in Section 5.1.2.

4 Shape sensitivities

Ways to calculate the shape sensitivities include finite difference, the direct, and the adjoint method. The finite difference method is the most straightforward approach and involves perturbing the shape parameter of interest and re-analyzing the response of the model for the perturbed values. In the direct approach, sensitivities are computed by differentiating the governing equations analytically using chain rule and solving a linear system for every shape parameter involved. In contrast, the adjoint method requires that a linear system of equations be solved as many times as the number of response functions. For CAD-free and topology optimization problems, the number of design variables

Fig. 5 Mapping of integration domains for an intersected element



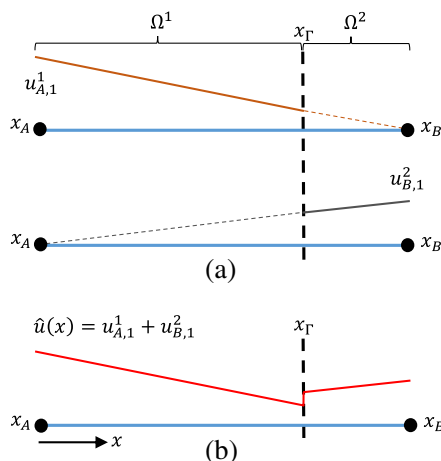


Fig. 6 **a** Variation in degrees of freedom in an element intersected by the material interface; **b** Solution field, $\hat{u}(x)$, approximated using (15)

typically far exceeds the number of response functions. Therefore we adopt the adjoint method for computing shape sensitivities. However, findings from the current study also apply to the direct method.

In the current study the vector of design variables, s , is a set of parameters that define the design geometry. For instance, in Section 5.1.2 the radius of the circular inclusion serves as the design variable. We begin by defining a response function that takes the form

$$\mathcal{Z}(\mathbf{u}, s) = \int_{\Omega^m} \mathcal{G}(\mathbf{u}, s) dx + \int_{\partial\Omega^m} \mathcal{G}'(\mathbf{u}, s) dx', \tag{18}$$

where \mathbf{u} denotes the physical solution evaluated over the complete spatial domain, Ω . The continuous function, \mathcal{G} ,

is defined over the material subdomain Ω^m . The continuous function, \mathcal{G}' exists only on the material boundaries. In the context of variational design sensitivity analysis, we follow the work by Materna and Barthold (2008) to define the response function using volume and surface reference configurations defined over the domains Ω_0 and $\partial\Omega_0$ with coordinates Θ and Θ' respectively as shown in Fig. 8. The response function in reference configuration is then given by

$$\mathcal{Z}(\mathbf{u}, s) = \int_{\Omega_0} \mathcal{G}(\mathbf{u}, s) \left| \frac{\partial \mathbf{x}}{\partial \Theta} \right| d\Theta + \int_{\partial\Omega_0} \mathcal{G}'(\mathbf{u}, s) \left| \frac{\partial \mathbf{x}}{\partial \Theta'} \right| d\Theta'. \tag{19}$$

Here, $|\partial \mathbf{x} / \partial \Theta|$ and $|\partial \mathbf{x} / \partial \Theta'|$ are the determinants of the matrices constituting the maps $\Omega_0 \mapsto \Omega^m$ and $\partial\Omega_0 \mapsto \partial\Omega^m$ respectively. Note that the design variables affect these determinants which depend on the definition of the design geometry. The design variables may also affect the material properties, in which case \mathcal{G} and \mathcal{G}' depend explicitly on s . In a similar fashion to (19), the residual function, \mathcal{R} , from Section 2.4 can be expressed as

$$\mathcal{R}(\mathbf{v}, \mathbf{u}, s) = \int_{\Omega_0} \mathcal{F}(\mathbf{v}, \mathbf{u}, s) \left| \frac{\partial \mathbf{x}}{\partial \Theta} \right| d\Theta + \int_{\partial\Omega_0} \mathcal{F}'(\mathbf{v}, \mathbf{u}, s) \left| \frac{\partial \mathbf{x}}{\partial \Theta'} \right| d\Theta', \tag{20}$$

where \mathcal{F} and \mathcal{F}' are defined over Ω^m and $\partial\Omega^m$ respectively, and assume the form of the residual contribution equations presented in Section 2.4. The set of admissible test functions is denoted by \mathbf{v} .

We augment (19) with (20) to introduce a Lagrangian functional, \mathcal{L} , such that

$$\begin{aligned} \mathcal{L}(\boldsymbol{\lambda}, \mathbf{u}, s) &= \mathcal{Z}(\mathbf{u}, s) + \mathcal{R}(\boldsymbol{\lambda}, \mathbf{u}, s) \\ &= \int_{\Omega_0} \mathcal{G}(\mathbf{u}, s) \left| \frac{\partial \mathbf{x}}{\partial \Theta} \right| d\Theta \\ &\quad + \int_{\partial\Omega_0} \mathcal{G}'(\mathbf{u}, s) \left| \frac{\partial \mathbf{x}}{\partial \Theta'} \right| d\Theta' \\ &\quad + \int_{\Omega_0} \mathcal{F}(\boldsymbol{\lambda}, \mathbf{u}, s) \left| \frac{\partial \mathbf{x}}{\partial \Theta} \right| d\Theta \\ &\quad + \int_{\partial\Omega_0} \mathcal{F}'(\boldsymbol{\lambda}, \mathbf{u}, s) \left| \frac{\partial \mathbf{x}}{\partial \Theta'} \right| d\Theta'. \end{aligned} \tag{21}$$

Here $\boldsymbol{\lambda}$ is the vector of adjoint variables which assume the role of test functions for the residual equations in Section 2.4, i.e. $\mathbf{v} = \boldsymbol{\lambda}$. We seek stationary points of \mathcal{L} that

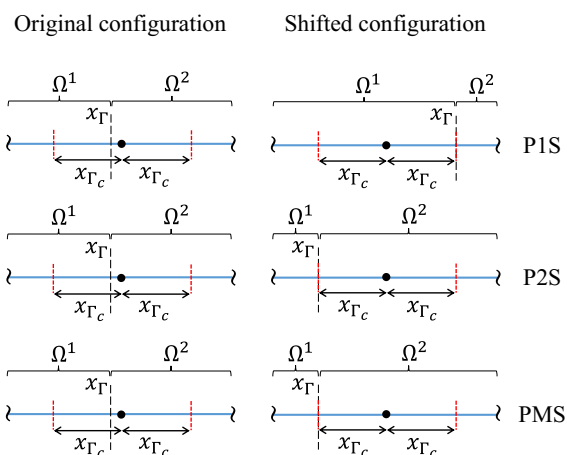
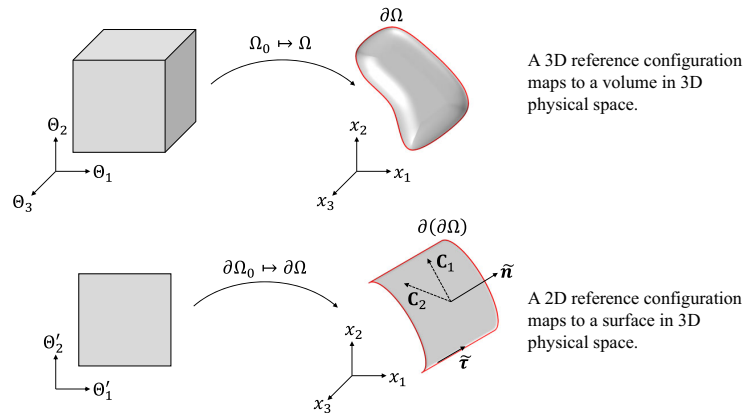


Fig. 7 Interface shift schematic

Fig. 8 Mapping between reference configurations and physical space



satisfy equilibrium. Thus, taking the variation of (21) with respect to λ and \mathbf{u} yields:

$$\begin{aligned} \delta\lambda \frac{\partial \mathcal{L}}{\partial \lambda} = 0 &\implies \int_{\Omega_0} \delta\lambda \frac{\partial \mathcal{F}}{\partial \lambda} \left| \frac{\partial \mathbf{x}}{\partial \Theta} \right| d\Theta \\ &+ \int_{\partial\Omega_0} \delta\lambda \frac{\partial \mathcal{F}'}{\partial \lambda} \left| \frac{\partial \mathbf{x}}{\partial \Theta'} \right| d\Theta' = 0. \\ \delta\mathbf{u} \frac{\partial \mathcal{L}}{\partial \mathbf{u}} = 0 &\implies \int_{\Omega_0} \delta\mathbf{u} \frac{\partial \mathcal{G}}{\partial \mathbf{u}} \left| \frac{\partial \mathbf{x}}{\partial \Theta} \right| d\Theta \\ &+ \int_{\partial\Omega_0} \delta\mathbf{u} \frac{\partial \mathcal{G}'}{\partial \mathbf{u}} \left| \frac{\partial \mathbf{x}}{\partial \Theta'} \right| d\Theta' \\ &+ \int_{\Omega_0} \delta\mathbf{u} \frac{\partial \mathcal{F}}{\partial \mathbf{u}} \left| \frac{\partial \mathbf{x}}{\partial \Theta} \right| d\Theta \\ &+ \int_{\partial\Omega_0} \delta\mathbf{u} \frac{\partial \mathcal{F}'}{\partial \mathbf{u}} \left| \frac{\partial \mathbf{x}}{\partial \Theta'} \right| d\Theta' = 0. \end{aligned} \quad (22)$$

The first equation in (22) is known as the primal problem, and vanishes if the governing equations are satisfied. The second equation in (22) constitutes the adjoint problem. Thus, the vector of adjoint variables, λ , is the solution satisfying the linear system of equations:

$$\begin{aligned} &\int_{\Omega_0} \frac{\partial \mathcal{F}}{\partial \mathbf{u}} \left| \frac{\partial \mathbf{x}}{\partial \Theta} \right| d\Theta + \int_{\partial\Omega_0} \frac{\partial \mathcal{F}'}{\partial \mathbf{u}} \left| \frac{\partial \mathbf{x}}{\partial \Theta'} \right| d\Theta' \\ &= - \left(\int_{\Omega_0} \frac{\partial \mathcal{G}}{\partial \mathbf{u}} \left| \frac{\partial \mathbf{x}}{\partial \Theta} \right| d\Theta + \int_{\partial\Omega_0} \frac{\partial \mathcal{G}'}{\partial \mathbf{u}} \left| \frac{\partial \mathbf{x}}{\partial \Theta'} \right| d\Theta' \right). \end{aligned} \quad (23)$$

The complexity of solving the adjoint equation is equal to solving a linear system of equations for each response function. Using the solution obtained from (23), the shape

sensitivities with respect to the design variable, s , are then computed by differentiating (21) with respect to s .

$$\begin{aligned} \frac{\partial \mathcal{L}}{\partial s} = \frac{\partial \mathcal{Z}}{\partial s} + \frac{\partial \mathcal{R}}{\partial s} &= \int_{\Omega_0} \frac{\partial}{\partial s} \left(\mathcal{G} \left| \frac{\partial \mathbf{x}}{\partial \Theta} \right| \right) d\Theta \\ &+ \int_{\partial\Omega_0} \frac{\partial}{\partial s} \left(\mathcal{G}' \left| \frac{\partial \mathbf{x}}{\partial \Theta'} \right| \right) d\Theta' \\ &+ \int_{\Omega_0} \frac{\partial}{\partial s} \left(\mathcal{F} \left| \frac{\partial \mathbf{x}}{\partial \Theta} \right| \right) d\Theta \\ &+ \int_{\partial\Omega_0} \frac{\partial}{\partial s} \left(\mathcal{F}' \left| \frac{\partial \mathbf{x}}{\partial \Theta'} \right| \right) d\Theta'. \end{aligned} \quad (24)$$

Recall that the adjoint variable is absorbed in the definition of \mathcal{R} , and thus in the definitions of \mathcal{F} and \mathcal{F}' . Based on (24), the shape sensitivities depend on: i) variation of the response function, \mathcal{Z} , with respect to the design variables and ii) the variation of the residual of the system of equations, \mathcal{R} , with respect to the design variables. The dependency of \mathcal{R} on s can be decomposed into explicit and implicit parts such that,

$$\frac{\partial \mathcal{R}}{\partial s} = \frac{\partial \mathcal{R}}{\partial s} + \frac{\partial \mathcal{R}}{\partial \mathbf{x}_\Gamma} \frac{\partial \mathbf{x}_\Gamma}{\partial s}. \quad (25)$$

While it is straightforward to determine the explicit dependency of the response function on the design variable, it is less obvious how the residual behaves with respect to the design variable within the context of the Heaviside-enriched XFEM. In the ensuing discussion, we present and investigate two contrasting approaches to computing the residual derivative. For simplicity throughout the derivation we will consider only one design variable, thus reducing the vector of design variables to a scalar, s .

4.1 A continuum approach to evaluating the residual derivative, $\partial \mathcal{R} / \partial s$

This approach to computing the shape sensitivities involves differentiating the residual of the system of equations, \mathcal{R} ,

with respect to the design variable, s , followed by the discretization of the resulting expressions. Using a reference configuration as in Fig. 8, we derive separately, the residual derivative for volumetric and surface functions. Expressions derived in this section are well known within the shape optimization community, and are presented here for completeness. Interested readers are referred to works by Sokolowski and Zolésio (1992), Delfour and Zolésio (2011), and Walker (2015) for further details.

4.1.1 Contribution to residual functions defined in Ω^m

Without any loss in generality, the volume contribution of the residual function, \mathcal{R}_Ω takes the form

$$\mathcal{R}_\Omega = \int_{\Omega_0} \mathcal{F}(\mathbf{x}(\Theta, s), s) \left| \frac{\partial \mathbf{x}}{\partial \Theta} \right| d\Theta, \tag{26}$$

where \mathcal{F} represents of any of the integrands in (10) or (13), defined in Ω^m . The derivative of the residual function with respect to the design variable is then given by

$$\begin{aligned} \frac{\partial \mathcal{R}_\Omega}{\partial s} &= \int_{\Omega_0} \left(\frac{\partial \mathcal{F}}{\partial s} + \nabla \mathcal{F} \cdot \frac{\partial \mathbf{x}}{\partial s} \right) \left| \frac{\partial \mathbf{x}}{\partial \Theta} \right| d\Theta \\ &+ \int_{\Omega_0} \mathcal{F} \frac{\partial}{\partial s} \left(\left| \frac{\partial \mathbf{x}}{\partial \Theta} \right| \right) d\Theta. \end{aligned} \tag{27}$$

Note that the only points in space that are design dependent lie along the material boundary. As a result, $\partial \mathbf{x} / \partial s = 0$ everywhere except along the material boundary. The third term in (27) is evaluated using Jacobi's formula for the derivative of a determinant to give

$$\begin{aligned} \frac{\partial \mathcal{R}_\Omega}{\partial s} &= \int_{\Omega_0} \left(\frac{\partial \mathcal{F}}{\partial s} + \nabla \mathcal{F} \cdot \mathbf{V} \right) \left| \frac{\partial \mathbf{x}}{\partial \Theta} \right| d\Theta \\ &+ \int_{\Omega_0} \mathcal{F} \nabla \cdot \mathbf{V} \left| \frac{\partial \mathbf{x}}{\partial \Theta} \right| d\Theta \\ &= \int_{\Omega_0} \left(\frac{\partial \mathcal{F}}{\partial s} + \nabla \cdot (\mathcal{F} \mathbf{V}) \right) \left| \frac{\partial \mathbf{x}}{\partial \Theta} \right| d\Theta. \end{aligned} \tag{28}$$

where $\mathbf{V} = \partial \mathbf{x} / \partial s$ denotes the boundary velocity vector which may or may not be of constant magnitude along the boundary. Applying the divergence theorem for a vector field to the second term in (28), and mapping the terms from reference configuration back to the physical space, the residual derivative takes the form,

$$\begin{aligned} \frac{\partial \mathcal{R}_\Omega}{\partial s} &= \int_{\Omega_0} \frac{\partial \mathcal{F}}{\partial s} \left| \frac{\partial \mathbf{x}}{\partial \Theta} \right| d\Theta \\ &+ \int_{\partial \Omega_0} \mathcal{F} \mathbf{V} \cdot \tilde{\mathbf{n}} \left| \frac{\partial \mathbf{x}}{\partial \Theta} \right| d\Theta' \\ &= \int_{\Omega^m} \frac{\partial \mathcal{F}}{\partial s} d\mathbf{x} + \int_{\partial \Omega^m} \mathcal{F} \mathbf{V} \cdot \tilde{\mathbf{n}} d\mathbf{x}'. \end{aligned} \tag{29}$$

Here, $\tilde{\mathbf{n}}$ is the outward unit normal vector depicted in Fig. 8. The second expression in (29) is commonly referred to as Hadamard's structure theorem (Delfour and Zolésio 1992) which states that shape sensitivities, for functions defined in Ω^m , depend only on the normal component of the deformations at the material boundary, $\partial \Omega^m$.

Unless the governing equations depend explicitly on the design variables, the first term in (29) vanishes. As a result, often only the second term needs to be computed. This however is not the case if using a C^0 -continuous enrichment wherein the enrichment function itself depends explicitly on the design variables. While integrating over the material boundary, $\partial \Omega^m$, only the velocity vector, \mathbf{V} , is design dependent. As a result in a discretized setting, the second term in (29) vanishes for elements not intersected by the material interface.

4.1.2 Contribution to residual functions defined on $\partial \Omega^m$

For boundary terms in the governing equations, including those defined over the material interface, the residual function \mathcal{R}_Γ takes the form

$$\begin{aligned} \mathcal{R}_\Gamma &= \int_{\partial \Omega_0} \mathcal{F}'(\mathbf{x}(\Theta', s), s) \|\mathbf{C}_1 \times \mathbf{C}_2\| d\Theta'; \\ \mathbf{C}_1 &= \frac{\partial \mathbf{x}}{\partial \Theta'_1}; \mathbf{C}_2 = \frac{\partial \mathbf{x}}{\partial \Theta'_2}, \end{aligned} \tag{30}$$

where \mathcal{F}' represents any of the integrands in (10) or (13), defined over $\partial \Omega^m$ including Γ_{12} . The tangent vectors are denoted by \mathbf{C}_1 and \mathbf{C}_2 , as depicted in Fig. 8. Following the chain rule in (27), the derivative of \mathcal{R}_Γ with respect to the design variable takes the form

$$\begin{aligned} \frac{\partial \mathcal{R}_\Gamma}{\partial s} &= \int_{\partial \Omega_0} \frac{\partial \mathcal{F}'}{\partial s} \|\mathbf{C}_1 \times \mathbf{C}_2\| d\Theta' \\ &+ \int_{\partial \Omega_0} \mathbf{V} \cdot \nabla_\Gamma \mathcal{F}' \|\mathbf{C}_1 \times \mathbf{C}_2\| d\Theta' \\ &+ \int_{\partial \Omega_0} \mathcal{F}' \frac{\partial \|\mathbf{C}_1 \times \mathbf{C}_2\|}{\partial s} d\Theta', \end{aligned} \tag{31}$$

where ∇_Γ is the surface divergent operator. Using the identities for surface mapping as presented, for example, by Walker (2015), (31) is mapped back to the physical space to give

$$\begin{aligned} \frac{\partial \mathcal{R}_\Gamma}{\partial s} &= \int_{\partial \Omega^m} \frac{\partial \mathcal{F}'}{\partial s} d\mathbf{x}' + \int_{\partial \Omega^m} \mathbf{V} \cdot \nabla_\Gamma \mathcal{F}' d\mathbf{x}' \\ &+ \int_{\partial \Omega^m} \mathcal{F}' \nabla_\Gamma \cdot \mathbf{V} d\mathbf{x}' \\ &= \int_{\partial \Omega^m} \left(\frac{\partial \mathcal{F}'}{\partial s} + \nabla_\Gamma \cdot (\mathcal{F}' \mathbf{V}) \right) d\mathbf{x}'. \end{aligned} \tag{32}$$



Applying integration by parts to $\nabla_\Gamma \cdot ()$, (32) is expanded into a normal and tangential component such that

$$\frac{\partial \mathcal{R}_\Gamma}{\partial s} = \int_{\partial \Omega^m} \left(\frac{\partial \mathcal{F}'}{\partial s} + \mathcal{F}' \mathcal{K} (\mathbf{V} \cdot \tilde{\mathbf{n}}) \right) dx' + \int_{\partial(\partial \Omega^m)} \mathcal{F}' (\tilde{\boldsymbol{\tau}} \times \tilde{\mathbf{n}}) \cdot \mathbf{V} dx'' \tag{33}$$

Here, $\mathcal{K} = -(\nabla_\Gamma \cdot \tilde{\mathbf{n}})/2$ is the mean curvature of the surface $\partial \Omega^m$, $\partial(\partial \Omega^m)$ is the boundary to the surface $\partial \Omega^m$ as highlighted in Fig. 8, and $\tilde{\boldsymbol{\tau}}$ is a unit tangent vector on $\partial(\partial \Omega^m)$ such that $\tilde{\boldsymbol{\tau}} \times \tilde{\mathbf{n}}$ points out of $\partial \Omega^m$. The second and third term in (33) quantify the normal and tangential components respectively, of the shape change for functions defined on the boundary. Note that the tangential component vanishes if Ω^m represents a closed domain. The curvature, \mathcal{K} , in the context of implicit curves and surfaces can be computed as described by Goldman (2005).

As is evident from (33), the sensitivities for functions defined on $\partial \Omega^m$ assume a more involved form resulting from quantifying the change in the map, $\partial \Omega \mapsto \Theta'$, with respect to the design variable. Unlike the case for functions defined in Ω^m , the derivative $\partial \mathcal{F}' / \partial s$ does not vanish in most scenarios. For instance, the weighting parameters in (11) depend on the position and size of the material interface.

4.2 A discrete approach to evaluating the residual derivative, $\partial \mathcal{R} / \partial s$

In contrast to the continuum approach, this approach involves discretization of the residual of the system of equations, followed by differentiation with respect to the design variable, s . We decompose (25) on an elemental level to obtain the discretized residual derivatives such that

$$\frac{\partial \hat{\mathcal{R}}}{\partial s} = \sum_{e \in N_e} \frac{\partial \hat{\mathcal{R}}_e}{\partial s} + \sum_{e \in N_e} \sum_{k=1}^{N_\Gamma} \frac{\partial \hat{\mathcal{R}}_e}{\partial \mathbf{x}_\Gamma^k} \mathbf{v}^k, \tag{34}$$

where N_e is the set of all elements that constitute the finite element mesh, and N_Γ is the number of interfaces present within the element e . Note that $\partial \hat{\mathcal{R}}_e / \partial \mathbf{x}_\Gamma^k$ vanishes for elements not intersected by the material interface. As in the previous section, we proceed by deriving the residual derivatives for functions defined over Ω^m followed by residual derivatives for functions defined over $\partial \Omega^m$. We illustrate the derivation using the 1D configuration shown in Fig. 5.

4.2.1 Contribution to residual functions defined on Ω^m

To maintain coherence of the derivation, we consider only the phase 1 residual contribution of the intersected element in Fig. 5. Assuming a function \mathcal{F} , that may take the form of

any of the terms evaluated over Ω_m in (10) or (13), the elemental residual contribution from phase 1 is then expressed as

$$\mathcal{R}_{e\Omega} = \int_{x_A}^{x_\Gamma} \mathcal{F}(x, s) dx = \int_{-1}^1 \mathcal{F}(\xi^0(\xi'), s) \frac{|x_\Gamma - x_A|}{2} d\xi', \tag{35}$$

The above equation is evaluated at specific integration points to arrive at the discretized form of the residual function given by

$$\hat{\mathcal{R}}_{e\Omega} = \sum_{i=1}^{N_{ip}} w_i \hat{\mathcal{F}}(\xi^0(\xi'), s) \Big|_{\xi'_i} \frac{|x_\Gamma - x_A|}{2}, \tag{36}$$

where N_{ip} is the number of integration points with associated weights, w_i . The finite element approximation of \mathcal{F} , based on (15), is given by $\hat{\mathcal{F}}$. The material interface, x_Γ is approximated based on (16) such that

$$x_\Gamma = \mathcal{N}_A(\xi_\Gamma^0) x_A + \mathcal{N}_B(\xi_\Gamma^0) x_B. \tag{37}$$

We now proceed to derive the derivatives of the discretized residual function in (36) with respect to the design variable, s . Based on (34), we express the residual derivative contribution at an elemental level as

$$\frac{\partial \hat{\mathcal{R}}_{e\Omega}}{\partial s} + \frac{\partial \hat{\mathcal{R}}_{e\Omega}}{\partial x_\Gamma} \mathbf{v} = \sum_{i=1}^{N_{ip}} w_i \frac{\partial \hat{\mathcal{F}}}{\partial s} \Big|_{\xi'_i} \frac{|x_\Gamma - x_A|}{2} + \sum_{i=1}^{N_{ip}} w_i \frac{\partial}{\partial x_\Gamma} \left(\hat{\mathcal{F}} \Big|_{\xi'_i} \frac{|x_\Gamma - x_A|}{2} \right) \mathbf{v}. \tag{38}$$

The first term in (38) is analogous to the first term in (27) and accounts for the explicit dependency of the governing equations on the design variable. The second term accounts for the change in the elemental residual with respect to the material interface position due to change in design. Making use of (17) and (37), we expand further, the derivative of the residual with respect to the interface position as shown below.

$$\begin{aligned} \frac{\partial \hat{\mathcal{R}}_{e\Omega}}{\partial x_\Gamma} &= \sum_{i=1}^{N_{ip}} w_i \frac{\partial \hat{\mathcal{F}}}{\partial x_\Gamma} \Big|_{\xi'_i} \frac{|x_\Gamma - x_A|}{2} + \sum_{i=1}^{N_{ip}} w_i \hat{\mathcal{F}} \Big|_{\xi'_i} \frac{1}{2} \\ &= \sum_{i=1}^{N_{ip}} w_i \frac{\partial \hat{\mathcal{F}}}{\partial \xi_\Gamma^0} \Big|_{\xi'_i} \frac{\partial \xi_\Gamma^0}{\partial x_\Gamma} \Big|_{\xi'_i} \frac{|x_\Gamma - x_A|}{2} \\ &\quad + \sum_{i=1}^{N_{ip}} w_i \hat{\mathcal{F}} \Big|_{\xi'_i} \frac{1}{2} \end{aligned} \tag{39}$$



where,

$$\begin{aligned} \frac{\partial \hat{\mathcal{F}}}{\partial \xi_\Gamma^0} \Big|_{\xi'_i} &= \frac{\partial \hat{\mathcal{F}}}{\partial \xi^0} \Big|_{\xi'_i} \frac{\partial \xi^0}{\partial \xi_\Gamma^0} \Big|_{\xi'_i} = \frac{\partial \hat{\mathcal{F}}}{\partial \xi^0} \Big|_{\xi'_i} \mathcal{N}_B(\xi'_i) \\ \frac{\partial \xi_\Gamma^0}{\partial x_\Gamma} &= \frac{\partial \xi^0}{\partial x} \Big|_{\Gamma_{12}} = \left(\frac{\partial \mathcal{N}_A}{\partial \xi^0} x_A + \frac{\partial \mathcal{N}_B}{\partial \xi^0} x_B \right)^{-1}. \end{aligned} \quad (40)$$

Here, ξ_Γ^0 is the material interface position in the Natural Configuration as shown in Fig. 5. The first and second terms in (39) are analogous to the second and third terms in (27) respectively. The derivative of the determinant of the mapping term, $|x_\Gamma - x_A|/2$, with respect to s is overly simplified in 1D. In higher dimensions, the complexity of determining and implementing the derivatives of the determinant of the mapping term increases as is seen in the study by Noël et al. (2016). The term $\partial \xi_\Gamma^0 / \partial x_\Gamma$ quantifies the change in the interface position in the Natural Configuration (see Fig. 5) with respect to the interface position in the Elemental Configuration. This indicates that the definition of the Integration Configuration is always relative to the position of the material interface. Note that $\partial \xi_\Gamma^0 / \partial x_\Gamma = \partial \xi^0 / \partial x \Big|_{\Gamma_{12}}$ is the inverse of the Jacobian mapping (Cook 1994) evaluated at the material interface, and is readily available during finite element computations. For a comparison against shape sensitivity analysis using a body-fitted mesh, the reader is referred to Appendix A.

Using the integration limits, x_Γ and x_B , the elemental residual derivative for phase 2 can be derived in the exact manner as described above. Using an appropriate set of maps, $(\xi')^d \mapsto (\xi^0)^d \mapsto (x)^d$, and integration subdomains (for instance, triangular subdomains for quad elements in 2D and tetrahedral subdomains for hexahedron elements in 3D), the proposed approach can be readily extended to $d > 1$ dimensions in space.

4.2.2 Contribution to residual functions defined on $\partial \Omega^m$

Assuming a function \mathcal{F}' , that may take the form of any of the terms evaluated over $\partial \Omega_m$ in (10) or (13) including Γ_{12} , the residual function in 1D takes the form

$$\begin{aligned} \mathcal{R}_{e_\Gamma} &= \int_{x_\Gamma} \mathcal{F}'(x, s) dx' \\ &= \int_{\xi_\Gamma^0} \mathcal{F}'(\xi^0(\xi'), s) d\xi'. \end{aligned} \quad (41)$$

Note that the material boundary in 1D collapses to a point. As a result, for functions defined on the material boundary, the residual derivative takes the form

$$\frac{\partial \hat{\mathcal{R}}_{e_\Gamma}}{\partial s} + \frac{\partial \hat{\mathcal{R}}_{e_\Gamma}}{\partial x_\Gamma} \frac{\partial x_\Gamma}{\partial s} = \frac{\partial \hat{\mathcal{F}}'}{\partial s} \Big|_{\xi'_i} + \frac{\partial \hat{\mathcal{F}}'}{\partial x_\Gamma} \Big|_{\xi'_i} \frac{\partial x_\Gamma}{\partial s}. \quad (42)$$

The second term in (42) is evaluated in a manner similar to that described in (39)–(40).

4.3 Choice of approach for evaluating $\partial \mathcal{R} / \partial s$

The choice of approach for computing $\partial \mathcal{R} / \partial s$ depends largely on the system of equations that needs to be solved as well as the generality and ease of implementation. The discretized approach, in higher dimensions, results in an involved derivation of the shape sensitivities due to the complexity of mapping between domains (17). The derivative of the mapping term with respect to design variables increases in complexity with the order of interpolation. The continuum approach on the other hand presents a more attractive option wherein the shape sensitivities for the volumetric terms can be computed conveniently using the second term in (29). However, for governing equations dependent on the design variables, the first term in (29) does not vanish. For terms defined at the interface, a map between an \mathbb{R}^d global domain and an \mathbb{R}^{d-1} reference domain is required as shown in Fig. 8. Accounting analytically for the change in this mapping with respect to design variables requires the computation of the curvature as demonstrated in (33). Computation of the curvature requires second order spatial derivatives (see Goldman 2005) which do not exist for lower order elements. Moreover, the dependency of certain interfacial terms, such as (11), on the interface position needs to be accounted for in the form of $\partial \mathcal{F}' / \partial s$.

As the preferred option in the current study we adopt a semi-analytical approach wherein great ease of implementation is achieved by finite differencing the term $\partial \hat{\mathcal{R}}_e / \partial x_\Gamma^k$ in (34), with a design perturbation size, Δ_{FD} :

$$\frac{\partial \hat{\mathcal{R}}}{\partial s} = \sum_{e \in N_e} \sum_{k=1}^{N_\Gamma} \sum_{i=1}^{N_{x_\Gamma}} \left(\frac{\hat{\mathcal{R}}_e \Big|_{x_{\Gamma_i}^k + \Delta_{FD}}}{2\Delta_{FD}} - \frac{\hat{\mathcal{R}}_e \Big|_{x_{\Gamma_i}^k - \Delta_{FD}}}{2\Delta_{FD}} \right) \mathbf{V}_{x_{\Gamma_i}}. \quad (43)$$

Alternatively, a hybrid scheme may be adopted wherein the continuum approach may be used for volumetric terms while the material boundary terms are subjected to finite differencing to give,

$$\begin{aligned} \frac{\partial \mathcal{R}}{\partial s} &= \int_{\Omega^m} \frac{\partial \mathcal{F}}{\partial s} dx + \int_{\partial \Omega^m} \mathcal{F} \mathbf{V} \cdot \tilde{\mathbf{n}} dx' \\ &+ \sum_{e \in N_e} \sum_{k=1}^{N_\Gamma} \sum_{i=1}^{N_{x_\Gamma}} \left(\frac{\hat{\mathcal{R}}_{e_\Gamma} \Big|_{x_{\Gamma_i}^k + \Delta_{FD}}}{2\Delta_{FD}} - \frac{\hat{\mathcal{R}}_{e_\Gamma} \Big|_{x_{\Gamma_i}^k - \Delta_{FD}}}{2\Delta_{FD}} \right) \mathbf{V}_{x_{\Gamma_i}}. \end{aligned} \quad (44)$$

The finite differencing in (43) and (44) is carried out by perturbing the individual edge intersection points, x_{Γ_i} , belonging to every intersected finite element, as shown in Fig. 9. Such a perturbation helps account for the arc length change, thus capturing the curvature related term in (33). In contrast, a global finite difference is achieved by perturbing the entire interface geometry via the design variable such that,

$$\frac{\partial \mathcal{Z}}{\partial s} = \frac{\int_{\Omega^m} \mathcal{G}|_{s+\Delta_{FD}} - \int_{\Omega^m} \mathcal{G}|_{s-\Delta_{FD}} dx}{2\Delta_{FD}} + \frac{\int_{\partial\Omega^m} \mathcal{G}'|_{s+\Delta_{FD}} - \int_{\partial\Omega^m} \mathcal{G}'|_{s-\Delta_{FD}} dx'}{2\Delta_{FD}} \quad (45)$$

Since we use the LSM to describe our interface geometry, we note an implication of computing the design velocity, $V = \partial x_{\Gamma} / \partial s$ using the level set field. Referring to Fig. 5, the interface position can be expressed in terms of the level set field such that,

$$x_{\Gamma} = x_A - \frac{x_B - x_A}{\phi_B - \phi_A} \phi_A. \quad (46)$$

The design velocity is then given by,

$$\frac{\partial x_{\Gamma}}{\partial s} \delta s = \frac{x_B - x_A}{(\phi_B - \phi_A)^2} \left(\phi_A \frac{\partial \phi_B}{\partial s} \delta s - \phi_B \frac{\partial \phi_A}{\partial s} \delta s \right). \quad (47)$$

To keep the design velocity from vanishing or becoming extremely large, it is important to maintain the gradient of the level set field at $|\nabla\phi| \approx 1$ i.e.,

$$\left| \frac{x_B - x_A}{\phi_B - \phi_A} \right| = |\nabla\phi| \approx 1. \quad (48)$$

5 Numerical examples

In this section, we present four numerical examples to discuss the behavior, such as smoothness and accuracy,

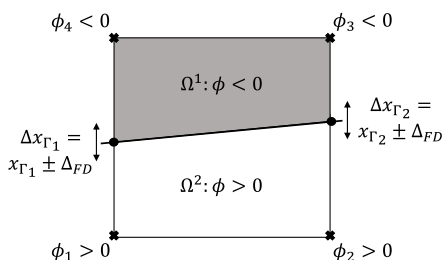


Fig. 9 Perturbing intersection points for finite differencing in (43) and (44)

of shape sensitivities within the framework of Heaviside-enriched XFEM. Examples 1 through 3 consider steady heat diffusion in 2D. The fourth example studies an incompressible fluid flow and showcases the applicability of the proposed framework to nonlinear systems in 3D. Through these examples we study the smoothness and accuracy of the XFEM-based shape sensitivities and its dependency on factors such as the choice of approach for evaluating $\partial R / \partial s$, interface conditions, and discretization of the interface geometry.

The 2D design domains are discretized in space using bilinear quadrilateral elements, and the 3D design domains are discretized using trilinear hexahedral elements. Unless mentioned otherwise, in all steady heat diffusion examples, an interface constraint penalty of $c_{\Gamma_u} = 1.0$ was used in (11). For the incompressible fluid flow example, we set the interface constraint penalty to $c_{\Gamma_v} = 1000$ in (14). To mitigate issues with ill-conditioning caused by an extremely small (or large) ratio of intersected areas within an intersected element, we use the geometric preconditioning scheme of Lang et al. (2014). The nonlinear problem of Section 5.4 is solved using Newton’s method. The linearized system of equations for all examples, of both the forward and the sensitivity analysis, are solved using a direct solver.

5.1 Example 1

We consider the two-phase problem setup shown in Fig. 10. A strip inclusion of conductivity $k_2 = 10$, is inclined at an angle θ to the vertical axis. This inclusion is embedded into a rectangular matrix of conductivity $k_1 = 1$. The center location of the strip is maintained constant at $\mathbf{x} = (15, 6)$. A Neumann boundary condition of $q_N = 1$ is applied along the left edge. A Dirichlet boundary condition of $u_D = 1$ is applied to the right edge. The top and bottom edges are adiabatic. The design variable, s , is half of the width of the strip inclusion, measured parallel to the horizontal axis.

The study of the current example is divided into three subsections. The first subsection establishes the accuracy of the proposed semi-analytical approach. Comparisons are made against i) finite differenced shape sensitivities, i.e. finite differencing $\partial Z / \partial s$ (45), ii) shape sensitivities computed using the hybrid approach of (44), and iii) shape sensitivities computed using a body-fitted mesh. The second subsection discusses the influence of shifting the interface

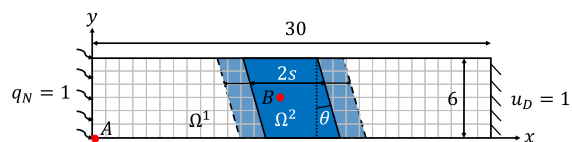


Fig. 10 Heat diffusion problem setup with strip inclusion

(Fig. 7) on the semi-analytically computed shape sensitivities. In the third subsection, we study the behavior of shape sensitivities when the response function is evaluated at a region that changes material phases over the course of design change.

5.1.1 Accuracy comparison of shape sensitivities

As described in Section 4.3, we adopt a semi-analytical approach to computing the shape sensitivities. In order to establish the accuracy of the proposed approach, we first use the problem setup of Fig. 10 with $\theta = 0^\circ$ to draw comparisons against finite differenced shape sensitivities as well as shape sensitivities computed using the hybrid approach of (44). The problem domain is discretized using a mesh size of $h = 1.0$. Shape sensitivities are recorded for every configuration as the design variable is varied between $s = 1.5$ and $s = 2.5$, in constant increments of $\Delta s = 0.02$. The response function, \mathcal{Z} , is the temperature measured at the node A located at $\mathbf{x} = (0, 0)$. Figure 11 plots the response function, \mathcal{Z} , and the corresponding shape sensitivities, $\partial\mathcal{Z}/\partial s$, as a function of the design variable for the approaches mentioned above.

Choosing $\theta = 0^\circ$ results in a vertical strip inclusion. Thus, the current problem setup is a 2D approximation of a 1D model with the analytical solution given by

$$u_A = u_D + \left(\frac{30 - 2s}{k_1} + \frac{2s}{k_2} \right) \frac{q_N}{6},$$

$$\frac{\partial u_A}{\partial s} = -0.3 \quad (49)$$

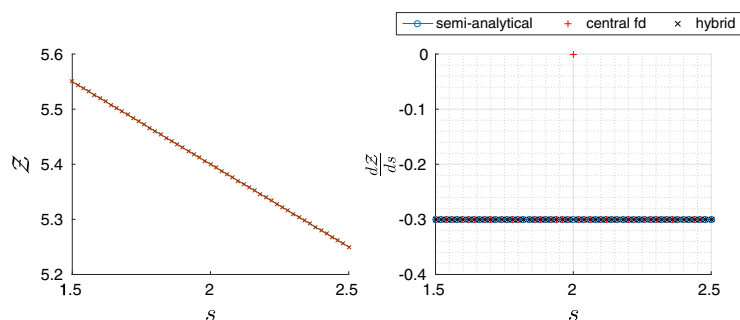
The analytical solution in (49) shows a linear dependency of \mathcal{Z} on the width of the vertical strip inclusion. As a result the corresponding shape sensitivities are constant as computed in (49). The shape sensitivities obtained using the different approaches are presented in Fig. 11. The relative difference in sensitivities between the three approaches was insignificant (approximately 10^{-8}) except at $s = 2.0$ which resulted in an intersection configuration wherein the

material interface coincides with finite element mesh nodes. Here, the finite differenced sensitivities vanish. This behavior is a result of the material interface shift depicted in Fig. 7 and is further discussed in the next subsection. A perturbation size of $\Delta_{FD} = 10^{-6}h/2$ was chosen. For various values of Δ_{FD} between $10^{-3}h$ and $10^{-10}h$, the relative difference (with respect to $\Delta_{FD} = 10^{-6}h/2$) in the XFEM-based shape sensitivities was measured to be approximately 10^{-5} . The choice of Δ_{FD} for the XFEM-based sensitivities is related to the material interface shift and is discussed in the next subsection.

Having established the accuracy of the shape sensitivities using the proposed semi-analytical approach, we now compare the smoothness of XFEM-based sensitivities against shape sensitivities obtained using a body-fitted mesh. The body-fitted FEM sensitivities are computed via finite differencing. To better comprehend the difference in smoothness of shape sensitivities, the strip is inclined at $\theta = 30^\circ$, for which the sensitivities are no longer expected to be constant. Two different body-fitted approaches were adopted: i) FEM-1, wherein all nodes move with the boundary using a design element concept (Bletzinger et al. 1991); ii) FEM-2, wherein only the nodes on the boundaries are moved during the finite difference perturbations. Body-fitted finite element meshes of 120 by 24 elements were used. A perturbation size of $\Delta_{FD} = 10^{-6}/2$ was used for computing the body-fitted shape sensitivities. Numerical experiments showed that the body-fitted FEM results were converged for this mesh and perturbation size.

Figure 12 presents the response function and the shape sensitivities as a function of the design variable. Even though the response function plots match closely, the shape sensitivities using the XFEM are not as smooth as those obtained using the body-fitted mesh. Mesh refinement leads to convergence of the sensitivities computed using the XFEM. It was also noticed that the interface constraint penalty (11) influences the accuracy of the sensitivities, relative to FEM-1. Table 1 presents the difference in shape sensitivities using the XFEM with respect to shape

Fig. 11 Accuracy of semi-analytical shape sensitivities: response function (left) and corresponding shape sensitivities (right)



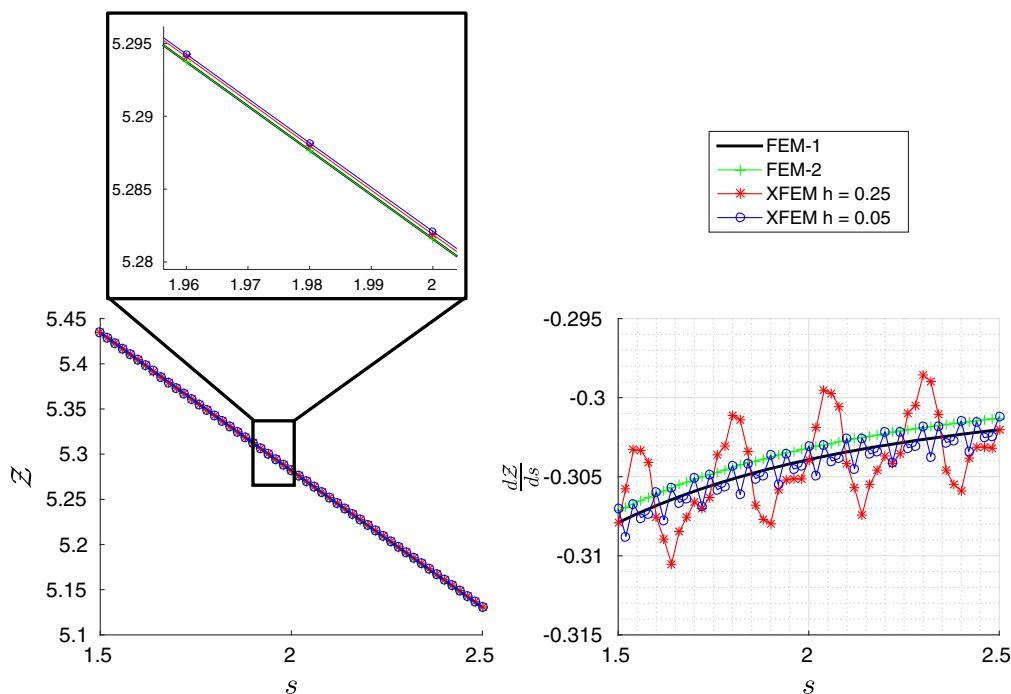


Fig. 12 Comparison with body-fitted mesh, $\theta = 30^\circ$: Response function (left) and corresponding shape sensitivities (right)

sensitivities evaluated using FEM-1. This relative difference is averaged over all designs considered. Also presented in Table 1 is the interface constraint error averaged over the number of different designs. Note that a higher interface constraint penalty does not guarantee a low relative difference in shape sensitivities.

Based on the above results, although less smooth than the body-fitted FEM-based approaches, the semi-analytical approach captures accurately the overall behavior of shape sensitivities. Spatial refinement can be used to further improve the smoothness of shape sensitivities computed using the semi-analytical approach. Section 5.2 provides a more comprehensive analysis of this issue.

Table 1 Influence of interface constraint penalty

h	c_{Γ_u}	Difference relative to FEM-1	Interface constraint error
0.25	1.0	0.68 %	$1.46 \cdot 10^{-3}$
0.25	10.0	0.39 %	$2.54 \cdot 10^{-4}$
0.25	100.0	0.63 %	$9.19 \cdot 10^{-5}$
0.125	1.0	0.32 %	$6.03 \cdot 10^{-4}$
0.05	1.0	0.22 %	$1.84 \cdot 10^{-4}$

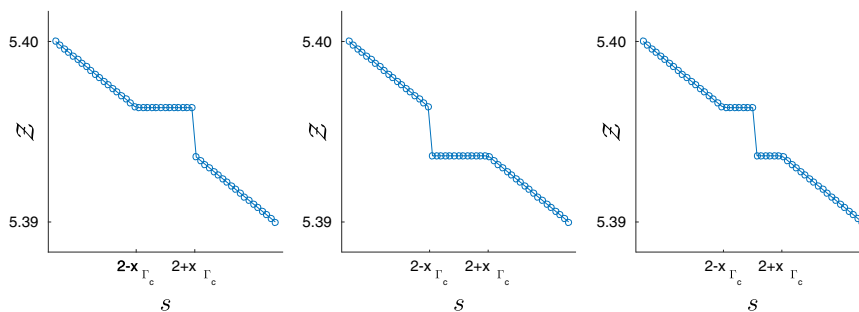
5.1.2 Influence of interface shift on semi-analytical shape sensitivities

In this subsection, we discuss the influence of the material interface shift on the computation of the semi-analytical shape sensitivities. As depicted in Fig. 7, the material interface is prevented from intersecting a node by shifting the interface as it comes within a critical distance of a node, referred to as the critical shift distance set here at $x_{\Gamma_c} = 10^{-6}h$. For all numerical results presented in this study, unless mentioned otherwise, the PIS approach is used alongside a finite difference perturbation size of $\Delta_{FD} = 10^{-6}h/2$. Using a mesh of size $h = 1$, and setting $\theta = 0^\circ$, the design variable is varied in increments of $\Delta s = 0.15x_{\Gamma_c}$. The response function, Z , is the temperature measured at node A. Such a setup, with $\Delta s < x_{\Gamma_c}$, allows us to study the behavior of shape sensitivities within the critical shift distance as the material interface crosses a node.

Figure 13 plots the response function for each of the shift options listed in Section 3. Note that the interface intersects a node at $s = 2$. Based on Fig. 7, the interface shift is performed such that the new position of the material interface is assumed at a distance x_{Γ_c} from the node in concern. This, as expected, results in a distinct discontinuity in the response function within the critical shift distance.

Figure 14 presents a comparison of XFEM-based shape sensitivities computed using the proposed semi-analytical

Fig. 13 Influence of shifting the interface on the response function: PIS (left), P2S (middle), PMS (right)



approach against shape sensitivities computed using central, forward, and backward finite differencing. Results are presented for perturbation sizes of $\Delta_{FD} = 2x_{\Gamma_c}$ and $\Delta_{FD} = x_{\Gamma_c}/2$ using the PIS approach. While finite differencing $\partial \mathcal{R}_e / \partial \hat{x}_{\Gamma}^k$, design perturbations may result in the material interface crossing over to a neighboring element. In such a scenario and to avoid an intersection point passing through a node, a forward or backward finite differencing of $\partial \mathcal{R}_e / \partial \hat{x}_{\Gamma}^k$ is performed depending on the interface configuration. A finite difference perturbation size of $\Delta_{FD} < x_{\Gamma_c}$ allows for central finite differencing at all times regardless of the interface position. Note that this issue does not affect the finite differencing approach, and strictly pertains to the computation of $\partial \mathcal{R}_e / \partial \hat{x}_{\Gamma}^k$ during semi-analytical sensitivity computations.

As established in Section 5.1.1, shape sensitivities are expected to remain constant with the varying thickness of a vertical strip inclusion. Figure 14 shows that accurate sensitivities are obtained via the semi-analytical approach regardless of the perturbation size, Δ_{FD} . When computing shape sensitivities via the semi-analytical approach, design perturbations (for finite differencing $\partial \mathcal{R}_e / \partial \hat{x}_{\Gamma}^k$) are performed about the interface configuration used to compute the response, as shown in Fig. 9. No interface shift is performed during any of these design perturbations. In contrast, inaccurate sensitivities are obtained via finite differencing.

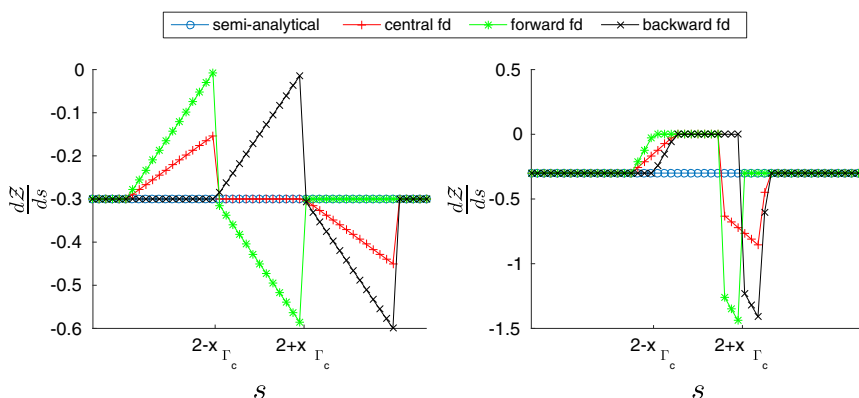
This is because finite differencing $\partial Z / \partial s$ at a global level provides no control over the elemental interface shift, i.e. $\mathcal{G}'|_{s+\Delta_{FD}}$, $\mathcal{G}'|_{s-\Delta_{FD}}$, $\mathcal{G}|_{s+\Delta_{FD}}$ and $\mathcal{G}|_{s-\Delta_{FD}}$ in (45) are evaluated based on design configurations subjected to the material interface shift.

Figure 15 presents the scenario wherein the material interface is shifted during the design perturbations for the semi-analytical sensitivity computations. Results are presented corresponding to each of the three shift options. A perturbation size of $\Delta_{FD} = 2x_{\Gamma_c}$ is used. Alongside the central, forward, and backward finite difference approaches, inaccurate sensitivities are also obtained through the semi-analytical approach as expected. Giving up control over the elemental interface shift results in semi-analytical sensitivities coinciding with at least one of the finite difference approaches depending on the interface configuration as discussed above.

5.1.3 D discontinuity in shape sensitivities

In this subsection we present shape sensitivities corresponding to a response function evaluated at a node that changes material phase. We use the problem setup of Fig. 10 with $\theta = 30^\circ$. Shape sensitivities are recorded for every configuration as the design variable is varied between $s = 1.5$ and $s = 2.5$, in constant increments of $\Delta s = 0.02$. The response

Fig. 14 Accuracy of semi-analytical sensitivities, PIS: $\Delta_{FD} = 2x_{\Gamma_c}$ (left) and $\Delta_{FD} = x_{\Gamma_c}/2$ (right)



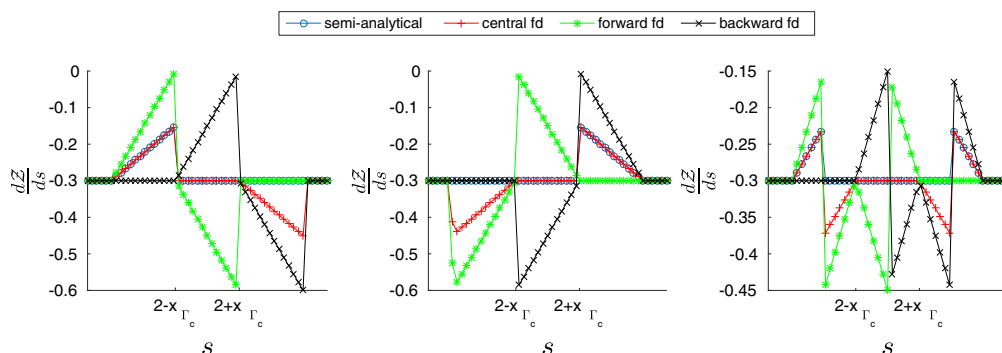


Fig. 15 Influence of shifting the interface during computation of shape sensitivities, $\Delta_{FD} = 2x\Gamma_c$: P1S (left), P2S (middle), PMS (right)

function, \mathcal{Z} , is the temperature measured at node B located at $x = (14.5, 3)$. Figure 16 presents the response function and the corresponding shape sensitivities as a function of the design variable. There is a kink in the variation of the response function leading to a strong discontinuity in the shape sensitivities. This discontinuity is not a byproduct of the XFEM framework, but corresponds to the material phase change that node B experiences as the material interface moves across the node.

Such discontinuities in shape sensitivities are often encountered in shape and topology optimization problems when certain nodes change material phase. This can cause issues when using gradient based optimization algorithms for solving optimization problems that measure the response function over small regions of the design domain.

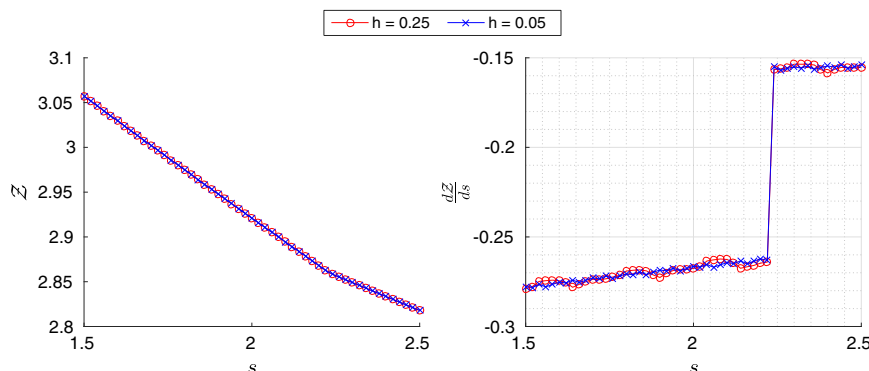
5.2 Example 2

The goal of this example is to investigate the dependency of the shape sensitivities on the discretization of the design geometry, i.e. mesh refinement. We consider the two-phase problem setup shown in Fig. 17. A circular inclusion of conductivity $k_2 = 10$, is embedded into a rectangular matrix

of conductivity $k_1 = 1$. The circular inclusion is centered at $x = (15, 3)$. A Neumann boundary condition of $q_N = 1$ is applied to the left edge. A Dirichlet boundary condition of $u_D = 1$ is applied to the right edge. The top and bottom edges are adiabatic. The design variable, s , is the radius of the circular inclusion. Shape sensitivities are recorded for every configuration as the design variable is varied between $s = 1.5$ and $s = 2.5$, in constant increments of $\Delta s = 0.02$. The response function, \mathcal{Z} , is the temperature measured at node A located at $x = (0, 0)$. In this example, we also focus on the sensitivities for the perimeter (*per*) of the inclusion. The circular inclusion has a perimeter of $2\pi s$. Consequently, the analytical solution for the sensitivity of the perimeter is 2π .

The response function and the corresponding shape sensitivities for a mesh size of $h = 0.25$ are plotted in Fig. 18. A visibly smooth response function is obtained. However, the shape sensitivities obtained are not smooth. Plotted alongside the sensitivities for the response function, are the sensitivities for the perimeter of the circular inclusion. A correlation is observed in the behavior of the two plots, implying a significant influence of the discretization

Fig. 16 Response function (left) and shape sensitivities (right) for temperature measured at node B



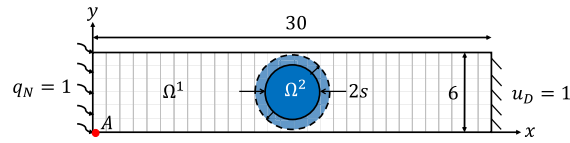


Fig. 17 Heat diffusion problem setup with circular inclusion

Fig. 18 Response function (left) and shape sensitivities (right) for circular inclusion, $h = 0.25$

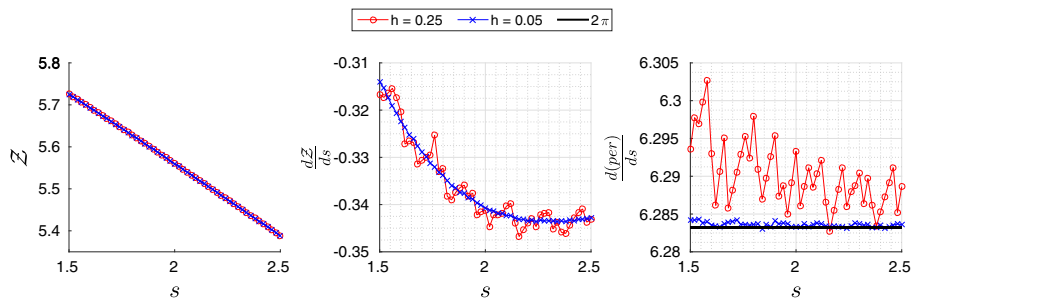
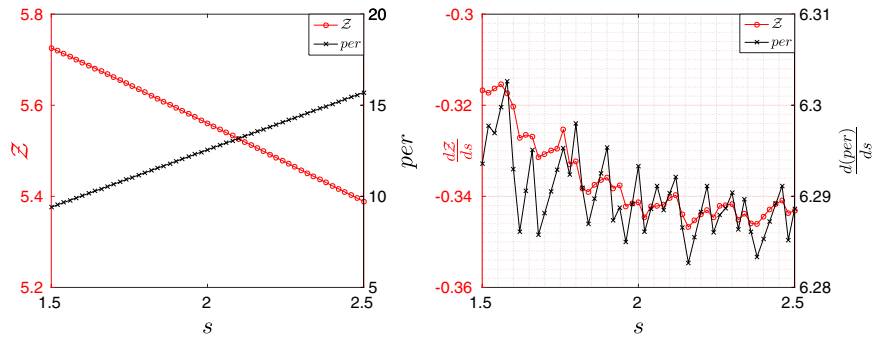


Fig. 19 Dependence of shape sensitivities on geometry discretization: Response function (left), and sensitivities corresponding to response function (middle) and perimeter (right)

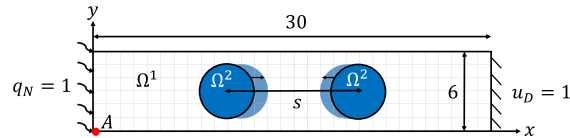


Fig. 20 Heat diffusion problem setup with two circular inclusions

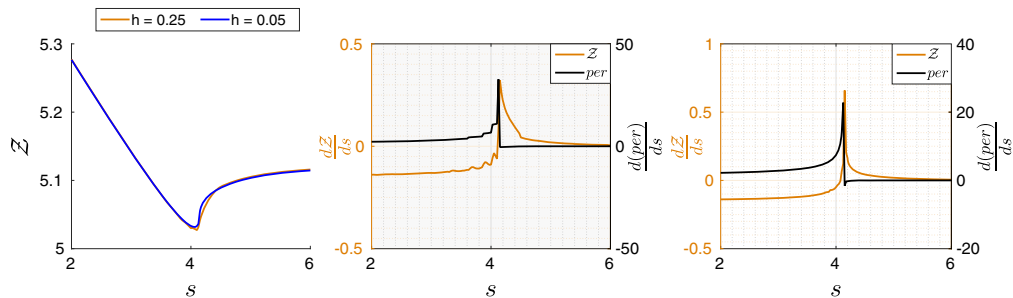


Fig. 21 Shape sensitivity analysis for merging inclusions: Response function comparison (left), and sensitivities for $h = 0.25$ (middle) and $h = 0.05$ (right)

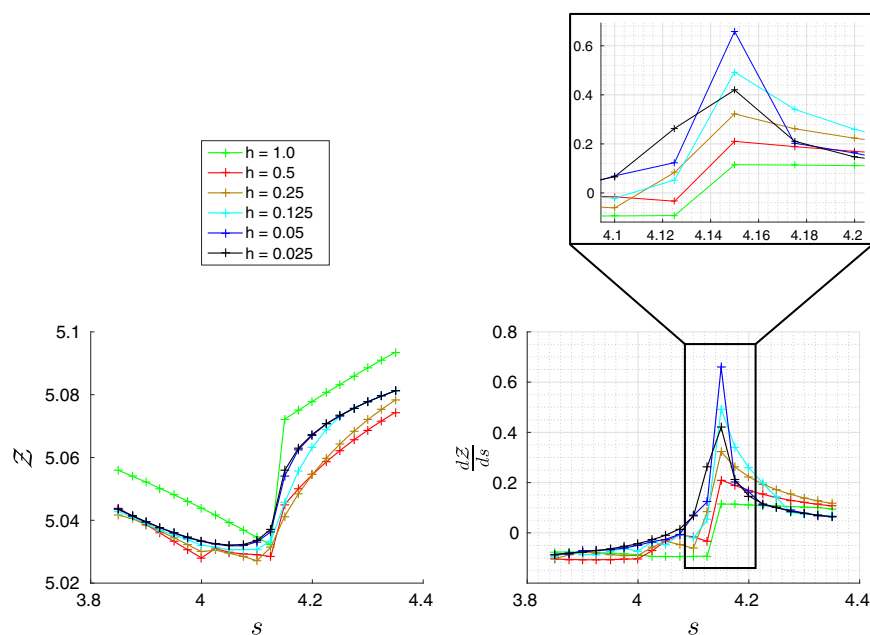


Fig. 22 Response function (*left*) and corresponding shape sensitivities (*right*) in the region where the inclusions merge for KS aggregation parameter of 10

of the design geometry on the computation of the shape sensitivities. Consequently, a comparison with a finer mesh is drawn in Fig. 19. With mesh refinement, the sensitivities for the inclusion interface perimeter approach the constant value of 2π indicating a more accurate approximation of the interface geometry. The improved approximation of the interface geometry leads to a smoother behavior of the shape sensitivities.

Since the smoothness of shape sensitivities depends greatly on the discretization of the geometry, the levels of mesh refinement required to obtain smoother shape sensitivities is geometry dependent. As a result, finer meshes are required to better approximate the geometries of smaller feature sizes. Alternatively, the order of the geometry description can be increased. Instead of using polygons in 2D and facets in 3D to approximate the material interface within an element as done in this study (see Section 2.1), higher-order approximations could be used. It is important to note that the smoothness of the shape sensitivities is not entirely dependent on the discretization of the geometry. This is observed from the sensitivity plots in Fig. 12 where the design geometry consists of only straight lines. The fluctuations observed there are attributed to the change in triangulation patterns as the interface moves through the background mesh. Recall from Section 3, the integration subdomains in the current study are constructed via Delaunay triangulation.

5.3 Example 3

This example investigates the evolution of the response function and the corresponding shape sensitivities for a scenario which simulates the merging of shapes in topology optimization. We consider the two-inclusion problem setup shown in Fig. 20. Two circular inclusions of conductivity $k_2 = 10$, are embedded into a rectangular matrix of conductivity $k_1 = 1$. The circular inclusions have a radius of 2. The left and right inclusions are initially centered at $\mathbf{x} = (12, 3)$ and $\mathbf{x} = (18, 3)$ respectively, with the mean of the centers fixed at $\mathbf{x} = (15, 3)$. The design variable, s , is the distance between the centers of the two circular inclusions. A Neumann boundary condition of $q_N = 1$ is applied to the left edge. A Dirichlet boundary condition of $u_D = 1$ is applied to the right edge. The top and bottom edges are adiabatic. Shape sensitivities are recorded for every configuration as the design variable is varied between $s = 6$ and $s = 2$, in constant increments of $\Delta s = -0.025$. The response function, \mathcal{Z} , is the temperature measured at the node A, located at $\mathbf{x} = (0, 0)$. Note, due to the intersection configurations encountered during the merging of inclusions, this example makes use of multiple enrichment levels.

To maintain differentiability of the response function with respect to the design variable, the two circles are incorporated into the design geometry using a Kreisselmeier-Steinhauser (KS) function (Kreisselmeier and Steinhauser

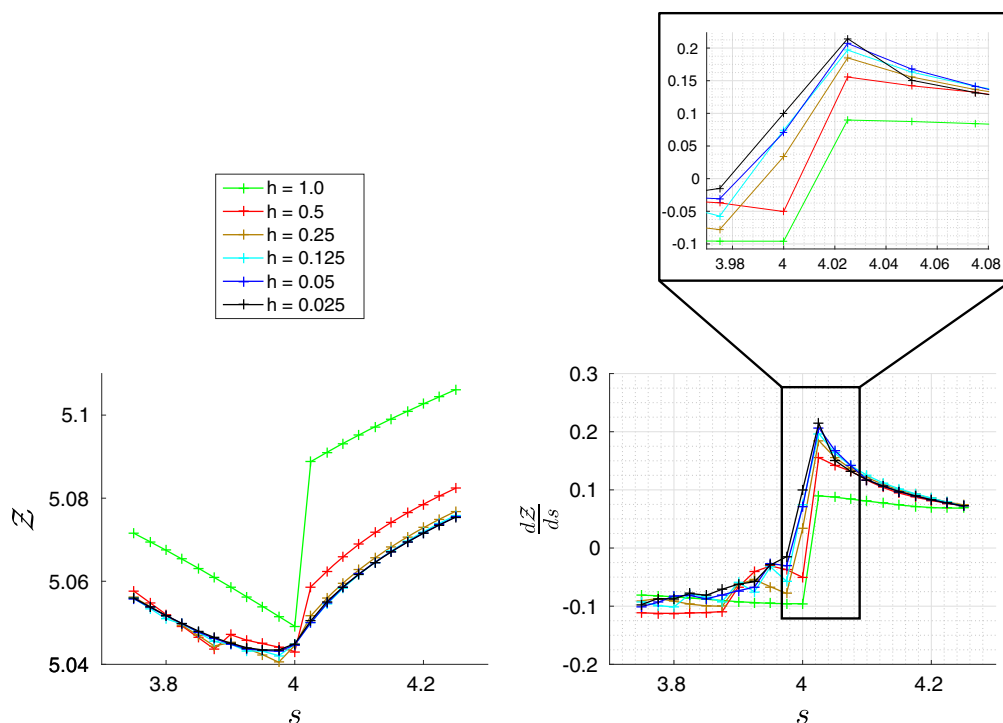


Fig. 23 Response function (left) and corresponding shape sensitivities (right) in the region where the inclusions merge for KS aggregation parameter of 200

1979) instead of a min/max function. The KS aggregation parameter was set to 10. The response function and the corresponding shape sensitivities for mesh sizes of $h = 0.25$ and $h = 0.05$ are plotted in Fig. 21. Because $\Delta_{FD} < \chi_{\Gamma_c}$, the inclusions do not merge when perturbing the designs for computing $\partial \mathcal{R}_c / \partial \hat{x}_T^k$ by finite differencing. Therefore, from the perspective of shape sensitivity analysis, we do not account for topological changes. Moreover, the merging of topological features is not a continuous phenomenon. This discontinuity is highlighted by the presence of a kink in the evolution of the response function in Fig. 21. Merging of the two inclusions is represented by a spike in the shape sensitivity plots.

Figure 22 shows the behavior of the response function and the corresponding shape sensitivities in the region where the inclusions merge, upon refinement in mesh. The magnitude of the spike oscillates at smaller values of the mesh size, h . This behavior is a result of using the KS function which smears out the level set field. The intensity of this smearing varies with the mesh size, further leading to inconsistent design geometries between different mesh sizes. This inconsistency is mitigated by using a high KS aggregation parameter. Figure 23 presents the shape sensitivities for design geometry constructed using a KS aggregation parameter of 200. The magnitude of the spike in Fig. 23 converges

with mesh refinement. It is thus inferred that the spike is not a byproduct of the Heaviside-enriched XFEM or the geometry discretization, but the spike is a result of the physics associated with the merging phenomenon itself.

5.4 Example 4

We consider a void spherical inclusion surrounded by an incompressible fluid in a rectangular box as depicted in Fig. 24. In contrast to the previous examples, the current problem setup is governed by a nonlinear set of equations in 3D. The goal is to show the applicability of the numerical framework discussed previously, to such problems. A flow

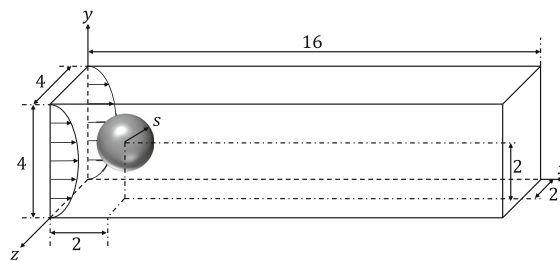
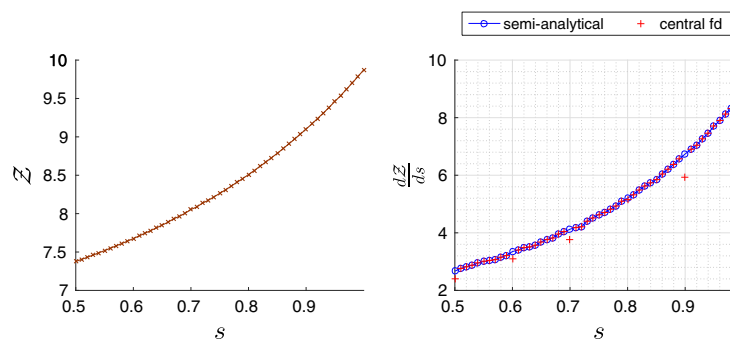


Fig. 24 Incompressible fluid flow with void spherical inclusion

Fig. 25 Response function and shape sensitivities for problem setup in Fig. 24



of Reynolds number 10 is considered. The fluid density and viscosity are assumed to be 1. The inclusion has an initial radius of 0.5, and is centered at $\mathbf{x} = (2, 2)$. No-slip conditions are enforced along the fluid-void interface. A parabolic laminar flow is prescribed at the inlet. Due to the uniform cross sections of the inlet and outlet, the pressure loss inside the channel depends solely on the geometry of the inclusion. Shape sensitivities are computed for the response function, \mathcal{Z} , defined as the difference in total pressure between the inlet and outlet, with the design variable, s , being the radius of the spherical inclusion. The radius is varied between $s = 0.5$ and $s = 1$ in constant increments of $\Delta s = 0.01$. The response function and the corresponding shape sensitivities for a uniform element size of $h = 0.1$ are plotted in Fig. 25. A smooth behavior of semi-analytical shape sensitivities is observed. Plotted alongside the semi-analytical sensitivities are the finite differenced shape sensitivities. As reported in Section 5.1.2, the semi-analytical sensitivities are in agreement with the finite differenced sensitivities except for when the material interface lies within the critical shift region, for instance at $s = 0.9$. Thus aside from being costly, finite differencing produces outliers in shape sensitivities.

6 Conclusions

Shape sensitivities with the Heaviside-enriched XFEM were studied. Shape derivatives are computed using the adjoint method. An important component of the adjoint and direct methods is the computation of the derivative of the residual of the governing equations with respect to the design variables, $\partial R/\partial s$. Consequently, we presented and studied a continuum and a discrete approach to computing the residual derivative.

Use of kink enrichments results in an explicit dependency of the solution field on the design variables which can complicate the derivation and implementation of shape sensitivities as shown by Noël et al. (2016). The Heaviside enrichment does not suffer from any such dependency.

For volumetric terms, analytical sensitivities can be computed in a straightforward manner by performing integration over the material boundary as discussed in Section 4.1. However, for terms evaluated along the material boundaries, the derivation is complicated by the mapping of global domains in d spatial dimensions to a reference domain in $d - 1$ dimensions. Accounting analytically for the change in this mapping with respect to design variables requires the computation of the curvature which requires second order spatial derivatives of the finite element discretized level set field. However, topology optimization problems typically make use of lower order elements, for which second order spatial derivatives do not exist.

Computing semi-analytical shape sensitivities which involve finite differencing the term $\partial \hat{\mathcal{R}}_e / \partial \hat{\mathbf{x}}_r^k$ in (34) is an effective and easy to implement alternative. The corresponding shape sensitivities were observed to be nearly insensitive to perturbation sizes ranging over six orders of magnitude. In accordance with the adopted multi-level enrichment strategy, the interface is not allowed to intersect a node. This is achieved by shifting the material interface when the interface comes within a critical distance of a node. It was observed that performing this shift in the interface position during the finite difference perturbations resulted in inaccurate computation of shape sensitivities. To maintain accuracy of the shape sensitivities, it is important that the finite difference perturbations do not undergo any interface shift within the critical shift distance. While finite differencing $\partial \hat{\mathcal{R}}_e / \partial \hat{\mathbf{x}}_r^k$, design perturbations may result in the material interface crossing over to a neighboring element. To ensure central finite differencing of $\partial \hat{\mathcal{R}}_e / \partial \hat{\mathbf{x}}_r^k$, the finite difference perturbation size is chosen to be less than the critical shift distance.

Accuracy of the semi-analytical shape sensitivities was established via comparisons against finite differenced shape sensitivities. A numerical comparison with shape sensitivities obtained using body-fitted meshes was made. Although the latter frameworks resulted in smoother sensitivities, the relative difference between XFEM-based and

FEM-based shape sensitivities was small. This relative difference further reduces upon mesh refinement. One disadvantage of the Heaviside-enriched XFEM is the need for interface conditions to enforce continuity in solution across the material interface. The accuracy (relative to a body-fitted mesh) of the shape sensitivities was found to be influenced by how strongly the interface conditions are enforced. The dependency of shape sensitivities on the discretization of the design geometry was illustrated through an example using a circular inclusion. Distinct correlation was observed between the smoothness of the shape sensitivity and discretization of the inclusion geometry. As a result, it is possible to obtain smoother sensitivities through mesh refinement. A two inclusion problem was studied to demonstrate the effect of merging topologies on shape sensitivities. Merging of topologies, not being a continuous phenomenon, resulted in a kink in the response function and a distinct spike in the shape sensitivities. For the particular problem considered, the magnitude of the spike was shown to converge with refinement in mesh, leading to the inference that the spike is independent of the Heaviside-enriched XFEM or the geometry discretization. Application to an incompressible fluid flow example demonstrated the suitability of the Heaviside-enriched XFEM framework for the computation of shape sensitivities for 3D nonlinear problems.

Future studies should focus on shape sensitivities for transient problems including temporally evolving material interfaces. Furthermore, the effect of gradient stabilization techniques, such as the fictitious domain approach of Burman and Hansbo (2012), on the computation of shape sensitivities needs to be studied.

Acknowledgments The first author acknowledges the support of the National Science Foundation under Grant EFRI-ODISSEI 1240374. The second author acknowledges the support of the National Science Foundation under Grant CMMI 1235532. The third author, in addition to the above grants, acknowledges the support of the Air Force Office of Scientific Research under grant FA9550-13-1-0088.

This work utilized the Janus supercomputer, which is supported by the National Science Foundation (award number CNS-0821794) and the University of Colorado Boulder. The Janus supercomputer is a joint effort of the University of Colorado Boulder, the University of Colorado Denver and the National Center for Atmospheric Research.

Appendix A

CAD-free based shape optimization studies use the nodal coordinates of the element as the design variables. Here we draw a quantitative comparison between shape sensitivities obtained using the approach proposed in the current study (Eulerian framework), and shape sensitivities obtained using a body-fitted mesh (Lagrangian framework).

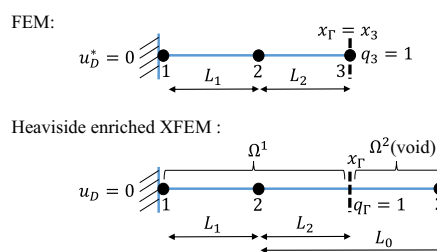


Fig. 26 Heat diffusion problem setup in 1D

We consider a 1D linear heat diffusion problem depicted in Fig. 26. A unit heat flux is applied to node 3 and to the interface x_Γ , in the body-fitted and XFEM cases respectively. For the XFEM case, phase 2 is void of any material. Consequently, the setups shown in Fig. 26 are physically equivalent. The response, \mathcal{Z} is the temperature measured at node 2. As discussed in Section 4.2, shape sensitivities vanish for elements not intersected by the material interface. Thus, we draw comparisons for the second element only, the system of equations for which can be expressed as

$$\begin{aligned}
 &\text{FEM:} \\
 &\begin{bmatrix} \frac{1}{L_1} + \frac{1}{L_2} & -\frac{1}{L_2} \\ -\frac{1}{L_2} & \frac{1}{L_2} \end{bmatrix} \begin{bmatrix} \hat{u}_2 \\ \hat{u}_3 \end{bmatrix} = \begin{bmatrix} 0 \\ 1 \end{bmatrix} \implies \\
 &\begin{bmatrix} \frac{1}{x_2-x_1} + \frac{1}{x_3-x_2} & -\frac{1}{x_3-x_2} \\ -\frac{1}{x_3-x_2} & \frac{1}{x_3-x_2} \end{bmatrix} \begin{bmatrix} \hat{u}_2 \\ \hat{u}_3 \end{bmatrix} = \begin{bmatrix} 0 \\ 1 \end{bmatrix}, \\
 &\text{XFEM:} \\
 &\begin{bmatrix} \frac{1}{L_1} + \frac{L_2}{L_0^2} & -\frac{L_2}{L_0^2} \\ -\frac{L_2}{L_0^2} & \frac{L_2}{L_0^2} \end{bmatrix} \begin{bmatrix} \hat{u}_2^* \\ \hat{u}_3^* \end{bmatrix} = \begin{bmatrix} \frac{L_0-L_2}{L_0} \\ \frac{L_2}{L_0} \end{bmatrix} \implies \\
 &\begin{bmatrix} \frac{1}{x_2-x_1} + \frac{(x_\Gamma-x_2)}{(x_3-x_2)^2} & -\frac{x_\Gamma-x_2}{(x_3-x_2)^2} \\ -\frac{x_\Gamma-x_2}{(x_3-x_2)^2} & \frac{x_\Gamma-x_2}{(x_3-x_2)^2} \end{bmatrix} \begin{bmatrix} \hat{u}_2^* \\ \hat{u}_3^* \end{bmatrix} = \begin{bmatrix} \frac{x_3-x_\Gamma}{x_3-x_2} \\ \frac{x_\Gamma-x_2}{x_3-x_2} \end{bmatrix}, \quad (50)
 \end{aligned}$$

where the force vector for the XFEM was obtained using the residual contribution from the Neumann boundary condition in (10). The discretized solution using FEM and XFEM are denoted by \hat{u} and \hat{u}^* respectively. Note, it is trivial to show following a few calculations that $\hat{u}^*(x_\Gamma) = \hat{u}_3 = L_1 + L_2$ and $d\hat{u}^*(x_\Gamma)/dx_\Gamma = d\hat{u}_3/dx_3 = 1$, thus proving the equivalence of the two approaches.

To compute the shape sensitivities using the adjoint approach (Section 4), we require the derivatives of the response function with respect to the solution, and derivative of the residual with respect to the solution and the material

interface. Following (50), the residual of the two systems is written as

FEM:

$$\mathcal{R} = \begin{bmatrix} \hat{u}_2 \frac{1}{x_2 - x_1} + \hat{u}_2 \frac{1}{x_3 - x_2} - \hat{u}_3 \frac{1}{x_3 - x_2} \\ -\hat{u}_2 \frac{1}{x_3 - x_2} + \hat{u}_3 \frac{1}{x_3 - x_2} - 1 \end{bmatrix},$$

XFEM:

$$\mathcal{R} = \begin{bmatrix} \hat{u}_2^* \frac{1}{x_2 - x_1} + \hat{u}_2^* \frac{x_\Gamma - x_2}{(x_3 - x_2)^2} - \hat{u}_3^* \frac{x_\Gamma - x_2}{(x_3 - x_2)^2} - \frac{x_3 - x_\Gamma}{x_3 - x_2} \\ -\hat{u}_2^* \frac{x_\Gamma - x_2}{(x_3 - x_2)^2} + \hat{u}_3^* \frac{x_\Gamma - x_2}{(x_3 - x_2)^2} - \frac{x_\Gamma - x_2}{x_3 - x_2} \end{bmatrix}. \quad (51)$$

The residual derivatives with respect to the material interface are then given by

FEM:

$$\frac{\partial \mathcal{R}}{\partial x_3} = \begin{bmatrix} -\hat{u}_2 \frac{1}{(x_3 - x_2)^2} + \hat{u}_3 \frac{1}{(x_3 - x_2)^2} \\ \hat{u}_2 \frac{1}{(x_3 - x_2)^2} - \hat{u}_3 \frac{1}{(x_3 - x_2)^2} \end{bmatrix},$$

XFEM:

$$\frac{\partial \mathcal{R}}{\partial x_\Gamma} = \begin{bmatrix} \hat{u}_2^* \frac{1}{(x_3 - x_2)^2} - \hat{u}_3^* \frac{1}{(x_3 - x_2)^2} + \frac{1}{x_3 - x_2} \\ -\hat{u}_2^* \frac{1}{(x_3 - x_2)^2} + \hat{u}_3^* \frac{1}{(x_3 - x_2)^2} - \frac{1}{x_3 - x_2} \end{bmatrix}. \quad (52)$$

The residual derivatives with respect to the solution are given by the left hand side matrices in (50). The derivative of the response function with respect to the solution is same for the two approaches, and is given by,

$$\frac{\partial \mathcal{Z}}{\partial \hat{\mathbf{u}}^*} = \frac{\partial \mathcal{Z}}{\partial \hat{\mathbf{u}}} = \begin{bmatrix} 1 \\ 0 \end{bmatrix}. \quad (53)$$

The vector of adjoint variables is computed using (23) to give

$$\lambda = - \left(\frac{\partial \mathcal{R}}{\partial \hat{\mathbf{u}}} \right)^{-1} \frac{\partial \mathcal{Z}}{\partial \hat{\mathbf{u}}} = \begin{bmatrix} x_1 - x_2 \\ x_1 - x_2 \end{bmatrix},$$

$$\lambda^* = - \left(\frac{\partial \mathcal{R}}{\partial \hat{\mathbf{u}}^*} \right)^{-1} \frac{\partial \mathcal{Z}}{\partial \hat{\mathbf{u}}^*} = \begin{bmatrix} x_1 - x_2 \\ x_1 - x_2 \end{bmatrix}, \quad (54)$$

where λ and λ^* denote the vector of adjoint variables for the FEM case and the XFEM case respectively. The shape sensitivities are readily obtained following a dot product between (54) and (52). Upon comparison of the sensitivities obtained using the two frameworks, a sign change in the sensitivities resulting from (52) is evident, along with the presence of an additional term in the XFEM case. This difference is the result of extrapolating the force vector from the material interface on to the finite element nodes.

References

- Allaire G, Jouve F, Toader AM (2004) Structural optimization using sensitivity analysis and a level-set method. *J Comput Phys* 194(1):363–393
- Allaire G, Gournay Fd, Jouve F, Toader AM (2005) Structural optimization using topological and shape sensitivity via a level set method. *Control Cybern* 34(1):59–80
- Annarapu C, Hautefeuille M, Dolbow JE (2012) A robust Nitsche's formulation for interface problems. *Comput Methods Appl Mech Eng* 225–228:44–54
- Azegami H, Shimoda SKM, Katamine E (1997) Irregularity of shape optimization problems and an improvement technique. *Transactions on The Built Environment* 28:309–326
- Babuška I, Melenk JM (1997) The partition of unity method. *Int J Numer Methods Eng* 40(4):727–758
- Bletzinger KU, Kimmich S, Ramm E (1991) Efficient modeling in shape optimal design. *Comput Syst Eng* 2(5–6):483–495
- Burman E, Hansbo P (2012) Fictitious domain finite element methods using cut elements: II. A stabilized Nitsche method. *Appl Numer Math* 62(4):328–341
- Chen S, Tortorelli D (1997) Three-dimensional shape optimization with variational geometry. *Structural Optimization* 13(2-3):81–94
- Coffin P, Maute K (2016a) A level-set method for steady-state and transient natural convection problems. *Struct Multidiscip Optim* 53(5):1047–1067
- Coffin P, Maute K (2016b) Level set topology optimization of cooling and heating devices using a simplified convection model. *Struct Multidiscip Optim* 53(5):985–1003
- Cook RD (1994) *Finite element modeling for stress analysis*. Wiley
- Delfour MC, Zolésio JP (1992) Structure of shape derivatives for nonsmooth domains. *J Funct Anal* 104(1):1–33
- Delfour MC, Zolésio JP (2011) *Shapes and geometries: metrics, analysis, differential calculus, and optimization*. SIAM
- Dijk N, Maute K, Langelaar M, Keulen F (2013) Level-set methods for structural topology optimization: a review. *Struct Multidiscip Optim* 48(3):437–472
- Duysinx P, Van Miegroet L, Jacobs T, Fleury C (2006) Generalized shape optimization using x-FEM and level set methods. In: *IUTAM Symposium on topological design optimization of structures, machines and materials*. Springer, pp 23–32
- Firl M, Wüchner R, Bletzinger KU (2013) Regularization of shape optimization problems using fe-based parametrization. *Struct Multidiscip Optim* 47(4):507–521
- Fries T, Belytschko T (2010) The extended/generalized finite element method: an overview of the method and its applications. *Int J Numer Methods Eng* 84(3):253–304
- Gain AL, Paulino GH (2013) A critical comparative assessment of differential equation-driven methods for structural topology optimization. *Struct Multidiscip Optim* 48(4):685–710
- Goldman R (2005) Curvature formulas for implicit curves and surfaces. *Comput Aided Geom Des* 22(7):632–658
- Haasemann G, Kästner M, Prüger S, Ulbricht V (2011) Development of a quadratic finite element formulation based on the XFEM and NURBS. *Int J Numer Methods Eng* 86(4–5):698–717
- Hafitka RT, Grandhi RV (1986) Structural shape optimization—a survey. *Comput Methods Appl Mech Eng* 57(1):91–106
- Hansbo A, Hansbo P (2004) A finite element method for the simulation of strong and weak discontinuities in solid mechanics. *Comput Methods Appl Mech Eng* 193(33-35):3523–3540
- Haslinger J, Maitre J, Tomas L (2001) Fictitious domains methods with distributed lagrange multipliers part ii: application to the solution of shape optimization problems. *Math Methods Appl Sci* 11(3):549–563
- Jameson A (1988) Aerodynamic design via control theory. *J Sci Comput* 3(3):233–260
- Jenkins N, Maute K (2015) Level set topology optimization of stationary fluid-structure interaction problems. *Struct Multidiscip Optim* 52(1):179–195
- Jeong S, Lim S, Min S (2016) Level-set-based topology optimization using remeshing techniques for magnetic actuator design. *IEEE Trans Magn* 52(3):1–4

- Juntunen M, Stenberg R (2009) Nitsche's method for general boundary conditions. *Math Comput* 78(267):1353–1374
- Kenway GK, Kennedy GJ, Martins JR (2010) A CAD-free approach to high-fidelity aerostuctural optimization. In: 13th AIAA/ISSMO multidisciplinary analysis optimization conference, 13–15 September 2010, Fort Worth, Texas
- Kim NH, Chang Y (2005) Eulerian shape design sensitivity analysis and optimization with a fixed grid. *Mech Struct Mach* 194(30-33):3291–3314
- Kreisselmeier G, Steinhauser R (1979) Systematic control design by optimizing a vector performance index. In: International federation of active controls symposium on computer-aided design of control systems, Zurich, Switzerland
- Kreissl S, Maute K (2012) Levelset based fluid topology optimization using the extended finite element method. *Struct Multidiscip Optim* 46(3):311–326
- Lang C, Makhija D, Doostan A, Maute K (2014) A simple and efficient preconditioning scheme for heaviside enriched XFEM. *Comput Mech* 54(5):1357–1374
- Lang C, Sharma A, Doostan A, Maute K (2015) Heaviside enriched extended stochastic fem for problems with uncertain material interfaces. *Comput Mech* 56(5):753–767
- Lawry M, Maute K (2015) Level set topology optimization of problems with sliding contact interfaces. *Struct Multidiscip Optim* 52(6):1107–1119
- Li L, Wang M, Wei P (2012) XFEM Schemes for level set based structural optimization. *Front Mech Eng* 7(4):335–356
- Liu P, Luo Y, Kang Z (2016) Multi-material topology optimization considering interface behavior via XFEM and level set method. *Comput Methods Appl Mech Eng* 308:113–133
- Makhija D, Maute K (2014) Numerical instabilities in level set topology optimization with the extended finite element method. *Struct Multidiscip Optim* 49(2):185–197
- Materna D, Barthold FJ (2008) Defect and material mechanics. Variational design sensitivity analysis in the context of structural optimization and configurational mechanics. Springer, Netherlands, pp 133–155
- Moës N, Dolbow J, Belytschko T (1999) A finite element method for crack growth without remeshing. *Int J Numer Methods Eng* 46(1):131–150
- Moës N, Cloirec M, Cartraud P, Remacle JF (2003) A computational approach to handle complex microstructure geometries. *Int J Numer Methods Eng* 192(28–30):3163–3177
- Mohammadi B, Pironneau O (2001) Applied shape optimization for fluids. Oxford University Press
- Mohammadi B, Pironneau O (2004) Shape optimization in fluid mechanics. *Annu Rev Fluid Mech* 36:255–279
- Najafi AR, Safdari M, Tortorelli DA, Geubelle PH (2015) A gradient-based shape optimization scheme using an interface-enriched generalized fem. *Comput Methods Appl Mech Eng* 296:1–17
- Noël L, Van Miegroet L, Duysinx P (2016) Analytical sensitivity analysis using the extended finite element method in shape optimization of bimaterial structures. *Int J Numer Methods Eng* 107(8):669–695
- Osher SJ, Sethian JA (1988) Fronts propagating with curvature dependent speed: algorithms based on Hamilton-Jacobi formulations. *J Comput Phys* 79(1):12–49
- Schleupen A, Maute K, Ramm E (2000) Adaptive FE-procedures in shape optimization. *Struct Multidiscip Optim* 19(4):282–302
- Schott B, Wall W (2014) A new face-oriented stabilized xfem approach for 2d and 3d incompressible navier–stokes equations. *Comput Methods Appl Mech Eng* 276(1):233–265
- Simon J (1980) Differentiation with respect to the domain in boundary value problems. *Numer Funct Anal Optim* 2(7-8):649–687
- Sokolowski J, Zolésio JP (1992) Introduction to shape optimization. Springer
- Stenberg R (1995) On some techniques for approximating boundary conditions in the finite element method. *J Comput Appl Math* 63(1-3):139–148
- Sukumar N, Chopp DL, Moës N, Belytschko T (2001) Modeling holes and inclusions by level sets in the extended finite-element method. *Comput Methods Appl Mech Eng* 190(46):6183–6200
- Terada K, Asai M, Yamagishi M (2003) Finite cover method for linear and non-linear analyses of heterogeneous solids. *Int J Numer Methods Eng* 58(9):1321–1346
- Tezduyar TE, Mittal S, Ray SE, Shih R (1992) Incompressible flow computations with stabilized bilinear and linear equal-order-interpolation velocity-pressure elements. *Comput Methods Appl Mech Eng* 95(2):221–242
- Tortorelli DA, Tomasko JA, Morthland TE, Dantzig JA (1994) Optimal design of nonlinear parabolic systems. part II: variable spatial domain with applications to casting optimization. *Comput Methods Appl Mech Eng* 113(1):157–172
- Tran A, Yvonnez J, He QC, Toulemonde C, Sanahuja J (2011) A multiple level set approach to prevent numerical artefacts in complex microstructures with nearby inclusions within XFEM. *Int J Numer Methods Eng* 85(11):1436–1459
- Villanueva CH, Maute K (2014) Density and level set-XFEM schemes for topology optimization of 3-D structures. *Comput Mech* 54(1):133–150
- Walker SW (2015) The shape of things: a practical guide to differential geometry and the shape derivative. SIAM
- Wang MY, Wang X, Guo D (2003) A level set method for structural topology optimization. *Comput Methods Appl Mech Eng* 192(1–2):227–246
- Wei P, Wang M, Xing X (2010) A study on x-FEM in continuum structural optimization using a level set model. *Comput Aided Des* 42(8):708–719
- Zabras N, Ganapathysubramanian B, Tan L (2006) Modelling dendritic solidification with melt convection using the extended finite element method. *J Comput Phys* 218(1):200–227
- Zhang J, Zhang W, Zhu J, Xia L (2012) Integrated layout design of multi-component systems using XFEM and analytical sensitivity analysis. *Comput Methods Appl Mech Eng* 245–246(15):75–89

Appendix C

**Publication 3: Stress-based Topology Optimization using Spatial Gradient
Stabilized XFEM [113]**



RESEARCH PAPER

Stress-based topology optimization using spatial gradient stabilized XFEM

Ashesh Sharma¹ · Kurt Maute¹ Received: 23 March 2017 / Revised: 7 October 2017 / Accepted: 11 October 2017
© Springer-Verlag GmbH Germany 2017

Abstract This paper presents an immersed boundary approach for level set topology optimization considering stress constraints. A constraint agglomeration technique is used to combine the local stress constraints into one global constraint. The structural response is predicted by the eXtended Finite Element Method. A Heaviside enrichment strategy is used to model strong and weak discontinuities with great ease of implementation. This work focuses on low-order finite elements, which given their simplicity are the most popular choice of interpolation for topology optimization problems. The predicted stresses strongly depend on the intersection configuration of the elements and are prone to significant errors. Robust computation of stresses, regardless of the interface position, is essential for reliable stress constraint prediction and sensitivities. This study adopts a recently proposed fictitious domain approach for penalization of displacement gradients across element faces surrounding the material interface. In addition, a novel XFEM informed stabilization scheme is proposed for robust computation of stresses. Through numerical studies the penalized spatial gradients combined with the stabilization scheme is shown to improve prediction of stresses along the material interface. The proposed approach is applied to the benchmark topology optimization problem of an L-shaped beam in two and three dimensions using material-void and material-material problem setups. Linear and hyperelastic

materials are considered. The stress constraints are shown to be efficient in eliminating regions with high stress concentration in all scenarios considered.

Keywords Topology optimization · Level set methods · Stress constraints · Spatial gradient stabilization · Hyperelasticity

1 Introduction

Since the seminal work on topology optimization by Bendsøe and Kikuchi (1988) a significant body of research has focused on stiffness oriented problems where structural compliance or displacements constitute the objective function subject to a volume constraint. Accounting for stress constraints is important for the design of engineering structures. Without considering appropriate stress constraints, the strength of the material is ignored. As a result, over the past decade, there has been a growing interest in the study of topology optimization problems considering stress-based objective or constraints. Alternatively, structures can be designed based on damage (cf. James and Waisman 2014; Verbart et al. 2016), fatigue (Holmberg et al. 2014), or elastoplasticity (Amir 2017) to prolong the structural life.

Density-based methods have been used widely to solve topology optimization problem considering stress-based criteria. Topology optimization of continuum structures with point-wise stress constraints was first addressed by Duysinx and Bendsøe (1998). Their study presents an approach for solving material distribution problems with stress constraints using the Solid Isotropic Material with Penalization (SIMP) framework. The ϵ -relaxed approach of Cheng and Guo (1997) was used to deal with the singularity phenomenon caused by degenerated design subspaces when

✉ Kurt Maute
maute@colorado.edu
Ashesh Sharma
ashesh.sharma@colorado.edu

¹ Department of Aerospace Engineering Sciences, University of Colorado at Boulder, Boulder, CO 427 UCB, USA

dealing with stress constraints in topology optimization. Imposing local stress constraints provides local control of the stress level. However, solving the optimization problem becomes more time consuming and complex as the number of nonlinear constraints increases with mesh refinement. To reduce the computational effort, there have been many studies on approaches for incorporating global stress measures into the optimization problem formulation (cf. Yang and Chen 1996; Duysinx and Sigmund 1998; Paris et al. 2008). The p-norm and the Kreisselmeier-Steinhauser (KS) function have been widely used for approximating local stresses at the global level. At the cost of some accuracy in satisfying stress constraints locally, the number of constraints is drastically reduced. Le et al. (2010) and Paris et al. (2010) employ regional stress constraints as a compromise between global and local stress constraints. The regional stress measures improve the local approximation of stresses while keeping computational costs in check. In contrast to most stress-based optimization studies, which adopt the von Mises yield criterion, Bruggi and Duysinx (2012) focused on the Drucker-Prager failure criterion to take into account the behavior of pressure-dependent materials such as concrete, polymers, and composite structures.

During the optimization process in density-based approaches, there may exist grey regions comprising of elements with intermediate densities. The geometry of the material interface is represented by either large spatial gradients or by jumps in the density fields, depending on the discretization of the density distribution and the method of enforcing convergence to a discrete material distribution. Unless the interface is aligned with the discretization of the density field, the interface is either smeared across elements or approximated by a jagged boundary. Either scenario leads to a description of the interface geometry that proves challenging when predicting stresses accurately along the material interface. Additionally, the relationship between the allowable stress and the material density needs to be specified, as discussed by Duysinx and Bendsøe (1998).

The above mentioned issues have been overcome in recent years through the use of the Level Set Method (LSM) which allows for a crisp representation of the material boundaries (cf. Osher and Sethian 1988; Osher and Santosa 2001). In the LSM, the geometry of the material boundaries is described explicitly by the iso-contour of the level set function (LSF), ϕ , at a particular value, typically $\phi = 0$ (cf. Sethian and Wiegmann 2000; Wang et al. 2003; Allaire et al. 2004). Smooth changes in the LSF lead to changes in the geometry of the domain including merging of geometric features. An important aspect of level set-based methods is the mapping of the geometry to a mechanical model. In the context of topology optimization, Ersatz material approaches and immersed boundary methods are the most popular options of geometry mapping. The Ersatz material

approach requires interpolation of physical properties as functions of the LSF. As in density-based methods, such as SIMP, this may lead to smearing of the material interface, affecting the resolution and accuracy of the finite element predictions along the material boundaries (Dijk et al. 2013).

To overcome the issues associated with density-based mapping we adopt an Eulerian approach that utilizes the eXtended Finite element Method (XFEM), developed by Moës et al. (1999), to model the physical response of the mechanical problem. The XFEM is an immersed boundary technique that uses an enrichment function to locally capture the non-smooth solution of state variable fields along the material interface without requiring a conforming mesh. Depending on the type of discontinuity, various enrichment strategies have been developed as discussed by Fries and Belytschko (2010). The combination of the LSM and the XFEM is referred to as the LSM-XFEM approach and is often classified as a generalized shape optimization approach (Duysinx et al. 2006). This classification stems from the fact that the approach allows for topology modifications as existing holes can merge or disappear altering the topology of the design.

The first study to focus on stress-based shape optimization using the LSM-XFEM approach was presented by Van Miegroet and Duysinx (2007). They studied the problem of minimizing stress concentration, in a 2D fillet in tension. They highlighted the problem of overestimation of stresses resulting from extremely small (or large) ratios of intersected areas within an intersected element. To maintain the accuracy of the computed stresses, strategies such as elimination of small intersections by shifting of the material interface were suggested. Guo et al. (2011) applied the LSM-XFEM approach to stress-related topology optimization problems. This approach was extended to problems involving multi-phase materials by Guo et al. (2014). However, issues concerning inaccurate computation of stresses resulting from position of the material interface were not dealt with in either of the studies. Recently Polajnar et al. (2017) performed structural optimization studies based on a global stress-deviation measure for material-void problems. To circumvent the problem of overestimation of stresses, elements with small intersection areas were ignored from the finite element analysis. Additionally, they post-processed the stresses using the patch recovery method of Zienkiewicz and Zhu (1992) to give smoothed stress values at the nodes. Noël and Duysinx (2017) applied the LSM-XFEM framework to shape optimization of microstructural designs subject to local stress constraints. They use an area weighted smoothing to post-process stresses associated with intersected elements. Cai et al. (2014) used the B-spline Finite Cell Method to achieve a high-order continuity and stress accuracy along cell boundaries, in shape and topology optimization.

As mentioned above, the accuracy of stresses in the XFEM around the material interface is affected by extreme ratios of intersected areas within an intersected element. Low-order finite elements, given their simplicity and ease of implementation are the most popular choice of interpolation for topology optimization problems. The influence of small intersection areas on the accuracy of spatial gradients is aggravated when using low-order elements. Inaccurate displacement gradients lead to inaccurate stresses which can further affect the outcome of the design optimization process. Focusing on this issue and improving the prediction of stresses presents the primary goal of this paper. We use the fictitious domain approach of Burman and Hansbo (2014) in conjugation with a novel XFEM informed smoothing scheme for the computation of stresses, to present a simple and efficient approach to improve the computation of the stresses on low-order elements. We incorporate the stabilized stresses in an optimization framework to solve material-void and material-material topology optimization problems. Material-void problems are solved using a compliance minimization formulation subject to volume and global stress constraints. Material-material problems are solved using a volume minimization formulation subject to global stress constraints. We adopt the von Mises stress measure to define the stress constraints. Shape sensitivities are computed by the adjoint method. Through a numerical study we investigate the accuracy and robustness of the proposed approach for computation of stresses and corresponding sensitivities along material interfaces. We present optimization studies in 2D and 3D using the benchmark topology optimization problem of an L-shaped beam. We consider linear and hyperelastic materials.

The remainder of the manuscript is organized as follows: Section 2 presents the LSM for the description of geometry; Section 3 presents the governing equations, the XFEM discretization, and a robust approach for computation of stresses; Section 4 presents the optimization problem formulations and the corresponding sensitivity analysis using the adjoint method; in Section 5 we present numerical examples to analyze and validate the proposed approach; finally, a summary and concluding remarks are presented in Section 6.

2 Geometry description

The current study is illustrated using the model problem depicted in Fig. 1. Our model problem consists of one or more stationary inclusions (material or void) embedded in a matrix. The spatial domain is defined by $\Omega \subset \mathbb{R}^d$ for d spatial dimensions. This spatial domain is composed of two non-overlapping material subdomains (also referred to as material phases), Ω^A and Ω^B , such that $\Omega = \Omega^A \cup$

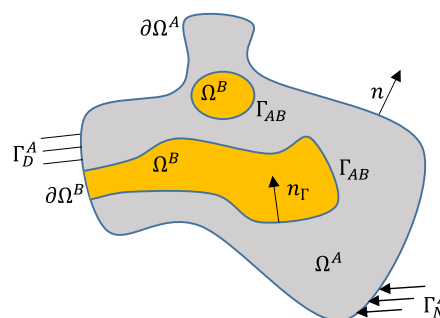


Fig. 1 Schematic of the model problem

Ω^B . The boundaries for the material domains Ω^A and Ω^B are expressed as $\partial\Omega^A$ and $\partial\Omega^B$ respectively. The outward normal vector to these boundaries is denoted by \mathbf{n} . The Dirichlet and Neumann boundaries are denoted by $\Gamma_D^m = \partial\Omega^m \cap \partial\Omega_D$ and $\Gamma_N^m = \partial\Omega^m \cap \partial\Omega_N$ respectively, where $m = A, B$. We consider a sharp material interface, Γ_{AB} , defined as $\Gamma_{AB} = \partial\Omega^A \cap \partial\Omega^B$. The outward normal along the material interface Γ_{AB} , with respect to $\partial\Omega^A$, is denoted by \mathbf{n}_Γ .

Using the LSM, the material layout in Fig. 1 is defined by a LSF $\phi(\mathbf{x})$ such that:

$$\begin{aligned} \phi(\mathbf{x}) &< 0, \forall \mathbf{x} \in \Omega^A, \\ \phi(\mathbf{x}) &> 0, \forall \mathbf{x} \in \Omega^B, \\ \phi(\mathbf{x}) &= 0, \forall \mathbf{x} \in \Gamma_{AB}, \end{aligned} \quad (1)$$

where the vector \mathbf{x} denotes the spatial coordinates. The LSF is mapped onto the XFEM mesh by evaluating the parametrized LSF at the nodes. Standard finite element shape functions are used to interpolate the LSF value at a point within an element. To this end we discretize the LSF using bilinear (in 2D) and trilinear (in 3D) finite elements.

Instead of updating the LSF by the solution of the Hamilton-Jacobi equation (see e.g. Wang et al. 2003; Allaire et al. 2004), in this work the parameters of the discretized LSF are defined as explicit functions of the optimization variables. Each node, i , of the finite element mesh is assigned an optimization design variable, s_i . The LSF value, ϕ_i , for node i is then defined through an explicit function of the optimization variables using a level set filter as follows:

$$\phi_i = \frac{\sum_{j=1}^{N_n} w_{ij} s_j}{\sum_{j=1}^{N_n} w_{ij}}, \quad (2)$$

where

$$w_{ij} = \max(0, r_\phi - |\mathbf{x}_i - \mathbf{x}_j|). \quad (3)$$

Here N_n is the number of nodes in the finite element mesh and r_ϕ is the smoothing filter radius. The linear filter (2) widens the zone of influence of the design variable on the level set field resulting in enhanced convergence of the optimization process (Kreissl and Maute 2012). In the absence of a level set filter $\phi_i = s_i$.

Level set-based optimization approaches require seeding the initial design with inclusions and/or introducing inclusions in the course of the optimization process, for example via topological derivatives (Burger et al. 2004). The optimization results using the LSM are typically dependent on the initial layout of such inclusions. For a detailed discussion on the LSM within the context of shape and topology optimization, the reader may refer to the comprehensive review by Dijk et al. (2013).

3 Structural analysis

This section presents the variational form of the governing equations for linear elastic and hyperelastic structural analysis of the model problem in Fig. 1, followed by a brief overview of the adopted XFEM discretization and a robust approach for accurate computation of stresses in the XFEM.

3.1 Variational form of governing equations

We adopt the standard Galerkin approach in defining the solution spaces $\mathcal{U} = \mathcal{U}^A \times \mathcal{U}^B$ and the weighting spaces $\mathcal{V} = \mathcal{V}^A \times \mathcal{V}^B$ over the domain Ω , such that

$$\begin{aligned} \mathcal{U}^m &= \left\{ \mathbf{u}^m \in H^1(\Omega^m); \mathbf{u}^m = \mathbf{u}_D \text{ on } \Gamma_D^m \right\}, \\ \mathcal{V}^m &= \left\{ \mathbf{v}^m \in H^1(\Omega^m); \mathbf{v}^m = 0 \text{ on } \Gamma_D^m \right\}, \end{aligned} \tag{4}$$

where \mathbf{u}^m and \mathbf{v}^m are the displacement field and the corresponding weighting function respectively, for material phases $m = A, B$. The spaces \mathcal{U} and \mathcal{V} are Hilbert manifolds consisting of vector functions with square integrable first derivatives.

The weak form for linear elastic structural analysis is augmented with the Nitsche's method (Stenberg 1995), to satisfy continuity of solution and traction across the interface in material-material problems. The weak form is stated as: Find \mathbf{u} such that

$$\mathcal{R}^E = \mathcal{R}_\Omega^E + \mathcal{R}_{\Gamma_N}^E + \mathcal{R}_{\Gamma_{AB}}^E = 0 \quad \forall \mathbf{v} \in \mathcal{V}, \tag{5}$$

where \mathcal{R}_Ω^E is the residual of the volumetric contribution, $\mathcal{R}_{\Gamma_N}^E$ is the residual contribution from the Neumann boundary,

and $\mathcal{R}_{\Gamma_{AB}}^E$ is the residual contribution from the interface conditions. These residual contributions are given by

$$\begin{aligned} \mathcal{R}_\Omega^E &= \sum_{m=A,B} \int_{\Omega^m} \boldsymbol{\epsilon}(\mathbf{v}^m) : \boldsymbol{\sigma}(\mathbf{u}^m) dx, \\ \mathcal{R}_{\Gamma_N}^E &= - \sum_{m=A,B} \int_{\Gamma_N^m} \mathbf{v}^m \mathbf{t}_N ds, \\ \mathcal{R}_{\Gamma_{AB}}^E &= - \int_{\Gamma_{AB}} \llbracket \mathbf{v} \rrbracket \{ \boldsymbol{\sigma}(\mathbf{u}) \} \cdot \mathbf{n}_\Gamma ds \\ &\quad - \int_{\Gamma_{AB}} \{ \boldsymbol{\sigma}(\mathbf{v}) \} \cdot \mathbf{n}_\Gamma \llbracket \mathbf{u} \rrbracket ds \\ &\quad + \gamma_\Gamma \int_{\Gamma_{AB}} \llbracket \mathbf{v} \rrbracket \llbracket \mathbf{u} \rrbracket ds. \end{aligned} \tag{6}$$

The displacement, \mathbf{u}_D , is specified on the Dirichlet boundary, Γ_D^m , and traction, \mathbf{t}_N , is specified on the Neumann boundary, Γ_N^m . The materials are assumed isotropic. The Cauchy stress tensor, $\boldsymbol{\sigma}^m$, is defined using the constitutive model

$$\boldsymbol{\sigma}^m = \mathbf{D}^m \boldsymbol{\epsilon}^m = \mathbf{D}^m \frac{1}{2} \left(\nabla \mathbf{u}^m + (\nabla \mathbf{u}^m)^T \right), \tag{7}$$

where \mathbf{D}^m is the fourth order constitutive tensor for the isotropic material belonging to material phase m , and $\boldsymbol{\epsilon}^m$ is the infinitesimal strain tensor.

The jump and averaging operators are defined as $\llbracket \mathbf{u} \rrbracket = (\mathbf{u}^B - \mathbf{u}^A)$ and $\{ \boldsymbol{\sigma} \} = \gamma^A \boldsymbol{\sigma}^A + \gamma^B \boldsymbol{\sigma}^B$ respectively. The constants γ_Γ , γ^A , and γ^B determine the accuracy with which the interface conditions are satisfied. Following the work of Annavarapu et al. (2012) we define these constants as

$$\begin{aligned} \gamma_\Gamma &= 2 c_\Gamma \frac{meas(\Gamma_{AB})}{meas(\Omega^A)/E^A + meas(\Omega^B)/E^B}, \\ \gamma^m &= \frac{meas(\Omega^m)/E^m}{meas(\Omega^A)E^A + meas(\Omega^B)/E^B}, \end{aligned} \tag{8}$$

where E^m is the Young's modulus associated with material phase m . The user defined penalty c_Γ determines how strongly the interface constraints are enforced. A high value of c_Γ ensures better enforcement of the interface conditions but may lead to poor conditioning of the underlying system of equations. The operator $meas(\cdot)$ refers to the Lebesgue measure of the respective quantity.

We also consider solid-void problems considering finite strains using the Saint Venant-Kirchhoff hyperelastic model. The hyperelastic model involves solving for the vector displacement field, $\mathbf{u}(\mathbf{x})$, in Ω^A . Phase B is void of any material. In the context of material nonlinearity, equilibrium is formulated with respect to a reference undeformed configuration and the weak form is stated as: Find \mathbf{u}^A such that

$$\mathcal{R}^H = \mathcal{R}_\Omega^H + \mathcal{R}_{\Gamma_N^A}^H \quad \forall \mathbf{v}^A \in \mathcal{V}^A. \tag{9}$$



Here \mathcal{R}_Ω^H is the residual of the volumetric contribution and $\mathcal{R}_{\Gamma_N^A}^H$ is the residual contribution from the Neumann boundary. These contributions are given by:

$$\begin{aligned}\mathcal{R}_\Omega^H &= \int_{\Omega^{A_0}} \mathbf{F}(\mathbf{v}^A) : \mathbf{P}(\mathbf{u}^A) dx, \\ \mathcal{R}_{\Gamma_N^A}^H &= - \int_{\Gamma_{N_0}^A} \mathbf{v}^A \mathbf{t}_N ds.\end{aligned}\quad (10)$$

Here \mathbf{u}^A is the restriction of \mathbf{u} to Ω^{A_0} . The displacement, \mathbf{u}_D , is specified on the Dirichlet boundary, $\Gamma_{D_0}^A$, and traction, \mathbf{t}_N , is specified on the Neumann boundary, $\Gamma_{N_0}^A$. The subscript '0' refers to entities defined in the undeformed configuration. The first Piola-Kirchhoff stress in phase A is denoted by \mathbf{P}^A . The Saint Venant-Kirchhoff hyperelastic material model is defined as:

$$\begin{aligned}\Psi^A &= \frac{\mu^A}{4} \left(\mathbf{C}^A (\mathbf{C}^A)^T - 2 \operatorname{tr}(\mathbf{C}^A) + 3 \right) \\ &\quad + \frac{\lambda^A}{8} \left(\operatorname{tr}(\mathbf{C}^A) - 3 \right)^2,\end{aligned}\quad (11)$$

with the corresponding nonlinear kinematic relations in phase A given by:

$$\begin{aligned}\mathbf{C}^A &= (\mathbf{F}^A)^T (\mathbf{F}^A), \\ \mathbf{F}^A &= \nabla_0(\mathbf{x}^A), \\ \mathbf{P}^A &= \det(\mathbf{F}^A) \boldsymbol{\sigma}^A (\mathbf{F}^A)^{-T}, \\ \mathbf{x}^A &= \mathbf{u}^A + \mathbf{x}_0^A,\end{aligned}\quad (12)$$

where Ψ^A denotes the strain energy density model for a Saint Venant-Kirchhoff hyperelastic material. The Lamé parameters are denoted by μ^A and λ^A . The right Cauchy strain tensor is denoted by \mathbf{C} , and \mathbf{F} is the deformation gradient that accounts for the motion of the spatial coordinate in the deformed configuration, \mathbf{x}^A , with respect to the spatial coordinate in the undeformed configuration, \mathbf{x}_0^A .

Note, we consider single-phase hyperelastic problems wherein the solution or traction are not required to be continuous across the material-void interface. Hence no interface conditions are enforced.

3.2 XFEM

To capture non-smooth displacement fields across material interfaces the traditional finite element method requires a conforming mesh. In the XFEM, this requirement is eliminated by augmenting the standard finite element interpolation by additional enrichment functions. These enrichment functions capture discontinuities in either the state variables or their spatial gradients. Following the work by Terada et al. (2003), Hansbo and Hansbo (2004), and Makhija and Maute (2014), a generalized Heaviside enrichment strategy with multiple enrichment levels is adopted. This enrichment strategy ensures that the solution field is interpolated in a

consistent manner, and avoids any artificial coupling due to disconnected material phases. This enrichment strategy has been successfully applied to topology optimization of linear elasticity problems by Villanueva and Maute (2014), to incompressible Navier-Stokes problems by Jenkins and Maute (2015), to heat diffusion by Lang et al. (2015), and to natural convection problems by Coffin and Maute (2016).

For a two-phase problem, the approximation of the displacement field, $\mathbf{u}(\mathbf{x})$, denoted as $\hat{\mathbf{u}}(\mathbf{x})$, using the Heaviside-enriched XFEM is given by

$$\begin{aligned}\hat{\mathbf{u}}(\mathbf{x}) &= \sum_{e=1}^{N_e} \left(H(-\phi(\mathbf{x})) \sum_{i \in I} \mathcal{N}_i(\mathbf{x}) \mathbf{u}_{i,e}^A \delta_{el}^{A,i} \right. \\ &\quad \left. + H(+\phi(\mathbf{x})) \sum_{i \in I} \mathcal{N}_i(\mathbf{x}) \mathbf{u}_{i,e}^B \delta_{el}^{B,i} \right),\end{aligned}\quad (13)$$

with the Heaviside function, H , defined as

$$H(z) = \begin{cases} 1 & z > 0 \\ 0 & z \leq 0 \end{cases}.\quad (14)$$

Here I is the set of all nodes in the finite element mesh, $\mathcal{N}_i(\mathbf{x})$ is the nodal basis function associated with node i , N_e is the maximum number of enrichment levels, and $\mathbf{u}_{i,e}^m$ is the vector of displacement degrees of freedom associated with node i for material phase $m \in (A, B)$. The Kronecker delta $\delta_{el}^{m,i}$ selects the active enrichment level l for node i and phase m such that only one set of degrees of freedom are used for interpolating the solution at point \mathbf{x} , thereby satisfying the partition of unity principle introduced by Babuška and Melenk (1997). The active number of enrichment levels depends on the number of disconnected regions of the same phase included in the support of $\mathcal{N}_i(\mathbf{x})$. For a more comprehensive understanding of the adopted enrichment strategy the reader is referred to the study by Makhija and Maute (2014).

The Heaviside-enriched XFEM requires integrating the weak form of the governing equations separately in each material phase. To this end integration subdomains are generated by decomposing the intersected elements into triangles in 2D and into tetrahedrons in 3D. The decomposition approach adopted in the current study is discussed in detail by Villanueva and Maute (2014). The adopted generalized Heaviside enrichment strategy requires that the material interface never intersect a node. Hence intersections directly through a node or an element edge are avoided by enforcing $\phi_i \neq 0$. Effects of enforcing this rule on the computation of shape sensitivities have been addressed by Sharma et al. (2017).

3.3 Ghost penalty: face oriented stabilization of spatial gradients

Material interface too close to a node can lead to small intersection areas. These small regions correspond to vanishing zone of influences for certain degrees of freedom. Aside from adversely affecting the condition number of the system, small intersections can result in uncontrolled displacement gradients across element edges leading to inaccurate prediction of these gradients around the material interface. As discussed in Section 1, in the context of stress-based topology optimization using low-order elements inaccurate displacement gradients lead to inaccurate stresses which can affect the optimization results. When considering stress-based objectives or constraints, inaccurate and oscillatory stresses can lead to unreliable sensitivities. For a nonlinear structural model inaccurate displacement gradients can affect the stability of the system of equations. To maintain stability of the system and ensure the convergence of stress prediction with mesh refinement, we adopt the ghost penalty approach introduced by Burman and Hansbo (2014).

We consider the set of element faces, \mathcal{F}_{cut} , belonging to intersected elements, \mathcal{E}_{cut} , as shown in Fig. 2. For each face, $F \in \mathcal{F}_{cut}$, there exist two elements (one of which is the intersected element itself), \mathcal{E}^1 and \mathcal{E}^2 , such that $F = \mathcal{E}^1 \cap \mathcal{E}^2$. The jump in the displacement gradients across this face is then penalized by augmenting the left hand side of (5) and (9) with the following term.

$$\mathcal{R}_F^E = \mathcal{R}_F^H = \sum_{F \in \mathcal{F}_{cut}} \sum_{m=A,B} \int_F \gamma_u E^m h [\nabla v^m] [\nabla u^m] ds, \tag{15}$$

where E^m is the elastic modulus of phase m , and γ_u is a penalty parameter. The choice of γ_u is discussed in Section 5.1. The jump in the displacement gradient is defined as $[\nabla u^m] = \mathbf{n}_F \cdot \nabla u^m|_{\mathcal{E}^1} - \mathbf{n}_F \cdot \nabla u^m|_{\mathcal{E}^2}$, where \mathbf{n}_F denotes the unit normal to the face, F . The orientation of \mathbf{n}_F

does not matter as long as it is normal to the face and consistent across neighboring elements. Note that only the jump of the displacement gradients in normal direction is penalized.

This face oriented stabilization of spatial gradients presents two advantages - i) Smooth displacement gradients are obtained along the material interface. ii) The zone of influence of degrees of freedom no longer vanishes because (15) requires integration over the entire face independent of the location of the intersection. A drawback is that the framework results in a non-smooth behavior of stresses as the material interface transitions from one element to another. This is a result of the on/off nature of (15), and is further discussed in Section 5.1. Since $F = \mathcal{E}^1 \cap \mathcal{E}^2$, by definition faces along the boundary of the mesh are excluded from the set \mathcal{F}_{cut} . A solution to this issue is presented in Section 5.2.

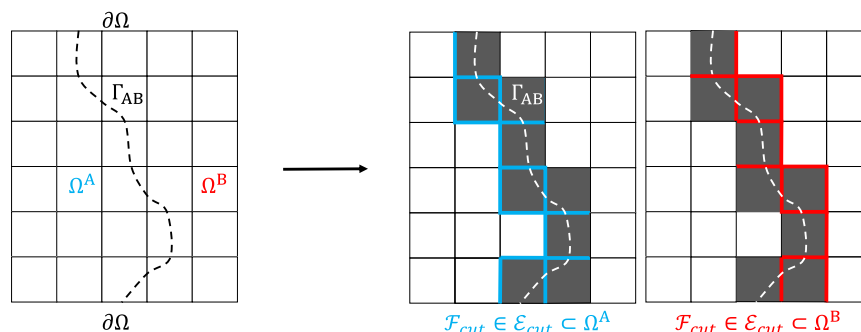
For further details on ghost penalty including analysis of a priori error estimates the reader is referred to the comprehensive study by Burman and Hansbo (2014).

3.4 XFEM informed smoothing of stresses

To avoid overestimation of stresses Van Miegroet and Duysinx (2007) proposed several strategies, most of which involved eliminating stresses when the intersected area was too small. Recently Noël and Duysinx (2017) adopted an area weighted smoothing using an elemental average strategy for post-processing of stresses in an intersected element. The authors noted that such a smoothing does not ensure avoidance of overestimation of stresses. For comparison with the approach proposed in the current study, we compute area weighted stresses using a nodal average strategy. This is because nodal averaged stresses provide a sharper stress distribution as compared to elemental stresses, in regards to the smoothing area as shown in Fig. 3. The smoothed stress tensor for node i , σ_i , using a nodal average strategy is computed as

$$\sigma_i = \frac{\sum_{\mathcal{E} \in Nb_i} \sigma_{\mathcal{E}} A_{\mathcal{E}}}{\sum_{\mathcal{E} \in Nb_i} A_{\mathcal{E}}}. \tag{16}$$

Fig. 2 Stabilized faces in a two-phase problem



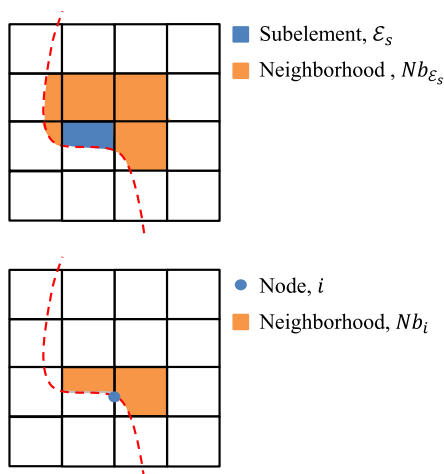


Fig. 3 Area weighted smoothing using an elemental average strategy (top) and a nodal average strategy (bottom)

Here Nb_i is the combined set of intersected and unintersected elements sharing the node i as shown in Fig. 3, $A_{\mathcal{E}}$ and $\sigma_{\mathcal{E}_i}$ are the area and nodal stress tensor of element, \mathcal{E} , respectively. Following the definitions of the respective neighborhoods, it is noted that the elemental average strategy is more diffusive as compared to the nodal average strategy. In Section 5.1 we demonstrate the ineffectiveness of an area weighted smoothing, resulting in overestimation of stresses and unreliable stress sensitivities.

In the current study, we introduce a scalar stress field, τ , using an XFEM informed smoothing procedure. Using the solution of the displacement field we solve the following equation, to obtain a gradient stabilized scalar stress field within a Heaviside-enriched XFEM framework.

$$\begin{aligned} \mathcal{R}_{\Omega}^S + \mathcal{R}_F^S = 0 \quad \forall \eta \in \mathcal{V} \implies \\ \sum_{m=A,B} \left(\int_{\Omega^m} \eta^m \tau^m dx - \int_{\Omega^m} \eta^m \mathcal{S}(\mathbf{u}^m) dx \right) \\ + \sum_{F \in \mathcal{F}_{cut}} \sum_{m=A,B} \int_F \gamma_{\tau} h [\nabla \eta^m] [\nabla \tau^m] ds = 0. \end{aligned} \quad (17)$$

Here \mathcal{S} is a scalar function of the components of the Cauchy stress tensor, e.g. axial stress, principal stress, and von Mises stress, computed using the displacement fields, \mathbf{u}^m . In the present study \mathcal{S} is the von Mises stress function. The smoothed scalar stress field is denoted by τ^m , with η^m being the corresponding weighting function. The functions τ^m and η^m belong to Hilbert manifolds, \mathcal{U} and \mathcal{V} respectively, consisting of scalar functions with square integrable first derivatives. Note, the scalar stress field is computed using the displacement field subjected to ghost penalty. Thus the ghost penalty terms in (17) provide a second level of spatial gradient stabilization.

In comparison with an area weighted smoothing, the XFEM informed smoothing ensures the avoidance of overestimation of stresses by penalizing the jump in spatial stress gradients across elemental faces. It should be noted, like the area weighted smoothing the XFEM informed smoothing is just a post-processing step.

4 Optimization problem

The majority of previous work on stress constrained optimization considers volume minimization problems subject to stress constraints. For a material-void problem such a formulation is ill-posed with the optimal solution being a structure with zero volume. To avoid this issue in this work, we formulate the optimization problem as a compliance minimization problem subject to stress and volume constraints. While compliance minimization leads to an overall decrease in stresses, stress constraints are required to eliminate designs with local stress peaks. To promote smooth shapes and discourage the formation of small geometric features we augment the objective with a measure of the interface perimeter (see Haber et al. 1996; Makhija and Maute 2014). The optimization problem is formulated as follows.

$$\begin{aligned} \min_s \quad & c_J \mathcal{J}(\mathbf{u}(s)) + c_P \mathcal{P}(s) \\ \text{s.t.} \quad & \begin{cases} g(\sigma_V(\tau(s))) \leq 0 \\ g(\sigma_{\Gamma}(\tau(s))) \leq 0 \\ \frac{V^A(s)}{V(s)} - c_V \leq 0 \end{cases}, \end{aligned} \quad (18)$$

where \mathcal{J} is the compliance integrated over the complete domain, and \mathcal{P} is the perimeter corresponding to the material domain boundary. The penalties c_J and c_P are associated with the compliance and perimeter respectively. These are chosen such that the terms constituting the objective function are of similar order throughout the optimization process. The volume ratio of the material phase, V^A , with respect to the total volume, V , is constrained to be less than or equal to c_V . As discussed in the next section, the stress constraints $g(\sigma_V)$ and $g(\sigma_{\Gamma})$ are evaluated via integration over the volume, Ω , and the material interface, Γ_{AB} , respectively. Unless operating on a fine mesh, $g(\sigma_V)$ alone is not sufficient for capturing the stress distribution along material interfaces. Hence an additional constraint, $g(\sigma_{\Gamma})$, capturing the stresses along the material is introduced. The need for $g(\sigma_{\Gamma})$ is pronounced in 3D problems using coarse meshes. This is because on coarse meshes, evaluating a stress constraint using solely volume integration points is sometimes ineffective in capturing stress singularities that might occur at the surface. Consequently in the current study $g(\sigma_{\Gamma})$ is employed for 3D problems only.

For material-material problems a different optimization problem formulation is considered wherein the objective is to minimize the volume fraction of phase A. In contrast to a

material-void setting, such a problem formulation is not ill-posed because the design domain consists of at least one material leading to a structural design with finite volume at all times during the optimization process. For material-material problems the optimization problem is formulated as follows.

$$\begin{aligned} \min_s \quad & c_W \frac{V^A(s)}{V(s)} + c_P \mathcal{P}(s) \\ \text{s.t.} \quad & g(\sigma_V(\tau(s))) \leq 0 \end{aligned} \quad (19)$$

Here c_W is the penalty associated with the volume fraction of phase A. Material-material problems are considered in 2D only. Hence $g(\sigma_\Gamma)$ is not included in the problem formulation of (19).

4.1 Formulation of stress constraints

Researchers have developed various approaches to include stress measures into the optimization problem. Duysinx and Bendsøe (1998) first applied point-wise or local stress constraints. Cheng and Jiang (1992) and París et al. (2008) have used global stress functions to approximate local stresses. Le et al. (2010) and París et al. (2010) employed regional stress constraints as a compromise between global and local stress constraints. Zhang et al. (2013) proposed a global stress measure enhanced by boundary curvature and stress gradient measures. Recently Polajnar et al. (2017) proposed a stress-based objective function based on a global stress-deviation measure. In the present study, we follow the work of París et al. (2008) in our definition of global stress constraint measures, based on the KS function for constraint aggregation proposed by Poon and Martins (2007). The approach of París et al. (2008) is easy to implement and sufficient to study the primary goal of this paper, which strictly pertains to the characteristic of the stresses and their derivatives that go into the stress-based optimization formulations. Consequently, the findings of the current work are applicable to any of the above mentioned approaches.

The global stress constraints approach implies the use of one constraint that represents all local constraints. Given a maximum allowable stress value, σ_{max} , the global stress constraints are defined as,

$$\begin{aligned} g(\sigma_V(\tau(s))) &= \frac{1}{\beta_V} \log \int_{\Omega} e^{\beta_V \left(\frac{\tau - \sigma_{max}}{\sigma_{max}} \right)} dx \\ &\quad - \frac{1}{\beta_V} \log \int_{\Omega} dx, \\ g(\sigma_\Gamma(\tau(s))) &= \frac{1}{\beta_\Gamma} \log \int_{\Gamma} e^{\beta_\Gamma \left(\frac{\tau - \sigma_{max}}{\sigma_{max}} \right)} ds \\ &\quad - \frac{1}{\beta_\Gamma} \log \int_{\Gamma} ds. \end{aligned} \quad (20)$$

The stress constraints in (20) are formulated using the smoothed stresses of (17). The parameters β_V and β_Γ are tuning coefficients which penalizes the failure to satisfy the

stress constraint. As they tend to infinity the stress constraints become equal to $(\max(\tau) - \sigma_{max})/\sigma_{max}$. However, a large value of β_V or β_Γ renders the optimization problem unstable and difficult to solve due to the increasing nonlinearity and badly scaled sensitivities of the stress constraints. Selection of the parameters β_V and β_Γ thus involves a trade-off between accuracy of the global stress capturing capability and stability of the optimization problem.

4.2 Sensitivity analysis

Within the framework of gradient based optimization, sensitivity analysis computes the derivative of a response function, $Z(\mathbf{u}(s), \tau(s), s)$ (e.g. compliance, global stress measure etc.), with respect to the vector of design variables, s . The gradient of the response function in the case where Z depends on \mathbf{u} and τ , is stated as

$$\frac{dZ}{ds_i} = \frac{\partial Z}{\partial s_i} + \left(\frac{\partial Z}{\partial \mathbf{u}} \right)^T \frac{d\mathbf{u}}{ds_i} + \left(\frac{\partial Z}{\partial \tau} \right)^T \frac{d\tau}{ds_i}, \quad (21)$$

where the first term on the right hand side accounts for the explicit dependency of the response function on the design variables. The second and third terms on the right hand side account for the dependency of the response function on the state variables \mathbf{u} and τ respectively.

We compute the implicit dependency using the adjoint method. We begin by defining the residual of the system of equations as follows:

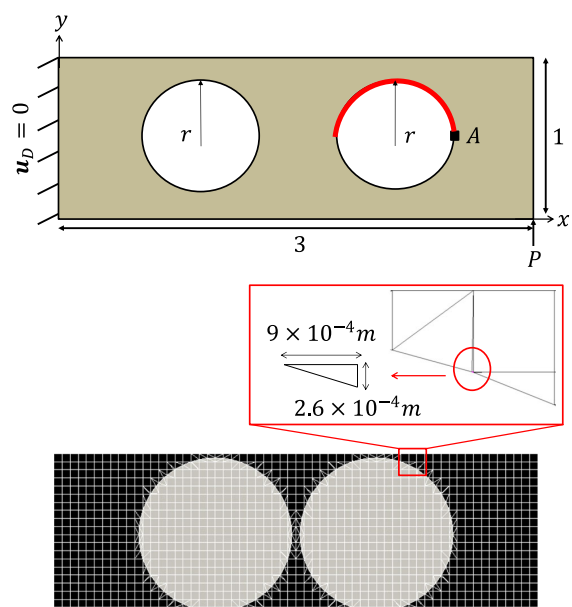


Fig. 4 Cantilever beam setup (top), and mesh $h = 0.05m$ (bottom). Stresses are monitored along the highlighted region. All dimensions are in m

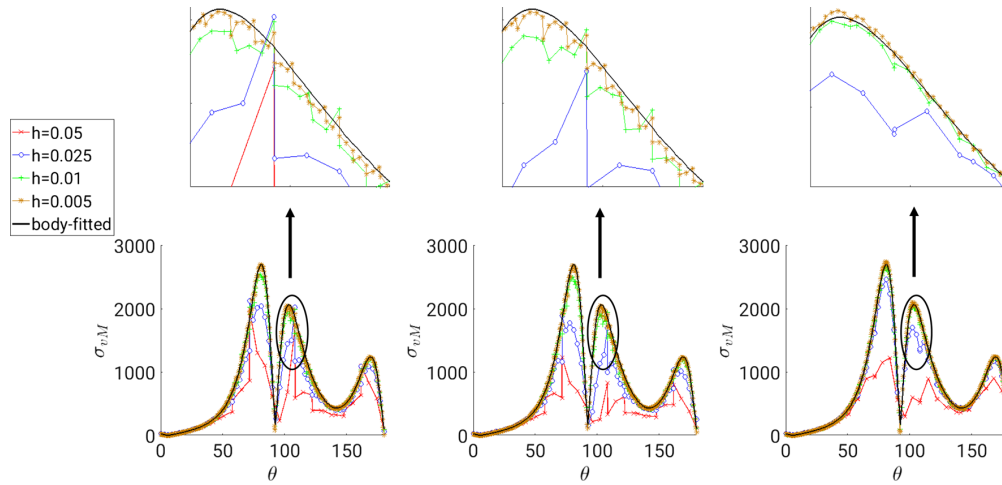


Fig. 5 Stress (N/m^2) profile along the material interface: Area weighted smoothing (left), Area weighted smoothing with $\gamma_u = 0.1h$ (middle), XFEM informed smoothing with $\gamma_u = 0, \gamma_\tau = 0$ (right)

$$\begin{aligned} \mathcal{R}^E, \mathcal{R}^H : \mathcal{R}_u &= 0, \\ \mathcal{R}^S : K_\tau \tau - \mathcal{S}(\mathbf{u}) &= 0. \end{aligned} \quad (22)$$

The first equation in (22) corresponds to the system of equations presented in Section 3.1 augmented with (15), and the second equation correspond to (17). Differentiating (22) with respect to the design variable, s_i , we have

$$\begin{aligned} \frac{d\mathcal{R}_u}{ds_i} &= \frac{\partial \mathcal{R}_u}{\partial \mathbf{u}} \frac{d\mathbf{u}}{ds_i} + \frac{\partial \mathcal{R}_u}{\partial s_i} = 0, \\ \frac{d\mathcal{R}^S}{ds_i} &= K_\tau \frac{d\tau}{ds_i} + \frac{\partial K_\tau}{\partial s_i} \tau - \frac{\partial \mathcal{S}}{\partial s_i} - \frac{\partial \mathcal{S}}{\partial \mathbf{u}} \frac{d\mathbf{u}}{ds_i} = 0. \end{aligned} \quad (23)$$

Using (23) we eliminate the derivative of the state variables with respect to the design variables in (21) to arrive at the gradient of the response function stated as

$$\frac{dZ}{ds_i} = \frac{\partial Z}{\partial s_i} - \frac{\partial \mathcal{R}_u}{\partial s_i} \lambda_u - \left(\frac{\partial K_\tau}{\partial s_i} \tau - \frac{\partial \mathcal{S}}{\partial s_i} \right) \lambda_\tau, \quad (24)$$

where the adjoint variables, λ_u and λ_τ , are obtained by solving the following linear system of equations.

$$\begin{aligned} K_\tau^T \lambda_\tau &= \frac{\partial Z}{\partial \tau}, \\ \left(\frac{\partial \mathcal{R}_u}{\partial \mathbf{u}} \right)^T \lambda_u &= \frac{\partial Z}{\partial \mathbf{u}} + \left(\frac{\partial \mathcal{S}}{\partial \mathbf{u}} \right)^T \lambda_\tau. \end{aligned} \quad (25)$$

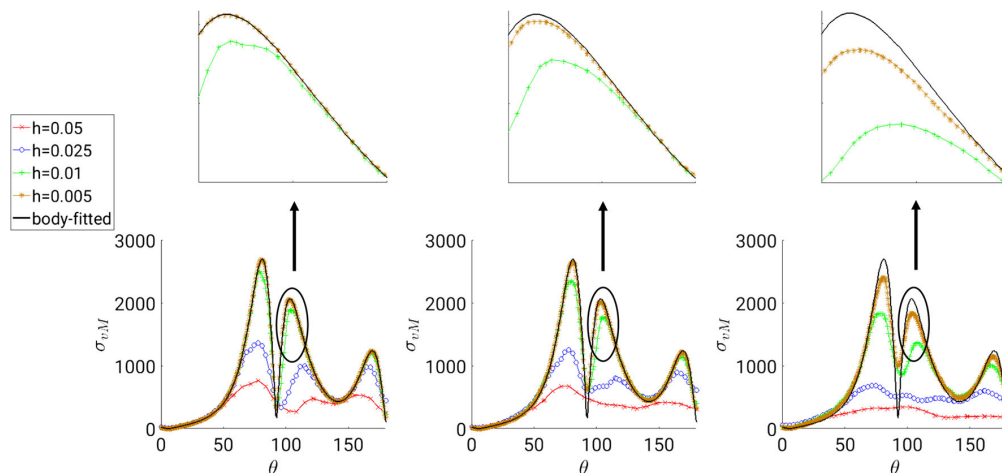
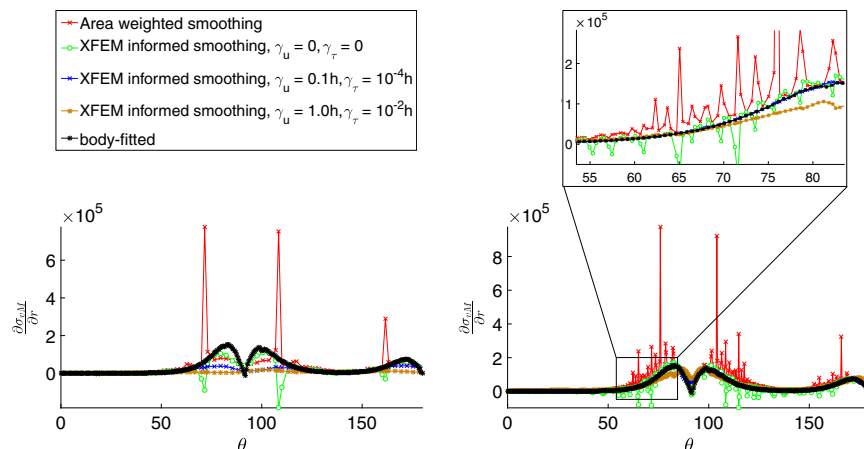


Fig. 6 Stress (N/m^2) profile along the material interface: XFEM informed smoothing with $\gamma_u = 0.1h, \gamma_\tau = 10^{-4}h$ (left), $\gamma_u = 0.1h, \gamma_\tau = 10^{-3}h$ (middle), and $\gamma_u = 1.0h, \gamma_\tau = 10^{-2}h$ (right)

Fig. 7 Comparison of stress sensitivities along material interface for $h = 0.025m$ (left) and $h = 0.005m$ (right)



In the adjoint approach presented above, the cost of solving the adjoint equations is equal to solving two linear system of equations for each response function.

Derivatives with respect to the design variable in (24) are discretized such that,

$$\frac{\partial(\cdot)}{\partial s_i} = \sum_{j \in I_{\mathcal{E}}} \sum_{k=1}^{N_{\Gamma}} \frac{\partial(\cdot)}{\partial \mathbf{x}_{\Gamma}^k} \frac{\partial \mathbf{x}_{\Gamma}^k}{\partial \phi_j} \frac{\partial \phi_j}{\partial s_i}. \tag{26}$$

Here N_{Γ} is the number of interfaces present within the element \mathcal{E} , and $I_{\mathcal{E}}$ is the set of all nodes belonging to the element. The parametrization of the interface, \mathbf{x}_{Γ} , is based on the definition of the level set field, ϕ . The product $\partial \mathbf{x}_{\Gamma}^k / \partial \phi_j \cdot \partial \phi_j / \partial s_i$ is computed analytically and depends on the gradient of the level set field as well as the definition of the level set filter (2). The term $\partial(\cdot) / \partial \mathbf{x}_{\Gamma}^k$ vanishes everywhere except for intersected elements, and is computed via finite differencing. The accuracy and robustness of the sensitivities computed using the proposed approach are discussed in detail by Sharma et al. (2017).

5 Numerical examples

We study the proposed LSM-XFEM approach by applying it to linear elastic and hyperelastic problems in 2D and 3D. In all examples presented, a 2D design domain is discretized in space using bilinear quadrilateral elements, and the 3D design domains are discretized using trilinear hexahedral elements. All 2D linear elastic examples are solved under the plane stress assumption. Enforcing plane stress conditions for hyperelasticity is nontrivial (Holzapfel 2000). For simplicity, the 2D hyperelastic examples are solved under plane strain assumptions.

The design sensitivities of the objective and constraints are computed using the adjoint approach presented in Section 4.2. The nonlinear optimization problems of (18) and (19) are solved by the Globally Convergent Method of Moving Asymptotes (GCMMA) (Svanberg 2002). The parameters controlling the adaptation of the initial, lower and upper asymptotes are set to 0.5, 0.7, and 1.43 respectively. A GCMMA constraint penalty of 10^4 was used for

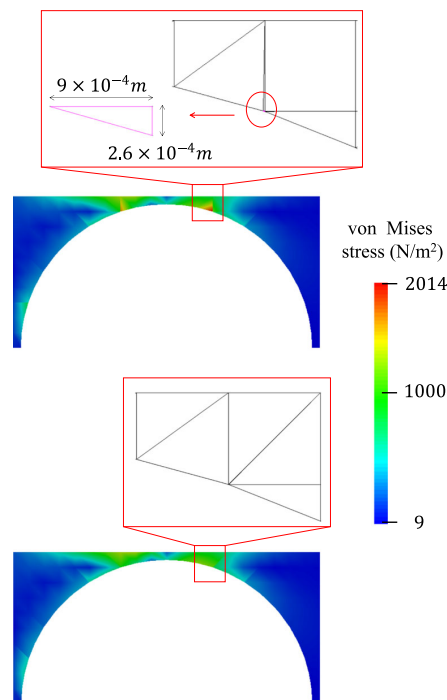
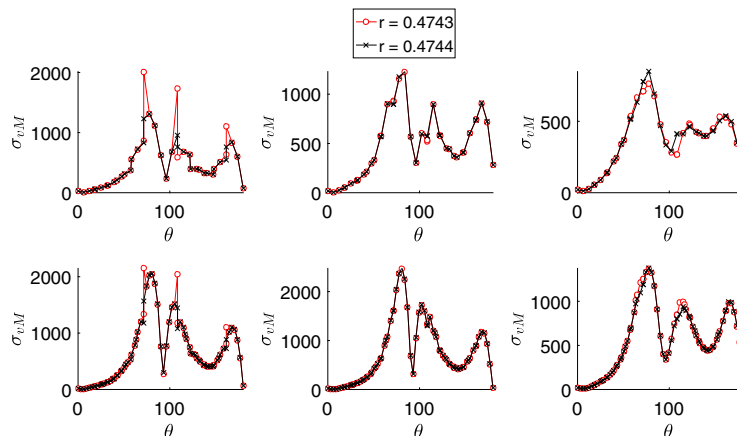


Fig. 8 Stress plots using area weighted smoothing for $r = 0.4743m$ (top) and $r = 0.4744m$ (bottom). Stress in N/m^2

Fig. 9 Stress profile along the material interface for $h = 0.05m$ (top), $h = 0.025m$ (bottom): Area weighted smoothing (left), XFEM informed smoothing with $\gamma_u = 0, \gamma_\tau = 0$ (middle), XFEM informed smoothing with $\gamma_u = 0.1h, \gamma_\tau = 10^{-4}h$ (right). Stress in N/m^2



all optimization examples. Convergence of the optimization process is achieved if all constraints are satisfied and the change in objective function is less than 0.1% for 10 consecutive iterations. The nonlinear problem of hyperelasticity is solved using Newton’s method. The linearized system of equations for all examples, of both the forward and the sensitivity analysis are solved using a direct solver. All numerical examples were solved in a quasi-static manner using a single load increment.

The numerical studies presented in the remainder of this section are organized as follows: In Example 1 we use a 2D cantilever beam to study the influence of ghost penalty combined with XFEM informed smoothing on the computation of stresses. In Examples 2 and 3 we optimize the design of a material-void L-shaped beam using an elastic and hyperelastic material respectively, in both 2D and 3D. Example 4 extends the proposed optimization approach to a material-material 2D L-beam using linear elastic materials.

5.1 Example 1

Through this example we illustrate the effect of stabilizing the spatial gradients on the computation of the stresses and stress sensitivities. We focus on the accuracy, robustness, and differentiability of the proposed approach. Comparisons are drawn against stresses computed using a body fitted mesh as well as stresses computed using area weighted smoothing (16). The problem setup consists of a material-void 2D cantilever beam of length $3m$ and height $1m$ as shown in Fig. 4. The beam is assumed elastic with a Young’s modulus, $E = 10^4 N/m^2$, and Poisson’s ratio, $\nu = 0.3$. The beam is fixed along its left edge. A point load of $P = 10N$ is applied at the bottom right corner of the beam. Within the beam are two circular inclusions, each of radius r , centers of which lie at $\mathbf{x} = (1, 0.5)$ and $\mathbf{x} = (2, 0.5)$. We monitor the stresses along the upper-half interface of the circular inclusion centered at $\mathbf{x} = (2, 0.5)$.

5.1.1 Accuracy

With $r = 0.4742m$ we investigate the accuracy of stresses along the material interface. The value of r is chosen such that the interface configuration results in small intersection areas for all mesh sizes used in the current example. Figures 5 and 6 plot the von Mises stress, σ_{vM} , as a function of the central angle, θ , measured in degrees counterclockwise from point A in Fig. 4. The stresses are plotted for various mesh sizes, h , for different values of stabilization penalty parameters, γ_u and γ_τ . These stresses are compared against a reference plot obtained using a body-fitted mesh of size $h = 0.005m$. The body-fitted solution was converged for this mesh size. Area weighted smoothing with and without ghost penalty, as well as XFEM informed smoothing without ghost penalty, i.e. $\gamma_u = 0$ and $\gamma_\tau = 0$, result in oscillatory stresses. Upon mesh refinement, these stresses do not converge to the body-fitted solution as shown in Fig. 5. In contrast, stresses obtained using XFEM informed smoothing of stress with ghost penalty (Fig. 6) have a smoother profile along the interface and converge with refinement in mesh. However, one should be careful with their choice for the gradient stabilization parameters. As expected and as shown in Fig. 6 a large value of the ghost penalty parameter smooths out the stresses extensively resulting in loss of stress profile capturing ability. Based on results presented in Figs. 5 and 6, for all optimization studies we chose $\gamma_u = 0.1h$ and $\gamma_\tau = 10^{-4}h$.

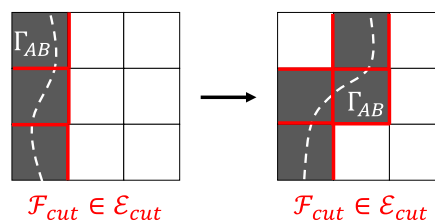


Fig. 10 Change in \mathcal{F}_{cut} due to change in interface position

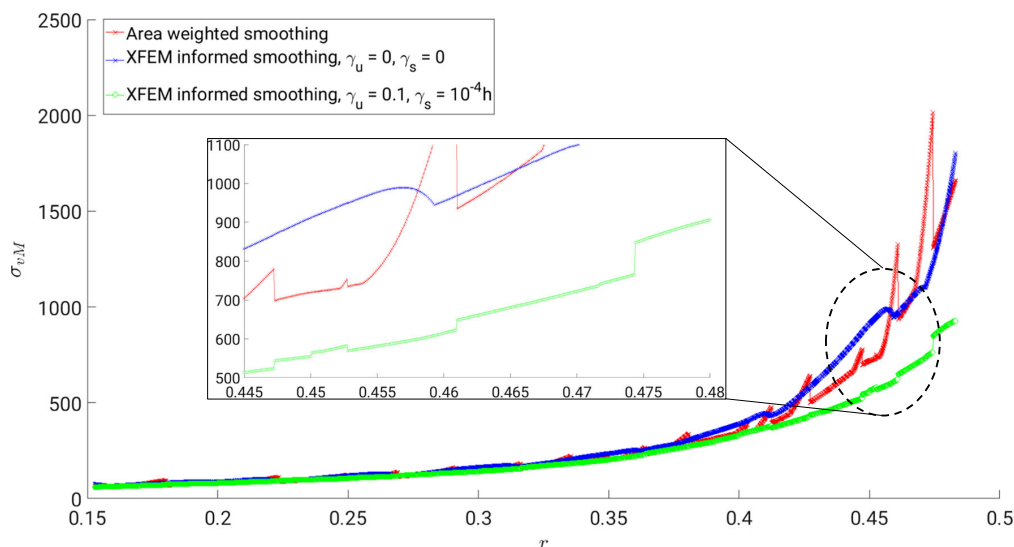


Fig. 11 Variation in maximum stress with radius for mesh size $h = 0.05m$

We now investigate the accuracy of the stress sensitivities with respect to the inclusion radius, r . Figure 7 plots the stress sensitivities corresponding to $r = 0.4742m$ for different mesh sizes of $h = 0.025m$ and $h = 0.005m$. Reference sensitivities are obtained using a body-fitted mesh. Area weighted smoothing and XFEM informed smoothing without ghost penalty result in oscillatory sensitivities. Mesh refinement further aggravates the oscillations. In contrast sensitivities corresponding to XFEM informed smoothing with $\gamma_u = 0.1h$ and $\gamma_\tau = 10^{-4}h$ are smooth and converge with refinement in mesh. Using larger values of γ_u and γ_τ results in smoother stress profiles. Consequently XFEM informed smoothing with $\gamma_u = 1.0h$ and $\gamma_\tau = 10^{-2}h$ results in diminished sensitivities especially on coarse meshes as can be seen for $h = 0.025m$.

5.1.2 Robustness

Having established the accuracy of the proposed approach we now investigate its robustness. As explained by Van Mieghroet and Duysinx (2007) and as also discussed in Section 1, small intersection areas lead to vanishing zone of influences for certain degrees of freedom. This can result in overestimation of stresses along the material interface. In the authors' experience this effect is exaggerated on coarse meshes. We use mesh sizes of $h = 0.05m$ and $h = 0.025m$ to analyze the stress profile along the material interface for configurations with small intersection areas. A radius of $r = 0.4743m$ results in one such configuration. A very small increase in radius to $r = 0.4744m$ results in a configuration without small intersection areas. We compare the change in stress profiles between the two intersection configurations to establish the robustness of the proposed approach.

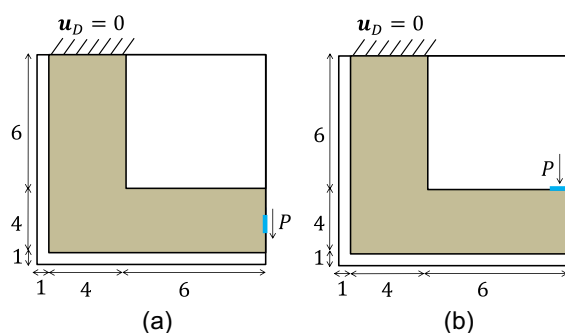


Fig. 12 L-beam with different load cases: **a** Load applied to right edge (RE); **b** Load applied to upper end of flange (UF). All dimensions are in m

Table 1 Parameter list for topology optimization of single-phase 2D linear elastic L-beam

Parameter	Load case RE	Load case UF
σ_{max}	$0.3N/m^2$	$0.3N/m^2$
r_ϕ	$2.4h$	$2.4h$
c_J	100	100
c_P	0.005	0.008
c_v	0.48	0.48
β_V	14.7	15
GCMMA step size	0.01	0.01

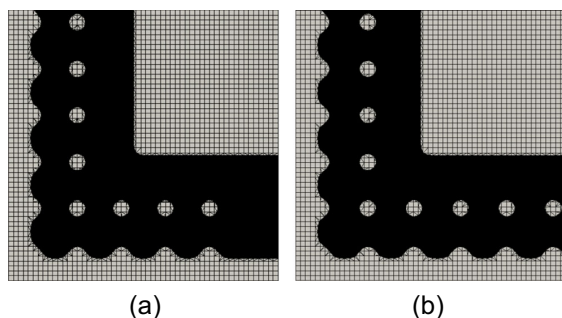


Fig. 13 Finite element mesh, $h = 0.2m$, with initial seeding for load cases: **a** RE; **b** UF

Figure 8 shows stress contour plots using area weighted smoothing. Stress peaks resulting from small intersection areas are evident. In Fig. 9 stress profiles along the material interface corresponding to the two radii are compared. In regions with small intersection areas, at $r = 0.4743m$, stress peaks are observed when using area weighted smoothing. In absence of small intersection areas, i.e. for $r = 0.4744m$, no stress peaks are recorded with area weighted smoothing. In contrast, stress profiles obtained via the XFEM informed smoothing are unaffected by the size of intersection areas and show minimal change in stress profiles between the two radii. Note, the case of XFEM informed smoothing without ghost penalty results in more conforming stress profiles as compared to XFEM informed smoothing with ghost penalty. This behavior is discussed in detail in the next section.

5.1.3 Differentiability

The framework of spatial gradient stabilization results in non-smooth behavior of stresses and presents a differentiability issue. Figure 10 demonstrates this issue. Recall from Section 3.3, \mathcal{F}_{cut} is the set of element faces across which the spatial gradient is penalized. The members of this set vary as the material interface crosses over into neighboring elements. Mathematically, a change in \mathcal{F}_{cut} leads to a discontinuous change in the stabilization penalty parameters, γ_u and γ_τ , with the parameters alternating between non-zero and zero values depending on whether the face is a member of \mathcal{F}_{cut} or not. As a result, the corresponding change in the local stresses is discontinuous too. Hence the stress profiles corresponding to XFEM informed smoothing with $\gamma_u = 0.1h$, $\gamma_\tau = 10^{-4}h$ in Fig. 9 are not as conforming as those in absence of ghost penalty.

Figure 11 plots the maximum stress along the material interface as the radius of the inclusion is varied from $r = 0.153m$ to $r = 0.483m$. For XFEM informed smoothing with $\gamma_u = 0.1h$, $\gamma_\tau = 10^{-4}h$, jumps for particular values of r are observed. These values of r correspond to changes in intersection configurations. Although XFEM informed smoothing with ghost penalty results in small jumps in stresses as the material interface transitions an element, the overall smooth sensitivity profiles obtained using the proposed approach make the proposed approach an attractive option for gradient-based optimization.

Shape sensitivities in the current work are computed semi-analytically, as discussed in Section 4.2. The finite differencing aspect of the sensitivity analysis adopted, requires

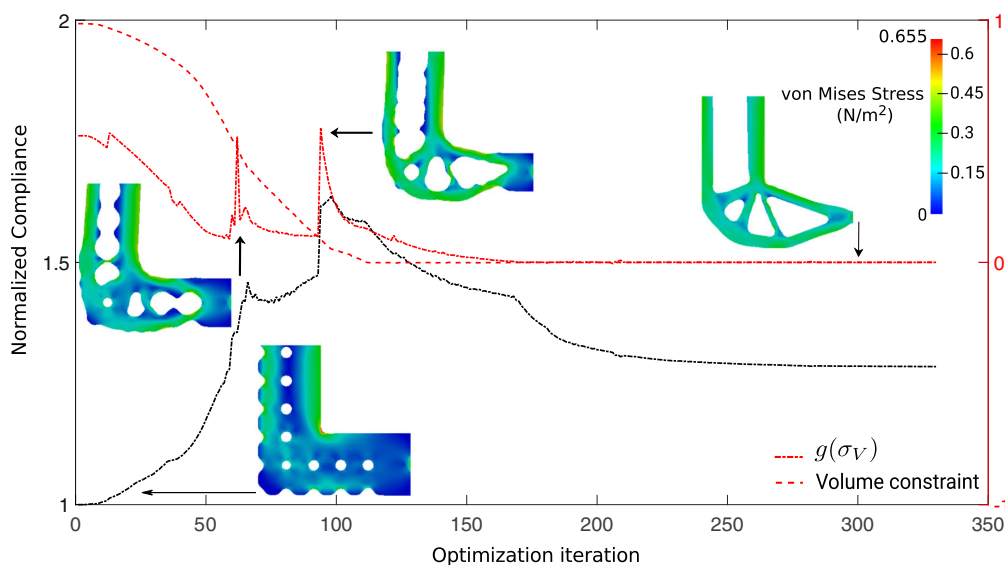


Fig. 14 Evolution of objective and constraints for load case RE

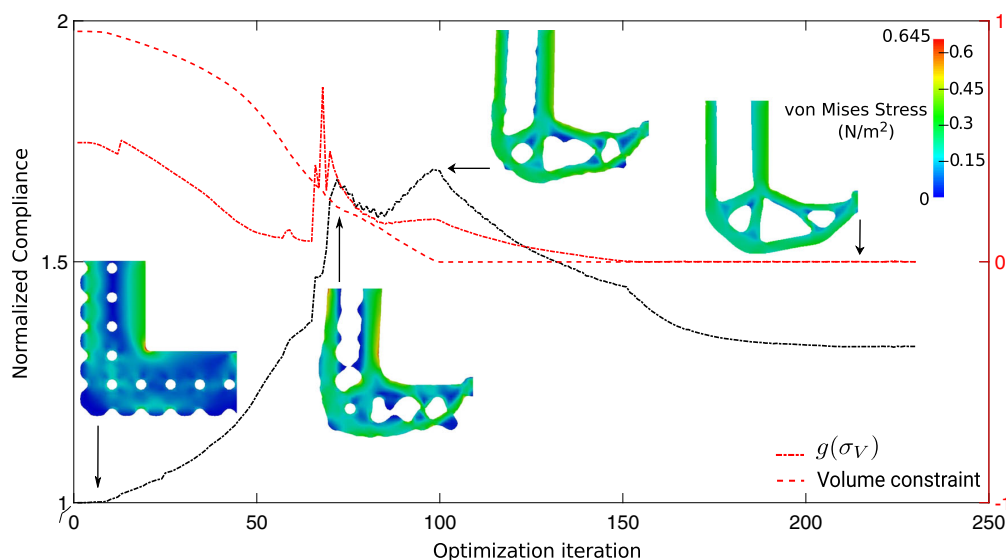


Fig. 15 Evolution of objective and constraints for load case UF

perturbation of the material interface. If these finite difference perturbations result in the material interface transitioning an element, the ghost penalty technique will result in inaccurate sensitivities due to jumps in stresses as discussed above. The sensitivity analysis approach adopted in this work (see Sharma et al. 2017), is however unaffected by this issue as it is ensured that a material interface does not transition an element over the course of sensitivity analysis.

5.2 Example 2

5.2.1 2D material-void linear elastic L-beam

Through this example we demonstrate the applicability of the proposed approach to stress-based topology optimization using the benchmark problem of a 2D L-shaped beam.

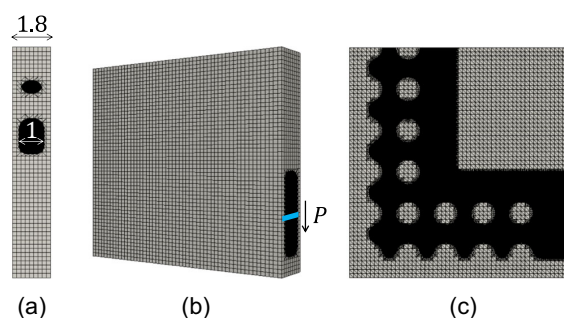


Fig. 16 Finite element mesh, $h = 0.2m$, with initial seeding in 3D for load case RE: **a** Top view; **b** Perspective view; **c** Slice along the thickness. All dimensions are in m

We solve the compliance minimization problem of (18). Two load cases are considered: i) Vertical load of $P = 0.1N$ applied to the middle of the right vertical edge (RE), distributed over two elements (Fig. 12a), ii) Vertical load of $P = 0.1N$ applied to the upper end of the flange (UF), distributed over two elements (Fig. 12b). The beam is made of an isotropic elastic material with Young's modulus, $E = 100N/m^2$, and a Poisson's ratio, $\nu = 0.3$. The problem domain is discretized using a mesh size of $h = 0.2m$. A list of problem parameters is presented in Table 1.

For a structure with a desired volume ratio, it is required that the maximum allowable stress be chosen carefully as too low of a value will hinder greatly the convergence of

Table 2 Parameter list for topology optimization of single-phase 3D linear elastic L-beam

Parameter	3D extension, load case RE
σ_{max}	$0.3N/m^2$
r_ϕ	$2.4 h$
c_J	100
c_P	0.006
c_v	0.48
β_V (up till iteration 360)	15
β_V (iteration 360 onward)	18
β_Γ	6
GCMMA step size (up till iteration 360)	0.002
GCMMA step size (iteration 360 onward)	0.005

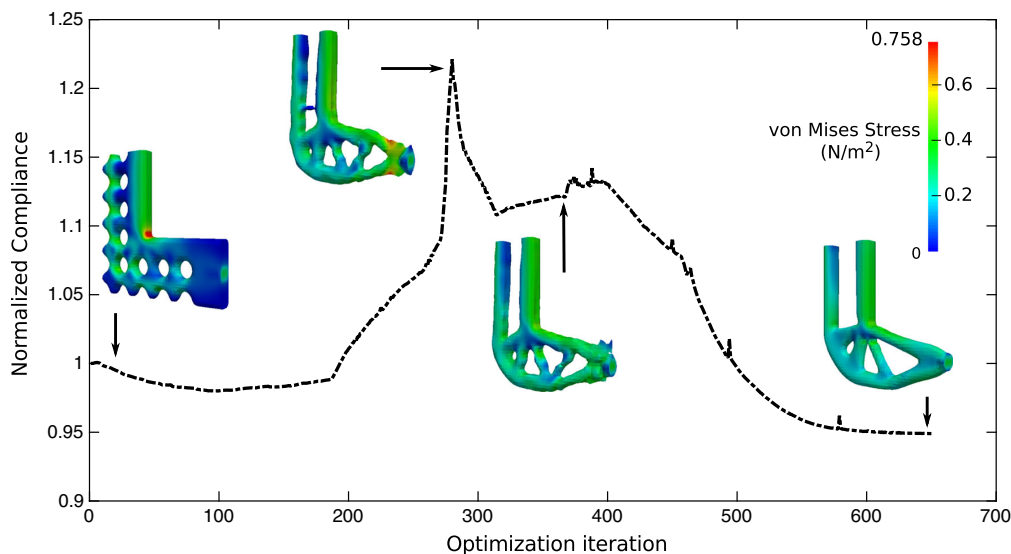


Fig. 17 Evolution of normalized compliance for 3D linear elastic L-beam

the optimization process. In contrast, a high value of maximum allowable stress will be ineffective in eliminating regions with high stress concentrations. Consequently the tuning parameters β_V in Table 1 correspond to the highest values that allowed for smooth convergence of the optimization process. In the current example, the value of maximum allowable stress and volume correspond to those describing the optimized designs presented by Duysinx and Bendsøe (1998).

Figure 13 shows the finite element mesh with the initial seeding of the design domains using circular inclusions of radius $0.4m$. The black regions are occupied by the elastic material (phase A). The void regions (phase B) are depicted in grey. As mentioned in Section 3.3 faces lying on the boundary of the mesh are not stabilized. To ensure that gradients across all material faces are stabilized, we expand the domain along the boundary of the beam. This extended boundary is denoted by unshaded regions in Fig. 12. The

extended domain boundary serves the purpose of providing a material interface along the original domain boundary. The resulting extra nodes created upon expansion of the boundary are constrained to phase B and excluded from the design domain. Also excluded from the design domain is a small area around the region of application of the load prescribed to phase A. This ensures that the load is applied to the material phase A throughout the optimization process.

Figures 14 and 15 present the evolution of the normalized compliance and constraints for load cases RE and UF, respectively. The compliance is normalized with respect to the compliance of the initial design presented in Fig. 13. Select design iterations are visualized. For both load cases, the initial design violates the constraints. Initially the optimizer tries to satisfy the stress constraints while ignoring the objective. Consequently, the compliance continues to rise and the re-entrant corner profile has a lower curvature. During this sequence, the flange remains horizontal.

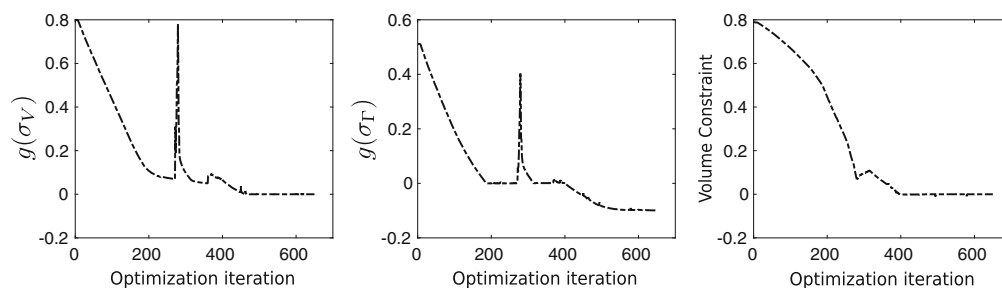


Fig. 18 Evolution of stress and volume constraints for 3D linear elastic L-beam

Subsequently, a decrease in the compliance of the structure and presence of active stress constraint result in an inclined flange. Owing to the use of global constraints, the maximum stress is violated point-wise in the optimized designs, the true maximum stress in which was $0.44N/m^2$ for both load cases.

5.2.2 3D material-void linear elastic L-beam

Through this example we demonstrate the applicability of the proposed to approach to linear elastic designs in 3D. We extend load case RE to a 3D domain. Material and load properties from Section 5.2.1 are used. The problem domain is discretized using a mesh size of $h = 0.2m$. As in the 2D case, we expand the domain along the original boundary of the beam including, along the thickness of the structure. Figure 16 shows the finite element mesh with initial seeding of the design domain using spherical inclusions of radius $0.7m$. A list of relevant problem parameters is presented in Table 2.

Figures 17 and 18 present the evolution of the normalized compliance and constraints, respectively. As in the 2D case, the initial design violates every constraint. As was observed in the 2D case, the compliance of the structure rises initially while the stress reduces. As a result, the re-entrant corner profile has a lower curvature. Subsequently a decrease in the compliance of the structure and presence of active stress constraints result in a completely inclined flange.

During the optimization process it was observed that the structure near the application of the load gets very thin as the volume is reduced and develops a tendency to break off completely. This phenomenon is represented by a spike in the evolution plots of Figs. 17 and 18. To prevent the

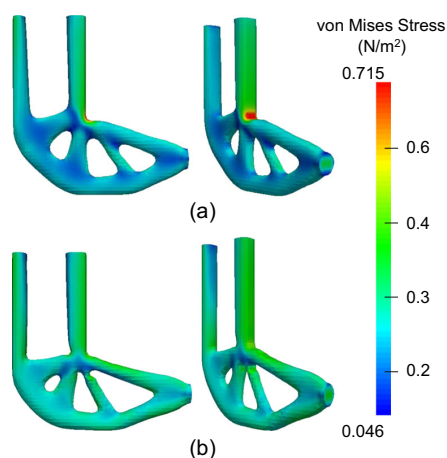


Fig. 19 Stress distribution in optimized design for 3D linear elastic L-beam: **a** Without stress constraints, **b** With stress constraints

Table 3 Parameter list for topology optimization of 2D hyperelastic L-beam

P	$0.1N$	$0.4N$	$0.8N$	$1.2N$
$\sigma_{max}(N/m^2)$	0.3	1.22	2.5	3.81
r_ϕ	$2.4h$	$2.4h$	$2.4h$	$2.4h$
c_J	100	10	10	1
c_P	0.005	0.01	0.02	0.006
c_v	0.48	0.48	0.48	0.48
β_V	20	20	20	20
GCMMA step size	0.005	0.005	0.0025	0.0025

structure from completely breaking off we adopt a continuation strategy for the GCMMA step size, starting with a small value and as the volume constraint is close to being satisfied the step size is increased. Reducing the volume of a structure is counteractive to reducing the stress. Thus, to facilitate smooth convergence of the optimization problem a continuation strategy is also adopted for the KS tuning coefficient, β_V .

Figure 19 presents a comparison of the final designs obtained with and without stress constraints. In the absence of stress constraints, the re-entrant corner is retained resulting in localized high stresses. Imposing stress constraints resulted in a design with 61.9% lower peak stress at only a cost of 3.8% higher compliance.

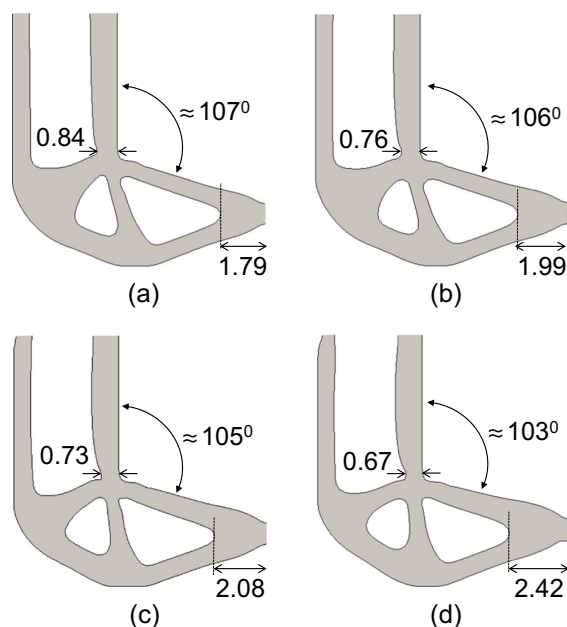


Fig. 20 optimized design for: **a** $P = 0.1N$; **b** $P = 0.4N$; **c** $P = 0.8N$; **d** $P = 1.2N$; All dimensions are in m

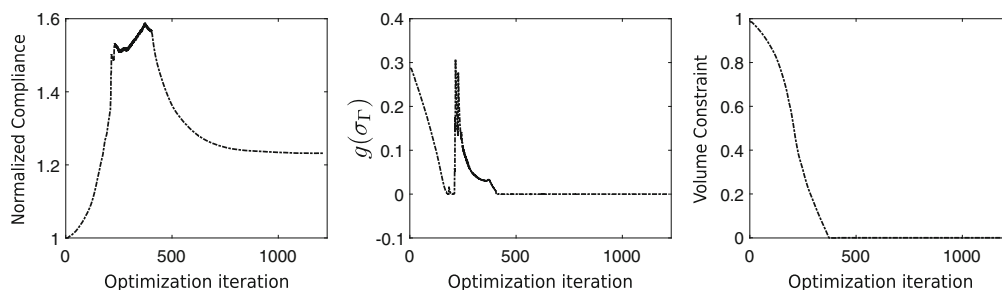


Fig. 21 Evolution of objective and constraints for 2D hyperelastic L-beam, $P = 1.2 N/m^2$

5.3 Example 3

In this section, we demonstrate the applicability of the proposed approach to 2D and 3D hyperelastic material-based designs. For a nonlinear structural model, stress peaks affect the stability of the system of equations, and can impede convergence of Newton’s method. XFEM informed smoothing with ghost penalty helps keep the stress peaks in check, thus providing smooth convergence of the structural analysis.

We consider load case RE from Section 5.2.1 to optimize an L-beam structure made of Saint Venant-Kirchhoff hyperelastic material. The 2D design is solved under plane strain assumptions. Comparisons are drawn against optimized designs obtained using linear elastic material under plane strain conditions. Material properties from Section 5.2 are used. The problem domain is discretized using the same mesh as in Fig. 13a. We compare designs optimized for 4 increasing magnitudes of load. Table 3 presents a complete list of relevant problem parameters. To be able to compare results for different load magnitudes, the maximum allowable stress values are chosen such that the initial stress constraint violation is similar in all loading cases considered. Alternatively, a constant value for maximum allowable

stress can be chosen across all loading cases. However, in such a scenario the appropriate maximum allowable volume should be determined.

Figure 20 presents a comparison of the optimized designs obtained under application of the different loads listed in Table 3. As the magnitude of the applied load is increased, the region around the flange tip (which is the region of application of load) ascends resulting in a flange with a lower slope. Moreover, increasing amounts of material are reinforced near the region of application of load further pushing the void features away from the flange tip. This increase in material near the flange tip is a clear countermeasure to the increased loading in the region. Another distinct design change with increased loading is the thinning of the web base near the re-entrant corner. Owing to the use of global constraints, the maximum stress is violated point-wise in the optimized designs, the true maximum stress in which were $0.42 N/m^2$, $1.7 N/m^2$, $3.5 N/m^2$, and $5.4 N/m^2$ for load cases $P = 0.1 N$, $P = 0.4 N$, $P = 0.8 N$, and $P = 1.2 N$, respectively.

Figure 21 presents the evolution of the normalized compliance and constraints for load case of $P = 1.2 N$. Smooth convergence of objective and constraints is observed. For all hyperelastic material-based studies presented here, smaller optimization steps were required with an increase in load for smooth convergence of the optimization problem. Consequently, more optimization steps were required to achieve an optimized design under increased loading.

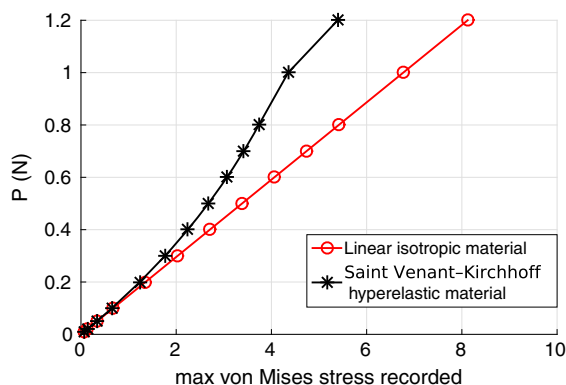


Fig. 22 Load vs stress plot for optimized design corresponding to $P = 1.2 N$

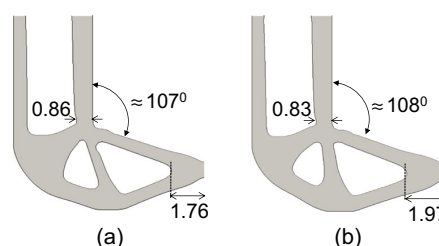


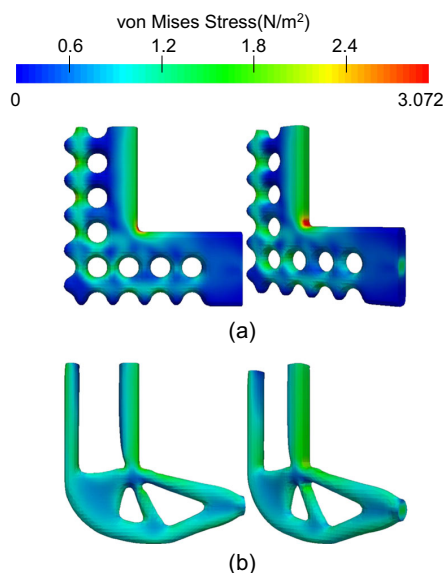
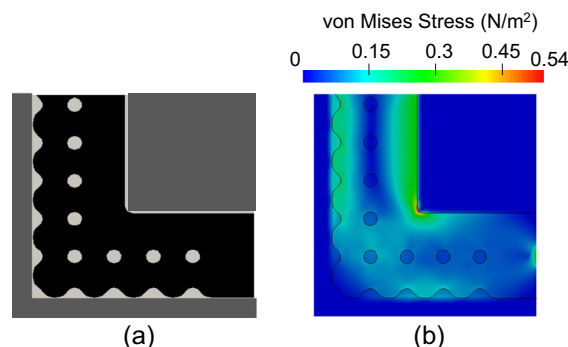
Fig. 23 optimized design for linear elastic material under plane strain assumptions: **a** $P = 0.1 N$, $\sigma_{max} = 0.3 N/m^2$; **b** $P = 1.2 N$, $\sigma_{max} = 3.81 N/m^2$; All dimensions are in m

Table 4 Parameter list for topology optimization of 3D hyperelastic L-beam

P	0.4N
σ_{max}	1.215N/m ²
r_ϕ	2.4 h
c_J	10
c_P	0.01
c_v	0.48
β_V	15
β_Γ	6
GCMMA step size (up till iteration 500)	0.002
GCMMA step size (iteration 500 onward)	0.005

Figure 22 presents the relationship between the applied load, P , and the maximum von Mises stress in the structure. The data plotted corresponds to the optimized design obtained for load case, $P = 1.2N$. Based on the plots it is deduced that the small strain limit assumptions, for the material properties in consideration, hold true up to the point where the maximum load applied is $\leq 0.1N$. Subsequently for higher loads, inaccurate optimized designs are expected with the use of linear elastic materials. To validate this discrepancy, we perform a comparison of designs using linear elastic material under plane strain assumptions.

Problem parameters for $P = 0.1N$ and $P = 1.2N$ from the hyperelastic material-based studies (Table 3) are used.

**Fig. 24** Stress distribution in (a) initial, and (b) optimized design for 3D hyperelastic L-beam**Fig. 25** Material-material L-beam problem setup: a Initial material-material seeding; b Initial stress profile

The optimized designs are presented in Fig. 23. The optimized design for $P = 0.1N$ (Fig. 23a) resembles very closely the optimized design obtained using the hyperelastic material load case of $P = 0.1N$ (Fig. 20a). This is expected as based on Fig. 22a load of $P = 0.1N$ is within the small strain limit. In contrast, load case $P = 1.2N$ (Fig. 23b) resulted in an optimized design that more closely resembles the design obtained using the hyperelastic material load case of $P = 0.1N$ rather than the design obtained using the hyperelastic material load case of $P = 1.2N$ (Fig. 20d). This further highlights the inaccuracies of using a linear elastic material for design optimization purposes outside the small strain limit.

We extend the load case of $P = 0.4N$ to 3D. As in the linear elastic case we adopt a continuation strategy, starting with a small optimization step size and as the volume constraint is close to being satisfied the step size is increased. Table 4 provides the list of relevant problem parameters. Figure 24b presents the stress plots for the initial and final design. The removal of the re-entrant corner in the optimized design shows the effectiveness of the proposed approach for 3D nonlinear stress-based optimization problems. The true maximum stress in the optimized design was $1.9N/m^2$.

Table 5 Parameter list for topology optimization of two-phase 2D linear elastic L-beam

$\sigma_{max}(N/m^2)$	0.27	0.25	0.23	0.21
r_ϕ	2.4 h	2.4 h	2.4 h	2.4 h
c_W	1	1	1	1
c_P	0.0005	0.0005	0.001	0.008
β_V	20	20	20	20
GCMMA step size	0.01	0.01	0.01	0.02

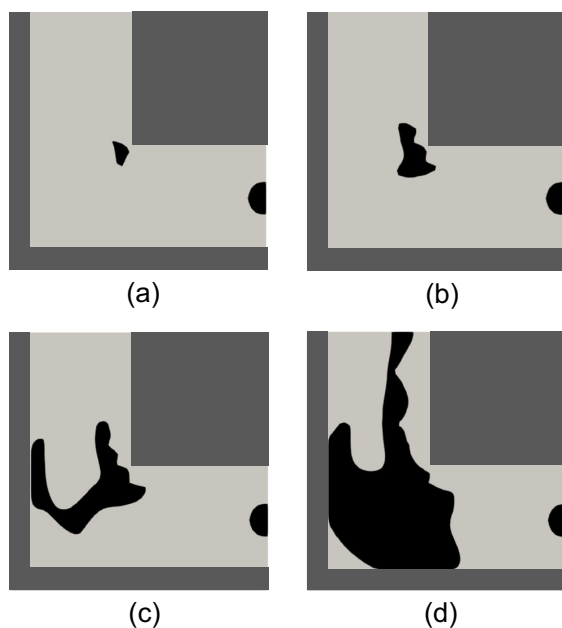


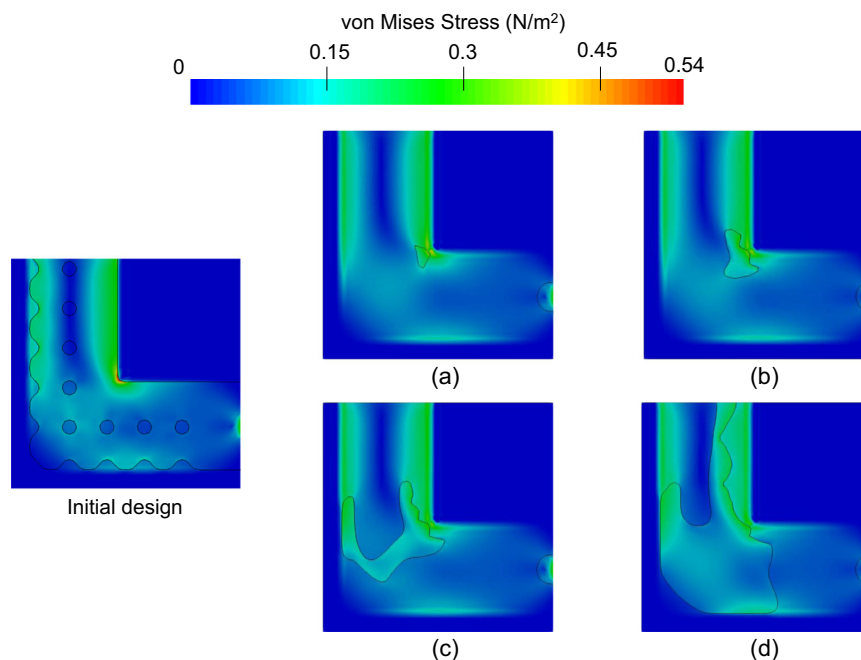
Fig. 26 Material distribution in optimized designs obtained for: **a** $\sigma_{max} = 0.27N/m^2$; **b** $\sigma_{max} = 0.25N/m^2$; **c** $\sigma_{max} = 0.23N/m^2$; **d** $\sigma_{max} = 0.21N/m^2$

5.4 Example 4

Through this example we demonstrate the applicability of the proposed approach to material-material designs. We solve the optimization problem presented in (19) using linear elastic materials. Load case RE from Section 5.2.1 with $P = 0.1N$ is considered in 2D. Elastic moduli of $E^A = 100N/m^2$ and $E^B = 50N/m^2$ are used for materials constituting material phases A and B , respectively. An interface constraint penalty of $c_\Gamma = 10$ was used in (8). The problem domain is discretized using a mesh size of $h = 0.2m$. The structural analysis is performed under plane stress assumptions.

Figure 25a shows the initial seeding of the design domains. The black regions are occupied by the stiffer material (phase A). The regions occupied by the less stiff material are depicted in light grey (phase B). To ensure gradients across all material faces are stabilized, we expand the domain along the boundary of the beam, denoted by dark grey regions in Fig. 25b. Phase B constitutes this extended domain boundary wherein the elastic modulus of phase B is set to $10^{-6}N/m^2$ to simulate a void region. The resulting extra nodes created upon expansion of the boundary are constrained to phase B , and thus excluded from the design domain. Also excluded from the design domain is a small area around the region of application of the load prescribed to phase A . This ensures that the load is applied to the material phase A throughout the optimization process.

Fig. 27 Stress distribution in optimized designs obtained for: **a** $\sigma_{max} = 0.27N/m^2$; **b** $\sigma_{max} = 0.25N/m^2$; **c** $\sigma_{max} = 0.23N/m^2$; **d** $\sigma_{max} = 0.21N/m^2$



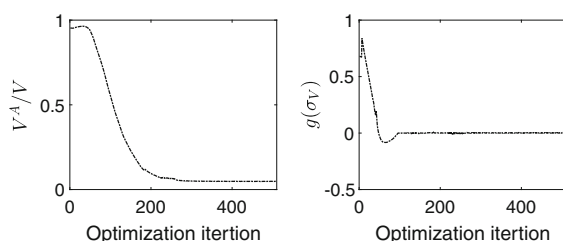


Fig. 28 Evolution of objective and constraints for $\sigma_{max} = 0.25N/m^2$

We optimize the design domain for different values of maximum allowable stress presented in Table 5. Figure 26 presents the material distribution for the optimized designs. The optimizer removes all of the stiff material except for near the re-entrant corner where the stiff material appears in the form of step-like features. Such a concentration of the stiff material provides reinforcement to the weak material present at the re-entrant corner which is a region of high stress concentration. As is expected, the amount of stiff material in the optimized design increases with decreasing maximum allowable stress. The volume occupied by the stiffer material in optimized designs presented in Fig. 26a through d is 2%, 5%, 14%, and 44%, respectively. Figure 27 presents the corresponding stress distribution. Figure 28 presents the evolution of objective and constraints corresponding to $\sigma_{max} = 0.25N/m^2$. We observe smooth convergence of stress constraints, thus showing the effectiveness of the proposed approach for material-material designs. The authors note, the number of optimization steps to achieve convergence increased with a decrease in the value of maximum allowable stress.

6 Conclusions

We presented and studied an LSM-XFEM approach for topology optimization problems subject to stress constraints. The issue of overestimation of stresses resulting from small intersection areas, following vanishing zone of influence of degrees of freedom, was addressed. For the computation of reliable stresses, i) we adopt the ghost penalty method of Burman and Hansbo (2014), and ii) introduce an XFEM informed stress smoothing method. The ghost penalty method, in addition to penalizing the spatial solution gradients across element edges, prevents the influence of degrees of freedom from vanishing and provides stability to the system of equations. However as shown through a numerical study, ghost penalty alone is not sufficient in obtaining convergence of stresses along the material interface with mesh refinement. The XFEM informed smoothing

in combination with ghost penalty provides a second level of spatial gradient stabilization which was shown to be effective in eliminating stress peaks and attain convergence with mesh refinement. We showed through a numerical study that stabilization of gradients across element faces helps to largely reduce oscillations in stress sensitivities. In comparison with an area weighted smoothing, the XFEM informed smoothing led to a more robust and accurate prediction of stresses and stress sensitivities along the material interface.

The spatial gradient stabilization framework results in non-smooth behavior of stresses across neighboring elements. Thus, the stress sensitivities are non-differentiable when the material interface transitions an element. The approach to computing sensitivities used in the current work is however unaffected by this behavior (see Sharma et al. 2017), as it is ensured that the material interface does not transition an element over the course of sensitivity analysis. These issues of non-differentiability are more than compensated by the overall gain in smoothness when compared to non-gradient stabilized XFEM formulations.

The proposed approach was applied to the benchmark topology optimization problem of a material-void L-shaped beam in 2D and 3D using elastic and hyperelastic materials. Stress constraints were imposed using a global approach, and were effective in mitigating peak stresses. This manifests itself in the removal of the re-entrant corner. Optimized designs obtained using hyperelastic material suggested a pattern in design change with increase in applied load. This indicates that optimizing a structure using a linear elastic model outside the small-strain limit may produce non-optimal designs.

We extended the topology optimization problem of an L-shaped beam to a material-material domain in 2D using elastic materials. Optimized designs were presented for different values of maximum allowable stress with each case resulting in the formation of stiff step-like structure near the re-entrant corner. As expected, a lower value of maximum allowable stress resulted in an optimized structure with more stiff material.

For all optimization examples considered smooth convergence of stress constraints was reported based on the constraint evolution plots presented.

The proposed method for computation of stresses is an improvement over existing methods. In its current framework stresses are non-differentiable as the material interface transitions an element. Future studies should focus on resolving this issue. Furthermore, more accurate measures for stress constraints such as the regional measure of Le et al. (2010) should be employed for better control of local stress levels. In addition, multi-phase problems involving more than two materials should be considered.

Acknowledgements The authors acknowledge the support of the National Science Foundation under Grant EFRI-ODISSEI 1240374 and of the US Air Force of Scientific Research under Grant FA9550-16-1-0169. The second author also acknowledges the support of the National Science Foundation under Grant CMMI 1463287. The opinions and conclusions presented in this paper are those the authors and do not necessarily reflect the views of the sponsoring organizations.

References

- Allaire G, Jouve F, Toader AM (2004) Structural optimization using sensitivity analysis and a level-set method. *J Comput Phys* 194(1):363–393
- Amir O (2017) Stress-constrained continuum topology optimization: a new approach based on elasto-plasticity. *Struct Multidiscip Optim* 55(5):1797–1818
- Annavarapu C, Hautefeuille M, Dolbow JE (2012) A robust nitsche's formulation for interface problems. *Comput Methods Appl Mech Eng* 225–228:44–54
- Babuška I, Melenk JM (1997) The partition of unity method. *Int J Numer Methods Eng* 40(4):727–758
- Bendsøe M, Kikuchi N (1988) Generating optimal topologies in structural design using a homogenization method. *Comput Methods Appl Mech Eng* 71(2):197–224
- Bruggi M, Duysinx P (2012) Topology optimization for minimum weight with compliance and stress constraints. *Struct Multidiscip Optim* 46(3):369–384
- Burger M, Hackl B, Ring W (2004) Incorporating topological derivatives into level set methods. *J Comput Phys* 194(1):344–362
- Burman E, Hansbo P (2014) Fictitious domain methods using cut elements: III. a stabilized nitsche method for stokes' problem. *ESAIM: Mathematical Modelling and Numerical Analysis* 48(3):859–874
- Cai S, Zhang W, Zhu J, Gao T (2014) Stress constrained shape and topology optimization with fixed mesh: A B-spline finite cell method combined with level set function. *Comput Methods Appl Mech Eng* 278:361–387
- Cheng G, Guo X (1997) ϵ -relaxed approach in structural topology optimization. *Structural Optimization* 13(4):258–266
- Cheng G, Jiang Z (1992) Study on topology optimization with stress constraints. *Eng Optim* 20(2):129–148
- Coffin P, Maute K (2016) A level-set method for steady-state and transient natural convection problems. *Struct Multidiscip Optim* 53(5):1047–1067
- Dijk N, Maute K, Langelaar M, Keulen F (2013) Level-set methods for structural topology optimization: a review. *Struct Multidiscip Optim* 48(3):437–472
- Duysinx P, Bendsøe MP (1998) Topology optimization of continuum structures with local stress constraints. *Int J Numer Methods Eng* 43(8):1453–1478
- Duysinx P, Sigmund O (1998) New developments in handling stress constraints in optimal material distributions. In: *Proceedings of 7th AIAA/USAF/NASA/ISSMO symposium on Multidisciplinary Design Optimization*, AIAA
- Duysinx P, Van Miegroet L, Jacobs T, Fleury C (2006) Generalized shape optimization using x-FEM and level set methods. In: *IUTAM symposium on topological design optimization of structures, machines and materials*. Springer, Netherlands, pp 23–32
- Fries T, Belytschko T (2010) The extended/generalized finite element method: an overview of the method and its applications. *Int J Numer Methods Eng* 84(3):253–304
- Guo X, Zhang W, Wang MY, Wei P (2011) Stress-related topology optimization via level set approach. *Comput Methods Appl Mech Eng* 200(47–48):3439–3452
- Guo X, Zhang W, Zhong W (2014) Stress-related topology optimization of continuum structures involving multi-phase materials. *Comput Methods Appl Mech Eng* 268:632–655
- Haber R, Jog C, Bendsøe M (1996) A new approach to variable-topology shape design using a constraint on perimeter. *Structural Optimization* 11(1):1–12
- Hansbo A, Hansbo P (2004) A finite element method for the simulation of strong and weak discontinuities in solid mechanics. *Comput Methods Appl Mech Eng* 193(33–35):3523–3540
- Holmberg E, Torstenfelt B, Klarbring A (2014) Fatigue constrained topology optimization. *Struct Multidiscip Optim* 50(2):207–219
- Holzzapfel GA (2000) *Nonlinear solid mechanics*. Wiley, West Sussex
- James KA, Waisman H (2014) Failure mitigation in optimal topology design using a coupled nonlinear continuum damage model. *Comput Methods Appl Mech Eng* 268:614–631
- Jenkins N, Maute K (2015) Level set topology optimization of stationary fluid-structure interaction problems. *Struct Multidiscip Optim* 52(1):179–195
- Kreissl S, Maute K (2012) Levelset based fluid topology optimization using the extended finite element method. *Struct Multidiscip Optim* 46(3):311–326
- Lang C, Sharma A, Doostan A, Maute K (2015) Heaviside enriched extended stochastic fem for problems with uncertain material interfaces. *Comput Mech* 56(5):753–767
- Le C, Norato J, Bruns T, Ha C, Tortorelli D (2010) Stress-based topology optimization for continua. *Struct Multidiscip Optim* 41(4):605–620
- Makhija D, Maute K (2014) Numerical instabilities in level set topology optimization with the extended finite element method. *Struct Multidiscip Optim* 49(2):185–197
- Moës N, Dolbow J, Belytschko T (1999) A finite element method for crack growth without remeshing. *Int J Numer Methods Eng* 46(1):131–150
- Noël L, Duysinx P (2017) Shape optimization of microstructural designs subject to local stress constraints within an x-fem-level set framework. *Struct Multidiscip Optim* 55(6):2323–2338
- Osher S, Santosa F (2001) Level set methods for optimization problems involving geometry and constraints: i. frequencies of a two-density inhomogeneous drum. *J Comput Phys* 171(1):272–288
- Osher SJ, Sethian JA (1988) Fronts propagating with curvature dependent speed: algorithms based on Hamilton-Jacobi formulations. *J Comput Phys* 79(1):12–49
- París J, Navarrina F, Colominas I, Casteleiro M (2008) Topology optimization of continuum structures with local and global stress constraints. *Struct Multidiscip Optim* 39(4):419–437
- París J, Navarrina F, Colominas I, Casteleiro M (2010) Block aggregation of stress constraints in topology optimization of structures. *Adv Eng Softw* 41(3):433–441
- Polajnar M, Kosel F, Drazumeric R (2017) Structural optimization using global stress-deviation objective function via the level-set method. *Struct Multidiscip Optim* 55(1):91–104
- Sethian J, Wiegmann A (2000) Structural boundary design via level set and immersed interface methods. *J Comput Phys* 163(2):489–528
- Sharma A, Villanueva H, Maute K (2017) On shape sensitivities with heaviside-enriched x-fem. *Struct Multidiscip Optim* 55(2):385–408
- Stenberg R (1995) On some techniques for approximating boundary conditions in the finite element method. *J Comput Appl Math* 63(1–3):139–148
- Svanberg K (2002) A class of globally convergent optimization methods based on conservative convex separable approximations. *SIAM J Optim* 12(2):555–573

- Terada K, Asai M, Yamagishi M (2003) Finite cover method for linear and non-linear analyses of heterogeneous solids. *Int J Numer Methods Eng* 58(9):1321–1346
- Van Miegroet L, Duysinx P (2007) Stress concentration minimization of 2D filets using x-FEM and level set description. *Struct Multidiscip Optim* 33(4-5):425–438
- Verbart A, Langelaar M, van Keulen F (2016) Damage approach: a new method for topology optimization with local stress constraints. *Struct Multidiscip Optim* 53(5):1081–1098
- Villanueva CH, Maute K (2014) Density and level set-XFEM schemes for topology optimization of 3-D structures. *Comput Mech* 54(1):133–150
- Wang MY, Wang X, Guo D (2003) A level set method for structural topology optimization. *Comput Methods Appl Mech Eng* 192(1-2):227–246
- Yang RJ, Chen CJ (1996) Stress-based topology optimization. *Structural Optimization* 12(2-3):98–105
- Zhang WS, Guo X, Wang MY, Wei P (2013) Optimal topology design of continuum structures with stress concentration alleviation via level set method. *Int J Numer Methods Eng* 93(9):942–959
- Zienkiewicz OC, Zhu JZ (1992) The superconvergent patch recovery and a posteriori error estimates. part 1: The recovery technique. *Int J Numer Methods Eng* 33(7):1331–1364

Appendix D

Implementation Details

D.1 A parallel multilevel filter framework

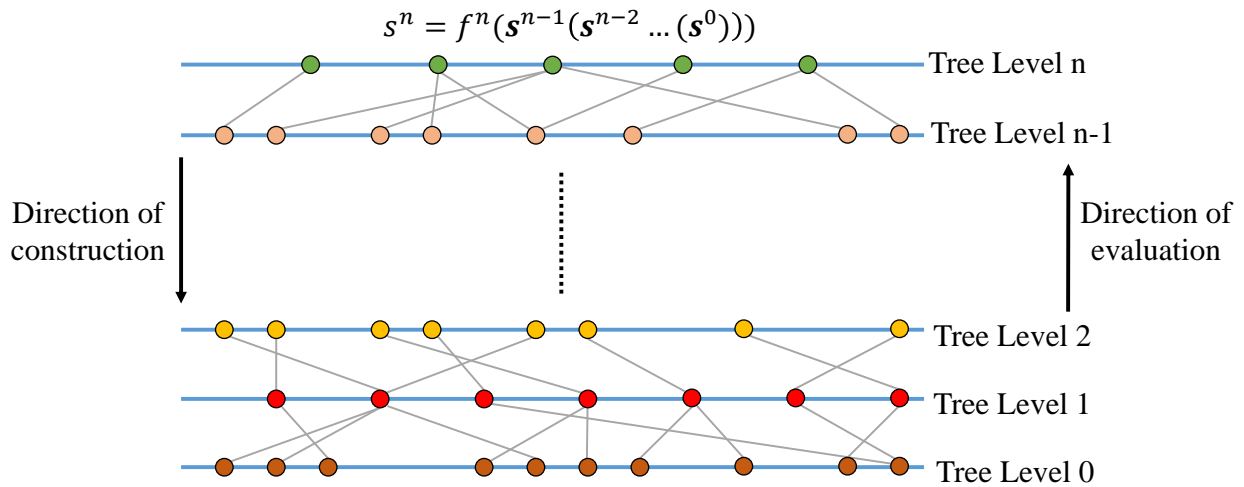


Figure D.1: Tree of variables.

This section describes the concept of a multilevel filter designed to operate in a parallel computing framework. The multilevel filter uses a tree of variables (Figure D.1) wherein a variable at any given level is a function of the variables from the level just below it. Any variable at level n in the tree is referred to as a 'tree node' with its 'branches' defined by the set of all tree nodes it is a function of from level $n - 1$. Every tree node has information about its current value, the list of branches it is dependent on, and the function determining that dependency. In addition, every tree node at level n owns a gradient vector containing the derivatives of s^n w.r.t. s^0 . In order to save memory this vector is stored in sparse format.

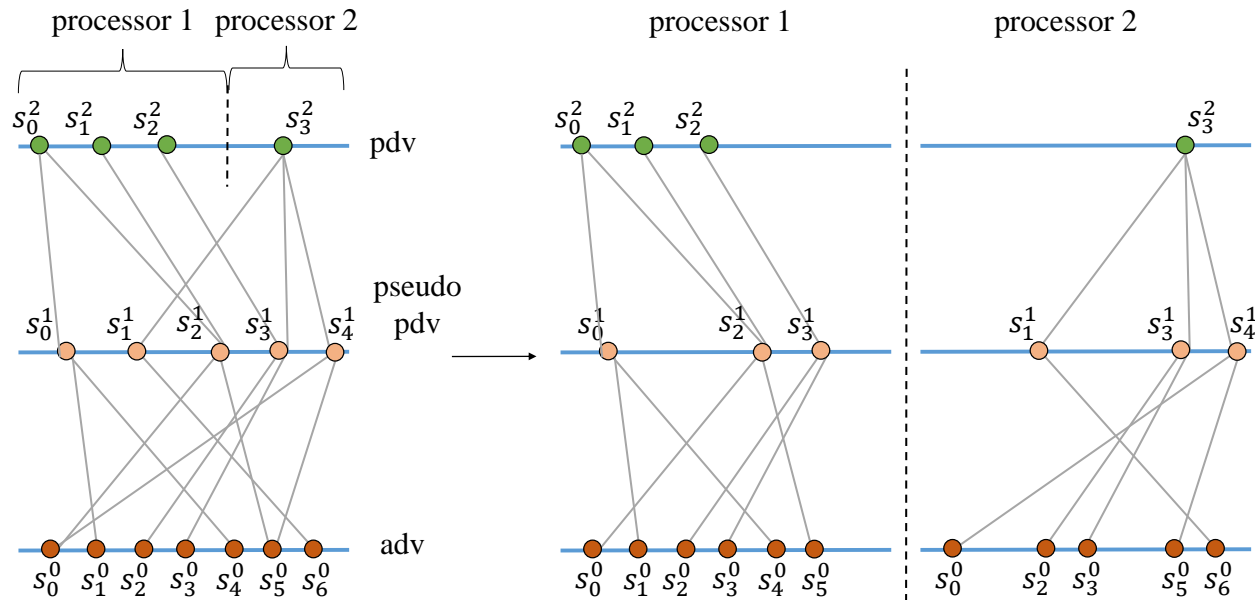


Figure D.2: Example decomposition of variables with dependencies in a parallel multilevel filter framework.

To avoid confusion against finite element nodes, from hereon we shall avoid the term 'tree node' and refer to them as variables.

To describe the basic concepts of such a tree we use the example problem presented in Figure D.2. A variable in the tree is denoted by s_{ind}^{lvl} where lvl and ind denote the variable level and global index respectively. The bottom level of the filter comprises of abstract design variables (adv). These are the design variables in an optimization problem such as the element density, nodal level set value, nodal coordinate, geometric primitive, or a combination of geometric and nodal/elemental design variables. The top level of variables comprises of physical design variables (pdv). These are the variables that determine the material layout in a topology optimization problem and are associated with an element or a node, such as filtered elemental density or regularized nodal level set values. Any level of variables between the pdv and adv are referred to as pseudo physical design variables (pseudo pdv), and are associated with a node or an element. Pseudo pdv levels are interpreted as

intermediate values assumed by the pdvs upon which further operations may be performed to obtain the desired material layout. For instance in Section 4.2 the anisotropic filter (4.8) is applied to the level set values computed using the definition of individual ribs (4.5).

In a parallel computing framework the decomposition of the pdv level follows directly the decomposition of the discretized physical subdomain [125]. The multilevel filter is then constructed for parallel computing by initializing all variables that influence directly or indirectly the variables at the pdv level specific to that processor. The construction of the multilevel filter thus begins at the top level going downwards as shown in Figure D.1. The following sections describe the algorithm behind constructing each level of the multilevel filter, using the example in Figure D.2. The ensuing discussion assumes access to a complete as well as processor-specific list of nodes and elements with relevant data (e.g. coordinates) arranged accordingly.

Before describing the construction of the multilevel filter we define the important lists and maps necessary to build the filter:

- (i) A *tree* with user-defined number of levels. The size of each level is determined as each level is constructed and depends on the number of variables required to build the processor-specific multilevel filter at that level. The number of levels in the example problem of Figure D.2 is 3.
- (ii) A map $var\ ind \mapsto node(element)\ data\ entry$. The map keeps track of the nodal or elemental variables which have been assigned user-desired data (e.g. coordinates) across all variable levels in the processor-specific multilevel filter. The map is build in the order in which the variables are assigned to the *tree*. For processor 2 in Figure D.2, this map would read [(3, 0) (1, 1) (4, 2) (0, 3) (2, 4) (5, 5) (6, 6)].
- (iii) The list $node(element)\ data$ stores the user-desired data in the order specified by the map. As evident from Figure D.2 certain variables such as s_0 (for processor 1) may be a part of more than one level. Although they assume different values, data

such as their coordinate (in an Eulerian setting) remains constant throughout these levels. This map and list combination helps avoid creating duplicate information by maintaining a global registry of the data allocated to each variable. It is assumed that the user has access to such a list of data ordered according to the complete (not processor-specific) list of nodes/elements.

- (iv) A list *lvl hosts var* indicating if the nodal(elemental) variable is used in the current level. For level 1 corresponding to processor 1 in Figure D.2, this list would read [1 0 1 1 0].
- (v) A two way map *var ind* \leftrightarrow *entry ind* mapping the variable index to it's entry in the *tree* at the current level, and vice versa. For level 1 corresponding to processor 1 in Figure D.2, this map would read [(0,0) (2,1) (3,2)].

D.1.1 Constructing the physical design variable level

Creating the pdv level assumes knowledge of the desired variable type (nodal or elemental) and the function $f^n(s^{n-1})$ that relates the pdv with pseudo pdv.

```

for every variable in pdv level do
  → Flag the nodes(elements) on the current processor using lvl hosts var.
  → Use var ind  $\leftrightarrow$  entry ind to assign an entry index to every variable in level.
end for

→ Allocate size of current variable level in tree ( size of var ind  $\leftrightarrow$  entry ind ).

for every entry in var ind  $\leftrightarrow$  entry ind do
  → Use var ind  $\mapsto$  node(element) data entry to check if data for this variable exists.
  if above is false then
    → Store data in node(element) data.
    → Update var ind  $\mapsto$  node(element) data entry.
  end if
  → Create entry in tree and assign variable data and  $f^n(s^{n-1})$ .
end for

```

D.1.2 Constructing the pseudo physical design variable level

Creating a pseudo pdv level assumes knowledge of the desired variable type (nodal or elemental) for both the current and pdv level. Also assumed is the knowledge of the filter radius [28] and function $f^n(s^{n-1})$ that relates the pseudo pdv with the adv.

```
for every variable flagged in lvl hosts var do
  for every node(element) in finite element mesh do
    → Build list of possible dependencies (node or element) based on user-desired criteria (e.g. radial distance).
  end for
end for
```

→ Concatenate and sort the unique list of all dependencies.
 → Clear *lvl hosts var* and *var ind* \leftrightarrow *entry ind*.

```
for every variable in the list of unique dependencies do
  → Flag the nodes(elements) on the current processor using lvl hosts var.
  → Use var ind  $\leftrightarrow$  entry ind to assign an entry index to every variable in level.
end for
```

→ Allocate size of current variable level in *tree* (size of *var ind* \leftrightarrow *entry ind*).

```
for every entry in var ind  $\leftrightarrow$  entry ind do
  → Use var ind  $\mapsto$  node(element) data entry to check if data for this variable exists.
  if above is false then
    → Store data in node(element) data.
    → Update var ind  $\mapsto$  node(element) data entry.
  end if
  → Create entry in tree and assign variable data and  $f^n(s^{n-1})$ .
end for
```

```
for every entry at the level  $n + 1$  in tree do
  for every dependency do
    → Extract variable index from the list of dependencies.
    → Assign branch from level  $n$  to level  $n + 1$  using var ind  $\leftrightarrow$  entry ind
  end for →
  Assign the list of branches to entry at level  $n + 1$ .
end for
```

Note, selecting dependencies based on radial distance is just an option. Depending on the requirements of the filter the dependencies may very well be selected based on any other

criteria.

D.1.3 Constructing the abstract physical design variable level

Creating an adv level assumes knowledge of the desired variable type (nodal or elemental) for both the current and pseudo pdv level. Also assumed is the knowledge of the filter radius [28] that determines the adv dependencies on the pseudo pdv. The construction of the adv level is performed in a very similar manner to the pseudo pdv level, except a few minor differences. If the adv type is not nodal or elemental, it is assumed that all adv constitute dependency to every single variable in the pseudo pdv level. Furthermore when creating a new entry in the tree at the adv level, each entry is assigned a sparse gradient vector which accounts for self-dependency (i.e. $\frac{\partial s_i^0}{\partial s_j^0} \delta_{ij} = 1$).

D.1.4 Updating the tree

Updating the tree is fairly straightforward and involves a bottom to top flow of information. Each level of variables is evaluated using the pre-assigned function to that variable and the relevant list of updated variables from the level right below. Gradient vectors associated with each variable follow a similar flow of information and are updated based on the following chain rule, e.g. for design variable s_0^2 in Figure D.2,

$$\frac{ds_0^2}{ds^0} = c_{0,0} \frac{ds_0^1}{ds^0} + c_{0,2} \frac{ds_2^1}{ds^0} ; \quad c_{j,i} = \frac{\partial s_j^n}{\partial s_i^{n-1}}. \quad (\text{D.1})$$

D.2 Constructing $\nabla\phi$ using a point cloud

Working on a modular research-based optimization framework entails having no knowledge about the connectivity of the finite element mesh. Consequently the gradient of the level set field required for evaluating the normal to a surface is computed using a point cloud as in meshfree methods [79]. Let $\hat{\phi}(\mathbf{x})$ be the field function defined in Ω . Using Moving

Least Squares (MLS), the approximation can be defined as:

$$\hat{\phi}(\mathbf{x}) = \sum_{j=1}^m p_j(\mathbf{x}) a_j(\mathbf{x}) = \mathbf{p}^T(\mathbf{x}) \mathbf{a}(\mathbf{x}), \quad (\text{D.2})$$

where m is the number of terms of polynomial basis, and $\mathbf{a}(\mathbf{x})$ is a vector of coefficients which are a function of the spatial coordinate, \mathbf{x} . Furthermore, $\mathbf{p}(\mathbf{x})$ is a vector of basis functions that consists most often of monomials of the lowest order. Thus, e.g. in 2D space, the complete polynomial basis of order m is given by

$$\mathbf{p}^T(\mathbf{x}) = \{1, x, y, xy, x^2, y^2, \dots, x^m, y^m\}. \quad (\text{D.3})$$

Given a set of n nodal values for the field function, ϕ , in the support domain, (D.2) is then used to calculate the approximated values of the field function at these nodes:

$$\hat{\phi}(\mathbf{x}, \mathbf{x}_i) = \mathbf{p}^T(\mathbf{x}_i) \mathbf{a}(\mathbf{x}), \quad i = 1, 2, \dots, n. \quad (\text{D.4})$$

Note that $\mathbf{a}(\mathbf{x})$ is an arbitrary function of the spatial coordinates. A functional, J of weighted residual is constructed using the approximated values of the field function and the nodal function values, $\phi_i = \phi(\mathbf{x}_i)$, such that

$$\begin{aligned} J &= \sum_i^n W(\mathbf{x} - \mathbf{x}_i) [\hat{\phi}(\mathbf{x}, \mathbf{x}_i) - \phi(\mathbf{x}_i)]^2 \\ &= \sum_i^n W(\mathbf{x} - \mathbf{x}_i) [\mathbf{p}^T(\mathbf{x}_i) \mathbf{a}(\mathbf{x}) - \phi_i]^2, \end{aligned} \quad (\text{D.5})$$

where $W(\mathbf{x} - \mathbf{x}_i)$ is a weight function which can be represented, e.g. using an exponential weighting function:

$$W(\mathbf{x} - \mathbf{x}_i) = W(\bar{\mathbf{d}}) = \begin{cases} e^{-(\bar{\mathbf{d}}/\alpha)^2} & \bar{\mathbf{d}} \leq 1 \\ 0 & \bar{\mathbf{d}} > 1 \end{cases}, \quad (\text{D.6})$$

where α is a constant and usually takes the value $\alpha = 0.3$ [79] or $\alpha = 0.4$ [10]. The normalized distance vector, $\bar{\mathbf{d}}$, takes the form $|\mathbf{x} - \mathbf{x}_i|/d_w$ with $d_w = \max(|\mathbf{x} - \mathbf{x}_i|)$. The weighting function plays two important roles:

- (1) The first is to provide weightings for the residuals at different nodes in the support domain such that nodes further from \mathbf{x} have small weights.
- (2) It ensures that the MLS shape functions satisfy the compatibility conditions [79].

The arbitrary function, $\mathbf{a}(\mathbf{x})$, is chosen to minimize (D.5) such that $\partial J/\partial \mathbf{a} = 0$. This results in the following system of linear equations:

$$\mathbf{A}(\mathbf{x})\mathbf{a}(\mathbf{x}) = \mathbf{B}(\mathbf{x})\mathbf{U}_s, \quad (\text{D.7})$$

where \mathbf{A} is called the weighted moment matrix given by

$$\mathbf{A}(\mathbf{x}) = \sum_i^n W_i(\mathbf{x})\mathbf{p}(\mathbf{x}_i)\mathbf{p}^T(\mathbf{x}_i), \quad W_i(\mathbf{x}) = W(\mathbf{x} - \mathbf{x}_i). \quad (\text{D.8})$$

The matrix \mathbf{B} has the form

$$\mathbf{B}(\mathbf{x}) = [\mathbf{B}_1, \mathbf{B}_2, \dots, \mathbf{B}_n], \quad \mathbf{B}_i(\mathbf{x}) = \mathbf{W}_i(\mathbf{x})\mathbf{p}(\mathbf{x}_i), \quad (\text{D.9})$$

and \mathbf{U}_s is the vector of field functions for all the nodes in the support domains. Solving (D.7) for $\mathbf{a}(\mathbf{x})$ leads to

$$\hat{\phi}(\mathbf{x}) = \sum_i^n \sum_j^m p_j(\mathbf{x}) (\mathbf{A}^{-1}(\mathbf{x})\mathbf{B}(\mathbf{x}))_{ji} \phi_i = \sum_i^n \mathcal{N}_i(\mathbf{x})\phi_i = \mathcal{N}(\mathbf{x})\mathbf{U}_s, \quad (\text{D.10})$$

where the MLS shape function, \mathcal{N}_i , is given by

$$\mathcal{N}_i = \mathbf{p}^T \mathbf{A}^{-1} \mathbf{B}_i. \quad (\text{D.11})$$

Note that m is the number of terms of polynomial basis $\mathbf{p}(x)$ which should be much smaller than n . This requirement prevents the singularity of the weighted moment matrix.

In order to obtain partial derivatives of the shape functions we write the shape functions as

$$\mathcal{N}_i(\mathbf{x}) = \boldsymbol{\gamma}^T(\mathbf{x})\mathbf{B}_i(\mathbf{x}), \quad (\text{D.12})$$

where $\boldsymbol{\gamma}(\mathbf{x})$ is the solution to the following system of equations.

$$\mathbf{A}(\mathbf{x})\boldsymbol{\gamma}(\mathbf{x}) = \mathbf{p}(\mathbf{x}). \quad (\text{D.13})$$

The partial derivatives of $\gamma(\mathbf{x})$ can then be obtained as follows:

$$\mathbf{A} \frac{\partial \gamma}{\partial x_k} = \frac{\partial \mathbf{p}}{\partial x_k} - \frac{\partial \mathbf{A}}{\partial x_k} \gamma. \quad (\text{D.14})$$

The partial derivative of the MLS shape functions is then given by,

$$\frac{\partial \mathcal{N}_i}{\partial x_k} = \frac{\partial \gamma}{\partial x_k} \mathbf{B}_i + \gamma \frac{\partial \mathbf{B}_i}{\partial x_k}. \quad (\text{D.15})$$

It is important to note that the MLS shape functions do not satisfy the Kronecker delta criterion $\mathcal{N}_i(\mathbf{x}_j) \neq \delta_{ij} \implies \hat{\phi}(\mathbf{x}_i) \neq \phi_i$. Therefore the MLS shape functions are approximants rather than interpolants. Thus, the approximation of the field function at node i , $\hat{\phi}(\mathbf{x}_i)$, depends not only on the nodal function value ϕ_i but on all nodal function values within the support domain.